IMPERIAL

Engineering Artificial Cell Adhesion, Motility and Haptotaxis using DNA Nanotechnology

Hannah Rachel Sleath

2024

Department of Chemistry
Imperial College London

Thesis submitted for the degree of Doctor of Philosophy

Statements

Statement of Originality

I hereby declare that except where specific reference is made to the work of others, the contents of this dissertation are original and have not been submitted in whole or in part for consideration for any other degree or qualification in this, or any other university. This dissertation is my own work and contains nothing which is the outcome of work done in collaboration with others, except as specified in the text and Preamble. This dissertation contains fewer than 100,000 words including appendices, bibliography, footnotes, tables and equations.

Copyright Statement

The copyright of this thesis rests with the author. Unless otherwise indicated, its contents are licensed under a Creative Commons Attribution-Non Commercial 4.0 International Licence (CC BY-NC). Under this licence, you may copy and redistribute the material in any medium or format. You may also create and distribute modified versions of the work. This is on the condition that: you credit the author and do not use it, or any derivative works, for a commercial purpose. When reusing or sharing this work, ensure you make the licence terms clear to others by naming the licence and linking to the licence text. Where a work has been adapted, you should indicate that the work has been changed and describe those changes. Please seek permission from the copyright holder for uses of this work that are not included in this licence or permitted under UK Copyright Law.

Acknowledgements

This thesis could not have been completed without the help and support from the people surrounding me. The most obvious thank you must go to my supervisors, Dr. Lorenzo Di Michele and Dr. Yuval Elani, for giving me the opportunity to work with them, and for all of their invaluable guidance, advice and contributions throughout this process. I also commend their extreme patience and tolerance with me as I slowly navigated my way through the twisting journey of this PhD.

My research has been hugely influenced and propelled by my collaborator, Prof. Bortolo Mognetti. I thank him for all of his tireless work on the theory and simulations in parallel with my experiments, as well as his never-ending enthusiasm and expertise on the topic of multivalent interactions. Thanks must also go to Dr. Janna Lowensohn, who spent a year working on the numerical modelling during her postdoc with Prof. Mognetti.

I am also grateful for all of the research ideas, experimental tips and welcoming atmosphere offered by members of the various research groups I have been fortunate to be a part of: the Elani group, the Di Michele group, and the wider Membrane Biophysics group.

On a more personal note, I'd like to thank my family for their endless love, support and encouragement, especially over the past few years when I've found myself needing it the most; words can't describe how lucky I am to have you. I'm sure that you'll be glad to no longer have to tiptoe around the forbidden th*sis word any more.

I am grateful to my friends for brightening up my life. I'd like to give a shout out to Vidya, who's been a good friend since our early undergraduate days. Thank you for all of the fun memories we've shared over the years, and for all of the moral support. Hopefully, once this is all over, we will *finally* get to go on that holiday we've been talking about! I'd also like to thank Siân, for our 13+ years of friendship, and for continuing to check in on me even when my WhatsApp response rate has been rather patchy.

To my partner, Connor, who has been by my side through this rollercoaster – I have you to thank for keeping me (somewhat) sane. Thank you for helping me to see the light at the end of the tunnel, and for always believing in me. I look forward to continuing to build our life together.

Lastly, I thank my funding body, the EPSRC, and more specifically the Department of Chemistry for offering me the Chemistry doctoral scholarship to allow me to undertake this PhD.

Abstract

The membrane of a living cell features a plethora of receptor molecules that enable the cell to interact with its external environment. These interactions are often mediated by *multivalent* binding between numerous receptor molecules and specific ligands. In the case of motile adherent cells, the combined strength of multiple weak bonds allows the cell to remain firmly attached to a surface while retaining the ability to perform locomotion, such as during cell crawling and pathogen-host invasion.

In this thesis, I investigate the biophysics of motile adherent cells, through the use of synthetic cells and DNA nanotechnology. I first present a passive motility system, in which lipid vesicles adhere to a substrate through receptor-ligand binding; here, the receptors and ligands consist of synthetic DNA linkers. In particular, I focus on the motion of vesicles over surface density gradients of ligands. Experimental data, supported by numerical and theoretical models, shows that vesicles preferentially drift towards regions with higher ligand density, in a simple form of *haptotaxis*. The haptotactic drift velocity also exhibits correlations with binding strength and vesicle size.

I also present an active motility system, with the aim of improving the motility of adherent vesicles through the incorporation of a burnt-bridges mechanism. Kinetic models are fitted to experimental data to verify the burnt-bridges mechanism and extract key parameters. These findings helped to design subsequent vesicle motility experiments, in which motility was observed to correlate with the rate of bridge burning. Furthermore, the system enables vesicles to remain adhered at lower bridge densities than in the passive system, corresponding to an order-of-magnitude increase in vesicle velocity.

Overall, the findings from this thesis provide insights into the biophysics of multivalent cell adhesion, motility and haptotaxis, along with design rules helpful for the future development of biomimetic motile systems.

Preamble

Publications

Some of the results from experiments, simulations and theory in Chapter 3 are included in a manuscript under revision:

- **Hannah Sleath**, Bortolo Mognetti, Yuval Elani, and Lorenzo Di Michele. Haptotactic motion of multivalent vesicles along ligand-density gradients.

A preprint of the above manuscript can be found on arXiv at Ref. [1].

Collaborations

Numerical modelling and theoretical derivations in Chapter 3 were conducted by Prof. Bortolo Mognetti, informed by experimental parameters and findings from my work. Dr. Janna Lowensohn also contributed to the writing of the simulations in Chapter 3.

Contents

List of Figures **15**

List of Tables **19**

List of Acronyms **21**

1 Introduction **23**

1.1 The biophysics of living cells . . . 23
1.1.1 Multivalent cell adhesion . . . 24
1.1.2 Cell motility . . . 25
1.2 Artificial cells: constructing cell mimics to understand biophysical phenomena . 26
1.2.1 An overview of synthetic biology . . . 26
1.2.2 Synthesis of biomimetic membranes . . . 29
1.3 An introduction to DNA nanotechnology . . . 31
1.3.1 The DNA molecule . . . 33
1.3.2 Thermodynamics of DNA hybridisation . . . 34
1.3.3 Dynamic DNA nanotechnology . . . 36
1.3.4 DNA-mediated multivalent interactions . . . 37
1.3.5 Locomotion facilitated by DNA nanotechnology . . . 41
1.4 Objectives and structure of the thesis . . . 45

2 Materials, Methods and Software **47**

2.1 Manufacturing DNA nanostructures . . . 47
2.1.1 Design and reconstitution of DNA oligonucleotides . . . 47
2.1.2 DNA nanostructure self-assembly . . . 47
2.1.3 Agarose gel electrophoresis . . . 48
2.2 Generating DNA-functionalised vesicles . . . 48
2.2.1 Preparation of giant unilamellar vesicles . . . 48
2.2.2 Functionalisation of vesicles with DNA constructs . . . 49
2.2.3 Preparation of vesicle samples for microscopy imaging . . . 49
2.3 Functionalisation of substrates with DNA constructs . . . 50
2.3.1 Generating DNA-density gradients attached to substrates . . . 50
2.3.2 Visualisation and characterisation of DNA-functionalised substrates . . . 51

2.4 Vesicle motility and burnt-bridge patterning experiments . . . 53
2.4.1 Applying vesicles to ligand-modified substrates . . . 53
2.4.2 Time lapse imaging . . . 53
2.5 Optical microscopy . . . 53
2.5.1 Epifluorescence microscopy . . . 54
2.5.2 Confocal microscopy . . . 54
2.6 Tracking vesicle motion in time lapse recordings . . . 54
2.6.1 Pre-processing image data . . . 54
2.6.2 Identifying vesicle trajectories . . . 55
2.6.3 Filtering trajectory data to relevant regions of the substrate . . . 56
2.6.4 Mean squared displacement analysis and filtering of vesicle data . . . 57

3 Haptotactic drift of multivalent vesicles over ligand-density gradients 59
3.1 Overview of the vesicle motility system . . . 60
3.2 Setting up the experimental system . . . 61
3.2.1 Designing and verifying the DNA constructs . . . 61
3.2.2 Functionalising vesicles with DNA constructs . . . 62
3.2.3 Establishing a method for generating substrate-bound molecular density gradients . . . 63
3.2.4 Verifying DNA-mediated multivalent adhesion of vesicles to substrates . . . 68
3.2.5 Developing a method to segment and track vesicles . . . 68
3.2.6 Apparent bimodal distribution of vesicle diffusion coefficients . . . 69
3.3 Theoretical and numerical modelling . . . 72
3.3.1 Numerical modelling of the vesicle motility system . . . 72
3.3.2 Theoretical estimation of the density of receptor-ligand bridges . . . 74
3.3.3 Theoretical predictions of vesicle drift velocity . . . 75
3.4 Results and discussion . . . 80
3.4.1 Effect of binding strength on directional motion . . . 80
3.4.2 Effect of varying DNA density on vesicle mobility . . . 90
3.4.3 Effect of vesicle size on directional motion . . . 90
3.5 Chapter summary and outlook . . . 94

4 A burnt-bridges adaptation of the vesicle motility system 97
4.1 Overview of the burnt-bridges vesicle motility system . . . 98
4.2 Modelling the kinetics of the burnt-bridges system . . . 99
4.2.1 Modelling the kinetics in bulk solution . . . 99
4.2.2 Modelling the bridge-burning patterns formed within vesicle adhesion patches . . . 101
4.3 Verifying and fitting the bridge-burning DNA mechanism in bulk solution . . . 110
4.3.1 Agarose gel electrophoresis to verify constructs and binding kinetics . . . 111
4.3.2 Fluorescence experiments to fit the kinetics in bulk . . . 113

4.4 Verifying the bridge-burning mechanism in the experimental vesicle system . . . 116
4.5 Fitting the reaction-diffusion dynamics of experimental bridge-burning patterning of substrates . . . 118
4.5.1 Fit results from the reaction-diffusion model . . . 120
4.6 Vesicle motility experiments . . . 125
4.6.1 Effect of varying fuel concentration on vesicle mobility . . . 127
4.6.2 Effect of varying substrate DNA density on vesicle mobility . . . 129
4.6.3 Vesicle motion relative to the gradient direction . . . 131
4.7 Chapter summary and outlook . . . 133

5 Conclusions and future research directions **135**
5.1 Summary . . . 135
5.2 Directions for future research . . . 136
5.2.1 Further exploration of the vesicle motility systems . . . 136
5.2.2 An enzymatic approach to the burnt-bridges system . . . 138
5.2.3 Extending the theoretical framework and numerical model . . . 140

References **143**

Appendix A Nanostructures and their sequences **171**
A.1 Nanostructures for Chapter 3 . . . 171
A.2 Nanostructures for Chapter 4 . . . 173

Appendix B Supplementary theory for Chapter 3 **174**
B.1 Proof of Equation 3.18 . . . 174

Appendix C Supplementary figures **176**

List of Figures

1.1 Key components of the biological cell and the plasma membrane 24
1.2 Artificial cells are engineered to mimic the structure and functions of their biological counterparts 27
1.3 Lipids self-assemble in solution as a result of their amphiphilic nature 30
1.4 DNA origami can be used to build a variety of shapes of nano-scaled structures . 32
1.5 DNA duplexes self-assemble into a double-helix structure as a result of base interactions 33
1.6 Toehold-mediated strand displacement (TMSD) is a mechanism used to exchange one strand of a DNA duplex with another 36
1.7 Biomimetic membranes can be functionalised with amphiphilic DNA nanostructures to mediate membrane interactions such as adhesion 38
1.8 Implementations of DNA-mediated multivalent interactions in biomimetic systems 39
1.9 Various designs for DNA walkers capable of autonomous locomotion have been implemented 43

2.1 Schematic of the method used to generate DNA-density gradients adhered to a substrate 50
2.2 Fluorescence images of ligand coverage are normalised to account for non-uniform illumination 51
2.3 Calibration curve for determining ligand density from fluorescence measurements 52
2.4 Processing and segmenting microscopy images of vesicles 55
2.5 Comparing the direction of vesicle motion to the direction of the DNA-density gradient 56
2.6 Plot of the DNA gradient vector field superimposed on a fluorescence image of the ligand coverage 57

3.1 Schematic of the experimental vesicle motility system 60
3.2 Agarose gel electrophoresis confirms the successful formation of receptor and ligand constructs, and binding of complementary sticky ends 62
3.3 The receptor-functionalised GUV samples are polydisperse and capable of adhering to ligand-coated substrates 63
3.4 Preliminary microfluidic designs for generating molecular gradients 65
3.5 A typical ligand-density gradient 67

3.6 Estimated vesicle diffusion coefficients appear to exhibit a bimodal distribution . 69
3.7 Examples of trajectories and mean squared displacements plotted for individual vesicles . . . 71
3.8 Vesicle motion is constrained by receptor-ligand bridges, forming the basis of numerical modelling . . . 73
3.9 Under experimental conditions, the density of receptor-ligand bridges is saturated and reaches its maximal value . . . 76
3.10 Experimental results reveal that drift velocity increases with decreasing sticky end length . . . 81
3.11 Simulation results support experimental findings that drift velocity increases with decreasing sticky end length . . . 82
3.12 Vesicles functionalised with longer sticky ends diffuse more slowly . . . 84
3.13 For weakly binding systems, the adhesion strength is insufficient for the vesicles to remain attached to the substrate . . . 86
3.14 Comparison of simulated and theoretical vesicle displacements along the gradient over time, for varying gradients and bridge densities . . . 88
3.15 Comparison of simulated and theoretical vesicle displacements along the gradient over time, for varying gradients . . . 89
3.16 Drift velocity increases with increasing vesicle diameter . . . 91
3.17 Vesicles do not exhibit a trend between average velocity perpendicular to the gradient and vesicle diameter . . . 92

4.1 Schematic of the burnt-bridges system . . . 99
4.2 Extracting the intensity profile of a bridge-burning pattern . . . 106
4.3 Comparison of an experimental bridge-burning pattern with a fitted model, and the corresponding residual map . . . 108
4.4 Fitting the quenching factor and experimental image resolution to the normalised intensity profile of an experimental bridge-burning pattern . . . 109
4.5 Agarose gel electrophoresis confirms the successful formation of DNA constructs for the burnt-bridges system . . . 111
4.6 Fluorescence experiments verify the burnt-bridges mechanism in bulk solution and the catalytic behaviour of the GUV construct . . . 114
4.7 A global fit of the rate constants and quenching ratio, for the bridge-burning mechanism in bulk solution . . . 115
4.8 Fluorescence quenching allows for visualisation of the bridge-burning process in the vesicle motility system . . . 116
4.9 Visible propagation of a bridge-burning front within the contact region of a vesicle on a substrate . . . 117
4.10 Increasing the concentration of magnesium in bulk solution appears to increase the rate of bridge-burning . . . 119
4.11 Distributions of parameters fitted to experimental bridge-burning pattern data . 121

4.12 Plots of the mean squared residuals reveal the precision and correlations of the reaction-diffusion model . . . 124
4.13 Distributions of GUV diameter and estimated diffusion coefficient for vesicles studied in the burnt-bridges motility experiments . . . 126
4.14 Increased fuel concentration in the burnt-bridges system results in increased vesicle mobility . . . 128
4.15 Increased density of substrate DNA results in decreased vesicle mobility . . . 130
4.16 Convection effects appear to overcome directional drift along the gradient in the more mobile burnt-bridges vesicle motility system . . . 132

5.1 Schematic of a vesicle motility system where enzymes are used to implement a burnt-bridges mechanism . . . 139

C.1 Full data showing that vesicles functionalised with longer sticky ends diffuse more slowly . . . 177
C.2 Size distributions of vesicles recorded in vesicle motility experiments in Chapter 3, shown for the mobile vesicle population and for all vesicles combined . . . 178
C.3 Full experimental data showing that vesicle drift velocity increases with decreasing sticky end length . . . 179
C.4 Full experimental distributions of vesicle velocities relative to the gradient direction 180
C.5 Full trajectory data from simulations, for varying vesicle diameter and sticky end length . . . 181
C.6 Full distributions of simulated vesicle velocities relative to the gradient, for varying vesicle diameter and sticky end length . . . 182
C.7 Full distributions of average vesicle velocity parallel to the gradient binned by vesicle size, from experimental data . . . 183
C.8 Full distributions of average vesicle velocity parallel to the gradient binned by vesicle size, from simulation results . . . 184
C.9 Full distributions of average vesicle velocity perpendicular to the gradient binned by vesicle size, from experimental data . . . 185
C.10 Full distributions of average vesicle velocity perpendicular to the gradient binned by vesicle size, from simulation results . . . 186
C.11 Full distributions of absolute vesicle displacement for varying fuel concentration in the burnt-bridges adaptation of the vesicle motility system . . . 187
C.12 Full data from burnt-bridges vesicle motility experiments where the density of substrate DNA has been varied . . . 188
C.13 Full data from burnt-bridges vesicle motility experiments, comparing vesicle motion to the direction of the gradient . . . 189

List of Tables

2.1 Fluorophores and their excitation and emission maxima 53

3.1 Hybridisation free energies and unbinding rates of sticky ends 74

A.1 Receptor and ligand constructs for Chapter 3, and the oligonucleotides they are composed of 171
A.2 Sequences and modifications of oligonucleotide strands for Chapter 3 172
A.3 Receptor and ligand constructs for Chapter 4, and the oligonucleotides they are composed of 173
A.4 Sequences and modifications of oligonucleotide strands for Chapter 4 173

List of Acronyms

18:1 Liss Rhod PE 1,2-dioleoyl-sn-glycero-3-phosphoethanolamine-N-(lissamine rhodamine B sulfonyl) (ammonium salt)

ATP adenosine triphosphate

CAM cell adhesion molecule

CB constraining bridge

DNA deoxyribonucleic acid

DOPC 1,2-Dioleoyl-*sn*-glycero-3-phophocholine

dsDNA double-stranded DNA

ECM extracellular matrix

GUV giant unilamellar vesicle

HA hemagglutinin

HPLC high performance liquid chromatography

ITO indium tin oxide

LED light-emitting diode

LUV large unilamellar vesicle

MHF microfluidic hydrodynamic focusing

MSD mean squared displacement

NBD-PE 1,2-dioleoyl-sn-glycero-3-phosphoethanolamine-N-(7-nitro-2-1,3-benzoxadiazol-4-yl) (ammonium salt)

PDMS polydimethylsiloxane

PiDSD proximity-induced DNA strand displacement

PSF point spread function

RNA ribonucleic acid

SA sialic acid

SLB supported lipid bilayer

ssDNA single-stranded DNA

SUV small unilamellar vesicle

TBE Tris-borate-EDTA

TE Tris-EDTA

TMSD toehold-mediated strand displacement

Chapter 1

Introduction

1.1 The biophysics of living cells

Cells are the basic units of all living organisms, with complex structures that are designed to enable specific biological functions. Since the discovery of the cell in 1665 [2], biologists have uncovered a range of intracellular processes, including DNA replication [3, 4], cellular respiration [5] and protein synthesis [6, 7]. Cells may also interact with their external environments in a variety of ways, including cell signalling [8], cell adhesion [9], or motion in response to external triggers [10]. The vast variety and complexity of living cells offer interesting challenges from a physics standpoint; the field of cell biophysics aims to deepen our current understanding of cell functions by studying their underlying physical principles [11, 12].

Cells generally consist of a cytoplasmic region enclosed in a membrane; a schematic of a biological cell and its key components is shown in Figure 1.1. The cell membrane (also referred to as the plasma membrane) is composed of a phospholipid bilayer, which, as its name suggests, consists of two lipid monolayers (also referred to as leaflets). The bilayer is interspersed with cholesterol molecules and proteins [13]; these proteins may interact transiently with the membrane (peripheral proteins), or may be permanently embedded in the cell membrane (integral proteins). The latter can be further categorised into transmembrane proteins that span the width of the membrane, or integral monotopic proteins that associate with one side of the membrane [14].

There are many types of cell membrane proteins that each play a key role in cell interactions with the external environment. Membrane proteins that receive and transduce signals are referred to as *receptors* [15]; typically, the signals consist of specific extracellular molecules referred to as *ligands*, which may be (but are not limited to) hormones, growth factors, neurotransmitters or nutrients. During signal transduction, an extracellular ligand binds to the membrane receptor, activating intracellular signalling proteins that initiate a signalling cascade and lead to changes in the behaviour of the cell [16]. Membrane receptors may alternatively mediate cell adhesion; in this case, the receptors are referred to as cell adhesion molecules (CAMs), and either bind with the extracellular matrix (ECM) or CAMs on other cells [17, 18].

This PhD focuses on the biophysics of multivalent adhesion and motility, two phenomena

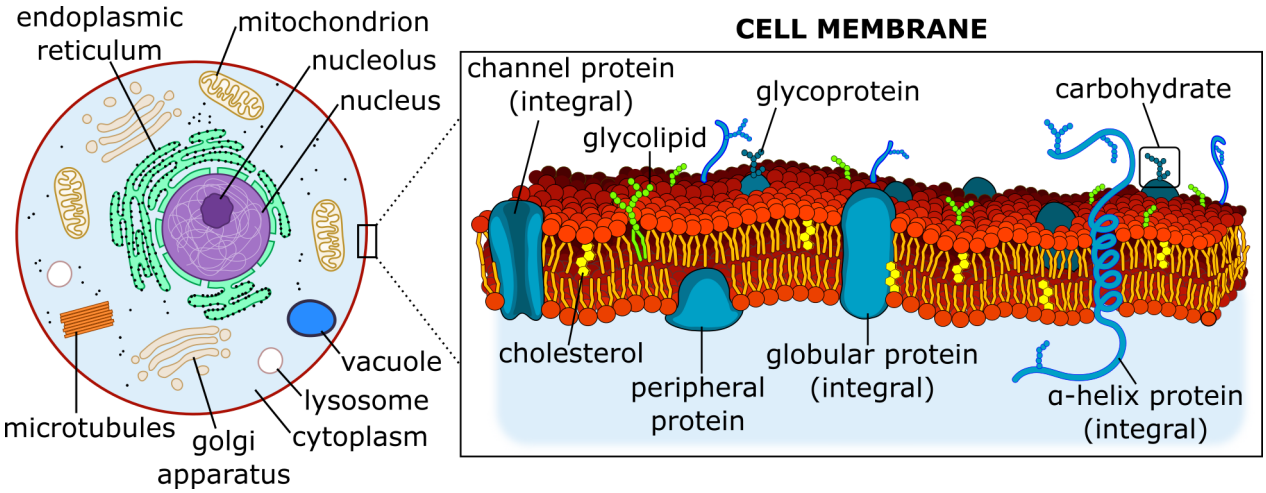


Figure 1.1: **Key components of the biological cell and the plasma membrane.** Biological cells have complex interior environments with organelles designed to perform specialised cellular tasks (diagram on the left of an animal cell and some of its key components; adapted from a diagram by Tomáš Kebert, available in Wikimedia Commons under a CC BY-SA 4.0 license). The cell is enclosed by a cell membrane (also referred to as the plasma membrane) that consists of a phospholipid bilayer decorated with many types of integral and peripheral proteins, glycoproteins and glycolipids (schematic in the inset; adapted from a diagram by Mariana Ruiz, available in Wikimedia Commons and released into the public domain).

that are crucial to the functioning of biological cells; these topics are discussed in the following sections 1.1.1 and 1.1.2. To investigate these phenomena, artificial cell mimics were used as the basis of experimental systems, along with synthetic receptors constructed from DNA; an overview of the field of synthetic biology and artificial cells is given in Section 1.2, while an introduction to DNA nanotechnology is provided in Section 1.3. Finally, the objectives of this PhD and the structure of this thesis are outlined in Section 1.4.

1.1.1 Multivalent cell adhesion

Many biological structures and functions rely on the attachment of cells to other cells, objects or surfaces *via* the binding of cell membrane receptors, in a process known as *cell adhesion*. One obvious example is the adhesion of cells to each other to form tissues, which subsequently make up the organs within a multicellular organism [9, 19]. Cell adhesion receptors play a central role in the migration of certain cells (*e.g.* human fibroblasts), by coupling interactions between the cytoskeleton-associated motile apparatus of the cell and the substrate over which the cell is migrating; the cell then uses the adhesive interaction to generate the tractive force required for motion [20]. Adhesion also contributes to biological phenomena such as viral invasion *via* endocytosis [21], and cell signalling [22].

Cell adhesion is typically mediated by a large number of molecular bonds between cell membrane receptors and ligands on the object or surface to which the cell is adhered, in which case it is known as *multivalent* adhesion (where valency refers to the number of simultaneous bonds) [23, 24, 25]. The accumulated adhesion strength is enhanced in comparison to the strength of the individual bonds, which may themselves be weak and labile [26, 27]. For

example, the influenza virus attaches to the host cell *via* multiple bonds between hemagglutinin (HA) glycoproteins on the viral surface and sialic acid (SA) moieties on the surface of the host cell [28]. The multivalency results in strong attachment of the virus to the host cell, despite the individual bonds being relatively weak with millimolar dissociation constants [29].

Another example of multivalent adhesion in biology is the formation of focal adhesions, which are large, dynamic protein complexes comprised of transmembrane receptors and intracellular proteins that continuously associate and disassociate with the complex over time [20]. Cells form focal adhesions to mechanically link the intracellular cytoskeleton with the extracellular substrate (usually the ECM) *via* multiple receptor proteins; the focal adhesions enable strong attachment of the cell to the substrate, while also acting as hubs for concentrating and directing biochemical signals [30]. The cell may use focal adhesions as stable anchoring points to push or pull itself over the extracellular substrate during cell migration [20].

Due to the interplay between enthalpic and configurational effects [31], complex and useful behaviours such as binding super-selectivity [32, 33] can emerge from multivalent interactions, making them a topic of interest in biophysics. Indeed, numerous biophysical studies have been conducted to investigate various aspects of multivalent adhesion. These include the strength and rate of adhesion [34, 35, 36, 37, 38]; the growth, size and stability of the contact region between adhering objects [39, 40]; the self-assembly or fusion of colloidal particles [41, 42, 43, 44, 45, 46, 47]; and receptor-mediated endocytosis [48]. Investigations into DNA-mediated multivalent adhesion in biomimetic systems are covered in more detail in Section 1.3.4.

1.1.2 Cell motility

Another theme of cell biology that has garnered the attention of biophysicists is cell motility, *i.e.* the ability of a cell to move from one point in space to another. Cell motility and the collective migration of cells play an essential role in a large variety of biological phenomena, such as embryonic development [49, 50], wound repair and tissue regeneration [51, 52], cancer invasion [49, 53], and the immune response [54, 55]. Different modes of cell motility exist, including the swimming of flagellates like animal sperm cells [56]; the twitching motility of bacteria due to the action of grappling hook-like filaments [57, 58]; and the gliding or crawling of eukaryotic cells adhered to a surface [59, 60].

Cell locomotion that occurs in response to an external stimulus is known as *taxis*. A common example is chemotaxis, the directed motion of a cell along gradients of soluble chemicals; this type of motion occurs in the directional swimming of algae [61] and bacteria [62] towards nutrients, and of sperm towards the egg cell [63]. Cell locomotion may alternatively be directed along gradients in temperature (thermotaxis) [64], light (phototaxis) [65] or other physical factors [66, 67]. Furthermore, cells may instead move along magnetic [68], electric [69] or gravitational [70] field lines; these types of motion are referred to as magnetotaxis, galvanotaxis and gravitaxis, respectively.

Haptotaxis

Cell motility often occurs in conjunction with cell adhesion, such that the cell moves along a surface while remaining adhered to it. Directed motion of adherent cells is observed in a range of biological contexts, such as the diffusion of Influenza A [71, 72] and Herpes [73] viruses along the host cell membrane prior to invasion.

In many instances, motion directionality in multivalent adhesion systems occurs as a result of gradients in surface-bound chemicals or cellular adhesion sites on the substrate to which the cell is attached; this type of motion is referred to as *haptotaxis*. For example, tumour cells have been observed to adhere and migrate along density gradients of serum spreading factor [74], a glycoprotein component of human serum that influences the growth, migration and differentiation of a variety of animal cells. Additionally, ECM proteins (fibronectin, vitronectin and collagen I) have been observed to induce chemotaxis and haptotaxis in mesenchymal stem cells, which are critical to tissue repair and regeneration [75]. Haptotaxis has also been observed in myoblasts, fibroblasts, leukocytes and Schwann cells [76, 77, 78, 79, 80].

The mechanisms governing the haptotaxis of adherent cells are not yet fully understood, and are an ongoing field of research. In some cases, the motion is considered to be driven by an active mechanism, in which internal biochemical cascades result in modification of the cell motility machinery to adapt their orientation along the gradient [78]. Alternatively, haptotactic motion or re-orientation of the cell along the gradient could arise as a result of a passive mechanism, due to the tug-of-war in the cell adherence zone; areas with lower binding strength detach spontaneously in favour of areas with higher binding strength [77, 81].

The passive mechanical drift of adherent cells along ligand gradients is a complex statistical mechanical process, requiring the dynamic formation and breakage of numerous adhesive bonds as the cell moves along the extracellular substrate. In the example of focal adhesions (mentioned in Section 1.1.1), focal adhesions near the trailing edge of the cell must dissolve to allow the cell to continue to travel, although the underlying mechanism is currently not fully understood [82, 83, 84]. Passive haptotactic drift along ligand-density gradients thus offers another interesting yet complex challenge for biophysicists to tackle.

1.2 Artificial cells: constructing cell mimics to understand biophysical phenomena

1.2.1 An overview of synthetic biology

Synthetic biology is a multidisciplinary branch of science centred around the application of engineering principles to develop new biological parts, devices and systems. A key example of a synthetic biological system is the artificial cell, an engineered particle that mimics the structure and functions of a biological cell, with the potential for additional non-biological capabilities [85]; a summary of some key functionalities of artificial cells is depicted in Figure 1.2. Further themes of synthetic biology include engineering synthetic mimics of tissues such as skin,

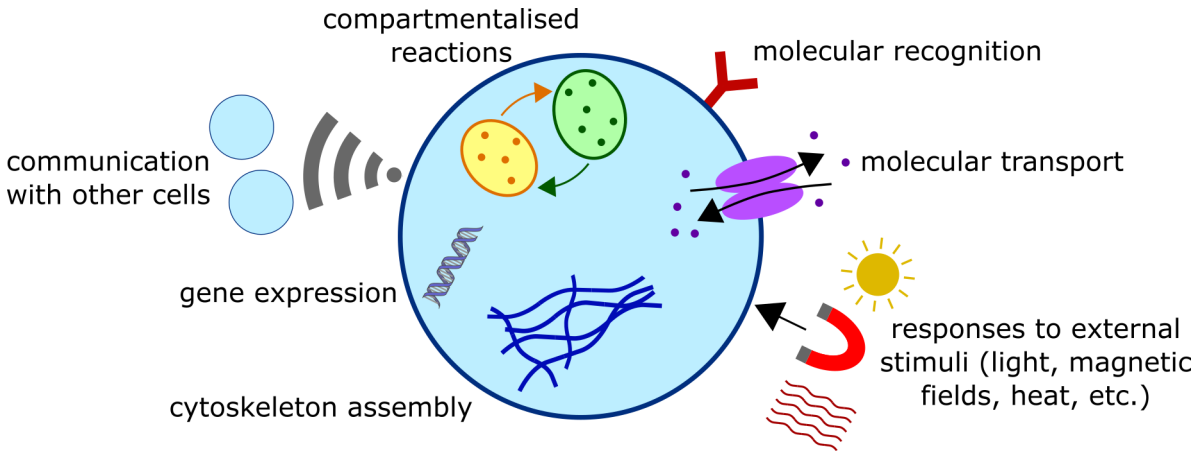


Figure 1.2: **Artificial cells are engineered to mimic the structure and functions of their biological counterparts.** Synthetic cells can be constructed from the bottom-up from simple chemical and biological components to impart functionalities ranging from sensing and molecular recognition to gene expression and inter-cellular communication.

muscles and vasculature [86]; and the manufacture of complete synthetic genomes that can be transplanted into living cells to reprogramme their metabolic functions [87].

Bottom-up versus top-down engineering

Synthetic biology and the production of artificial cells can be tackled from either a top-down or bottom-up approach. The top-down methodology involves taking pre-existing, living cells and altering them to impart new functions [88, 89]. A well-known example of top-down synthetic biology is genetic engineering; for instance, certain strains of bacteria have long been used in the food production industry, and have been genetically modified to operate more efficiently, increase output, reduce toxic by-products and create improved compounds [90]. Bacteria, plant cells, yeast and mammalian cells have also been genetically modified to make vaccines [91], enzymes [92], antibiotics [93], antibodies [94] and much more. Top-down engineering is the more developed approach to synthetic biology compared with building the artificial cell from scratch [85]. Furthermore, the top-down approach has the inherent advantage of exploiting the existing components and functionalities of the living cell, generating cells that closely approximate non-engineered cells with their intricate metabolic pathways. However, this comes with the caveat that the complexity of top-down synthetic cells can hinder their use as cell models or in further applications [85]. For example, in applications where a living cell has been engineered to generate a target product, the multitude of pre-existing cellular processes can compete with the production of the target product and reduce the efficiency of the application. Living cells may also suffer from toxicity issues when artificial components are introduced.

In contrast, the bottom-up approach makes use of simple biological and chemical components, such as lipids, proteins, sugars and DNA, to construct mimics of biological systems *in vitro* [95]. In the context of building artificial cells, one key advantage of the bottom-up approach is that it reduces the complexity of a living cell to its basic fundamental features, thus making the artificial cell easier to design, control and study. As artificial cells can be engineered

to carry out specific functions, this reduces waste of resources and energy on other functions that biological cells perform. Additionally, bottom-up synthetic cells provide the opportunity for incorporation of non-biological components or processes which would interfere with the functioning of a living cell (or even cause cell death) [96]

Uses of artificial cells

Artificial cells have been designed for a wide range of purposes, including modelling biological cells to study their structures and functionalities. The plasma membrane has historically been the most well-developed cellular component to be mimicked and studied in synthetic biology [85]. The ability to fine-tune various aspects of artificial cell membranes allows for studies of their effects on biological processes, such as membrane composition [97], asymmetry [98], and lateral organisation [99]. For example, artificial cells have been built to mimic bacteria and study the diffusion of antibiotics through the bacterial cell membrane [100]. This line of research is important in the development of antibiotics, as one key factor in antibiotic resistance is the permeability (or rather the lack thereof) of the bacterial cell membrane to drug molecules [101, 102, 103]. Direct measurements of passive transport of antibiotics across living bacterial cells have proven to be difficult, due to the small size of bacteria and the complication of isolating the diffusive motion across the membrane from other transport modes [104, 105]. Artificial cells provide a solution to these issues, as well as offering high control over membrane composition and ease of measurement relative to living bacterial systems.

Artificial cells have also been used to study the biophysics of the cytoskeleton, a network of protein filaments and microtubules within the cell cytoplasm that maintains the shape of the cell, is responsible for the organisation and movement of various organelles within the cell, and often plays a key role in the locomotion of the cell itself. Locomotion of eukaryotic cells is typically driven by the elongation of protein polymers by successive addition of monomeric units; the extending filament mechanically deforms the cell and causes the growth of temporary protrusions at the surface known as *pseudopodia*, which contributes to the crawling motion of eukaryotic cells such as amoeba [106, 107]. Actin is a highly abundant protein that forms filaments in the cytoskeleton, and its role in cell deformation and locomotion has been extensively studied with the use of artificial cells [108, 109]. For example, by coupling an artificial cell to actin filaments and monitoring changes in the shape of the cell, the spatial distribution and temporal dynamics of actin polymerisation forces exerted on the lipid bilayer were characterised [110].

Beyond the aforementioned studies on the plasma membrane and cytoskeleton, artificial cells have been used as compartments to investigate the behaviour of biomolecules and metabolic reaction *in vitro*. The effects of confinement and compartmentalisation on protein function and enzymatic reactions have been investigated; it has been demonstrated that macromolecular crowding increases the robustness of gene expression [111]. These findings are relevant to biological cells, as up to 40% of the total cellular volume is occupied by macromolecules [112]. In addition, artificial cells are a powerful tool for studying gene circuitry and protein expres-

sion [113, 114], as they allow systematic variation of the concentrations of relevant biomolecules such as genes, ribosomes polymerases, and adenosine triphosphate (ATP); and fine control over parameters such as the redox state of ATP.

Artificial cells have also been manufactured for practical applications, made possible by the versatility of the cells with respect to their composition, size and capacity for embedding and encapsulating materials. By generating cells using biocompatible components, the cells can be introduced to the body and employed for medical uses [115, 116]. Applications include the use of synthetic cells as microscopic vehicles for drug transport in the body [117], and as analytical tools [118] in immunoassays [119] and biosensors [120].

1.2.2 Synthesis of biomimetic membranes

At its most basic level, the structure of a living cell can be simplified to an aqueous compartment contained within a semi-permeable boundary or membrane. Common components used to construct this membrane include lipids [121], polymers [122] and proteins [123]. Alternatively, artificial cells have been engineered using droplets [124] and Pickering emulsions [125]. Artificial cell membranes composed of lipids bear the most similarity to the phospholipid membrane that encloses biological cells, and form the basis of experimental systems in this PhD.

Biophysics of lipid self-assembly

Lipids are a diverse group of fatty, oily or wax-like organic compounds that are insoluble in water, and soluble in organic solvents such as alcohol, ether and chloroform [126]. Examples of lipids include phospholipids, fatty acids, and sterols [127]. Phospholipids are amphiphilic molecules, with a hydrophilic "head" consisting of a phosphate group, and two hydrophobic "tails" derived from fatty acids; these are typically joined by a glycerol "backbone" [128]. Due to their amphiphilic nature, phospholipids self-assemble when dispersed in aqueous solution; the self-assembly is driven by hydrophobic interactions, as the molecules arrange themselves to protect their hydrophobic "tails" from the surrounding liquid while exposing their hydrophilic heads [129]. Lipids may self-assemble into a variety of supramolecular structures, categorised as spherical micelles, cylindrical micelles or bilayers (schematised in Figure 1.3). The self-assembly structure is influenced by the geometry of the individual lipid molecules; this can be summarised with the dimensionless packing parameter p of the lipid *i.e.*

$$p = \frac{v_0}{a_0 l_c}, \tag{1.1}$$

where v_0 and l_c are the volume and critical length of the hydrocarbon tail respectively, and a_0 is the area of the phosphate head. Typically, spherical micelles form when $p \leq 1/3$, while cylindrical micelles form when $1/3 < p \leq 1/2$ [130]. The lipids self-assemble into bilayers (also referred to as the lamellar phase) for $1/2 < p \leq 1$, taking on a planar bilayer form when $p \approx 1$, and forming a closed spherical structure (known as a *vesicle*) otherwise. Finally, inverted micelles form when $p > 1$ if the lipids are instead immersed in oil-based solvents.

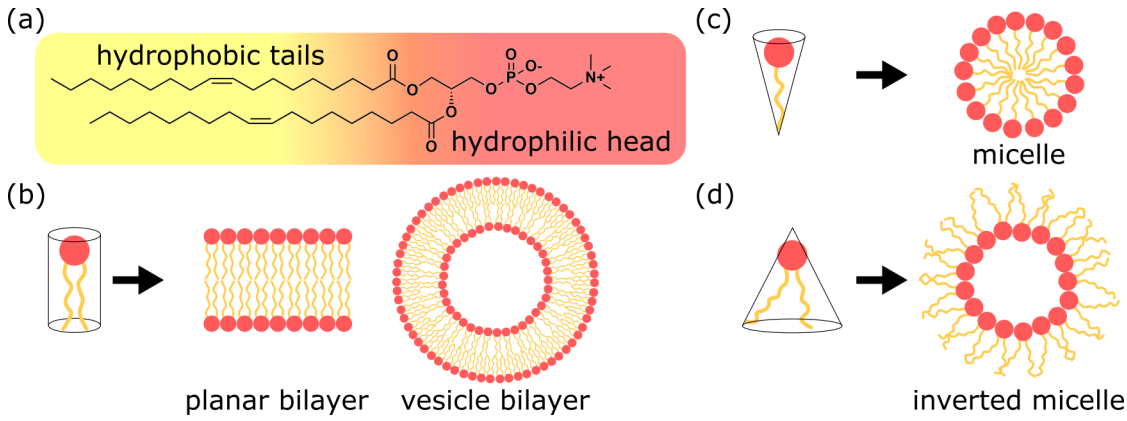


Figure 1.3: **Lipids self-assemble in solution as a result of their amphiphilic nature.** The chemical structure of a lipid (DOPC) is shown in (a), highlighting the hydrophobic "tails" and hydrophilic "head". When in solution, lipids self-assemble into various structures; the conformation of the self-assembled structure depends on the geometry of the individual lipid molecules. These structures include micelles and bilayers (in aqueous solution) or inverted micelles (in non-aqueous solution).

The lipid bilayer structure consists of two layers (also referred to as leaflets) of lipid molecules, arranged with the hydrophobic tails from both leaflets directed towards each other in the centre of the bilayer, and the hydrophilic heads exposed to the aqueous phase surrounding the bilayer [131]. Various characteristics of the lipid molecules influence the physical properties of the overall bilayer. For example, the length and degree of saturation (or number of double carbon-carbon bonds) of the fatty acid tails influences the packing and relative mobility of lipid molecules within the bilayer, which characterises the different phases in which bilayers may exist. In the liquid (or fluid) phase the lipids can diffuse laterally across the surface of the membrane, whereas in the gel phase the bilayer is solid-like and lateral motion of lipids is impeded. All lipids have a characteristic melting temperature (T_{m}) at which the thermal energy is sufficient to overcome the attractive van der Waals forces between the lipid molecules, and the bilayer transitions from gel to liquid phase [132]. For example, the melting temperature of the lipid 1,2-Dioleoyl-*sn*-glycero-3-phophocholine (DOPC) is -17°C; DOPC bilayers exist in the fluid phase above this temperature [133]. Note that it is possible for different phases to co-exist within a bilayer [134].

Structure and production of vesicles

Lipid bilayers behave like elastic membranes and can easily deform and bend, although most cannot stretch more than a few percent before breaking [135]. They may exist as 2D planar sheets, or may bend to form spherical vesicles where the additional bending energy is accounted for by the absence of the energetic cost of edges. Vesicles can comprise of a single lamellar phase lipid bilayer, in which case they are referred to as *unilamellar* vesicles; alternatively, vesicles may comprise of several lipid bilayers arranged in an "onion-like" structure, in which case they are referred to as *multilamellar* vesicles. Unilamellar vesicles may be further identified by their size, and fall into the following categories: small unilamellar vesicles (SUVs) with a size

<0.1 μm, large unilamellar vesicles (LUVs) with a size between 0.1–1 μm, and giant unilamellar vesicles (GUVs) with a size >1 μm [136]. Unless specified otherwise, GUVs were chosen for vesicle experiments in this PhD, as the larger size allows for increased ease of visualisation.

Vesicles can be produced *via* a variety of methods, which may be broadly classified into traditional bulk-scale and emulsion-based methods, along with more recently developed microfluidic methods. The bulk production of vesicles relies on self-assembly of lipids in a bulk phase, and includes methods such as thin-film hydration [137], ethanol injection [138] and detergent dialysis [139]. Thin-film hydration is one of the most widely used vesicle preparation techniques, and involves hydration of a lipid film, along with mechanical agitation to encourage the film to peel away from its support and enable vesicles to form. This typically results in the formation of multilamellar vesicles [137]. Other types of vesicles (*e.g.* unilamellar vesicles) can then be prepared from these multilamellar vesicles *via* sonication or extrusion through filters; the diameter of extruded vesicles depends on the filter pore size [140]. GUVs can also be synthesised directly from thin-films by applying an alternating electric field during the hydration of the film; this method is known as electroformation [141], and was used to generate GUVs throughout this PhD (see Section 2.2.1 for further details). In contrast, emulsion-based approaches such as phase transfer [142] start with an emulsion of water-in-oil (or oil-in-water) droplets stabilised by lipid monolayers, which are then enclosed in a second layer of lipids to form the bilayer. Emulsion-based methods have the advantage of higher encapsulation efficiency, offering the ability to control the composition of the solution within the vesicles separately from the surrounding fluid [140].

The methods of bulk vesicle production are typically straightforward, but the reliance on self-assembly of lipids is heterogeneous and uncontrolled, leading to vesicle samples that are polydisperse in size and lamellarity. Conversely, microfluidic methods enable high control over the production of vesicles, with the careful manipulation of liquid flows through micron-scale channels [143]. A variety of microfluidic methods for vesicle production have been developed, including droplet-based microfluidic methods [144, 145, 146] and microfluidic hydrodynamic focusing (MHF) methods [147, 148].

1.3 An introduction to DNA nanotechnology

Described as the "molecule of life", deoxyribonucleic acid (DNA) carries the genetic information for the development and functioning of all living organisms [149]. Consequently, DNA is often considered in its biological context as a key component of the central dogma of molecular biology [150]. However, progress in DNA synthesis [151] and modification [152] has subsequently led to expanded interest in DNA beyond its role in biology. In the field of DNA nanotechnology, DNA is instead used as a structural or functional material. The unique and predictable binding of DNA molecules enables the construction of two- or three-dimensional DNA nanostructures with useful and versatile properties [153]. Furthermore, the biocompatibility of DNA and its resistance to degradation (in comparison with other biomolecules such as proteins and

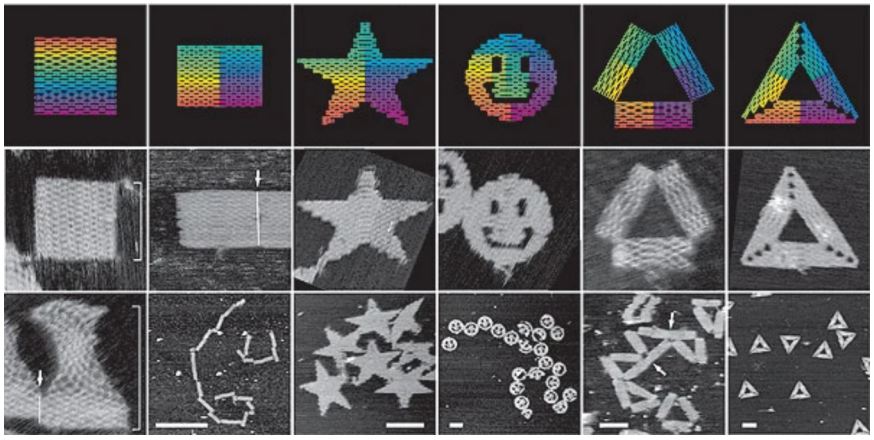


Figure 1.4: **DNA origami can be used to build a variety of shapes of nano-scaled structures.** Examples of various DNA structures designed and built *via* DNA origami by Rothemund Lab are shown here, with computer-generated designs in the top row and corresponding atomic force microscopy images in the bottom two rows (scale bar = 50 nm). Adapted with permission from Ref. [153].

RNA) offers great potential for application to biological and therapeutic systems. For example, DNA nanotechnology has been used to engineer synthetic versions of biological cell components including cytoskeletons [154] and cell membrane-sculpting proteins [155], as well as entire synthetic cells [156].

DNA nanotechnology is conventionally divided into two main branches: *structural* and *dynamic*. Structural DNA nanotechnology concerns the use of DNA molecules as building blocks to assemble two- and three-dimensional structures in a static, equilibrium-end state [157]. As the nucleotide occupies an approximate cylindrical space that is 0.34 nm wide and 1 nm long, this allows the design of structures at a similar nanoscale resolution [158]. Since structural DNA nanotechnology was founded in 1982 by Nadrian Seeman [159], a wide variety of nanostructures have been engineered, including crystal lattices [160, 161], nanotubes [162, 163, 164] and polyhedra [165, 166]. Even more complex and arbitrary shapes can be built *via* DNA origami, a process involving the folding of a long single strand of DNA, which is then held in shape by multiple smaller "staple" strands [153]. Examples of DNA origami structures built by Rothemund Lab are shown in Figure 1.4.

On the other hand, dynamic DNA nanotechnology focuses on the construction of DNA complexes with interesting non-equilibrium behaviour [158]. Typical functionalities include the ability of the DNA complex to undergo controlled motion or reconfigure in response to a chemical or physical stimulus. Dynamic DNA nanotechnology is discussed in further detail in Section 1.3.3.

In the rest of this introduction to DNA nanotechnology, the structure of the DNA molecule is explored, before delving into the thermodynamics of DNA hybridisation and the applications of DNA nanotechnology.

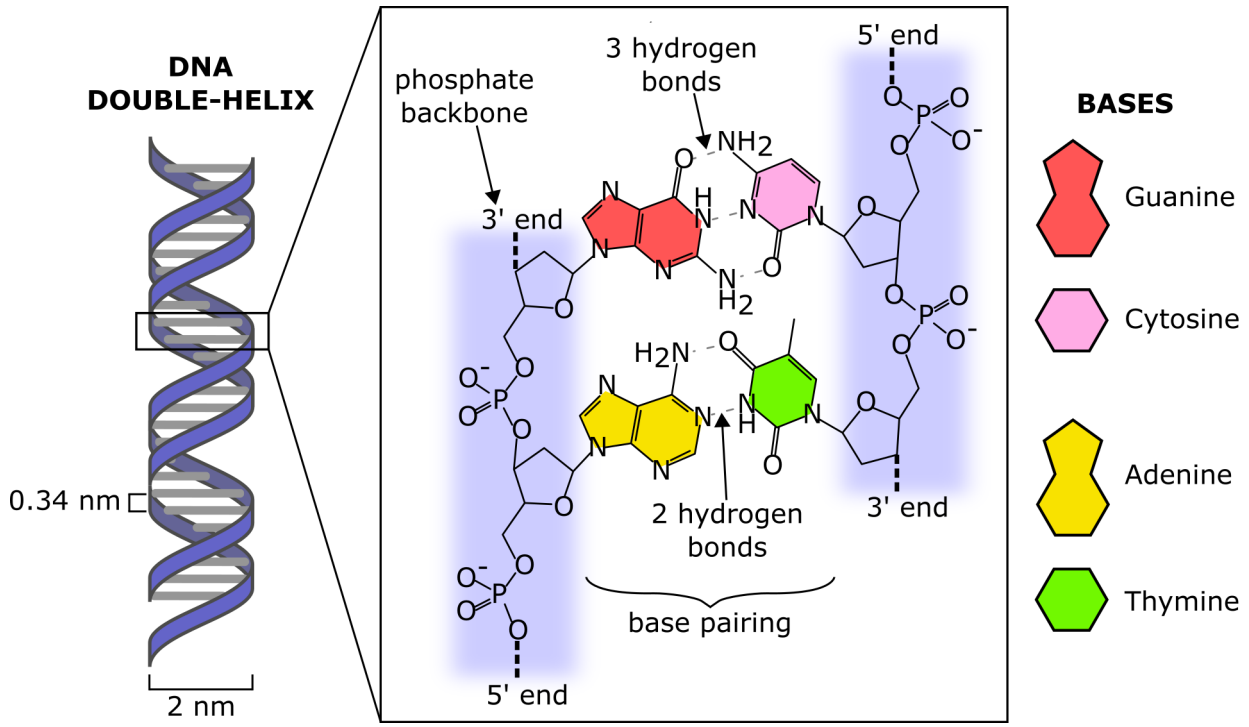


Figure 1.5: **DNA duplexes self-assemble into a double-helix structure as a result of base interactions.** Schematic of the structure of DNA. The two polynucleotide chains are coiled in a double-helix structure that is 2 nm wide and twists 360° every 10.5 base pairs (in its B-form); the chains are joined by Watson-Crick base pairs, which are stacked above one another at a spacing of 0.34 nm. The schematic of the chemical structure has been adapted from a diagram by Thomas Shafee, available in Wikimedia Commons under a CC BY 4.0 license.

1.3.1 The DNA molecule

DNA was first discovered in 1869 by Friedrich Miescher [167, 168], who at the time was working on characterising proteins in the nuclei of human white blood cells. During this work, Miescher isolated a component of the nuclei that had chemical properties that differed from proteins, such as a much higher phosphorous content and resistance to proteolysis; this component was initially named as "nuclein", which was later changed to "nucleic acid' and finally to "deoxyribonucleic acid" (or DNA for short) [169]. However, it wasn't until 1953 that the 3D structure of DNA (schematised in Figure 1.5) was discovered, thanks to X-ray crystallography imaging by Rosalind Franklin, Maurice Wilkins and Raymond Gosling [170] along with the proposal of the now-famous double helix model by James Watson and Francis Crick [171]. The model proposed by Watson and Crick describes the structure of B-DNA, the most common form of DNA. It must be noted that DNA may alternatively exist in two other forms, referred to as A-DNA and Z-DNA; these also form helical structures, but differ from B-DNA in terms of their geometry and dimensions [172, 173]. Due to its biological significance and vast potential for use in nanotechnology, the physical and chemical properties of DNA have since been studied extensively.

The DNA molecule is a polymer consisting of two polynucleotide chains, coiled around each other in a double helix (see Figure 1.5) [171]. These polynucleotide chains are composed of

simple monomeric units called nucleotides, which each consist of a phosphate group, a deoxyribose sugar, and a nitrogenous base. The latter is also referred to as a nucleobase, which can be one of four: cytosine, guanine, adenine and thymine (shortened to C, G, A and T respectively). Monomers within a polynucleotide chain are covalently linked by phosphodiester bonds between the 5'-hydroxyl group of the sugar in one nucleotide and the 3'-end phosphate of the next. This results in a sugar-phosphate backbone of the chain, as well as an asymmetry that gives directionality to the DNA molecule. The directionality of a polynucleotide chain is often described by referring to the end with the free hydroxyl as the 5' end, and the end with the free phosphate as the 3' end (*e.g.* DNA nucleobase sequences are typically quoted in the 5' to 3' direction).

The two polynucleotide chains are held together by anti-parallel hybridisation of nucleobases on the complementary strands, which bind according to Watson-Crick base pairing [171]: adenine with thymine (*via* two hydrogen bonds), and guanine with cytosine (*via* three hydrogen bonds). The double helix structure of the DNA molecule arises due to base stacking interactions; consecutive bases are stacked above one another in a helical arrangement that enhances the van der Waals interactions between the bases [174].

1.3.2 Thermodynamics of DNA hybridisation

Complementary DNA strands bind selectively in accordance with the Watson-Crick base pairing rules. The hybridisation and binding of short DNA strands (also known as oligonucleotides) can be quantitatively predicted through straightforward thermodynamic models; one example is the nearest neighbour model, which assumes that the stability of a base pair depends on the identity and ordering of neighbouring base pairs [175]. The free energy of hybridisation of two untethered oligonucleotides to form a DNA duplex is thus given by

$$\Delta G^\circ_{\text{total}} = \Delta G^\circ_{\text{initiations}} + \sum_{i=1}^{10} n_i \Delta G^\circ(i), \tag{1.2}$$

where $\Delta G^\circ_{\text{initiations}}$ is the free energy associated with the initiation and termination base pairs of the duplex; $\Delta G^\circ(i)$ is the free energy associated with one of the ten possible nearest-neighbour nucleotide pairs (*e.g.* AA, AT, AC, AG, and so on); and n_i is the number of occurrences of this pair in the sequence. Note that the nearest neighbour model can be extended to account for mismatched bases that disobey the Watson-Crick base pairing rules.

Each ΔG term can be decomposed into enthalpic and entropic contributions, such that the total free energy change can be calculated as

$$\Delta G^\circ_{\text{total}} = \Delta H^\circ_{\text{total}} - T\Delta S^\circ_{\text{total}}, \tag{1.3}$$

where $\Delta H^\circ_{\text{total}}$ and $\Delta S^\circ_{\text{total}}$ are the enthalpy and entropy of hybridisation respectively, and T is the temperature. $\Delta H^\circ_{\text{total}}$ is dominated by the change in enthalpy due to base stacking and hydrogen bonding between base pairs, while $\Delta S^\circ_{\text{total}}$ arises from various entropic contributions

including the entropy loss of flexible oligonucleotides as they assemble into the helical duplex. Values of ΔH° and ΔS° have been determined for the ten possible nearest-neighbour nucleotide pairs, such as the values identified through empirical measurements of DNA hybridisation free energies by Santa Lucia [175, 176].

In cases where one or both of the oligonucleotides are tethered, there is generally a loss in configurational (rotational and/or translational) freedom as the strands bind to form a duplex. This corresponds to a configurational entropy loss ΔS_{conf}, which appears as an additional term $-T\Delta S_{\text{conf}}$ on the right hand side of Equation 1.3 [177, 34].

DNA duplex formation becomes less likely with increasing temperature, as the thermal energy overcomes the attractive interactions between base pairs. This can be seen from Equation 1.3; assuming that $\Delta H^\circ_{\text{total}}$ and $\Delta S^\circ_{\text{total}}$ are temperature-independent, as $\Delta S^\circ_{\text{total}} < 0$ (*i.e.* entropy is lost during hybridisation), it follows that $\Delta G^\circ_{\text{total}}$ increases linearly with temperature. As temperature increases, more DNA duplexes unwind and separate into single-stranded species; this process is known as melting or thermal denaturation [178].

The hybridisation of two complementary oligonucleotides A and B can thus be thought of as a second-order reversible reaction, where an equilibrium exists between the single-stranded species and the duplex AB. This can be represented as

$$A + B \underset{k_{\text{off}}}{\overset{k_{\text{on}}}{\rightleftharpoons}} AB \tag{1.4}$$

where k_{on} and k_{off} are the rate constants of hybridisation and denaturing respectively. It must be noted that this assumes a two-state model in which A and B are either fully hybridised or fully de-hybridised; this is generally true for short, complementary oligonucleotides, but not in general. The equilibrium constant for this reaction is given by

$$K_{\text{eq}} = \frac{[AB]}{[A][B]} = \frac{k_{\text{on}}}{k_{\text{off}}}. \tag{1.5}$$

The equilibrium constant and free energy of hybridisation can be related *via* the Van 't Hoff equation [179], giving $\Delta G^\circ_{\text{total}} = -RT\ln(K_{\text{eq}}\rho^\circ)$, where R is the ideal gas law constant and $\rho^\circ = 1\,\text{M}$ is a reference concentration. This, in conjunction with the expression for K_{eq} in Equation 1.5, can be used to calculate the melting temperature, with is defined as the temperature at which half of the DNA duplexes have dissociated into the single stranded species. The stronger the binding between the DNA strands, the greater the thermal energy required to denature the duplex, and thus the higher the melting temperature.

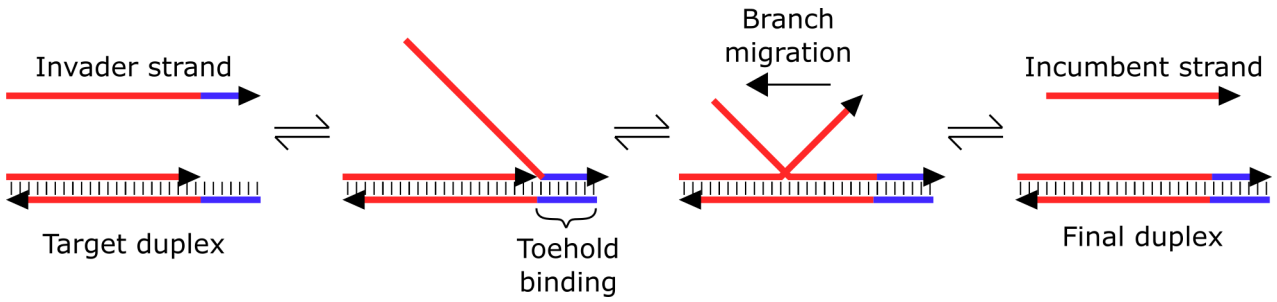


Figure 1.6: **Toehold-mediated strand displacement (TMSD) is a mechanism used to exchange one strand of a DNA duplex with another.** A schematic of the TMSD mechanism is shown; the invader strand binds to a complementary single-stranded "toehold" region on the target duplex, forming a three-stranded complex. Branch migration of the invading domain eventually leads to displacement of the incumbent strand from the duplex.

1.3.3 Dynamic DNA nanotechnology

Dynamic DNA nanotechnology focuses on the construction of DNA complexes with dynamic, non-equilibrium functionalities, including mechanical motion [180, 181], reconfiguration [182, 183] and computation [184, 185]. These functionalities are achieved by exploiting the reversibility of the DNA base pair interactions, and can be triggered by a variety of actuation mechanisms such as environmental factors (*e.g.* pH [186], ionic concentration [187], light [188], temperature [189] and hydrophobicity [190]); externally applied electromagnetic fields [191, 192]; and molecular binding [193, 194].

Molecular binding actuation mechanisms are based on the binding of an external molecule to the DNA nanostructure, initiating processes known as *branch migration* and *strand displacement*. The most popular mechanism is toehold-mediated strand displacement (TMSD) [193, 195, 196], which uses "invading" DNA strands for actuation; a schematic of the TMSD mechanism is shown in Figure 1.6. The single-stranded DNA invader binds to a short unhybridised overhang or *toehold* on the target DNA nanostructure, creating a complex composed of three strands of DNA. Energetically-favoured branch migration of the invading domain then leads to the displacement of the initial hybridised *incumbent* strand. An alternative to TMSD is proximity-induced DNA strand displacement (PiDSD), which relies on close proximity of the invader strand to the target nanostructure (rather than binding of a toehold) to catalyse the displacement reaction [194].

Dynamic DNA nanotechnology is not solely limited to base-pairing interactions between DNA strands. For example, DNAzymes are artificial DNA oligonucleotides that are capable of performing specific chemical reactions, mimicking the behaviour of biological enzymes [197, 198]. DNAzymes have been engineered to catalyse the cleavage and ligation of DNA and ribonucleic acid (RNA) [199, 200, 201]; the majority of DNAzymes are ribonucleases (commonly abbreviated as RNases) which catalyse RNA cleavage. In addition, artificial DNA oligonucleotides known as aptamers are capable of binding to specific target molecules, mimicking the behaviour of antibodies. These target molecules include heavy metal ions [202], proteins [203, 204], and even whole cells such as viruses [205] and bacteria [206].

The aforementioned functionalities have enabled the design of DNA constructs for a plethora of applications, including reconfigurable DNA nanodevices such as autonomous walkers [180, 181], switches [207] and tweezers [195]. Dynamic DNA nanotechnology has also been used to engineer molecular circuits capable of complex information processing and computation, such as synthetic gene regulatory and signalling networks [208], and computational networks using *in vitro* transcription [209]. Furthermore, dynamic DNA nanotechnology has vast potential for medical and therapeutic applications, such as the use of aptamers in medical tests to identify molecular markers of cancers and other diseases [210, 211].

1.3.4 DNA-mediated multivalent interactions

Over the past few decades, DNA nanotechnology has been a popular tool for engineering multivalent adhesion and other interactions between substrates, as the selective and reversible binding properties of the DNA molecule enables precise control over the resulting multivalent interactions. The interacting substrates are typically functionalised with complementary DNA "linker" constructs, which bind to each other to provide the adhesive force. The structure of DNA linkers is schematised in Figure 1.7, and features three distinct parts: an anchor, a spacer region, and a reactive moiety such as a single-stranded sticky end [34]. The anchor chemically or physically tethers the DNA nanostructure to the substrate; the choice of anchor depends on the nature of the substrates and the functionalisation strategy. The spacer may consist of either single-stranded DNA (ssDNA) or double-stranded DNA (dsDNA), and determines the length and flexibility of the nanostructure, which in turn affect the hybridisation free energy and thus the overall multivalent adhesion. dsDNA is significantly stiffer than ssDNA, with a persistence length of $\approx 50\,\text{nm}$ [212]; a dsDNA spacer region shorter than this length thus behaves like a rigid rod. Finally, the reactive moiety mediates interactions with complementary DNA constructs. A simple example of a reactive moiety is a single-stranded sticky end that selectively binds to complementary sticky ends; the base-sequence and length of the sticky end enable fine-tuning of the binding strength [34].

Early implementations of DNA-mediated multivalent adhesion focused on the self-assembly of gold nanoparticles functionalised with complementary DNA linker constructs by Mirkin *et al* [213] and Alivisatos *et al* [214] in 1996. Since then, a variety of self-assembled phases driven by DNA-mediated multivalent adhesion have been developed, from crystalline superlattices [215, 216] to amorphous gels [217, 218, 219]. In all of these examples, the functionalised substrates are solid, which means that the DNA linkers are anchored to fixed points on their surface and that the particles cannot be deformed by the multivalent forces.

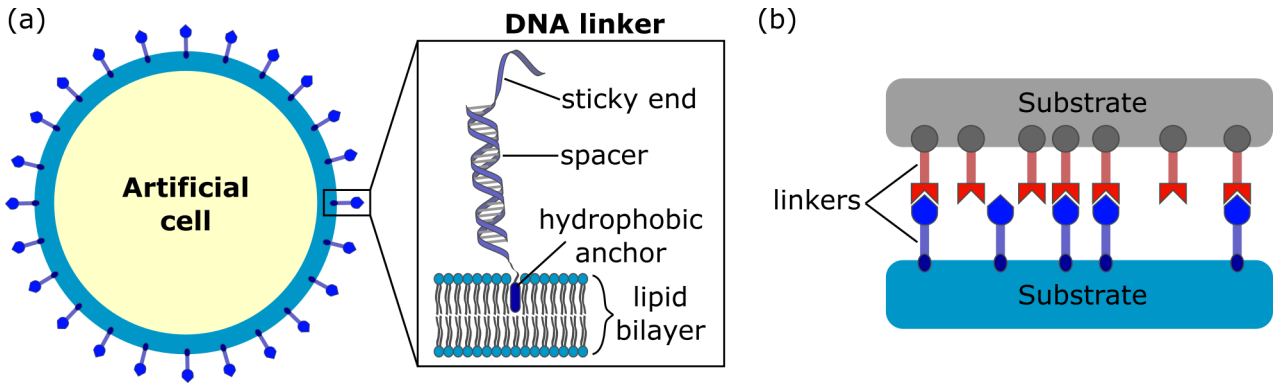


Figure 1.7: **Biomimetic membranes can be functionalised with amphiphilic DNA nanostructures to mediate membrane interactions such as adhesion.** Artificial cells such as lipid vesicles may be functionalised with DNA linker constructs which mediate multivalent interactions with other artificial cells, objects or substrates; this is schematised in (a). The structure of DNA linkers commonly consists of three parts [34]: a hydrophobic anchor for tethering to the lipid membrane, a spacer to control the physical extent of the linker, and a sticky end that can bind to complementary sticky ends. Multivalent adhesion between substrates may be mediated by complementary linkers that bind to each other; an example configuration of interacting linkers is schematised in (b).

DNA-mediated multivalent interactions in biomimetic systems

Functionalisation of fluid and deformable substrates (in particular biomimetic membranes such as lipid bilayers) with DNA linkers has uncovered an even wider variety of complex biophysical phenomena, owing to changes in the particle shape and lateral diffusion of the linkers; this has relevancy to the multivalent behaviour of biological cell membrane receptors. To attach DNA linkers to biomimetic lipid membranes, one can functionalise the construct with a hydrophobic anchor, such that the anchor spontaneously inserts within the hydrophobic core of the bilayer. Previously tested anchor moieties include cholesterol, lipid, tocopherol or carbon chains, as reviewed in Ref. [220]. Cholesterol is commonly used as the anchor due to the commercial availability of cholesterol-modified oligonucleotides, as well as the stability of its insertion in the lipid bilayer. Indeed, an individual cholesterol anchor has been observed to provide relatively stable anchoring of DNA nanostructures, albeit reversibly with off rates $\approx 5.8 \times 10^{-4} \mathrm{s}^{-1}$, while double cholesterol anchors result in irreversible attachment [221].

The first studies into the application of DNA-mediated interactions between lipid bilayers were conducted by the groups of Boxer [222] and Höök [223], focusing on the specific adhesion of lipid vesicles to supported lipid bilayers (SLBs) *via* the binding of DNA linkers with complementary sticky ends. These SLB-tethered vesicles could still diffuse laterally and interact with each other *via* DNA linkers orthogonal to the linkers mediating vesicle-SLB adhesion, as depicted in Figure 1.8a. Controlled rupture of GUVs adhered to the SLBs resulted in the formation of bilayer patches tethered to the underlying SLB by DNA linkers [224, 225]. When using linkers with spacers of different lengths, phase separation was observed in the patches as a result of bending energy minimisation of the suspended membrane [226]; this phenomenon is reminiscent of the size-induced phase separation of receptor-ligand complexes observed in

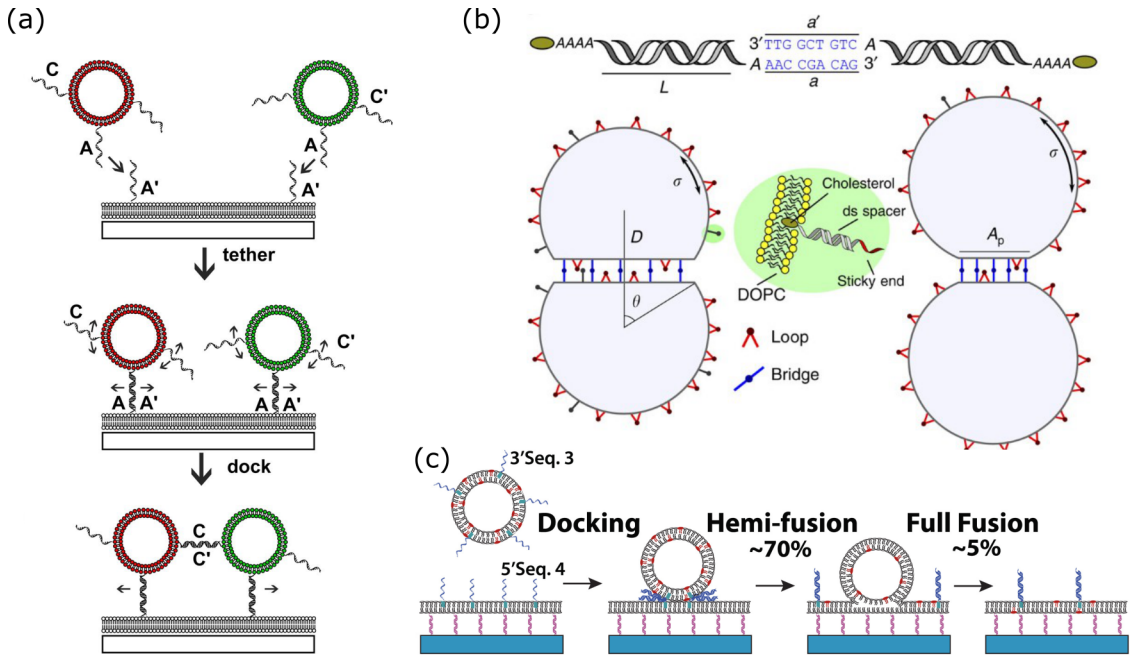


Figure 1.8: **Implementations of DNA-mediated multivalent interactions in biomimetic systems.** Schematics are shown of previously implemented experimental systems in which multivalent interactions between lipid bilayers are mediated by DNA interactions. In (a), vesicles attach to supported lipid bilayers and interact with each other *via* DNA linkers (figure adapted with permission from Ref. [222]; Copyright (2007) National Academy of Sciences, U.S.A.). In (b), vesicles adhere to each other due to the binding of complementary DNA linkers; the size of the adhesion patch can be tuned by varying the temperature (figure adapted from Ref. [40], which is licensed under a Creative Commons Attribution 4.0 International License). In (c), the binding of complementary DNA constructs cause vesicles to fully fuse with lipid bilayers (figure adapted with permission from Ref. [46]).

the intercellular junction during immunological synapse formation [227, 228]. An alternative approach to tethering GUVs to SLBs was developed by Amjad *et al* [38], in which tetravalent streptavidin proteins act as bridging moieties between biotinylated DNA constructs attached to the lipid bilayers. In this system, adhesion of GUVs to the SLBs was observed at an intermediate range of streptavidin concentration; too little streptavidin would result in an insufficient number of tethering complexes, while too much streptavidin would result in saturation of the available biotin such that only one DNA construct would bind to each streptavidin protein.

Another popular theme within DNA-mediated adhesion of biomimetic membranes is the self-assembly of GUVs suspended in solution [40, 41, 47]. Again, the GUVs are typically functionalised with complementary DNA linkers to mediate multivalent adhesive interaction between the vesicles. Microscopy imaging of DNA-mediated adhesion of GUVs has revealed that the GUVs deform to form flat contact regions, where DNA linkers are preferentially recruited due to their tendency of forming bridges [41]. The degree of GUV clustering increases with monovalent salt concentration, while no aggregating is observed in the absence of salt; this is due to the high negative charge of the sugar-phosphate DNA backbones, which requires screening by positive ions to allow hydrogen bonding between complementary DNA strands. The size of the GUV-GUV contact region has been observed to (reversibly) increase with temperature,

as thermal expansion of the bilayer increases its excess area, resulting in a more "deflated" and deformable GUV as depicted in Figure 1.8b [40]. Furthermore, "Janus" vesicles have been generated by functionalising phase-separated GUVs with DNA linkers [42]; the linkers preferentially partition to one of the phases of the lipid bilayer, resulting in localisation of the linkers on one hemisphere of the GUV. The resulting interactions between such Janus vesicles have been observed to be highly directional, enabling control over the size and morphology of vesicle clusters [42].

LUVs have also been functionalised with DNA linkers to study multivalent adhesion and self-assembly. Bachmann *et al* [229] demonstrated that both the DNA melting temperature and dissociation temperature of DNA-functionalised LUV aggregates increase monotonically with linker concentration, which corresponds to a greater attractive combinatorial contribution to the interaction free energy. However, both the DNA melting temperature and vesicle dissociation temperature saturate at high surface coverage, which is likely due to steric interactions between the DNA linkers; crowding effects in the LUV-LUV contact region hinder the binding of complementary linkers between the two surfaces. Control over the kinetics of DNA-mediated LUVs aggregation has also been demonstrated, relying on toehold-mediated strand displacement (introduced in Section 1.3.3) to provide additional reaction pathways to the system [230]. By varying the relative abundances of interacting DNA constructs, this enabled the vesicle aggregation rate to be tuned over more than one order of magnitude.

Beyond self-assembly phenomena, DNA linkers have also been used to induce fusion of lipid bilayers. Flavier *et al* [46] designed a system in which SUVs fuse with lipid bilayers tethered to a solid support. The vesicles initially adhere *via* the binding of complementary DNA constructs, and the proximity of the vesicle to the supported lipid bilayer results in lipid mixing and fusion, as depicted in Figure 1.8c. In this case, the DNA constructs do not feature spacers (as is the case for adhesion-inducing linkers), and the sticky ends are designed to bind in a "zipper-like" configuration to bring the lipid membranes close to each other. This system was used to model the formation of the SNARE four-helix bundle that mediates synaptic vesicle fusion, and it was observed that anchors that span the bilayer increase the efficiency of full fusion compared with anchors that only span the outer leaflet.

Theoretical modelling of DNA-mediated multivalent interactions

As well as experimental implementations of DNA-functionalised biomimetic membranes, these systems have been simulated and studied from a theoretical standpoint using various approaches. Ref. [34] provides a review of equilibrium statistical-mechanical models of DNA-mediated multivalent interactions, which are applicable to systems where the linkers remain in thermal equilibrium. The models in Ref. [34] derive the multivalent free energies between two linker-functionalised interfaces through Boltzmann averages over all possible binding configurations, thus taking entropic contributions (which play a key role in multivalent interactions) into account. For each binding configuration, the multivalent free energy is a sum of the total hybridisation free energy of a given number of bound complementary linkers, along with addi-

tional contributions such as the entropic cost of confining a given number of mobile linkers in the contact region between the two interfaces, and any configurational restrictions experienced by the linkers in the contact region. Both fluid interfaces (with mobile linkers that can diffuse laterally) and solid interfaces (with linkers tethered to fixed positions) are considered, as well as different interface geometries including finite particles and infinite planes. The models also extend to the self-assembly and collective behaviour of many-particle systems.

For example, a statistical-mechanical approach was employed by Di Michele *et al* [48] to investigate the biophysics of passive endocytosis. This was achieved by modelling the multivalent interactions between a rigid particle representing a virus or parasite, and a deformable membrane representing a cell membrane. The model demonstrated that a particle functionalised by fixed linkers is more easily wrapped by the membrane, compared with a particle with mobile linkers; wrapping of the latter tends to be incomplete, due to recruitment of the linkers within the adhesion regions. However, the introduction of excluded volume interactions limits the local concentration and accumulation of mobile linkers, thus facilitating complete wrapping.

Altogether, investigations into the behaviour of DNA-functionalised biomimetic membranes have elucidated key biophysical principles of biological phenomena such as cell adhesion, membrane fusion and endocytosis. The specificity and programmability of DNA makes it a powerful and versatile tool for engineering multivalent systems, and the design of novel DNA nanostructures continues to contribute to the ever-expanding functionalities of artificial cellular systems.

1.3.5 Locomotion facilitated by DNA nanotechnology

The topic of engineering synthetic components capable of locomotion is a common goal to the fields of DNA nanotechnology and synthetic biology. *Autonomous* locomotion, or the ability to move without the necessity for external changes such as the addition of chemicals to trigger each step, is of particular interest. As well as modelling locomotion in biological systems, synthetic autonomous locomotion has potential for applications in drug delivery [231, 232, 233]; biosensing and diagnostics [234, 235]; micro- and nanorobotics [236, 237]; and much more. In this section, I review designs of DNA nanomachines known as "DNA walkers" that are capable of moving along nucleic acid tracks, along with implementations of artificial cell motility mediated or facilitated by DNA nanotechnology.

DNA walkers

DNA walkers are nanomachines comprised of DNA that are capable of motion over 2D or 3D tracks, akin to the motion of dynein and kinesin motor proteins along microtubules in cells [238]. Further functionalities can be programmed into DNA walkers, such as the ability to carry molecular cargo and deposit them at their target destinations [232], and the ability to perform DNA-templated synthesis [239]. Directional locomotion is typically achieved with burnt-bridges Brownian ratchet mechanisms, where the walker attaches to a binding site on the track, followed by a transformation step that diminishes the affinity of the binding site, thus breaking symmetry and biasing motion towards an adjacent unoccupied binding site. This can

be driven by a variety of mechanisms, including DNA hybridisation and strand displacement reactions [180, 232, 240, 241]; enzymatic activity [181]; chemical stimuli such as changes in pH [242]; and photolysis [243].

The term "DNA walker" was first coined in 2003 by John Reif [244], who designed two theoretical DNA walkers that were capable of autonomous, random motion along a circular strand of ssDNA while rotating; the designs achieve motion *via* distinct mechanisms. The first design (referred to as "walking DNA") moves as a result of enzymatic activity. At each step, the bipedal DNA walker is ligated to the next anchorage point on the ssDNA path, then cleaved from the previous one by a restriction endonuclease; Reif's group went on to achieve the first experimental implementation of an autonomous DNA walker in 2004 [181], based on this enzyme-driven design. The second design (referred to as "rolling DNA") moves as a result of DNA hybridisation. In this case, the "wheel" structure of the DNA walker binds to the circular ssDNA path, and subsequently rolls along the path by binding and unbinding of base pairs in the hybridised region at the leading and trailing ends respectively. The binding and unbinding of base pairs is either left to occur spontaneously, or accelerated *via* toehold-mediated strand displacement triggered by additional "fuel" strands of DNA.

Since then, many designs for DNA walkers driven by strand displacement cascades have been generated [180, 232, 240, 241]. In 2008, Yin *et al* presented an autonomous bipedal DNA walker comprised of a duplex "torso" and two identical walker "legs" [241]; the walker is capable of stochastic motion along a short, linear DNA track consisting of hairpin structures arranged at regular intervals along a nicked duplex. The walker binds to the hairpins, causing them to open to form fully hybridised duplexes with the walker legs. An additional DNA fuel strand in bulk then catalyses the displacement of the walker legs from the track and prevents them from re-binding to previously-bound sites. This induces the walker to move *via* a foot-over-foot gait, unidirectionally along the track. The mechanism driving the motion of this DNA walker is illustrated in Figure 1.9a, and forms the basis of the burnt-bridges mechanism in Chapter 4.

With the introduction of DNA origami, larger and more complex DNA walkers systems have been designed. For example, polyvalent walkers (*i.e.* with three or more legs) have been designed with the aim of improving on the limited processivity of uni- or bipedal walkers, which typically can only take a limited number of steps [247, 248]. Lund *et al* designed three-legged DNA walkers referred to as "molecular spiders" that move at an average speed of 3 nm per minute over a 2D DNA origami landscape, driven by DNAzyme activity [249]. The walker achieves directionality by sensing trails of recognition elements on the origami, and autonomously carrying out sequences of actions such as "start", "follow" and "stop". Gu *et al* designed DNA walkers that, along with three legs for stepping over an origami tile, featured three additional "hands" to collect cargo at specific locations along its track [250]. Furthermore, DNA walkers have been constructed from DNA origami, to investigate the effect of the shape and flexibility of the walker on its motion, as well as the number and distribution of legs [245]. Optimisation of these parameters led to the design of DNA origami-based walkers that can roll over micron-scale distances at speeds of up to 100 nm per minute, such as the DNA origami

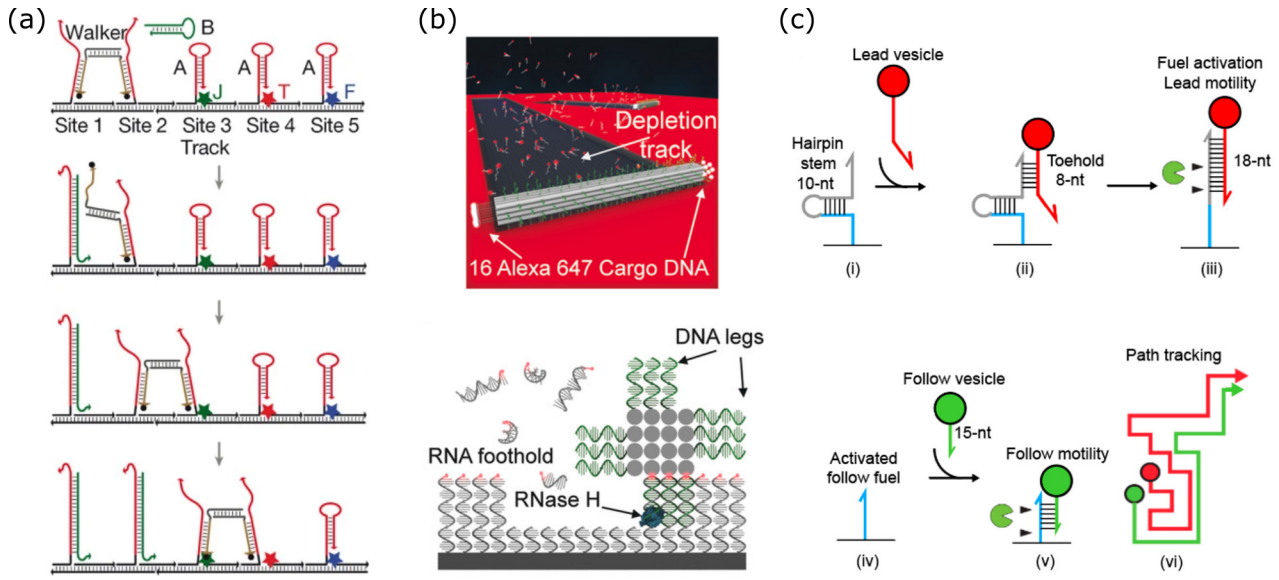


Figure 1.9: **Various designs for DNA walkers capable of autonomous locomotion have been implemented.** In (a), a bipedal DNA walker steps in one direction along a DNA track, as a result of successive stages of toehold-mediated strand displacement (figure adapted with permission from Ref. [241]). In (b), a DNA origami motor rolls over an RNA-functionalised substrate as a result of enzymatic cleavage (figure adapted with permission from Ref. [245]). In (c), the DNA-functionalised "lead" vesicle performs a random walker over an RNA-functionalised substrate, leaving a track of activated RNA "fuel" as a result of enzymatic activity; the "follow" vesicle then moves along the path of activated fuel, again due to enzymatic activity (figure adapted with permission from Ref. [246]).

motor schematised in Figure 1.9b [245].

Motility of DNA-functionalised nanoparticles and artificial cells

A natural extension of polyvalent DNA walkers is the functionalisation of nanoparticles with numerous strands of DNA to impart motility. Khalid Salaita's group have modified nano- and microparticles with thousands of DNA strands [251, 252, 253]; the particles bind to a substrate modified with complementary RNA, and then roll along the substrate at speeds of up to 5 μm per minute [251]. The motion is driven by the action of RNase H, a ribonuclease enzyme that cleaves the phosphodiester bonds of RNA in RNA-DNA duplexes. Cleavage of RNA in the particle tracks results in the particles moving in a self-avoiding manner. Interestingly, the particles were observed to undergo Lévy-type motion, with bursts of speed punctuated by periods of slower motion; the authors rationalised this with stalling of the particle while all proximal RNA sites are consumed, before the particle is free to take a step [253]. Unidirectional motion was achieved by spatially patterning RNA into 3 μm-wide tracks, before hybridising the particles to the patterned RNA; a subset of particles were observed to move unidirectionally along the tracks, although other particles became entrapped, either due to RNA cross-contamination of regions outside the tracks, or self-entrapment in regions of cleaved RNA [251].

DNA-mediated unidirectional motion of nanoparticles has also been implemented by Cha *et al* [254], who designed a DNA-functionalised nanoparticle that binds to and moves along an

RNA-decorated nanotube track. In this case, the DNA constructs feature a DNAzyme moiety that drives the motion by cleaving hybridised RNA strands. Furthermore, the particle motion could be controlled by adjusting the concentration of metal cations; for instance, in the absence of metal cations, the DNAzyme moieties could no longer catalyse RNA hydrolysis, such that the particles could no longer move.

DNA nanotechnology has also been used to impart motility in synthetic biological systems, by functionalising artificial cells with DNA nanostructures. A mechanism for the RNase H-driven motion of DNA-functionalised SUVs along RNA-decorated filaments was proposed by Kerstin Göpfrich's group, relying on a burnt-bridges mechanism to cause the SUV to travel along the filament in one direction [255]. This is reminiscent of the previously mentioned system engineered by Cha *et al* [254]; these systems mimic the active vesicle transport by cytoskeletal motor proteins along microtubules within cells [238].

Jong Hyun Choi's group demonstrated a synthetic vesicle system in which DNA-functionalised LUVs chase one another over an RNA-modified substrate; a schematic of the system can be seen in Figure 1.9c [246]. Again, the LUV motion is driven by the action of RNase H, which cleaves RNA-DNA duplexes. The "lead" vesicle initially moves over the substrate, leaving behind it a trail of "activated" RNA that has been cleaved. The "follow" vesicle is modified with DNA constructs that are complementary to the activated RNA, such that the follow vesicle experiences a strong bias towards activated regions of the substrate and follows the tracks of the lead vesicle. The system thus exhibits behaviour akin to the chemotaxis of white blood cells as they chase infectious pathogens [256]. The Choi group also applied mean squared displacement (MSD) to study the trajectories of DNA-functionalised SUVs or particles [257], observing four distinct migration modes: ballistic, Lévy, self-avoiding and diffusive motion; a given vesicle can switch between different migration modes along its trajectory. It was found that a particular migration mode can be promoted or suppressed with changes in cargo sizes and strand designs. For example, smaller particles are attached to the RNA-functionalised substrate by fewer linkages, which accelerates the cleavage process and leads to faster kinetics.

1.4 Objectives and structure of the thesis

The objective of this thesis is to engineer artificial cell systems that are capable of multivalent adhesion, motility and haptotaxis, with the goal of mimicking biological cell behaviour and investigating the biophysics of multivalent interactions. DNA nanotechnology is employed as the tool to impart these functionalities, as its specificity and programmability allows for precise control over the multivalent system. Furthermore, lipid vesicles are chosen as the biomimetic cell model, due to their structural similarity to the biological cell and its phospholipid membrane.

Chapter 2 summarises the main materials, experimental methods and data analysis pipelines used throughout this PhD.

Chapter 3 presents a system in which vesicles adhere to substrates *via* multivalent interactions mediated by numerous DNA linkers; the reversibility of linker binding allows the vesicle to gradually diffuse over the substrate, in a passive form of motility. In particular, I study the motion of vesicles over regions of the substrate featuring a surface density gradient of DNA linkers, using a combination of experiments, theory and numerical modelling. A key finding is that the vesicles preferentially drift towards higher DNA densities, constituting a simple form of haptotaxis. The vesicle drift velocity is shown to depend on the binding strength of individual DNA linker pairs, and the size of the vesicle relative to the gradient.

In **Chapter 4**, I present an active adaptation of the vesicle motility system, with the goal of improving on the vesicle mobility of the passive system. Here, a burnt-bridges mechanism is incorporated, such that the vesicle leaves a path of "burned" DNA linkers on the substrate in its wake. A reaction-diffusion model is fitted to experimental data, to verify and investigate the mechanism, and to help design subsequent motility experiments. The updated mechanism enables the implementation of vesicle motility systems at lower linker densities, thus achieving an order-of-magnitude increase in vesicle speed. Furthermore, the vesicle mobility is shown to increase with increased rate of bridge-burning. Finally, the direction of the motion relative to the surface density gradient of DNA on the substrate is investigated to determine if there is scope for improving on the haptotactic drift velocities achieved with the passive system.

Finally, **Chapter 5** presents a summary of the key findings of this thesis, before offering ideas for future research avenues on the topic of artificial cell motility in multivalent adhesion systems.

Chapter 2

Materials, Methods and Software

This chapter summarises the materials, experimental methods and data analysis pipelines used throughout this work.

2.1 Manufacturing DNA nanostructures

2.1.1 Design and reconstitution of DNA oligonucleotides

All DNA nanostructures were designed using the nucleic acid suite NUPACK [258]; the structures and strand sequences are listed in Appendix A. DNA oligonucleotides with 5'-cholesteryl modifications were purchased from Eurogentec, while all other oligonucleotides were purchased from Integrated DNA Technologies. Strands with modifications were purified *via* high performance liquid chromatography (HPLC), while unmodified strands were purified by standard desalting; purification was carried out by the suppliers. The DNA strands were shipped lyophilised and reconstituted to a concentration of approximately 100 μM in 1×Tris-EDTA (TE) (10 mM Tris+1 mM EDTA, pH 8.0; Sigma-Aldrich) buffer. Note that the buffer had been filtered prior to reconstitution of the DNA, using 0.22 μm pore poly(ether sulfone) filters (Millex). The concentration of the reconstituted DNA was determined *via* UV-vis spectrophotometry on a Thermo Scientific NanoDrop One. Stock solutions of DNA were then stored at −20°C.

2.1.2 DNA nanostructure self-assembly

For each DNA construct, the constituent strands were mixed in a stoichiometric ratio to a final concentration of 2 μM in 1×TE buffer with 100 mM NaCl (BioUltra, >99.5%; Sigma-Aldrich). Self-assembly of the DNA nanostructures was achieved *via* thermal annealing on a Bio Rad C1000 Thermal Cycler; the strand mixture was first heated to 90°C for 5 minutes to ensure melting of all DNA duplexes, and then cooled to 20°C at a rate of -0.5°C min^{-1}. Self-assembled DNA constructs were characterised *via* agarose gel electrophoresis, and stored at 4°C.

2.1.3 Agarose gel electrophoresis

Gels were prepared by mixing agarose (Sigma-Aldrich) at a concentration of 3% (w/v) in 1×Tris-borate-EDTA (TBE) buffer (89mM Tris-borate, 2mM EDTA, pH 8.3; ThermoFisher Scientific). The mixture was dissolved by heating in a microwave. 10,000×SYBR Safe DNA gel stain (APExBIO Technology LLC) was added at 0.01% (v/v) concentration and gently dissolved through swirling. The mixture was cast to a thickness of approximately 5 mm and left to set for one hour. The gel was then placed in an electrophoresis chamber and covered with 1×TBE buffer. 10 μl samples containing ≈300 ng DNA and 1×TrackIt Cyan/Yellow loading buffer (ThermoFisher Scientific) were loaded into the gel. The two outer wells were loaded with Ultra Low Range DNA ladder (ThermoFisher Scientific), to enable comparison with the DNA samples. The gel was run for 90 minutes at 120 V (electric field strength of 6 V cm^{-1}) and then imaged using a Syngene Dyversity 4 gel imager with a UV lamp for illumination.

2.2 Generating DNA-functionalised vesicles

2.2.1 Preparation of giant unilamellar vesicles

GUVs were produced *via* electroformation, a common method of vesicle generation [141]. All lipids were purchased from Avanti Polar Lipids Inc. unless specified otherwise. DOPC was dissolved at 1 mg ml^{-1} in chloroform (Sigma-Aldrich). For imaging purposes, 1 mol% of fluorescent lipid was also added to the solution; depending on the experiment, either 1,2-dioleoyl-sn-glycero-3-phosphoethanolamine-N-(7-nitro-2-1,3-benzoxadiazol-4-yl) (ammonium salt) (NBD-PE) or 1,2-dioleoyl-sn-glycero-3-phosphoethanolamine-N-(lissamine rhodamine B sulfonyl) (ammonium salt) (18:1 Liss Rhod PE) was used. 30 μl of this solution was spread evenly on an indium tin oxide (ITO) slide (Sigma-Aldrich) with a surface resistivity 15-25 Ω sq^{-1}. The slide was vacuum-desiccated for 30 minutes to remove residual chloroform, resulting in a lipid film.

A 5 mm-thick polydimethylsiloxane (PDMS) spacer with a central cut-out was sandwiched between this film and another ITO slide to create a chamber, and the chamber was filled with a solution consisting of 300 mM sucrose (Sigma-Aldrich) in MilliQ water. 50 μM calcein (Sigma-Aldrich) was optionally included in the solution, to aid fluorescence imaging and vesicle segmentation during image analysis.

A TG315 function generator (Aim-TTi) was used to apply an alternating electric field at a peak-to-peak voltage of 1.5 V across the ITO slides at 10 Hz for two hours, followed by one further hour at 2 Hz. During this time, the chamber was left in a 60°C oven to ensure that the lipid was in the fluid phase. Finally, the chamber was opened and the resulting vesicles were collected.

2.2.2 Functionalisation of vesicles with DNA constructs

GUVs were functionalised by incubating the vesicles with cholesterolised DNA constructs. A sample was prepared with 20 v/v% 2 μM DNA constructs in 1×TE and 100 mM NaCl buffer, 11 v/v% GUVs (prepared via electroformation) in 300 mM glucose solution, and 69 v/v% "correction buffer". This correction buffer consists of 116 mM NaCl, 78.2 mM glucose and 1.16×TE buffer, and was included to match the osmolarity of the interior and exterior of the GUVs and thus to prevent osmotic-shock-induced rupture, while tuning the concentrations of NaCl and TE in the sample to 100 mM and 1×, respectively. The sample was left to incubate on a roller mixer overnight. During this time, the amphiphilic cholesterol molecules self-insert into the lipid bilayer, and the use of a double cholesterol anchor ensured irreversible attachment of the DNA construct to the outer leaflet of the vesicle membrane.

After incubating overnight, the vesicle sample was washed to remove excess DNA constructs remaining in bulk solution. This was achieved by centrifuging the sample at 1600 rpm for 90 seconds to draw the vesicles towards the bottom of the sample, and then replacing approximately 90% of the eluent with an iso-osmolar solution consisting of 100 mM NaCl and 87 mM glucose in 1×TE buffer. The washing process was carried out at least three times. To check that the vesicles had been successfully functionalised and the lipid membranes were saturated with DNA constructs, the vesicles were prepared with fluorescently-tagged lipids and DNA constructs, and imaged *via* epifluorescence and confocal microscopy.

2.2.3 Preparation of vesicle samples for microscopy imaging

Vesicle samples were visualised using fluorescence microscopy, as detailed in Section 2.5. To aid the imaging process, vesicle samples were optionally diluted with an iso-osmolar solution of 300 mM glucose (Sigma-Aldrich) in MilliQ water, such as in a 1:10 ratio of vesicles to glucose solution. This reduces crowding of vesicles in images, and introduces a density difference which causes the vesicles to settle at the bottom of the viewing chamber, as well as a refractive index contrast to enable viewing in brightfield.

Vesicles were either imaged on glass slides or in well plates. For the former, a PDMS spacer was attached to the glass slide to form a chamber; the vesicles were then carefully pipetted into the chamber, and the chamber was covered with a glass coverslip to prevent evaporation. When imaging in well plates, the vesicles were carefully pipetted into the wells, and the well plate was sealed with a transparent adhesive foil (Sarstedt Ltd). In samples with a density difference between the vesicle interior and exterior, the vesicles were allowed to sink for at least 15 minutes before image acquisition.

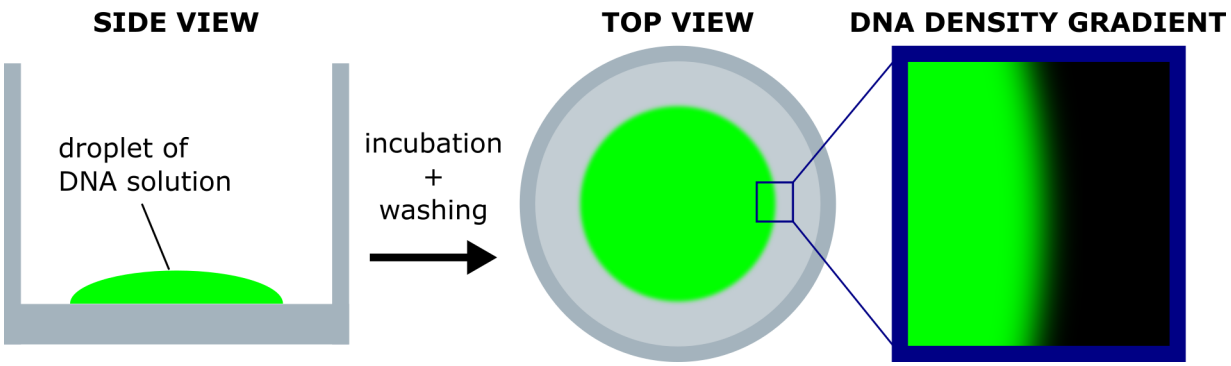


Figure 2.1: **Schematic of the method used to generate DNA-density gradients adhered to a substrate.** A droplet of biotinylated DNA solution is applied to the bottom surface of a streptavidin-coated well, resulting in DNA adhering to a circular region within the well (as described in Section 2.3.1). At the perimeter of the circular region there is a steep gradient in surface density of DNA, depicted in the inset; the density of DNA can be visualised by exciting fluorescence in the Alexa Fluor 488 fluorophore attached to the DNA constructs.

2.3 Functionalisation of substrates with DNA constructs

2.3.1 Generating DNA-density gradients attached to substrates

Various methods of generating surface density gradients of DNA attached to substrates were considered and investigated, as discussed in Section 3.2.3. The method chosen for the following vesicle motility experiments involved functionalising a small circular region of the substrate with DNA, as schematised in Figure 2.1. This was achieved by depositing a 0.5 μl droplet of 2 μM DNA constructs in buffer solution (100 mM NaCl+1×TE) on the substrate. The DNA constructs are modified with biotin, allowing for covalent attachment to the substrate, a streptavidin-coated high capacity 96-well strip plate (Sigma-Aldrich). The constructs were also tagged with a fluorophore (Alexa Fluor 488) to enable fluorescence imaging of the DNA coverage on the substrate. This was left to incubate for five minutes to allow the DNA constructs to bind to the substrate. Excess DNA was then washed away by quickly rinsing the substrate with buffer solution (100 mM NaCl and 1×TE). This left a small circular region on the substrate coated with DNA constructs, with a steep DNA-density gradient at the perimeter of this region; an example image of a well with a circular ligand-coated region is shown in Figure 2.2. See Figure 3.5b for an example plot of a typical gradient profile.

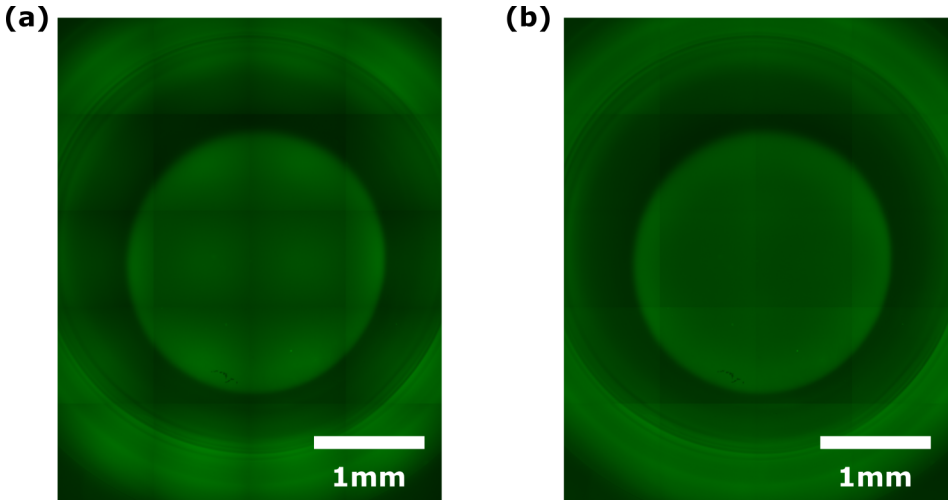


Figure 2.2: **Fluorescence images of ligand coverage are normalised to account for non-uniform illumination.** (a) shows a microscopy image of a well, of which a circular region has been functionalised with Alexa Fluor 488-tagged ligand constructs by the method described in Section 2.3.1. the image is a composite of multiple fields of view stitched together; non-uniform illumination results in darkening of the fluorescence signal near the edges of each field of view. (b) shows the same composite image after normalisation to account for the non-uniform illumination; the images were normalised by the method described in Section 2.3.2.

2.3.2 Visualisation and characterisation of DNA-functionalised substrates

The DNA coverage of substrates was imaged with epifluorescence microscopy (see Section 2.5), exciting fluorescence in the DNA constructs tagged with Alexa Fluor 488. To account for non-uniform illumination of the sample, the fluorescence images were normalised by a control image taken within a non-functionalised well containing calcein solution; examples of images pre- and post-normalisation are shown in Figure 2.2. A Gaussian filter with a standard deviation of 15 pixels (9.66 μm) was then applied to smooth and reduce noise in the image.

The ligand density in the maximum-density region of the wells was estimated by applying a 0.5 μl droplet of 2 μM ligand solution (with the Alexa Fluor 488 modification) to the well for five minutes, like in the gradient generation procedure. The supernatant was then diluted by a factor of 200 by adding 99.5 μl of buffer solution (100 mM NaCl and 1×TE) and mixing with a pipette. 80 μl of the diluted supernatant was extracted, and its fluorescence was recorded on a BMG LABTECH CLARIOstar Plus microplate reader. To estimate the quantity of ligand constructs that had been deposited on the substrate, the fluorescence of the diluted supernatant was compared with the fluorescence of control samples *i.e.* 80 μl ligand solutions with known concentrations (0 nM, 0.1 nM, 1 nM, 5 nM and 10 nM) and the same buffer conditions (100 mM NaCl and 1×TE). Note that all samples (including the sample with unknown ligand concentration) were repeated four times to improve measurement accuracy; background signal was removed from the fluorescence measurements by subtracting the average fluorescence intensity of the control samples with 0 nM ligand concentration. A straight line was fitted to the fluorescence of the control samples, to determine a calibration curve between ligand con-

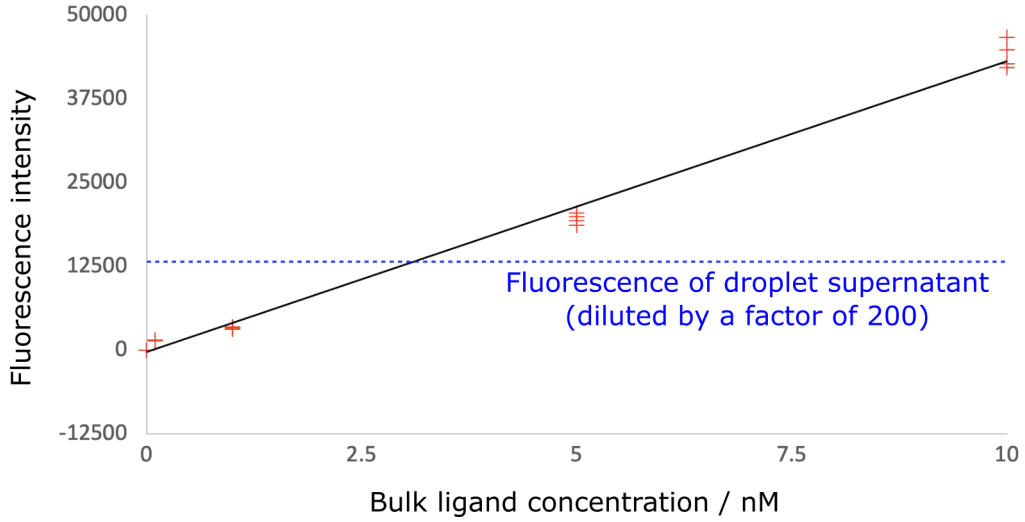


Figure 2.3: **Calibration curve for determining ligand density from fluorescence measurements.** This calibration curve was generated and used as part of the method of estimating the ligand density in the maximum density regions of wells in experiments, outlined in Section 2.3.2. The plot shows the background-subtracted fluorescence signals of samples with known bulk ligand concentrations (0, 0.1, 1, 5 and 10 nM) in buffer solution (100 mM NaCl and 1×TE). A straight line has been fitted to the fluorescence measurements to establish a calibration curve. The mean fluorescence intensity of the supernatant of a droplet of ligand solution applied to a well (subsequently diluted by a factor of 200) is indicated with a blue dashed line.

centration and fluorescence signal (see Figure 2.3). From this, it was deduced that the ligand concentration of the supernatant of the droplet applied to the well (diluted by a factor of 200) was 3.0 nM, which corresponds to a loss of 70% of ligands from the droplet solution. Assuming that this loss is entirely due to binding of ligands to the well within the droplet region, and an approximate diameter of the droplet region of 4 mm, this corresponds to an estimated density of $\rho_{L,\max} = 0.33\,\mathrm{nm}^{-2}$ of ligands bound to the well within the droplet region.

Finally, the ligand density ρ_L was estimated by interpolating between the background fluorescence signal I_0 and the maximum ligand-density fluorescence signal $I_{\max}$. I_0 was measured from a manually selected region within a non-functionalised well filled with buffer solution (100 mM NaCl+1×TE), while $I_{\max}$ was calculated as the intensity averaged over a manually selected area of the maximum density region of the well). The normalised fluorescence intensity I_{norm} was thus converted to the ligand density as follows:

$$\rho_L = \frac{I_{\mathrm{norm}} - I_0}{I_{\max} - I_0}\rho_{L,\max} \tag{2.1}$$

2.4 Vesicle motility and burnt-bridge patterning experiments

2.4.1 Applying vesicles to ligand-modified substrates

After functionalising GUVs and well surface with DNA, the vesicle sample was carefully pipetted into the well (150 μl or 30 μl for the experiments in Chapters 3 and 4 respectively). After being pipetted into the wells, the samples were left for at least 15 minutes to allow the vesicles to settle to the bottom and adhere. For the experiments in Chapter 4, 70 μl of correction solution containing the DNA fuel construct (F), magnesium chloride (Sigma-Aldrich), potassium chloride (Sigma-Aldrich), glucose and TE was added to the wells, to attain the desired buffer composition (1×TE, 30 mM NaCl, 15 mM KCl, and $MgCl_2$ concentration specified by the experiment) and concentration of fuel construct (again specified by the experiment) in the bulk solution, while maintaining iso-osmolarity. The well plate was sealed with a transparent adhesive foil to minimise evaporation of the sample, as well as evaporation-driven flows.

2.4.2 Time lapse imaging

A time lapse recording was then taken of the vesicle sample, typically over a duration of 10–15 hours at half- or one-hour intervals. Time lapses were recorded on an epifluorescence microscope, making sure to adjust the focal plane to the vesicles for vesicle motility experiments, or to the substrate for burnt-bridge patterning experiments (see Chapter 4). Depending on the purpose of the experiment, the fluorescence channels were selected to image the DNA coverage on the substrate, the fluorescently-tagged lipids in the vesicle membranes, or the DNA with which the vesicle membranes were functionalised. Experiments were conducted at room temperature.

2.5 Optical microscopy

Imaging was either conducted with bright-field or fluorescence microscopy. For the latter, fluorescence was excited in the relevant fluorophores in the sample; see Table 2.1 for a list of fluorophores used throughout this thesis, and their excitation and emission maxima (λ_{ex} and λ_{em} respectively).

Table 2.1: **Fluorophores and their excitation and emission maxima.**

Fluorophore	λ_{ex} / **nm**	λ_{em} / **nm**
NBD	460	535
Calcein	470	509
Alexa Fluor 488	492	517
Lissamine rhodamine	560	583

2.5.1 Epifluorescence microscopy

Unless otherwise stated, all epifluorescence microscopy was conducted on a Nikon Eclipse Ti2-E inverted microscope. Two separate microscopes were used. One microscope was equipped with a Hamamatsu C11440-22C camera; imaging was conducted using a Nikon CFI Plan Apochromat Lambda D 10× dry objective (NA 0.45), with an image resolution of 0.64432 μm per pixel. The other microscope was equipped with a Prime BSI Express A22E726095 camera; imaging was conducted using a Nikon Plan Fluor 10× dry objective (NA 0.30), with an image resolution of 0.66116 μm per pixel. Illumination was provided by single-colour light-emitting diodes (LEDs). When imaging the fluorescence signal from Alexa Fluor 488 or calcein, the sample was imaged with a 470 nm LED and a 515/30 nm emission filter. When imaging the fluorescence signal from 18:1 Liss Rhod PE, the sample was imaged with a 555 nm LED and a 595/31 nm emission filter. The microscopes were controlled via the Nikon NIS-Elements software, including automation of complex image acquisitions involving multiple time points, fluorescence channels or microscope stage positions.

2.5.2 Confocal microscopy

Confocal microscopy was performed on a Leica TCS SP5 Confocal microscope using a HCX PL APO CS 63.0× oil-immersion objective (NA 1.40). Micrographs were recorded at a scan speed of 400 Hz. 18:1 Liss Rhod PE was tracked using a He-Ne laser (543 nm) for excitation. Alexa Fluor 488 was tracked using an Argon laser (488 nm) for excitation.

2.6 Tracking vesicle motion in time lapse recordings

2.6.1 Pre-processing image data

The time lapse recordings were first stabilised using the *Image Stabilizer* plugin on ImageJ [259] to mitigate unwanted effects of stage drift or inaccuracies in stage positioning. Typically the stabilisation process was initially conducted on a manually-selected rectangular region containing an immobile object or feature (*e.g.* a fixed impurity in the sample); the logged stabilisation coefficients were then used to apply the same stabilisation to the entire frame.

The remainder of the image processing was conducted in Python; key steps of the image processing are highlighted in Figure 2.4. A top-hat transform was first applied to the image data, to remove the non-uniform background fluorescence signal from the DNA coverage on the substrate. Gaussian smoothing (with a standard deviation of two pixels) was applied to the images for noise reduction. The images were then binarised, setting the threshold value such that the fluorescent vesicles were discerned from the background signal. Morphological opening operations were applied to the images to remove noise (*i.e.* bright specks in the dark background signal), followed by morphological closing operation to further remove noise (*i.e.* dark specks in the bright vesicles).

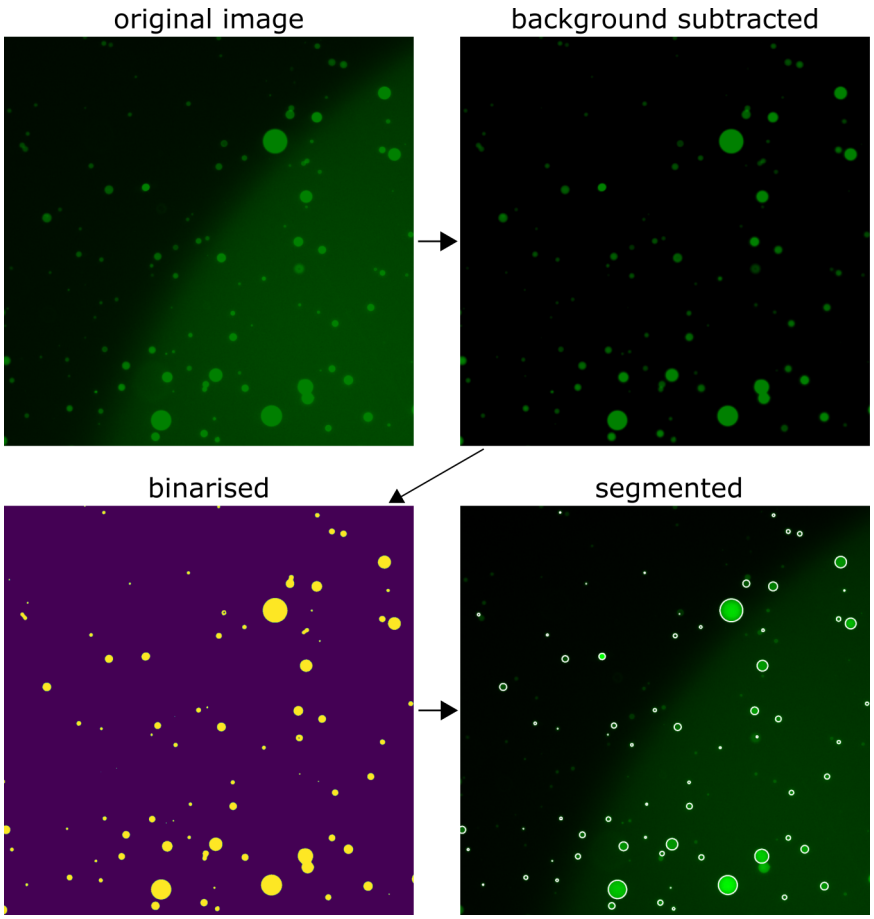


Figure 2.4: **Processing and segmenting microscopy images of vesicles.** Example images highlighting some of the key stages of processing image data from vesicle motility experiments, including background subtraction with a top-hat function and binarisation of the image. The processing enables segmentation of the images via an automated process detailed in Section 3.2.5, to identify vesicle positions within the frame; located vesicles are circled with white rings in the final image.

2.6.2 Identifying vesicle trajectories

Vesicles were located in each frame of the time lapse recordings using a template-matching method. Rather than directly applying template-matching to the binarised image data, the image data were further processed by applying a distance transform, labelling each pixel with the distance to the nearest dark pixel. The distance transform was applied to deal with issues arising from segmenting polydisperse samples; this is further discussed in Section 3.2.5. The distance transform of the vesicle template (also referred to as the kernel) was generated, providing a template which the *matchTemplate* function of the Python module was then used to search for in the image data, identifying the approximate positions and radii of bright disks in the original image data [260].

To fine-tune the position and radius estimates to sub-pixel accuracy, a function-fitting approach was employed. A function was first defined to map the radius and centre position of a bright disk in a two-dimensional image to the distance transform of the disk. The function was then fitted to regions of the distance-transformed image data in which a vesicle had been

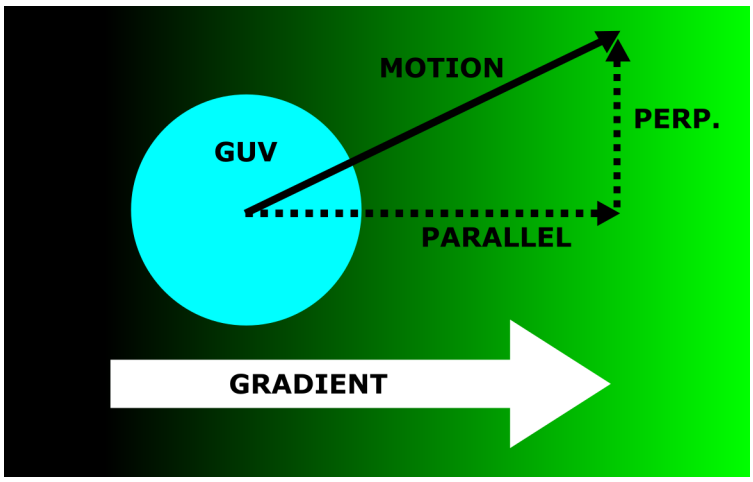


Figure 2.5: **Comparing the direction of vesicle motion to the direction of the DNA-density gradient.** The vesicle motion is split into components parallel and perpendicular to the local direction of the DNA-density gradient on the substrate, *via* the method described in Section 3.2.5.

located, thus providing fitted values for the size and position of the vesicle. Vesicles that were measured to have a radius of less than one pixel were removed from the data set, to avoid erroneous tracking of noise or impurities in the sample.

After locating vesicles in each frame of the time lapse data, vesicle trajectories were identified by linking vesicle positions between successive frames. This was achieved using the Python module *Laptrack*, which applies a linear assignment problem approach to link vesicle positions between frames [261, 262].

Finally, for experiments studying the direction of vesicle motion over DNA density gradients, the vesicle motion was split into components parallel and perpendicular to the local direction of the gradient (see Figure 2.5). First, the directional derivative of the DNA density in the image (estimated as described in Section 2.3.2) was computed; the resulting vector field described the magnitude and direction of the density gradient at each point in the image. An example of a ligand density gradient vector field superimposed on a fluorescence image of the ligand coverage on a region of a substrate can be seen in Figure 2.6. The components of the vesicle velocities parallel and perpendicular to the gradient direction were then measured by calculating the vector dot and cross products (respectively) of the velocities with the unit vectors describing the gradient directions at each vesicle position.

2.6.3 Filtering trajectory data to relevant regions of the substrate

The data was filtered to only include the trajectories of vesicles in relevant regions of the substrate, which was either the DNA density-gradient region, or the uniform, maximum DNA density region. This was achieved either by automated filtering of the images or by manual selection. Automated filtering was conducted by identifying regions of the substrate with high variation in DNA density (*i.e.* the DNA density-gradient region on the substrate). Manual selection was conducted by using Python to display images of the DNA coverage on the substrate

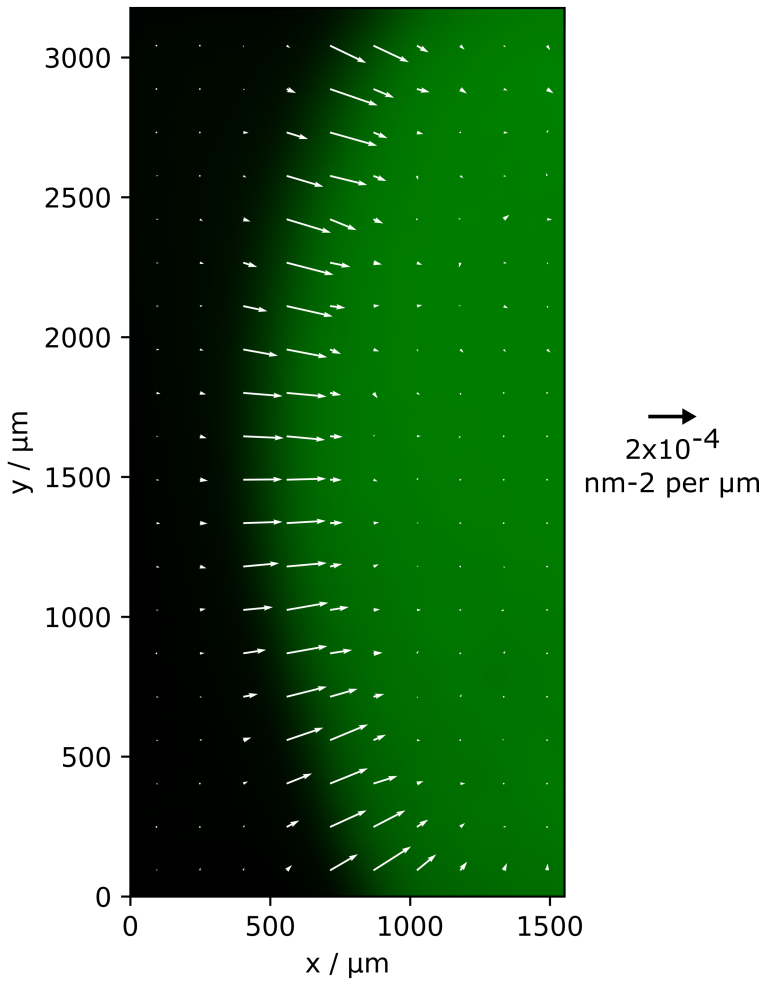


Figure 2.6: **Plot of the DNA gradient vector field superimposed on a fluorescence image of the ligand coverage.** The fluorescence image of the ligand coverage was recorded *via* epifluorescence microscopy, exciting the Alexa Fluor 488 modifications on the ligand constructs attached to the substrate; the brightness of the green background corresponds to the local density of ligands. The arrows indicate the local directions of the ligand density gradient at evenly spaced points across the image. The arrow lengths are proportional to the local magnitudes of the ligand gradient; a scale bar has been included to the right of the image.

overlayed with the identified trajectories; the boundary of the desired region was selected by manually clicking on the image, using the *ginput* function of the Python module *matplotlib* to store the selected points and then filtering the vesicle data to the selected region.

2.6.4 Mean squared displacement analysis and filtering of vesicle data

MSD analysis was applied to the vesicle data to study the diffusive motion of the vesicles, and to subsequently filter vesicle data. The MSD for a given lag time τ was calculated by slicing the trajectory into sections of duration τ and averaging the square displacement over these sections, as follows:

$$MSD(\tau) = \frac{1}{\lfloor \frac{T}{\tau} \rfloor} \sum_{n=0}^{\lfloor \frac{T}{\tau} \rfloor - 1} (\vec{r}_{(n+1)\tau} - \vec{r}_{n\tau})^2 \tag{2.2}$$

where T is the total recorded duration of the trajectory, and $\vec{r}_t$ is the position of the vesicle at time t.

The MSD was plotted as a function of τ, to identify the type of diffusive motion. In general, particles undergoing Brownian diffusion exhibit a linear relationship between MSD and lag time [263, 264]. To gain an initial insight into the vesicle motion, straight lines were fitted to the plots of MSD versus τ with a least-squares approach, only taking into account values of MSD that had been averaged over at least two trajectory slices. Non-negative constraints were enforced on the intercept and slope of the fitted lines, as negative values would be non-physical and possibly result from errors in the tracking process. Rough estimates of the vesicle diffusion coefficients were extracted from the slopes of the fitted lines.

Chapter 3

Haptotactic drift of multivalent vesicles over ligand-density gradients

Multivalent binding interactions underpin numerous biological cellular processes, such as cell adhesion [9, 19], signalling [22] and migration [20]. The accumulated strength of multiple bonds is enhanced in comparison to the individual binding interactions, which may themselves be weak and labile. In some cases, the adherent cell undergoes directed motion, such as the diffusion of the Influenza A [71, 72] and Herpes [73] viruses along the host cell membrane prior to invasion. Despite relevant studies of directed motion occurring in low valency systems [265, 266], the biophysics of directed motion of adherent cells mediated by multivalent interactions remains largely unexplored. In particular, the relative importance of factors such as binding strength and the size of the adhering cell or particle on the haptotactic motion is yet to be clarified.

In this chapter, these questions are addressed using a combination of experiments, numerical modelling and theory. The experiments were conducted on a biomimetic model system consisting of GUVs as synthetic cellular mimics. The GUVs interact with a solid substrate through multivalent adhesion mediated by binding interaction between receptors attached to the GUV membranes, and ligands attached to the substrate. The receptors and ligands were built from synthetic DNA constructs which interact through selective base-pairing interactions; this enabled precise control over the affinity and kinetics of receptor-ligand binding [34, 40, 267]. The motion of vesicles over ligand-density gradients on the substrate was tracked, and a directional drift of the vesicles towards regions of higher ligand density was observed. The vesicle drift velocity was found to be approximately proportional to the unbinding rate of the receptor-ligand bridges, in agreement with theoretical considerations. A positive correlation was also observed between the vesicle size and drift velocity. Coarse-grained simulation based on the model developed in Ref. [268] produce consistent trends in vesicle motion when varying receptor-ligand affinity and vesicle size.

All work in this chapter has been done by me unless otherwise specified. Theoretical and numerical work in Section 3.3 has been done by Prof. Bortolo Mognetti, to which I contributed through discussion by informing on experimental parameters and findings.

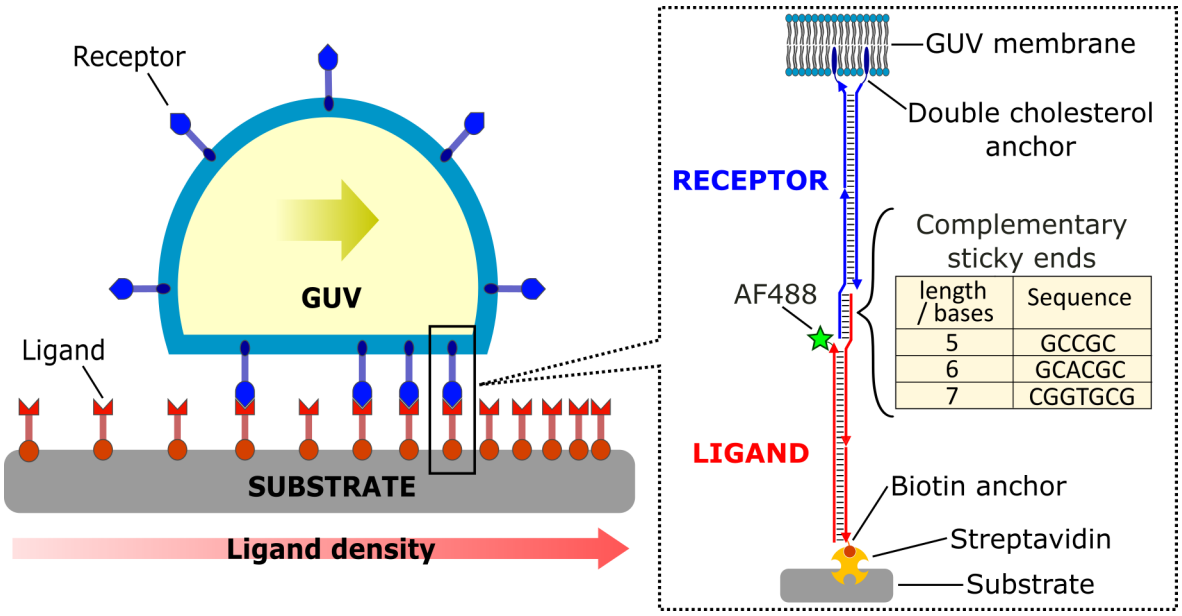


Figure 3.1: **Schematic of the experimental vesicle motility system.** A giant unilamellar vesicle (GUV) functionalised with DNA "receptor" constructs interacts with a surface density gradient of complementary DNA "ligand" constructs attached to a substrate. Double-cholesterol anchors are used for anchoring the constructs to the GUVs, while biotin-streptavidin connections are used for the substrate. The sticky end sequences for the receptor construct are shown in the inset, for systems with sticky end length $l = 5$–7 nt.

3.1 Overview of the vesicle motility system

Lipid vesicles were chosen as the biomimetic platform with which to study adhesion and motility in multivalent systems, due to their structural similarity to biological cells (*i.e.* a fluid compartment surrounded by a lipid bilayer). Meanwhile, DNA nanotechnology was used to incorporate adhesive interactions into the system, as the programmability of DNA-DNA interactions allows precise tuning of the resulting multivalent interaction strength and dynamics.

A schematic of the DNA-vesicle motility system is shown in Figure 3.1. Vesicles are functionalised with DNA constructs, here referred to as "receptors" to evoke their biological counterparts. The receptors feature a double cholesterol anchor that irreversibly partitions within the lipid bilayer. [34, 221] As the lipid bilayers of the vesicles are fluid, the receptors can diffuse laterally and redistribute across the surface of the GUV. The receptors interact with a second set of DNA constructs, here referred to as "ligands", which feature a biotin moiety for anchoring to a streptavidin-coated substrate. The receptor and ligand constructs feature complementary ss-DNA sticky ends with lengths l ranging from five to seven nucleotides (nt), which can reversibly bind to each other, forming bridges that anchor the vesicle to the substrate. The receptor and ligand constructs also feature rigid dsDNA spacers designed to control their spatial extent, and short poly-T domains to increase the flexibility and configurational freedom [34].

Despite the relatively weak binding between individual receptor-ligand pairs, the combined multivalent adhesion strength anchors the vesicle to the substrate. At any given point in time, the region on the substrate over which the vesicle can move is limited by the current set of

receptor-ligand bridges, as the bridges are constrained to remain inside the perimeter of the circular contact patch between the GUV and the substrate. Therefore, the vesicle rattles (due to Brownian motion) around the subset of n_{cb} "constraining bridges (CBs)" that can make direct contact with its perimeter; in Ref. [268] it was found that $\langle n_{\mathrm{cb}} \rangle = 5$ in the limit of a large number of bridges. However, the reversibility of receptor-ligand binding means that the vesicle is not permanently limited to rattle around the same limited region of the substrate; upon breakage of one of the CBs, the vesicle is able to explore an extended region on the substrate, before its motion is again constrained upon bridge formation and reconfiguration of the subset of CBs. The motion of the vesicle can thus be decomposed into two components [268]: the rattling of the particle around the current CBs at short timescales, and the gradual diffusion of the particle over longer distances at larger timescales.

The presence of a ligand-density gradient introduces a directional component to the stochastic motion of the vesicle. As discussed, the motion of the vesicle is limited by the set of bridges, in particular the constraining bridges that can make direct contact with the perimeter of the contact region. Assuming that receptors diffuse across the vesicle membrane and rearrange much faster than the timescales of vesicle motion, the probability of binding any given ligand under the vesicle is approximately equal. However, as there is a gradient in the distribution of ligands, a bridge is more likely to form on the side of the vesicle facing up the gradient (*i.e.* towards higher ligand density). Over time, the bias for bridges to form on the side of the vesicle facing up the gradient leads to the gradual migration of the set of CBs up the ligand-density gradient. This results in a directional bias of the diffusive motion of the vesicle along the gradient towards higher ligand densities.

3.2 Setting up the experimental system

3.2.1 Designing and verifying the DNA constructs

All DNA constructs were designed using the nucleic acid suite NUPACK [258]; the structures and sequences of all DNA constructs in this chapter are listed in Tables A.1 and A.2. The strand sequences were first designed using the NUPACK Design tool, and then passed through the Analysis tool to ensure that there were no unwanted secondary structures or significant self-complementarity of the sticky ends. The sequences for the sticky ends of varying lengths $l = 3$–10 nt were chosen such that the melting temperatures of complementary sticky ends in bulk solution under experimental conditions were (approximately) evenly spaced apart.

Formation of the desired nanostructures were experimentally verified with agarose gel electrophoresis. First, individual ligand and receptor constructs with sticky end lengths $l = 3$–10 nt were assembled *via* the annealing process detailed in the Methods. The samples were run through agarose gel electrophoresis; in Figure 3.2a, all sample bands are located between 35 bp and 50 bp of the reference DNA ladder, as expected. No other bands are significantly visible, indicating minimal excess strands or unwanted dimerisation of constructs.

Next, binding of complementary ligand and receptor constructs and the effect of varying

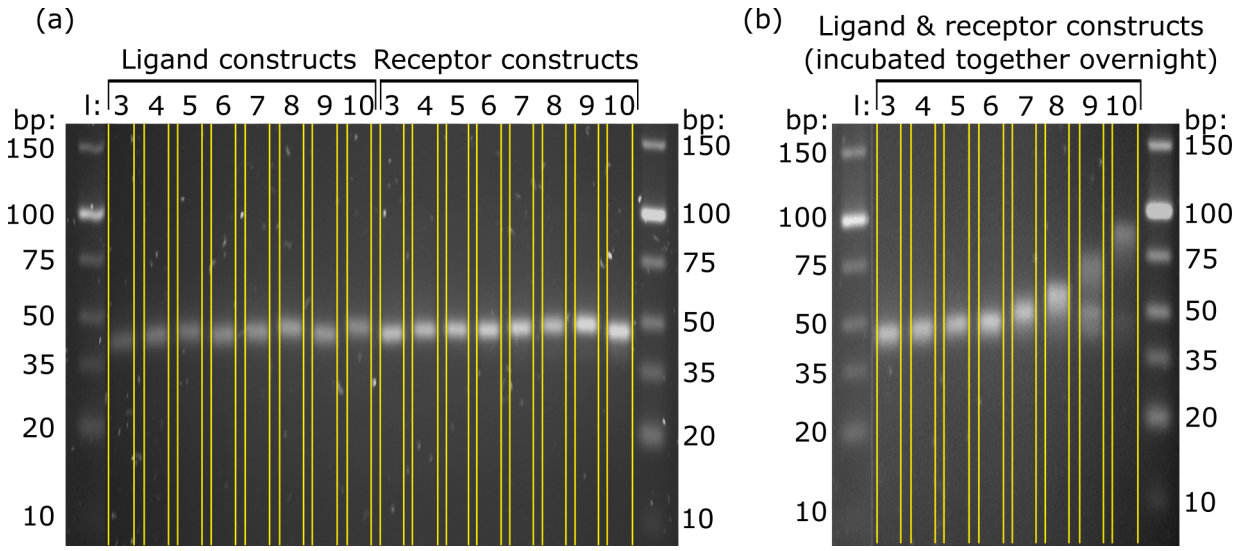


Figure 3.2: **Agarose gel electrophoresis confirms the successful formation of receptor and ligand constructs, and binding of complementary sticky ends.** Gel results for individual ligand and receptor constructs are shown in (a), while gel results for samples of ligands and receptors incubated together overnight are shown in (b); reference ladder bands are displayed in the outer two lanes. Results are shown for sticky end lengths $l = 3$–10 nt.

l on the binding strength was investigated. Complementary ligand and receptor constructs were incubated together overnight at equal concentrations of 2μM; the mixed samples were also run through agarose gel electrophoresis. The gel results in Figure 3.2b show that for some samples, a significant second band appears between 75 bp and 100 bp of the reference DNA ladder. This indicates the desired formation of a larger construct consisting of a ligand and receptor bound together. As l increases, the intensity of the band corresponding to the larger structure increases, while the intensity of the band(s) corresponding to the individual ligand and receptor constructs decreases. This implies that as l increases, the proportion of ligands and receptors bound together also increases, which is as expected as the binding strength between complementary sticky ends has increased. Smearing of the bands and increase in the apparent size of the larger construct with increasing l is most likely due to the reversible binding and unbinding of complementary sticky ends during the gel electrophoresis process, leading to variations in the velocities of individual constructs.

3.2.2 Functionalising vesicles with DNA constructs

GUVs were prepared from DOPC by electroformation, which produced polydisperse GUV samples with diameters typically ranging between 1–50 μm; the size distributions of experimental vesicles can be seen in Figure 3.3b. GUVs were chosen (as opposed to SUVs or LUVs) as their relatively large size increases ease of visualisation *via* microscopy imaging. The vesicle membranes were doped with 1 mol % NBD-PE, allowing the vesicle samples to be visualised with fluorescence imaging. After the vesicle samples were verified to be of sufficient quality, the vesicles were functionalised with DNA receptor constructs, as described in the Methods. The density of receptor constructs in the vesicle membrane was estimated to be approximately

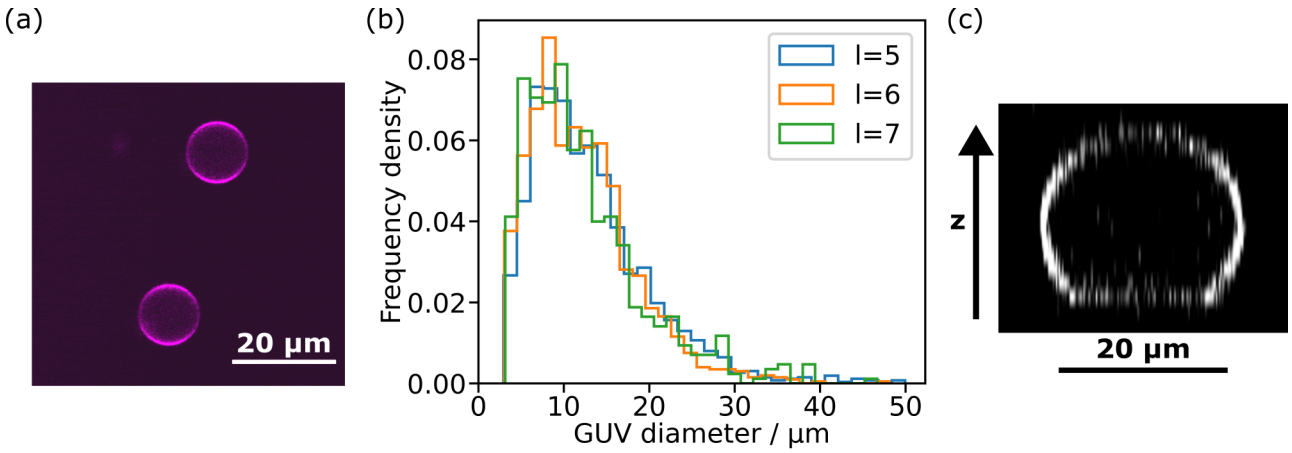


Figure 3.3: **The receptor-functionalised GUV samples are polydisperse and capable of adhering to ligand-coated substrates.** (a) shows a cross-sectional image of two vesicles recorded on a confocal microscope by exciting fluorescence of the fluorophore-modified ligand constructs attached to the vesicle membranes; the fluorophore is Alexa Fluor 488. (b) shows the size distributions of vesicles recorded in the vesicle motility experiments presented in this chapter, for the three sticky end length systems ($l = 5$, 6 and 7 nt); the vesicle sizes were measured from microscopy image data during the automated tracking process outlined in Section 2.6. Note that the size distribution data has been filtered to only the mobile population; data for all vesicles is shown in Figure C.2 in the Appendix. (c) shows a confocal cross-sectional image of a receptor-functionalised vesicle adhered to a ligand-coated substrate, where the vesicle has formed a flat adhesion patch; to record this image, fluorescence was excited in the rhodamine-tagged lipids within the vesicle bilayer.

$0.008\,\mathrm{nm}^{-2}$, by calculating the ratio of DNA to lipid molecules during the DNA-functionalisation of GUVs, and assuming 100% efficiency of GUV synthesis, as well as an average area per DOPC head group of $72.5\,\text{Å}^2$ [269]. To check that the method of attaching the receptors to the vesicle membranes was successful, the receptors were tagged with a fluorophore (Alexa Fluor 488), allowing for fluorescence imaging of the DNA-functionalised vesicles such as in Figure 3.3a.

3.2.3 Establishing a method for generating substrate-bound molecular density gradients

Various methods of generating ligand-density gradients on substrates were experimented with, before settling on the method outlined in Section 2.3.1. In this section, some of the key ideas for gradient generation that were considered are discussed, along with the thought process that led to the final method.

Preliminary ideas: microfluidic designs

One initial idea for generating substrate-bound molecular density gradients was to generate a concentration gradient of ligand molecules in bulk solution, which would then translate to a surface density gradient as the ligands bind to the substrate; this idea would be applicable to systems where the time scale of generating the concentration gradient in bulk solution is short in comparison with the time scale of attachment of the ligands to the substrate. There are numerous methods of generating concentration gradients in bulk solution in the literature, many of which involve the use of microfluidic devices that manipulate fluid flows through micron-scaled channels. For example, in Ref. [270], a microfluidic design was developed to generate concentrations of avidin in solution, which then adsorb to the underlying substrate to form surface-bound density gradients. This design consisted of a tree-like network, in which streams of two different solution are repeatedly split and recombined to generate tunable gradient profiles. Similar tree-like microfluidic devices for concentration gradient generation has also been presented by Noo Li Jeon [271, 272, 273].

Another microfluidic approach reported in literature is to generate concentration gradients as a result of diffusion. Typically, these microfluidic designs involve flowing two different solutions through separate channels; the channels are connected by a chamber in which there is minimal convection flow, allowing for gradual diffusion of the solutions between the two channels. Convection flow in the connecting chamber is minimised by a combination of pressure balancing between the two channels, and optionally with the addition of membranes or hydrogels to further minimise flow. Multiple examples of such designs have been presented in the literature, capable of generating complex spatio-temporal gradients in both 2D and 3D [274, 275, 276, 277, 278, 279].

For the purpose of experimental work in this chapter, an attempt was made at designing a microfluidic device capable of generating concentration gradients in solution as a result of diffusion, closely based on the microfluidic device presented in Ref. [274]; a schematic of the design can be seen in Figure 3.4a. However, experiments with early prototypes suffered from difficulties with fine-tuning the pressure balance in the device, resulting in undesired convection flow in the diffusion chamber. This was partly due to the use of syringe pumps to drive flows in the microfluidic device; these generate less precise flow rates than microfluidic pressure pumps, which were not available in the laboratory at the time. The microfluidic designs also would have needed to be optimised to increase ease of balancing pressure and reducing risk of air bubble formation. Due to these technical challenges, the decision was made to pursue simpler alternative solutions for gradient generation.

Continuing with the theme of generating gradients as a result of diffusion, an attempt was also made at designing a microfluidic device consisting of two solutions contained within separate static reservoirs, connected by a chamber through which the solutions can diffuse with minimal convection flow; a schematic of the microfluidic design can be seen in Figure 3.4b. Similar devices for gradient generation have been presented in Refs [280, 281, 282]. However, prototypes of this design suffered from similar issues with unwanted convection flows in the

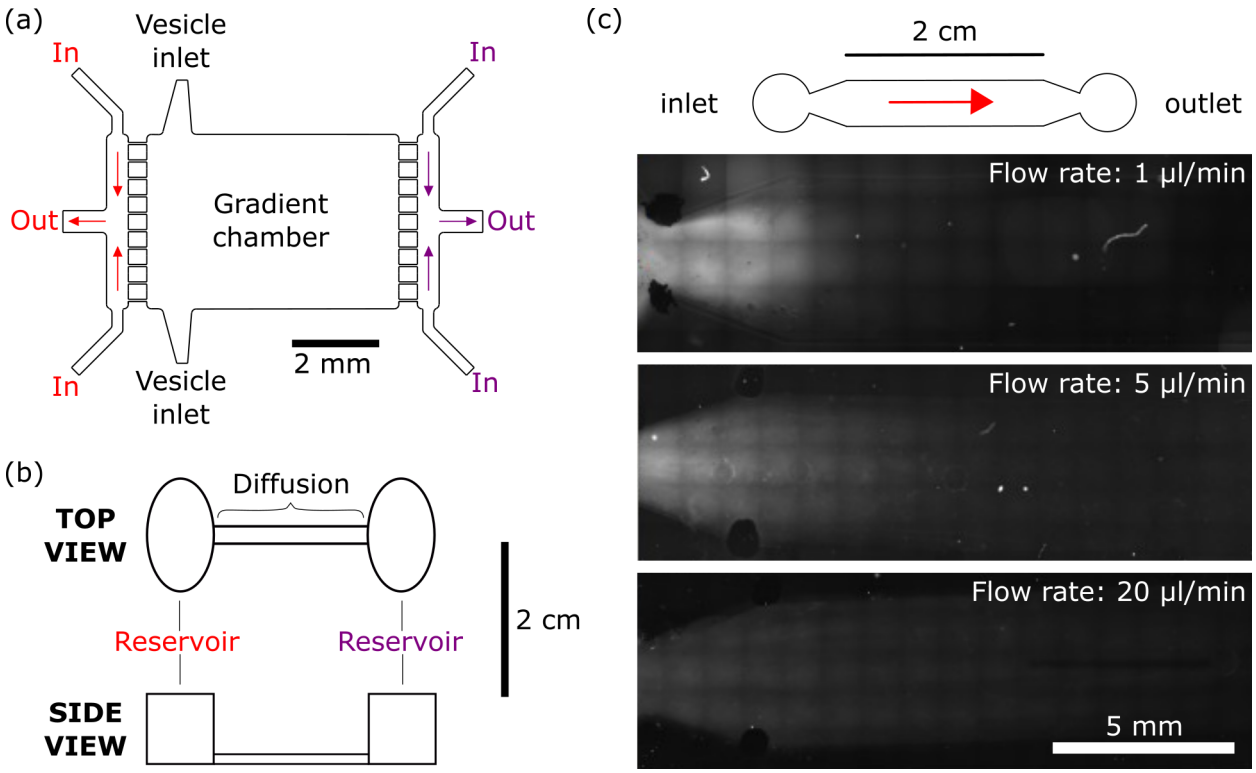


Figure 3.4: **Preliminary microfluidic designs for generating molecular gradients.** (a) shows a schematic of a microfluidic design for generating a concentration gradient in solution; two different solutions are flowed through separate channels, connected by a gradient channel through which the solutes can diffuse, generating concentration gradients. (b) shows a schematic of a design in which two static reservoirs filled with solutions are connected by a channel, through which the solutes can diffuse, generating concentration gradients. (c) shows a schematic of a design in which a solution is flowed through a channel, allowing the solute to gradually adsorb to the bottom of the channel and generate a surface density gradient. Epifluorescence microscopy images of streptavidin surface-density gradients generated using this method are included, where fluorescence has been excited in the Texas Red modification on the streptavidin; the panels show the gradient profiles generated when using different flow rates. The microscopy images have been constructed by stitching multiple fields of view together; they are displayed with the same brightness and contrast settings.

diffusion chamber due to small amounts of air left in the reservoirs.

Preliminary ideas: gradual exposure of the substrate to the coating substance

An alternative theme of surface density gradient generation entails gradual exposure of the substrate to the coating substance. For example, Ref. [283] presents a simple approach for fabricating surface density gradients by gradually immersing the substrate in a dilute solution of the coating substance. Due to the variation of exposure time to the coating substance along the substrate, this results in a density gradient in the coating. This methodology offers advantages in reproducibility and control over the gradient profile. Another approach was presented in Ref. [284], in which elastomeric stamps with curved surfaces were coated in a substance and then gradually pressed on a substrate; as the stamp is compressed, more of its surface touches the substrate, and the coating substance is deposited on the substrate with

a corresponding surface gradient. It was observed that this method is capable of generating micron-scaled gradients with a gradient steepness 1–3 orders of magnitude higher than those generated using diffusion-based techniques [284]. A third example of such a design was presented in Ref. [285], in which a protein solution is flowed through microfluidic channels; as the solution travels through the channels, the fluid is gradually depleted of proteins as they adsorb onto the substrate, resulting in a surface density gradient of the protein.

Taking inspiration from the latter approach, a simple device was designed, schematised in Figure 3.4c; this consisted of a glass-bottomed channel through which a solution of a coating substance could be flowed. During experimentation with this design, a modified form of the co-polymer poly-L-lysine-polyethylene glycol (PLL-PEG) was used as the coating substance. PLL-PEG has a bottle-brush structure, consisting of a polylysine backbone with a molecular weight of 20 kDa, and 2 kDa PEG side chains grafted every 3.5 lysines along the backbone on average; the backbone has a positive charge, which results in electrostatic adsorption of PLL-PEG to glass surfaces (which are negatively charged). For these experiments, a version of PLL-PEG with biotin modifications on approximately 50% of the PEG side chains was used, purchased from Surface SolutionS GmbH (Switzerland). A solution of $0.1\,\mathrm{mg\,ml^{-1}}$ PLL-PEG-biotin in $1\times$ PBS buffer was flowed through the channel gradually until the solution had reached the channel outlet; the flow rate was varied between experiments to investigate the effect on the resulting surface density gradient profile. The channel was then rinsed with $1\times$ PBS buffer to wash away any excess PLL-PEG, before being filled with a solution of $0.1\,\mathrm{mg\,ml^{-1}}$ streptavidin (conjugated with Texas Red, and purchased from ABCAM, UK) in $1\times$ PBS and left to incubate for 30 minutes to allow the streptavidin to bind to the biotinylated PLL-PEG. The channel was then rinsed again to wash away any excess streptavidin, and imaged with an epifluorescence microscope to visualise the coverage of streptavidin on the substrate.

As can be seen in the epifluorescence microscopy images in Figure 3.4c, increased flow rate corresponds to a reduction in the steepness of the streptavidin-density gradient. This is as expected; for higher flow rates, the variation in exposure time of the substrate to the coating substance along the channel reduces, which means that the variation of the density of the coating substance also reduces. This method of generating surface-density gradients thus appeared to be a promising approach to generating tunable gradient profiles, although it still required a significant amount of time and effort to fabricate the single channel device for the generation of each gradient. It was noted that a further simplification of this method would be to apply a static droplet of the coating substance to the substrate; this would essentially equate to the limiting case where the flow rate is zero, and thus result in a gradient of maximum steepness at the edge of the droplet. This gave rise to the finalised method of generating surface density gradients, summarised in the next section.

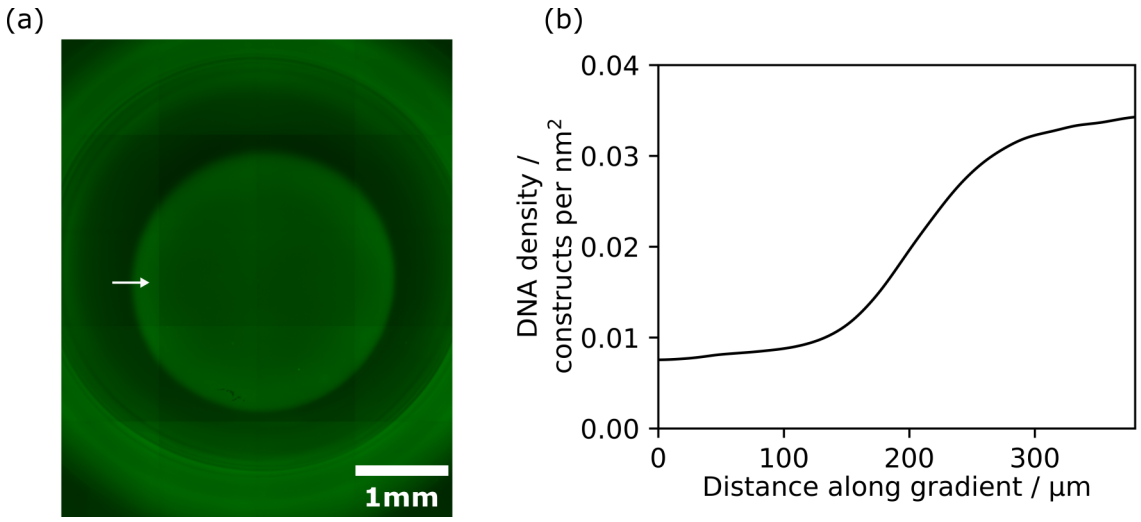


Figure 3.5: **A typical ligand-density gradient.** (a) shows an example image of a substrate (a streptavidin-coated well) functionalised with biotinylated ligand constructs, such that a circular region of the substrate is coated with ligands; the surface functionalisation method is detailed in Section 2.3.1. The image was created by stitching multiple fields of view recorded on an epifluorescence microscope; the fluorescence signal is from the Alexa Fluor 488 modification on the ligands. The arrow marks the location at the edge of the circular coated region of the substrate over which the ligand-density gradient profile plotted in (b) was measured. The base and point of the arrow correspond to the left- and right-hand sides of the plot in (b), respectively.

Finalised method: coating substrates with single droplets of DNA

After observing the relationship between flow rate and gradient steepness with the gradient generation method discussed in the previous section, it was noted that applying a static droplet of ligand solution to a fixed point on a biotinylated substrate would essentially be a limiting case of the previous method (*i.e.* zero flow rate). This new method (described in further detail in Section 3.2.3) resulted in a coating of DNA on a circular region of the substrate, with a diameter of $\approx 3.5\,\text{mm}$.

The ligand-density gradient profiles were characterised with the methods outlined in Section 2.3.2. It was estimated that the ligand density within the circular, coated region of the substrate was $\approx 0.03\,\text{nm}^{-2}$. Due to the fast rate of binding between streptavidin and biotin, a small amount of excess DNA bound to the surrounding region during the washing process; the surface density of DNA in this region was estimated to be 0.005–0.01 nm^{-2} on average. At the perimeter of the circular maximally-coated region, there was a steep surface density gradient spanning a distance of approximately $100\,\mu\text{m}$; an example of a typical ligand-density gradient profile can be seen in Figure 3.5.

3.2.4 Verifying DNA-mediated multivalent adhesion of vesicles to substrates

Receptor-functionalised GUVs were deposited onto substrates coated with ligand constructs and left to settle and adhere to the surface. For sufficiently strong adhesion (*i.e.* for sticky end lengths $l \geq 5\,\text{nt}$), confocal images show that the GUVs deform in shape to a truncated sphere geometry with a flat adhesion patch, as can be seen in Figure 3.3c. Deformation of vesicles to form flat adhesion patches in multivalent systems has previously been observed, such as in Refs [41] and [40]. Note that the electroformed vesicles have some excess area without the need to include an osmotic mismatch, allowing for deformation of their shape to form a flat adhesion patch [40, 267].

Time lapse recordings of the adhered GUVs in the $l \geq 5\,\text{nt}$ systems showed minimal motion, further indicating adhesion of the vesicles to the substrate (see Figure 3.13). On the contrary, in systems with sticky end lengths $l = 3$ or $4\,\text{nt}$, the vesicles were observed to gradually drift unidirectionally across the well; this was attributed to the binding strength being insufficient to keep the GUVs adhered to the surface, causing them to drift driven by convection or gravity (also shown in Figure 3.13). This provides evidence that the adhesion of vesicles in the $l \geq 5\,\text{nt}$ systems is mediated by the binding of complementary sticky ends, as opposed to non-specific adhesion.

3.2.5 Developing a method to segment and track vesicles

Initially, attempts were made to use the TrackMate plugin [286, 287] on ImageJ to segment and track vesicles in the image data. However, as the vesicle samples were polydisperse, direct application of a template matching method to search for bright circular objects in the binarised images did not perform sufficiently well. For instance, the algorithm would sometimes incorrectly identify a larger vesicle as comprising of multiple smaller vesicles.

The decision was thus made to write up an automated tracking process in Python, that could be tailored to segment the experimental image data more effectively. In particular, to achieve size-invariant identification of vesicles in the images, the distance transform was applied to the image data before conducting template-matching. The distance transform re-labels each pixel with the distance to the nearest dark pixel in the pre-transformed image. Therefore, the pixels within a bright circular region (*i.e.* a vesicle) in the pre-transformed image are re-labelled according to their radial position within the circle, with maximum value at the centre equal to the radius of the circle. Applying the distance transform to the image data prevents erroneous identification of multiple smaller vesicles within the area of a larger vesicle, and enables identification of circular objects in the image without being constrained to searching for objects of a specified radius. The automated tracking process is outlined in further detail in Section 2.6.

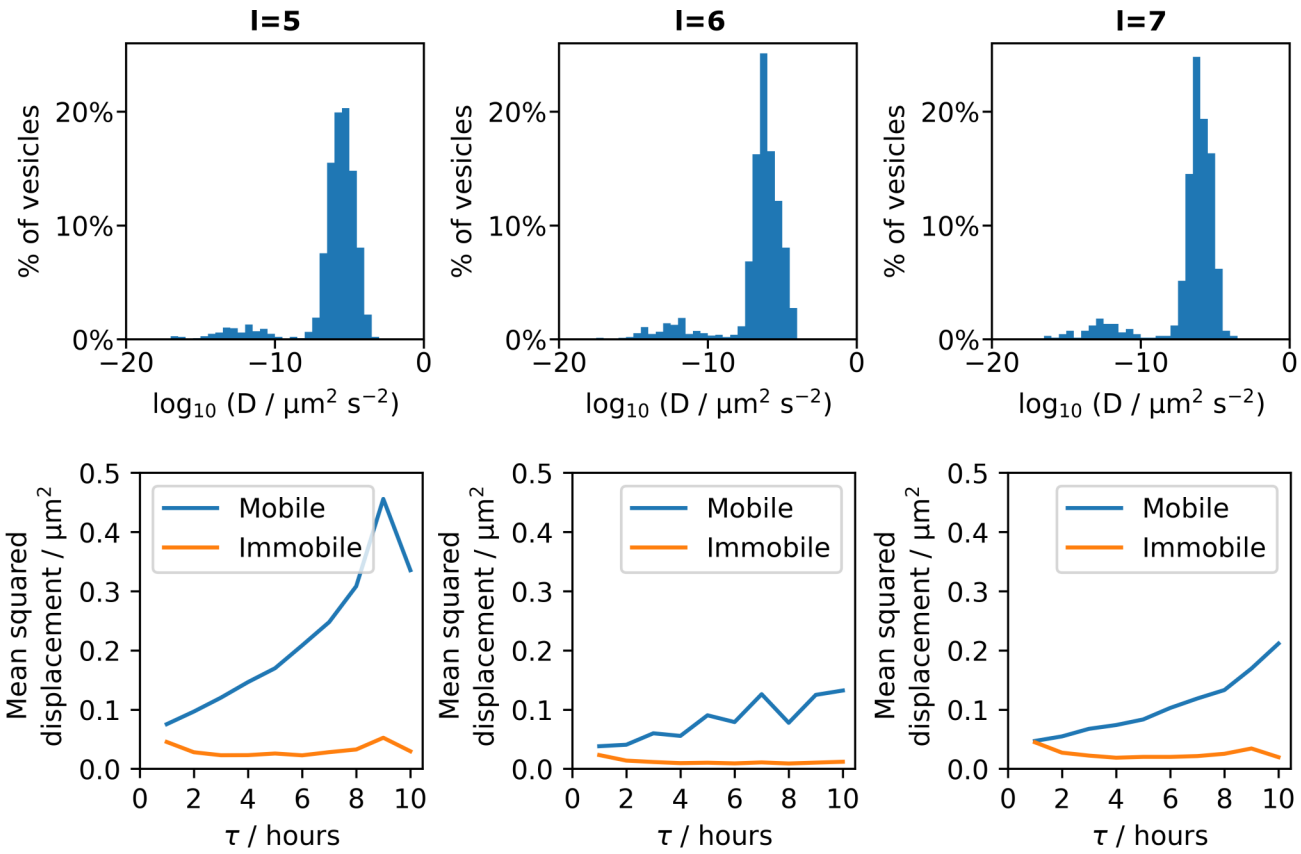


Figure 3.6: **Estimated vesicle diffusion coefficients appear to exhibit a bimodal distribution.** Histograms of vesicle diffusion coefficients D are shown in the top row, for sticky end lengths $l = 5$, 6 and 7 nt. The diffusion coefficients were estimated from experimental trajectory data *via* mean squared displacement (MSD) analysis, as described in Section 2.6.4. Plots of mean squared displacement versus lag time τ are shown in the bottom row. These were generated by first calculating the MSDs for individual GUVs, and extracting the estimated diffusion coefficient for each vesicle from the gradient of the linear fit; vesicles were then classified as "mobile" or "immobile" depending on if their estimated diffusion coefficient is smaller than or greater than $10^{-8}\,\mu\text{m}^2\text{s}^{-2}$, respectively. The MSDs were then averaged over the mobile and immobile populations separately.

3.2.6 Apparent bimodal distribution of vesicle diffusion coefficients

MSD analysis was applied to the vesicle trajectory data to extract estimates for vesicle diffusion coefficients, as described in Section 2.6.4. Histograms of the estimated diffusion coefficients were plotted separately for the different sticky end lengths ($l = 5$, 6 and 7 nt), shown in Figure 3.6. Bimodal distributions were observed in the diffusion coefficients, with two distinct peaks corresponding to a "faster" and "slower" vesicle population, with approximately 5–6% of the vesicles in the latter. Although this result was unexpected, it must be noted that bimodal distributions of particle mobility featuring an immobile population have also been observed in other particle motility studies. For example, in Ref. [288] a study was conducted on the motility of influenza virus particles along surface density gradients of adhesive molecules. In this study, approximately 58% of the virus particles appeared to be immobile, which was attributed to heterogeneity of the virus samples such as non-uniformity of the coverage of adhesive molecules expressed on the surface of the virus.

To understand the underlying factor behind the bimodal distribution of vesicle diffusion coefficients, MSD plots for vesicles in the "slower" (or "immobile") and "faster" (or "mobile") populations were inspected. In Figure 3.6, the plots of MSD averaged over the mobile population show an increasing trend between MSD and lag time, which illustrates that the particles (on average) gradually travel over the substrate. There does appear to be a slight upward curve in the plots of MSD averaged over the mobile population, which would suggest the presence of directed motion (rather than purely being Brownian motion). For context, a linear relationship between MSD and lag time with a positive gradient would indicate Brownian motion, while a quadratic relationship with a positive quadratic coefficient would indicate directed, ballistic motion (*e.g.* moving at constant velocity). Furthermore, note that the MSD increases at a noticeably greater rate with lag time for $l = 5$, compared with $l = 6$ and 7; this effect is discussed in more detail in Section 3.4.1.

In contrast, the plots of MSD averaged over the immobile population (also in Figure 3.6) show a decreasing trend between MSD and lag time. This likely explains the unusually small diffusion coefficients fitted for vesicles in the immobile population. Due to the non-negative constraints on the intercept and slope of the linear fits of MSD versus lag time, the fitting algorithm assigned negligible, near-zero values to the fitted parameters, resulting in an apparent secondary population of slower-moving vesicles.

The next step towards understanding the reasoning behind this apparent negative correlation between MSD and lag time was to study the trajectories of vesicles exhibiting this negative relationship; some example trajectories of vesicles in the "immobile" population can be seen in Figure 3.7. Generally, the trajectories of the "immobile" vesicles span limited regions, smaller than the distance of a pixel ($0.64432\,\mu$m). The algorithmically tracked vesicle trajectories were compared with the imaged vesicle motion by eye. It was found that the apparent negative correlation was largely due to errors and noise in the tracking process, causing spurious jumps in the tracked vesicle location. This resulted in trajectories that erroneously suggested a gradual confinement of the vesicle over time and thus a negative correlation between MSD and lag time.

A second contributing factor to the "slower" vesicle population was the presence of a small proportion of immobile vesicles in the samples, which were observed by eye in our experimental image data. The immobility could be due to non-uniformity in DNA density on the substrate and vesicle surfaces, resulting in vesicles being trapped in high DNA density regions. However, even in systems with no DNA ligands or receptors, a small proportion of immobile vesicles were observed. This is likely due to vesicles being pinned to surface defects, or trapped by strong non-specific adhesion. Furthermore, erroneous tracking of surface defects or sample impurities could also contribute to the apparent population of immobile vesicles.

As the "slow" vesicles are thought to be due to tracking errors and surface defects, the decision was made to exclude this population from the experimental data used in following analysis, by filtering the vesicles to those with diffusion coefficients estimated to be greater than $10^{-8}\,\mu\text{m}^2\text{s}^{-2}$. This would reduce the number of inaccurate trajectories included in the data analysis, and also the number of vesicles that are immobile due to factors other than

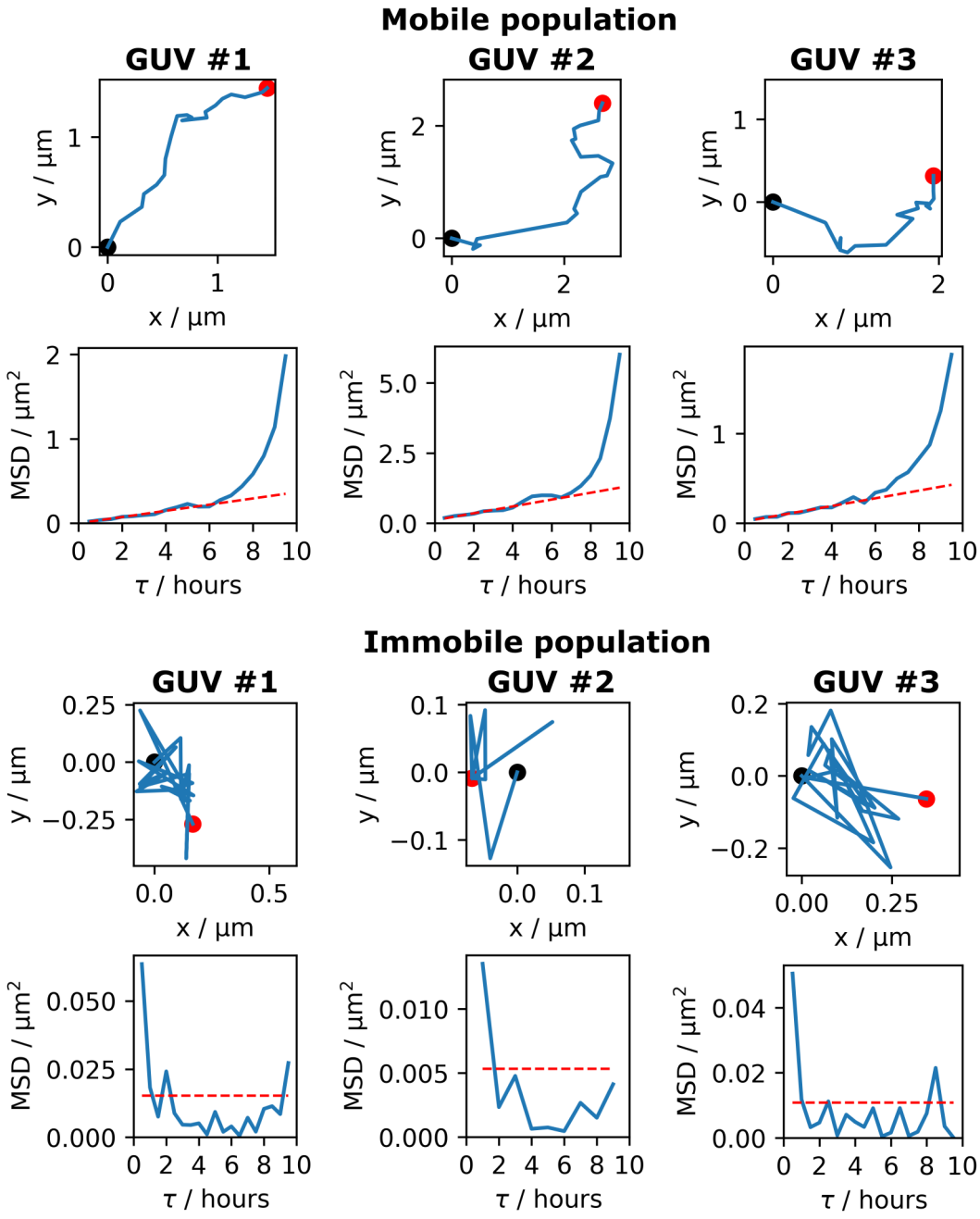


Figure 3.7: **Examples of trajectories and mean squared displacements plotted for individual vesicles.** Data for three example vesicles from the "mobile" vesicle population and three example vesicles from the "immobile" vesicle population are plotted; further discussion of the mobile and immobile populations can be found in Section 3.2.6. All examples are of vesicles in the $l = 5$ nt-sticky end length system. The trajectory plots show the evolution of the vesicles x-y displacements over the duration of the experiments; the black and red markers indicate the start and end points of the trajectories. The mean squared displacement plots corresponding to these vesicle trajectories have been displayed, with the linear fit indicated by the dashed red line. Note that the straight line was fitted to the first half of the MSD plots (*i.e.* only fitted to values of MSD that had been averaged over at least two trajectory slices, as discussed in Section 2.6.4).

the designed DNA-DNA interactions. It must be noted that including the "slow" vesicles in data analysis has no significant impact on the qualitative findings reported in this thesis, but

results pre- and post- filtering are nevertheless presented in Section C of the Appendix for transparency.

3.3 Theoretical and numerical modelling

As mentioned, the theoretical and numerical modelling summarised in this section was conducted by Prof. Bortolo Mognetti, in close collaboration with my experimental work.

3.3.1 Numerical modelling of the vesicle motility system

The numerical modelling in this section extends on previous investigations by Prof. Bortolo Mognetti into the emerging dynamics of particles that are bound to an interface *via* reversible receptor-ligand bonds [268]. Ref. [268] focused on the mobility of such particles over a surface featuring a uniform coverage of binding sites; coarse-grained reaction-diffusion simulations demonstrated the lateral diffusion of the particles over the interfaces. The simulations were then adapted to study the motion of receptor-functionalised particles over a surface featuring a ligand-density gradient, for comparison with the experimental work in this chapter.

In the model, the vesicles are mapped onto two-dimensional disks of radius R to represent the flat adhesion patch, as schematised in Figure 3.8. The disks are modelled to be rigid such that thermal membrane fluctuations and deformations of the vesicle shape are neglected, and the disk-substrate distance is maintained constant. The average density of receptors on the vesicles was set to $\rho_{\mathrm{R}} = 0.008\,\mathrm{nm}^{-2}$, consistent with the nominal experimental values. Disks with diameter $2R = 0.2\,\mu\mathrm{m}$, $1\,\mu\mathrm{m}$ and $1.8\,\mu\mathrm{m}$ were simulated. Note that these diameters are smaller than experimental GUVs by one order of magnitude, as experimental GUVs typically had diameters on the order of $10\,\mu\mathrm{m}$. The decision to simulate smaller vesicles was made to keep simulations affordable, as simulations on the same size scales as experiments would be impractical. On the flip side, reducing the size of experimental vesicles would not have been feasible with the experimental setup, as smaller vesicles would cover a smaller extent of the gradient (and thus have a smaller directional bias in motion, resulting in a lower signal-to-noise ratio); smaller vesicles would also be more difficult to image and track. All in all, the decision was made to simulate smaller length scales than experiments in the interest of practicality, and focus on comparing trends in vesicle drift velocity between experiments and simulations rather than absolute values. The simulated gradients were adjusted to be steeper than experimental gradients, to maintain the ratio of vesicle size to gradient steepness.

The substrate is randomly decorated by ligands to generate a linear ligand-density profile with slope λ, and average ligand surface density of $\rho_{\mathrm{L}} = 0.021\,\mathrm{nm}^{-2}$ at the starting location of the vesicles. The simulated gradient slope was set to be an order of magnitude higher than experimental gradients ($\lambda = \rho_{\mathrm{L}}/10\,\mu\mathrm{m}^{-1}$), such that the steepness of the gradient relative to vesicle size was maintained, as mentioned before. Simulating smaller values of λ would rapidly make the system computationally untreatable, as for milder gradients the drifting component of the motion is overwhelmed by the stochastic component.

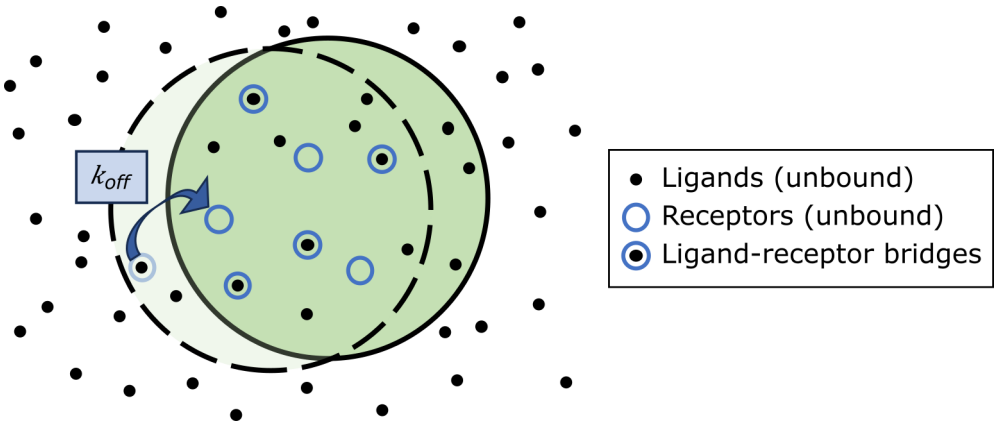


Figure 3.8: **Vesicle motion is constrained by receptor-ligand bridges, forming the basis of numerical modelling.** Receptor-ligand bridges break at a rate of k_{off}, which enables receptors to bind to other ligands under the vesicle. The reversibility of bridge formation thus allows the vesicle to gradually move over the substrate, as the bridge configuration evolves over time.

Receptors on the vesicle may bind with free ligands on the substrate within the projected area of the disk, forming receptor-ligand bridges. The rate constants at which these bridges form and break were calculated as [34]

$$k_{\text{on}} = \frac{\alpha\, k_{\text{on}}^{\text{sol}}}{3\pi R^2 L} \qquad k_{\text{off}} = \alpha\, \rho_0\, k_{\text{on}}^{\text{sol}} \exp[\beta \Delta G_0], \tag{3.1}$$

where $k_{\text{on}}^{\text{sol}}$ is the hybridisation rate of free oligonucleotides in solution, L is the length of the dsDNA spacer of the ligands and receptors, ΔG_0 is the standard hybridisation free energy of the sticky ends, $\rho_0 = 1\,\text{M}$ is the standard concentration and $\beta = 1/(k_B T)$, where k_B is the Boltzmann constant and T is the temperature. α is a non-dimensional factor < 1, accounting for the fact that the hybridisation kinetics are expected to be slower as a result of the DNA constructs being tethered to surfaces. α was set to 0.1 as an estimate based loosely on observations made in Ref. [33]; however, it must be noted that as simulated and theoretical drift velocities are proportional to α, changing the value of α affects the absolute values but not the trends generated by varying other system parameters. Finally, the factor of $1/3\pi R^2 L$ in the expression for k_{on} expresses the volume within which the receptor sticky ends are distributed. For clarification, the vesicles were represented as hemispheres with a total surface area equal to $3\pi R^2$; if the free sticky ends are assumed to be uniformly distributed within a layer of thickness equal to the length of the DNA constructs surrounding the vesicle, this results in a density of $1/(3\pi R^2 L)$. To evaluate k_{on} and k_{off}, $k_{\text{on}}^{\text{sol}}$ was set to be $10^6\,\text{M}^{-1}\text{s}^{-1}$, an approximate estimate for short DNA oligomers [193]. L was set equal to 10 nm, an estimate based on the length of the DNA constructs in base pairs, given that one base pair equates to an approximate distance of 0.34 nm along a dsDNA strand [289]. The temperature T was set to 293.15 K (25°C). ΔG_0 was estimated using the nearest neighbour thermodynamic model [175, 290, 291, 292], and then plugged into Equation 3.1 to calculate the rate constants. Numerical values for ΔG_0 and k_{off} are listed in Table 3.1.

Table 3.1: **Hybridisation free energies and unbinding rates of sticky ends.** Values for hybridisation free energies(ΔG_0 / J mol^{-1}) and unbinding rate constants (k_{off} / s^{-1}) are listed for sticky end lengths $l = 5$, 6 and 7 nt.

	ΔG_0 / J mol^{-1}	k_{off} / s^{-1}
$l = 5$	-11.4	1.10
$l = 6$	-13.3	0.174
$l = 7$	-16.3	0.0084

In the model, it is assumed that free receptors (*i.e.* receptors that are not bound to a ligand) diffuse laterally over the vesicle bilayer and rearrange much faster than the timescales of vesicle motion. This assumption is based on observations made in previous studies of DNA constructs attached to lipid bilayers *via* cholesterol anchors, in which the constructs diffuse laterally over the membranes with diffusion constants of a few squared micrometers per second [40, 33, 230, 293]. Therefore, instead of tracking the specific positions of free receptors, it is assumed that a free receptor is equally likely to bind any ligand within the projection of the vesicle on the substrate. Furthermore, this means that the system equilibrates over time scales much shorter than experimental durations, such that the density of receptor-ligand bridges has reached its equilibrium value prior to the start of experimental time lapse recordings, as opposed to a gradual enrichment of bridges in the adhesive fingerprint during experiments. To match this behaviour in simulations, the simulated system was allowed to equilibrate before initialising the vesicle motion.

The system was simulated using a reaction-diffusion algorithm [34, 294, 268]. At each simulation time step, of duration Δt, the Gillespie algorithm [295] is used to sample one reaction corresponding to the breakage of an existing receptor-ligand bridge or the formation of a new bridge, and compute the time required for the reaction. The sampling of receptor-ligand (de)complexation reaction is repeated until the total reaction time exceeds Δt. Following the reaction step, the position of the disk is updated by randomly (uniformly) selecting a new centre of mass from all the possible locations compatible with the new configuration of bridges [268]. The simulation code can be found online [296].

3.3.2 Theoretical estimation of the density of receptor-ligand bridges

The equilibrium predictions for the density and number of bridges (ρ_b and n_b, respectively) under a vesicle at a given position x along the gradient can be calculated by solving the following equation:

$$\rho_b(x) = K_{\text{eq}} \left[\rho_L(x) - \rho_b(x)\right] \left[N_R - n_b(x_{\text{CM}})\right] \tag{3.2}$$

where $\rho_L(x)$ is the density of ligands at position x, N_R is the total number of receptors over the vesicle membrane, $K_{\text{eq}} = k_{\text{on}}/k_{\text{off}}$ is the equilibrium constant controlling the formation of bridges [34], and x_{CM} is the x-position of the vesicle's centre of mass along the gradient. The number of bridges is obtained by integrating $\rho_b(x)$ over the contact region between the vesicle and the surface ($\Omega(x_{\text{CM}})$); similarly, the total number of ligands underneath the vesicle

is obtained by integrating $\rho_L(x)$ as so:

$$n_b(x_{\mathrm{CM}}) = \int_{\Omega(x_{\mathrm{CM}})} \rho_b(x)\mathrm{d}x\mathrm{d}y \qquad N_L(x_{\mathrm{CM}}) = \int_{\Omega(x_{\mathrm{CM}})} \rho_L(x)\mathrm{d}x\mathrm{d}y \tag{3.3}$$

where y is the coordinate orthogonal to the gradient. Integrating Equation 3.2 over $\Omega(x_{\mathrm{CM}})$ thus gives

$$n_b(x_{\mathrm{CM}}) = K_{\mathrm{eq}}\left[N_L(x_{\mathrm{CM}}) - n_b(x_{\mathrm{CM}})\right]\left[N_R - n_b(x_{\mathrm{CM}})\right] \tag{3.4}$$

which is solved *via* the quadratic formula to give the total number of bridges,

$$n_b(x_{\mathrm{CM}}) = \frac{K_{\mathrm{eq}}N_L(x_{\mathrm{CM}}) + K_{\mathrm{eq}}N_R + 1 - \sqrt{\Delta^2}}{2K_{\mathrm{eq}}} \tag{3.5}$$

$$\Delta^2 = \left[K_{\mathrm{eq}}N_L(x_{\mathrm{CM}}) - K_{\mathrm{eq}}N_R\right]^2 + 2K_{\mathrm{eq}}N_L(x_{\mathrm{CM}}) + 2K_{\mathrm{eq}}N_R + 1. \tag{3.6}$$

Given $n_b(x_{\mathrm{CM}})$, Equation 3.2 can be rearranged to calculate the density of bridges as

$$\rho_b(x) = \frac{K_{\mathrm{eq}}\left[N_R - n_b(x_{\mathrm{CM}})\right]}{1 + K_{\mathrm{eq}}\left[N_R - n_b(x_{\mathrm{CM}})\right]}\rho_L(x). \tag{3.7}$$

Experimental values for receptor densities as well as K_{eq} for the three sticky end length systems ($l = 5$, 6 and 7 nt) yields the plot of bridge density versus ligand density in Figure 3.9. The plot shows that under experimental conditions, the density of receptor-ligand bridges is saturated and reaches its maximal value limited by the densities of receptors and ligands.; while $\rho_L < 3\rho_R$ the bridge density is limited by ρ_L, whereas when $\rho_L > 3\rho_R$ the bridge density saturates at $3\rho_R$. The factor of 3 results from the redistribution of receptors on the vesicle membrane, from an initial uniform concentration of ρ_R across the vesicle (approximated as a hemisphere with total surface area $3\pi R^2$) to being concentrated within the contact region (with a surface area of πR^2).

3.3.3 Theoretical predictions of vesicle drift velocity

This section presents derivations of theoretical predictions for the scaling and absolute value of the drift velocities of receptor-functionalised vesicles along ligand-density gradients.

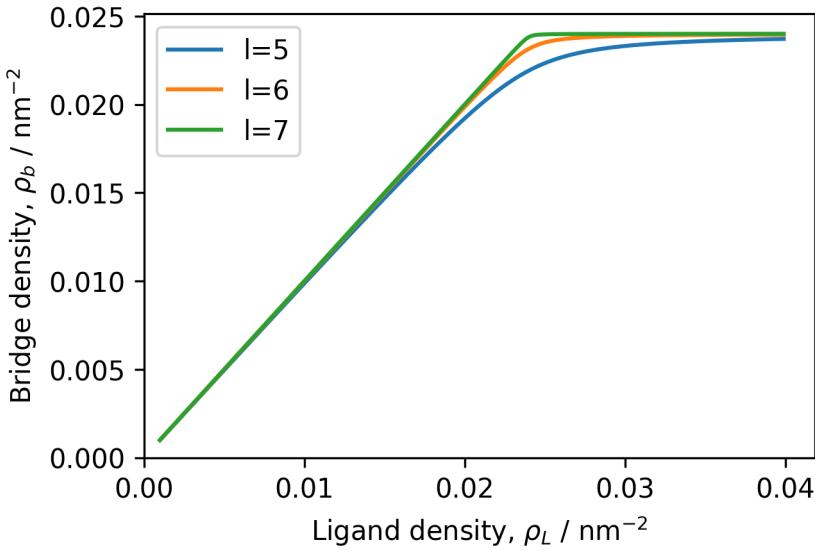


Figure 3.9: **Under experimental conditions, the density of receptor-ligand bridges is saturated and reaches its maximal value.** The bridge density ρ_b is plotted against ligand density ρ_L, while the initial density of receptors over the membrane ρ_R is fixed at 0.008 nm^{-2}, for 0.2 μm-diameter vesicles and sticky end lengths l = 5, 6 and 7 nt. The bridge density has been estimated using Equation 3.7.

Scaling relation for the vesicle drift velocity

For a given number of ligands and receptors, the drift velocity is expected to be a function of the following variables: the rate of unbinding of receptor-ligand bridges (k_{off}), bridges (n_{b}), and the diffusion constant of non-adhering vesicles (D). In systems featuring many bridges or low unbinding rates (as is the case for the experimental vesicle motility system), the displacement dynamics of the vesicles is limited by the timescales of ligand/receptor reactions. This can be verified by comparing two characteristic timescales: the typical timescale over which the translational configurational space available to the vesicles changes as a result of (un)binding of receptor-ligand bridges (τ_{r}), and the diffusion timescale needed by a vesicle to explore the available space (τ_{d}). These timescales are considered in Ref. [268], in which a theoretical model was designed to study the behaviour of a particle functionalised with mobile receptors that binds to a substrate coated with fixed ligands.

As the translational configurational space available to the vesicle depends on the set of constraining bridges near the perimeter of the contact region, τ_{r} equates to the timescale of the reconfiguration of CBs. This can be estimated as $\tau_{\text{r}} = 1/(2k_{\text{off}}n_{\text{cb}})$, where the average number of CBs $\langle n_{\text{cb}}\rangle \approx 5$ as mentioned previously; a derivation can be found in Ref. [268]. Using the values for the unbinding rates k_{off} stated in Table 3.1, τ_{r} is estimated to be 0.091 s, 0.57 s, and 11.9 s for sticky ends with l = 5, 6, and 7 nt respectively.

Regarding the diffusion timescale τ_{d}, the average area of the configurational space Ω available to the vesicle is well approximated by $\langle|\Omega|\rangle = \pi R^2\langle n_{\text{cb}}\rangle/\langle n_{\text{b}}\rangle^2$, as found in Ref. [268]. The diffusion timescale for the vesicle to explore the available configurational space can thus be estimated as $\tau_{\text{d}} = \pi R^2 n_{\text{cb}}/(Dn_{\text{b}}^2)$. Using the Stokes-Einstein equation for the diffusion constant of a spherical particle, D for a 5 μm-radius vesicle can be estimated to be 0.049 μm^{2}s^{-}1. In

Figure 3.9 it can be seen that the bridge density is comparable to the density of receptors and ligands (*i.e.* on the order of $0.01\,\mathrm{nm}^{-2}$). Altogether, τ_d can be estimated to be $1.30\times10^{-8}\,\mathrm{s}$ for a $5\,\mu$m-radius vesicle.

In conditions considered here, τ_r is at least 7 orders of magnitude bigger than τ_d, which means that the displacement dynamics of the vesicles is limited by the timescales of ligand/receptor reactions. Therefore, it is expected that the scaling relationship of v_drift is entirely determined by k_off, such that

$$v_\mathrm{drift} \propto k_\mathrm{off} f(R, n_\mathrm{b}), \tag{3.8}$$

where $f(R, n_\mathrm{b})$ is a general function on the variables R and n_b.

Analytic prediction of the vesicle drift velocity

As an initial step in the derivation, we postulate that the dynamics of the vesicle's centre of mass (at position x_CM along the gradient) is described by an over-damped Langevin equation, *i.e.*

$$\frac{\partial x_\mathrm{CM}}{\partial t} = -\beta D(x_\mathrm{CM})\frac{\partial V_\mathrm{multi}(x_\mathrm{CM})}{\partial x_\mathrm{CM}} + f_1(x_\mathrm{CM}) + \sqrt{2D(x_\mathrm{CM})}\eta(t), \tag{3.9}$$

where $V_\mathrm{multi}(x_\mathrm{CM})$ is the multivalent free energy of the vesicle at a given x_CM [34, 297], $\eta(t)$ is a Gaussian white noise ($\langle\eta(t)\rangle = 0$, $\langle\eta(t)\eta(t')\rangle = \delta(t-t')$), and $D(x_\mathrm{CM})$ is the position-dependent diffusion constant [268]. To fully determine the solutions of Equation 3.9, one needs to specify a prescription to interpret the stochastic term of this equation in which the noise source multiplies a non-constant function. Such a prescription identifies the value of the following integral

$$\int_t^{t+\Delta t} \mathrm{d}t' g(x(t'))\eta(t') = g(\gamma x(t+\Delta t) + (1-\gamma)x(t)) \int_t^{t+\Delta t} \mathrm{d}t'\eta(t'), \tag{3.10}$$

where γ is a parameter with $\gamma \in [0, 1]$. For instance, $\gamma = 0$, $1/2$, and 1 when considering, respectively, the Ito, Stratonovich, and isothermal convention. Ref. [298] has shown the necessity of considering the extra drifting term $f_1(x_\mathrm{CM})$ in Equation 3.9 to ensure recovering of the expected equilibrium state, $P(x_\mathrm{CM}) \sim \exp[-\beta V_\mathrm{multi}(x_\mathrm{CM})]$. In particular, this is achieved when using

$$f_1(x_\mathrm{CM}) \;=\; 2(1-\gamma)\frac{\partial}{\partial x_\mathrm{CM}} D(x_\mathrm{CM}) \tag{3.11}$$

which gives rise to the following Fokker-Planck equation that is not a function of γ [298]:

$$\frac{\partial}{\partial t}P(x_\mathrm{CM}, t) = \frac{\partial}{\partial x_\mathrm{CM}} D(x_\mathrm{CM}) \left(\beta\frac{\partial V_\mathrm{multi}(x_\mathrm{CM})}{\partial x_\mathrm{CM}} + \frac{\partial}{\partial x_\mathrm{CM}}\right) P(x_\mathrm{CM}, t)\,. \tag{3.12}$$

From Equation 3.12, we then calculate the drifting velocity $v_\mathrm{drift}(x_\mathrm{CM})$ as follows:

$$\int \mathrm{d}x_\mathrm{CM} \cdot v_\mathrm{drift}(x_\mathrm{CM})P(x_\mathrm{CM}, t) \;\equiv\; \int \mathrm{d}x_\mathrm{CM} \cdot x_\mathrm{CM}\frac{\partial}{\partial t}P(x_\mathrm{CM}, t). \tag{3.13}$$

Substituting in the Fokker-Planck equation then gives

$$\int \mathrm{d}x_{\mathrm{CM}} \cdot v_{\mathrm{drift}}(x_{\mathrm{CM}}) P(x_{\mathrm{CM}}, t) = \int \mathrm{d}x_{\mathrm{CM}} \left[\frac{\partial}{\partial x_{\mathrm{CM}}} D(x_{\mathrm{CM}}) - \beta D(x_{\mathrm{CM}}) \frac{\partial V_{\mathrm{multi}}(x_{\mathrm{CM}})}{\partial x_{\mathrm{CM}}} \right] P(x_{\mathrm{CM}}, t) \,. \tag{3.14}$$

In particular,

$$\begin{gathered} v_{\mathrm{drift}}(x_{\mathrm{CM}}) = v_x(x_{\mathrm{CM}}) + v_{x,\gamma}(x_{\mathrm{CM}}) \\ v_x(x_{\mathrm{CM}}) = -\beta D(x_{\mathrm{CM}}) \tfrac{\partial V_{\mathrm{multi}}(x_{\mathrm{CM}})}{\partial x_{\mathrm{CM}}} \qquad v_{x,\gamma}(x_{\mathrm{CM}}) = \tfrac{\partial}{\partial x_{\mathrm{CM}}} D(x_{\mathrm{CM}}) \end{gathered} \tag{3.15}$$

It must be noted that Equation 3.9 has not been derived using a rigorous bottom-up coarse-grained procedure, which would be expected to result in a more general Langevin equation [299, 300]. Moreover, the systematic coarse-graining of our current simulation model is complicated by the fact that our system is not Hamiltonian.

We now focus on deriving an expression for the drift velocity in the context of our model. In Ref. [268], the diffusion constant of a particle functionalised with mobile receptors on a substrate with a uniform coverage of fixed ligands was predicted to be

$$D(x_{\mathrm{CM}}) = c \frac{k_{\mathrm{off}}}{\langle n_{\mathrm{b}}(x_{\mathrm{CM}}) \rangle^2}, \tag{3.16}$$

where c is a constant in units of area, well approximated by $c = \pi R^2/2$. To evaluate Equation 3.15, we first calculate v_x and then show that $v_{x,\gamma}$ is negligible compared to v_x. In our system, the multivalent free energy is given by [34]

$$\beta V_{\mathrm{multi}}(x_{\mathrm{CM}}) = N_R \log \left[1 - \frac{n_b(x_{\mathrm{CM}})}{N_R} \right] + N_L(x_{\mathrm{CM}}) \log \left[1 - \frac{n_b(x_{\mathrm{CM}})}{N_L(x_{\mathrm{CM}})} \right] + n_b(x_{\mathrm{CM}}). \tag{3.17}$$

Differentiating Equation 3.17 with respect to x_{CM} yields

$$\beta \frac{\mathrm{d}V_{\mathrm{multi}}(x_{\mathrm{CM}})}{\mathrm{d}x_{\mathrm{CM}}} = N_L'(x_{\mathrm{CM}}) \log \left[1 - \frac{n_b(x_{\mathrm{CM}})}{N_L(x_{\mathrm{CM}})} \right], \tag{3.18}$$

where $N_L'(x_{\mathrm{CM}}) = \mathrm{d}N_L(x_{\mathrm{CM}})/\mathrm{d}x_{\mathrm{CM}}$. A proof of Equation 3.18 can be found in Section B.1 in the Appendix. Plugging Equation 3.18 into Equation 3.17 then gives the following expression for v_x:

$$v_x(x_{\mathrm{CM}}) = -\frac{c k_{\mathrm{off}}}{n_b(x_{\mathrm{CM}})^2} N_L'(x_{\mathrm{CM}}) \log \left[1 - \frac{n_b(x_{\mathrm{CM}})}{N_L(x_{\mathrm{CM}})} \right]. \tag{3.19}$$

For a linear gradient of ligands ($\rho_L(x) = c_0 + \lambda x$), it follows that $N'_L(x_{\mathrm{CM}}) = \lambda \pi R^2$. Therefore,

$$v_x(x_{\mathrm{CM}}) = -\frac{c\lambda k_{\mathrm{off}}}{\pi R^2}\left[\frac{\pi R^2}{n_b(x_{\mathrm{CM}})}\right]^2 \log\left[1 - \frac{n_b(x_{\mathrm{CM}})}{N_L(x_{\mathrm{CM}})}\right] \tag{3.20}$$

$$= -\frac{c\lambda k_{\mathrm{off}}}{\pi R^2 \rho_b(x_{\mathrm{CM}})^2} \log\left[1 - \frac{\rho_b(x_{\mathrm{CM}})}{\rho_L(x_{\mathrm{CM}})}\right], \tag{3.21}$$

where the last equality in Equation 3.21 comes from the fact that $\rho_b(x_{\mathrm{CM}})$ is proportional to $\rho_L(x_{\mathrm{CM}})$ for a given x_{CM} (see Equation 3.7).

We now estimate $v_{x,\gamma}$ (Equation 3.15)

$$v_{x,\gamma}(x_{\mathrm{CM}}) = D'(x_{\mathrm{CM}}) = -2\frac{ck_{\mathrm{off}}}{n_b(x_{\mathrm{CM}})^3} n'_b(x_{\mathrm{CM}})\,. \tag{3.22}$$

Using Equation B.3 to express n'_b in terms of N'_L, we obtain

$$v_{x,\gamma}(x_{\mathrm{CM}}) = -2\frac{c\lambda k_{\mathrm{off}}}{\pi R^2}\left[\frac{\pi R^2}{n_b(x_{\mathrm{CM}})}\right]^2 \frac{N_R - n_b(x_{\mathrm{CM}})}{N_L(x_{\mathrm{CM}})N_R - n_b(x_{\mathrm{CM}})^2} \tag{3.23}$$

$$= -2\frac{c\lambda k_{\mathrm{off}}}{\pi R^2 \rho_b(x_{\mathrm{CM}})^2} \frac{\rho_R^{\mathrm{patch}} - \rho_b(x_{\mathrm{CM}})}{\rho_L(x_{\mathrm{CM}})N_R - \rho_b(x_{\mathrm{CM}})n_b(x_{\mathrm{CM}})} \tag{3.24}$$

where ρ_R^{patch} is the density of receptors calculated using the patch area (instead of the total area of the vesicle).

We now compare $v_{x,\gamma}(x_{\mathrm{CM}})$ with $v_x(x_{\mathrm{CM}})$. First, we consider the weak–binding regime (not relevant to this study) for which $\rho_b \ll \rho_L \approx \rho_R^{\mathrm{patch}}$. In this regime we find

$$\frac{\rho_R^{\mathrm{patch}} - \rho_b(x_{\mathrm{CM}})}{\rho_L(x_{\mathrm{CM}})N_R - \rho_b(x_{\mathrm{CM}})n_b(x_{\mathrm{CM}})} \approx \frac{1}{N_R}\,, \tag{3.25}$$

from which we derive

$$\frac{v_{x,\gamma}}{v_x} \approx \frac{\rho_L}{\rho_B N_R}\,. \tag{3.26}$$

The previous equality states that, at a given ρ_B/ρ_L, $v_{x,\gamma}$ readily become negligible when increasing the size of the vesicle (and therefore N_R at a given ρ_R^{patch}). Interestingly, $v_{x,\gamma}$ may become important for small particles.

We then consider the regime (relevant to the present study) in which bridge saturation is reached, in which case the bridge density is limited either by the density of receptors ($\rho_b \approx \rho_R^{\mathrm{patch}} < \rho_L$) or by the density of ligands ($\rho_b \approx \rho_L < \rho_R^{\mathrm{patch}}$). If $\rho_b \approx \rho_L < \rho_R^{\mathrm{patch}}$ (see the linear regime in Figure 3.9), we have

$$\frac{\rho_R^{\mathrm{patch}} - \rho_b(x_{\mathrm{CM}})}{\rho_L(x_{\mathrm{CM}})N_R - \rho_b(x_{\mathrm{CM}})n_b(x_{\mathrm{CM}})} \approx \frac{\rho_R^{\mathrm{patch}} - \rho_L}{\rho_L(N_R - n_b)}\,, \tag{3.27}$$

and

$$\frac{v_{x,\gamma}}{v_x} \approx \frac{1}{N_R - n_b}\,. \tag{3.28}$$

The previous equation implies that, for the vesicles considered in this work, $v_{x,\gamma}$ is negligible compared to v_x. Alternatively, when $\rho_b \approx \rho_R^{\text{patch}} < \rho_L$ (see the constant regime in Figure 3.9), Equation 3.22 predicts $v_{x,\gamma}/v_x = 0$ as the diffusion constant becomes uniform. On the contrary v_x remains finite also in this limit.

Given that $v_{x,\gamma}$ is negligible, the expression for the drifting velocity can then be reduced to

$$v_{\text{drift}}(x_{\text{CM}}) = -\frac{c\lambda k_{\text{off}}}{\pi R^2 \rho_b(x_{\text{CM}})^2} \log\left[1 - \frac{\rho_b(x_{\text{CM}})}{\rho_L(x_{\text{CM}})}\right] \tag{3.29}$$

Finally, comparison of Equation 3.29 with Equation 3.8 shows that the analytic prediction of the vesicle drift velocity agrees with the expected scaling relationship of drift velocity being directly proportional to k_{off}.

3.4 Results and discussion

3.4.1 Effect of binding strength on directional motion

A key factor affecting the overall strength of multivalent binding and the corresponding vesicle mobility is the strength and (un)binding rates of individual receptor-ligand bonds. If the receptor-ligand binding strength is higher, the overall multivalent adhesion strength would be increased, which could affect the vesicle motion in various ways; for example, stronger adhesion could result in reduced lateral mobility of the vesicle. The effect of receptor-ligand binding strength was explored by varying the length of the complementary sticky ends, l. Vesicle motion in systems with sticky end lengths of $l = 5$, 6 and 7 nt was compared *via* experiments and simulations; the DNA sequences were designed such that the unbinding rates span several orders of magnitude (see Table 3.1).

For each sticky end length, the GUVs were functionalised with the relevant receptor constructs, and then applied to the ligand-functionalised substrate (as outlined in Section 3.1; detailed methods can be found in Chapter 2). Experimentally, under all these conditions, the vesicles adhere to the substrate and remain attached during the entirety of the time lapses.

To study the motion of the GUVs relative to the ligand-density gradient in experiments and simulations, each trajectory was decomposed into components parallel and perpendicular to the local ligand-density gradient, as outlined in Section 2.6. Experimental results for $l = 5$–7 nt are displayed in Figure 3.10, while simulation results are displayed in Figure 3.11. From the average velocity distributions, it is evident that the motion is predominantly stochastic in all cases. However, there appears to be a small but observable directional bias in the GUV motion, when studying the means of the average velocity distributions. While the projection of the average velocity onto the direction perpendicular to the gradient is centred around zero,

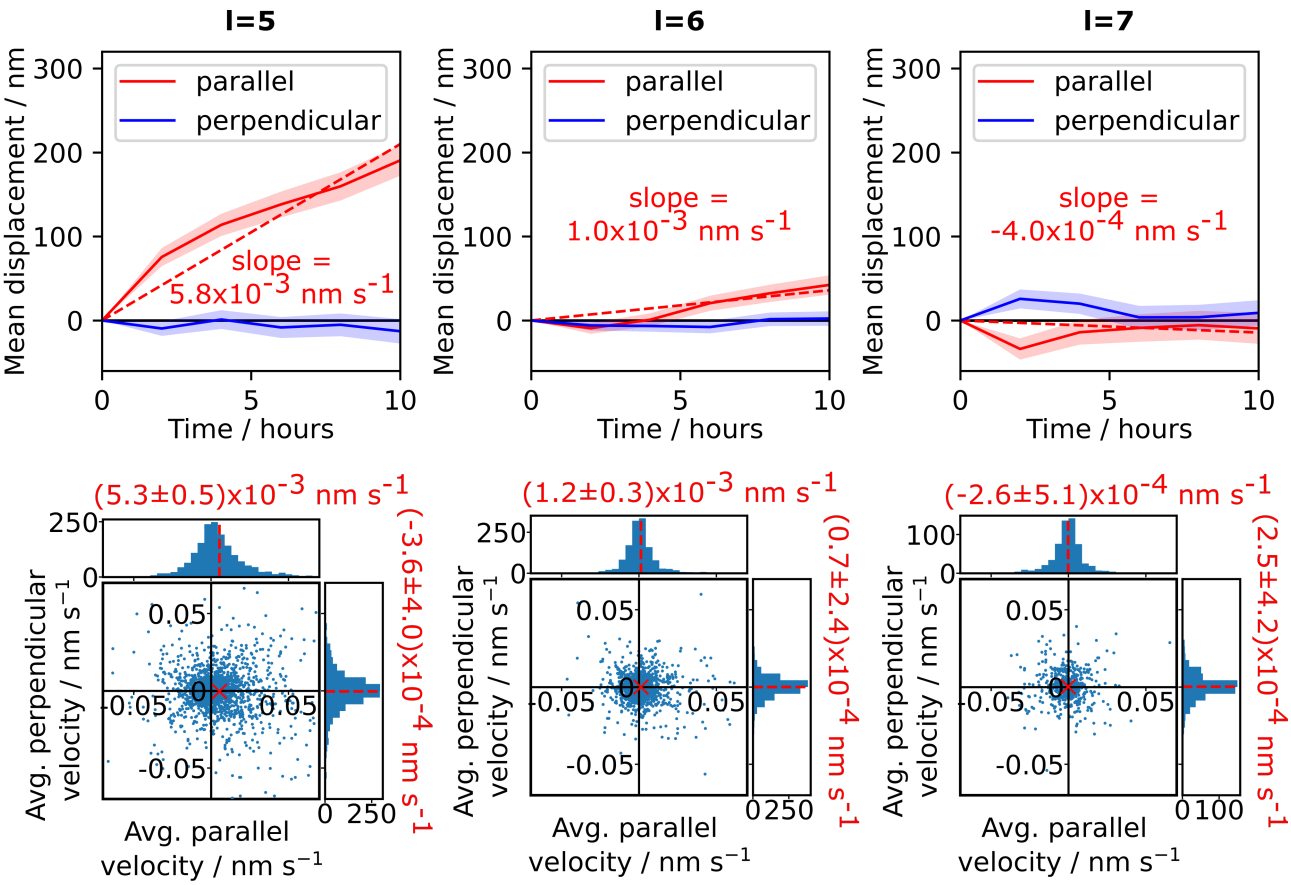


Figure 3.10: **Experimental results reveal that drift velocity increases with decreasing sticky end length.** The plots summarise data from vesicle motility experiments illustrating the effect of sticky end length l on GUV motion along ligand-density gradients, for $l = 5$–7 nt. In all plots, the motion has been decomposed into components parallel and perpendicular to the gradient. The line plots show the mean vesicle displacement over time (solid lines) with standard error of the mean shaded; a straight line (dashed) has been fitted to the motion parallel to the gradient, with the slope annotated. The scatter plots with marginal histograms show the average velocities of individual vesicles, calculated as total trajectory displacement divided by duration; the y-axes of the histograms indicate the number of vesicles in each bin, and the distribution means are annotated in red. Note that the axes have been cropped to aid visualisation of the majority of data points. The plots also show the data filtered to the "fast" population; full data (including the "slow" population and uncropped axes) can be seen in Figures C.3 and C.4 in the Appendix.

the projection parallel to the gradient has non-zero, positive mean (for both $l = 5$ and 6 nt in experimental data, and for $l = 5$–7 nt in simulation data). This indicates a directional bias of the vesicle motion towards denser regions of the ligand carpet, as expected. Furthermore, regarding the plots of mean squared displacement averaged over the mobile vesicle populations (shown in Figure 3.6), the MSD for the more mobile $l = 5$ system exhibits an upward curve, which could indicate a directed or ballistic component to the motion of the vesicles.

To investigate the statistical significance of vesicle drift along the gradient direction, the one-sample Student's t-test was conducted; this tests the null hypothesis that the mean of a distribution is equal to zero. The t-test was applied to the experimental data for $l = 5$ shown in the scatter plots in Figure 3.10, thus testing if the means of the vesicle velocity

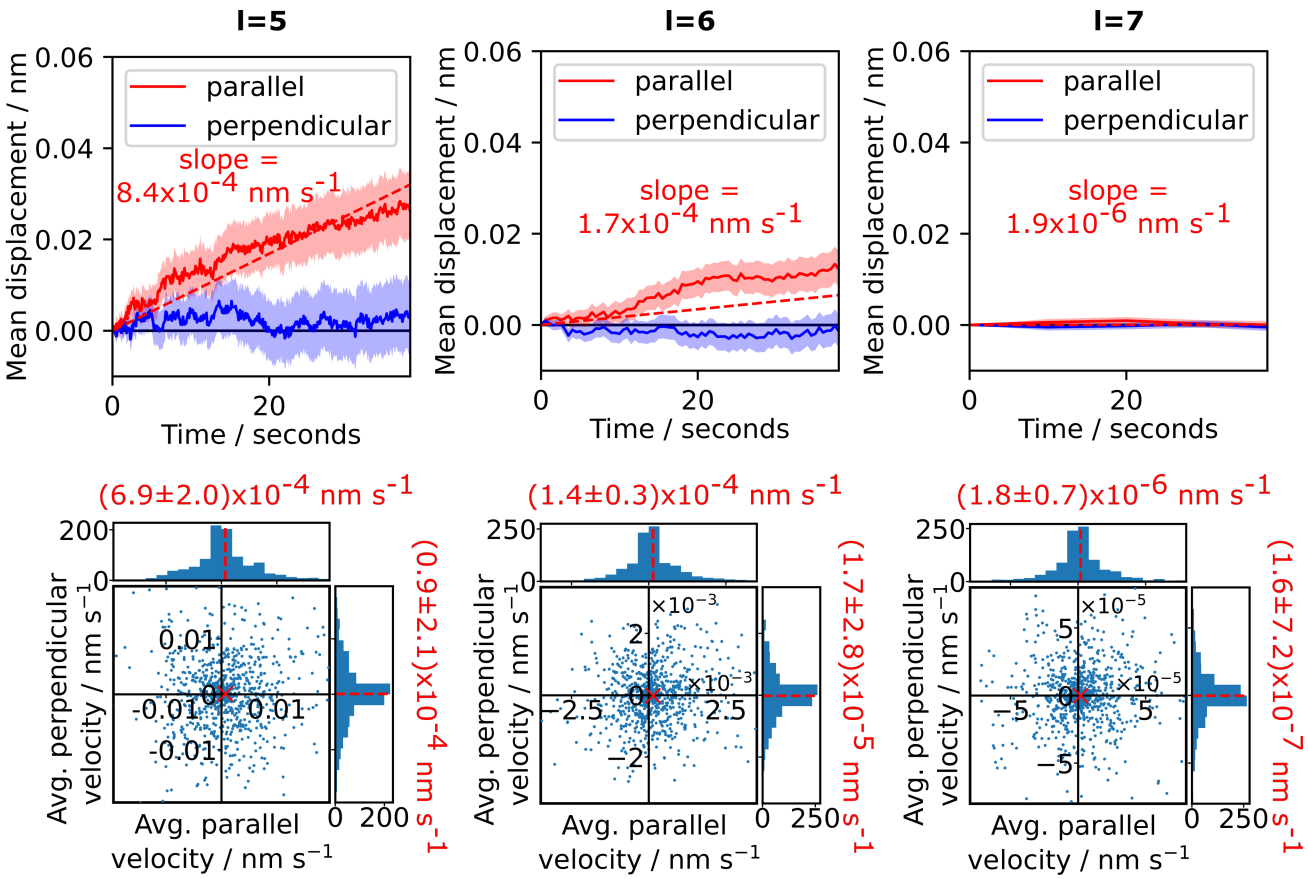


Figure 3.11: **Simulation results support experimental findings that drift velocity increases with decreasing sticky end length.** Here, simulation data for 1 μm-diameter GUV is presented in the same way as the experimental data in Figure 3.10. The line plots show the mean vesicle displacement over time, parallel and perpendicular to the gradient with standard error of the mean shaded; a straight line has bee fitted to motion parallel to the gradient with the slope annotated. Note that the simulated trajectories have been cropped to the same duration to enable visual comparison, while the straight lines have been fitted to the entire, uncropped trajectories,shown in Figure C.5 in the Appendix. The scatter plots with marginal histograms show the distribution of vesicle velocity averaged over each trajectory, where the y-axes of the histograms indicate the number of vesicles in each bin, and the distribution means are annotated in red. The axes have been cropped to aid visualisation of the majority of data points; graphs including all data points are shown in Figure C.6 in the Appendix.

distributions are equal to zero, or if there instead is a non-zero drift. The t-test on the data for experimental vesicle velocities *parallel* to the gradient yields a p-value of 6.96×10^{-25}, while the t-test on the data for vesicle velocities *perpendicular* to the gradient yields a p-value of 0.377. For $l = 6$, applying the t-test to experimental vesicle velocities parallel to the gradient yields a p-value of 2.44×10^{-4}, while the t-test on velocities perpendicular to the gradient yields a p-value of 0.783. Finally, regarding the experimental data for $l = 7$, the t-test yields a p-value of 0.607 when applied to vesicle velocities parallel to the gradient, and a p-value of 0.546 for vesicle velocities perpendicular to the gradient. The results from the t-tests demonstrate a significant non-zero average drift parallel to the gradient for $l = 5$ and $l = 6$. This is not the case for the $l = 7$ system, although the stronger adhesion in the $l = 7$ system likely reduces the mobility of the vesicles to the point that any

motion is indistinguishable from tracking errors. The t-test results support that the vesicles do not drift perpendicular to the gradient on average, for either of the $l = 5$, 6 and 7 nt systems.

The statistical significance of the vesicle drift in *simulations* was also tested, applying the one-sample Student's t-test to the velocity distributions plotted in the scatter plots in Figure 3.11, for vesicles with 1 μm diameter. For $l = 5$, the t-test yields p-values of 4.69×10^{-4} and 0.683 for vesicle velocities parallel and perpendicular to the gradient, respectively. For $l = 6$, the t-test yields p-values of 3.89×10^{-6} and 0.545, for vesicle velocities parallel and perpendicular to the gradient. Finally, for $l = 7$, the t-test yields p-values of 0.0101 and 0.824, for vesicle velocities parallel and perpendicular to the gradient. In each of the $l = 5$, 6 and 7 systems, the t-test results show that the mean vesicle velocity parallel to the gradient is significantly different to zero, whereas the data for vesicle velocities perpendicular to the gradient is consistent with having zero mean.

To further test that the vesicle drift parallel to the gradient is in the direction of *increasing* ligand density (rather than in the opposite direction), the *one-sided* Student's t-test was performed. This tests the null hypothesis that the mean velocity parallel to the gradient is less than or equal to zero. Referring to the same set of data as above (shown in Figures 3.10 and 3.11), for experimental vesicles, the t-test yields p-values of 3.48×10^{-25}, 1.22×10^{-4} and 0.697 for $l = 5$, 6 and 7, respectively. For simulated vesicles, the t-test yields p-values of 2.35×10^{-4}, 1.95×10^{-6} and 5.06×10^{-3} for $l = 5$, 6 and 7, respectively. The results indicate that, on average, vesicles exhibit a significant non-zero drift along the gradient in the direction of increasing ligand density, in all cases except for the case of experimental vesicles in the $l = 7$ system (which is likely due to the low signal-to-noise ratio, as mentioned before).

Altogether, the findings from the statistical significance tests on experimental and simulated vesicle motion support the result in the main text: vesicles preferentially drift in a direction parallel to the local ligand density gradient. Please note that we have added this discussion to Section 3.1 of the SI, and referred to it in the main text.

The width of the average velocity distributions decreases with increasing l (see Figure 3.12), indicating that vesicles with longer ends diffuse less, regardless of directionality. This makes sense as a decrease in sticky end length corresponds to weaker receptor-ligand binding and thus higher unbinding rates. When a vesicle is adhered to a point on the substrate, its motion is constrained by receptor-ligand bridges that anchor the vesicle; these bridges must unbind to allow the vesicle to diffuse laterally. Therefore, weaker binding allows for increased vesicle mobility. It must be noted that the trend between width of average velocity distribution and sticky end length is more pronounced in simulations than it is in experiments. This is expected, given that experimental data are inevitably impacted by errors in the tracking of vesicles.

Directional bias of the GUV motion towards higher ligand densities becomes more apparent when visualising the mean displacement as a function of time, also shown in Figures 3.10 and

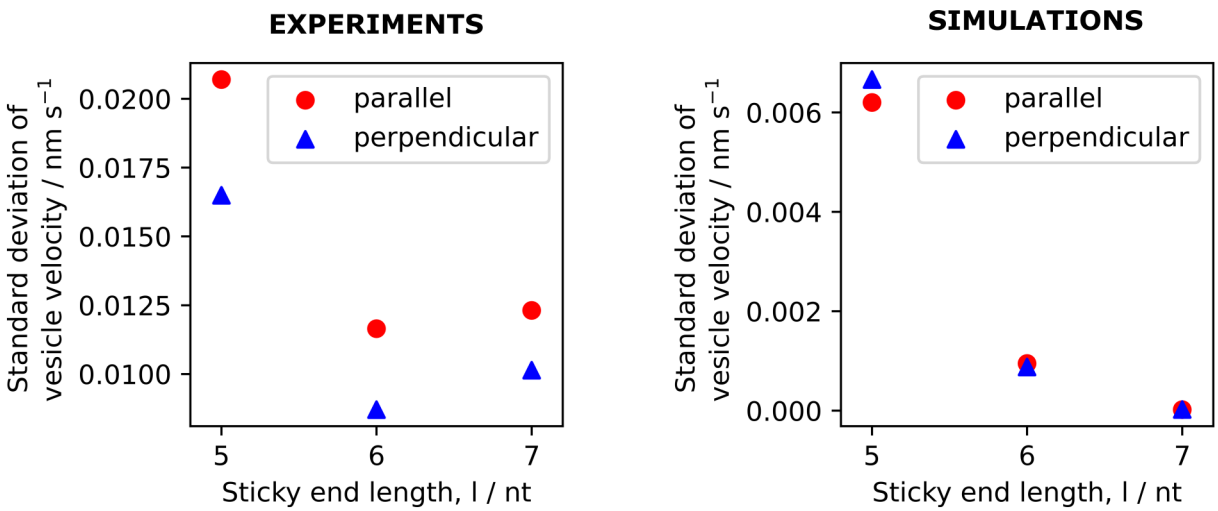


Figure 3.12: **Vesicles functionalised with longer sticky ends diffuse more slowly.** The plots illustrate the standard deviation of average vesicle velocity (calculated as total displacement divided by trajectory duration) versus sticky end length; the velocity is decomposed into components parallel and perpendicular to the gradient direction. Experimental data are shown for the "mobile" vesicle population. while simulation data are shown for vesicles with diameter $d = 1\,\mu$m. Experimental data for the "immobile" vesicle population and simulation data for $0.2\,\mu$m and $1.8\,\mu$m-diameter vesicles are plotted in Figure C.1 in the Appendix.

3.11. In all cases, the vesicle displacements perpendicular to the gradient average to zero (within standard error), while the displacements parallel to the gradient display a non-zero, positive slope for $l = 5$ and 6 nt. For $l = 7$ nt, mean displacement parallel to the gradient shows a negligible slope. However, it is possible that GUV motion in the $l = 7$ nt system also exhibits a directional bias along the gradient, although the signal is overwhelmed by noise from stochasticity of the motion, as well as localisation errors in experimental data.

Regarding the typical speed of motion, the average experimental drift velocities for the $l = 5$ and 6 nt systems (calculated from the scatter plots in Figure 3.10) are 5.3×10^{-3} nm s^{-1} and 1.2×10^{-3} nm s^{-1} respectively. Over experimental timescales (*i.e.* 10 hours), this equates to total displacements of 190 nm and 43 nm respectively, which are significantly smaller than the typical vesicle diameter ($\approx 10\,\mu$m; vesicle size distributions are shown in Figure 3.3). However, we note that the distribution of vesicle displacements parallel to the gradient is not normally distributed, but instead features a positive skew. For $l = 5$ and 6 nt, GUVs travel maximum displacements along the gradient of $5.8\,\mu$m and $5.1\,\mu$m respectively, which are comparable with the average vesicle radius. As a source of comparison, a non-anchored, freely diffusing vesicle with a $10\,\mu$m diameter would travel $\approx 80\,\mu$m along the surface in this time scale (using the Stokes-Einstein equation to estimate the diffusion constant). This demonstrates that the vesicle mobility is reduced by the multivalent adhesion, as expected; GUV motion is constrained by receptor-ligand bridges, which must break to allow the vesicle to move away.

The speed of vesicle motion may sound limited, but is understandable from the perspective of the receptor-ligand bridge spacing. As can be seen in Figure 3.9, the system is in a saturation regime where the receptor-ligand bridge density reaches its maximal value, limited by either the density of ligands or the density of receptors. This means that the typical bridge density for

vesicles in the gradient region is on the order of $0.01\,\mathrm{nm}^{-2}$, which corresponds to an inter-bridge spacing of 10 nm. The average vesicle displacement of $\approx 200\,\mathrm{nm}$ in the $l = 5\,\mathrm{nt}$ system is 20 times higher than the inter-bridge spacing, while $\approx 10\%$ of vesicles travelled further than $1\,\mu\mathrm{m}$ along the gradient, which is >100 times higher than the inter-bridge spacing. This indicates that the observed motion cannot simply be due to the rattling of vesicles around fixed bridging points, but must require the formation and breakage of a large number of bridges.

The limited speed of vesicle motion can be put into further perspective by considering the system from a probabilistic standpoint. As discussed previously, the vesicle motion is constrained by receptor-ligand bridges that anchor the vesicle to the substrate, and a directional gradient in binding affinity results in a gradual directional migration of the GUV. A $10\,\mu$m-diameter GUV located centrally in the gradient plotted in Figure 3.5 spans ligand densities from $0.019\,\mathrm{nm}^{-2}$ to $0.021\,\mathrm{nm}^{-2}$, *i.e.* a $\approx 10\%$ difference in ligand density. Therefore, during each formation of a new ligand-receptor bridge, the receptor is only 10% more likely (at most) to bind a ligand on the side of the contact region facing towards higher ligand density, compared to the opposite side. This small difference in binding probability across the span of the vesicle suggests that a large number of bridge formation and breakage events are required for the directional vesicle drift along the gradient to be distinguishable from stochastic motion.

When comparing the average drift velocities calculated from experimental data (Figure 3.10) and from simulation data (Figure 3.11) for $l = 5\,\mathrm{nt}$, the experimental velocities are an order of magnitude higher than the simulated velocities. One obvious factor that differs between experiments and simulations is the length scale of the system, as the simulated vesicle diameters are an order of magnitude smaller than in experiments. The simulated gradients were adjusted to achieve the same gradient steepness relative to vesicle size, although it is likely that this does not fully cancel out the the effect of vesicle size on the resulting motion. The relationship between vesicle size and drift velocity is further discussed in Section 3.4.3. Beyond this, the difference in magnitude of drift velocity between experiments and simulations could be due to differences in the ligand-density gradient profiles, such as if the typical gradient steepness is higher in experiments than in simulations. Small convective flows in the samples and tracking inaccuracies could also inflate experimental estimates of vesicle drift velocity. Furthermore, calculations of the bridge formation and breakage rates (see Equation 3.1) for the simulations involve estimation of the correction factor α, which is the biggest source of uncertainty in simulation results for vesicle drift velocity. Nonetheless, as mentioned before, the focus is on comparing trends between experiments and simulations rather than absolute values for the drift velocity; together, they consistently show that a decrease in binding strength corresponds to an increase in vesicle mobility.

After observing the increased mobility vesicle as a result of decreased receptor-ligand binding strength, a natural next step would be to consider systems with even weaker receptor-ligand binding (*i.e.* even shorter sticky ends). Receptor and ligand constructs with sticky end lengths of $l = 3$ and 4 nt were indeed designed and experimentally tested, with the aim of achieving increased vesicle drift velocities. However, it was found that at such short sticky end lengths,

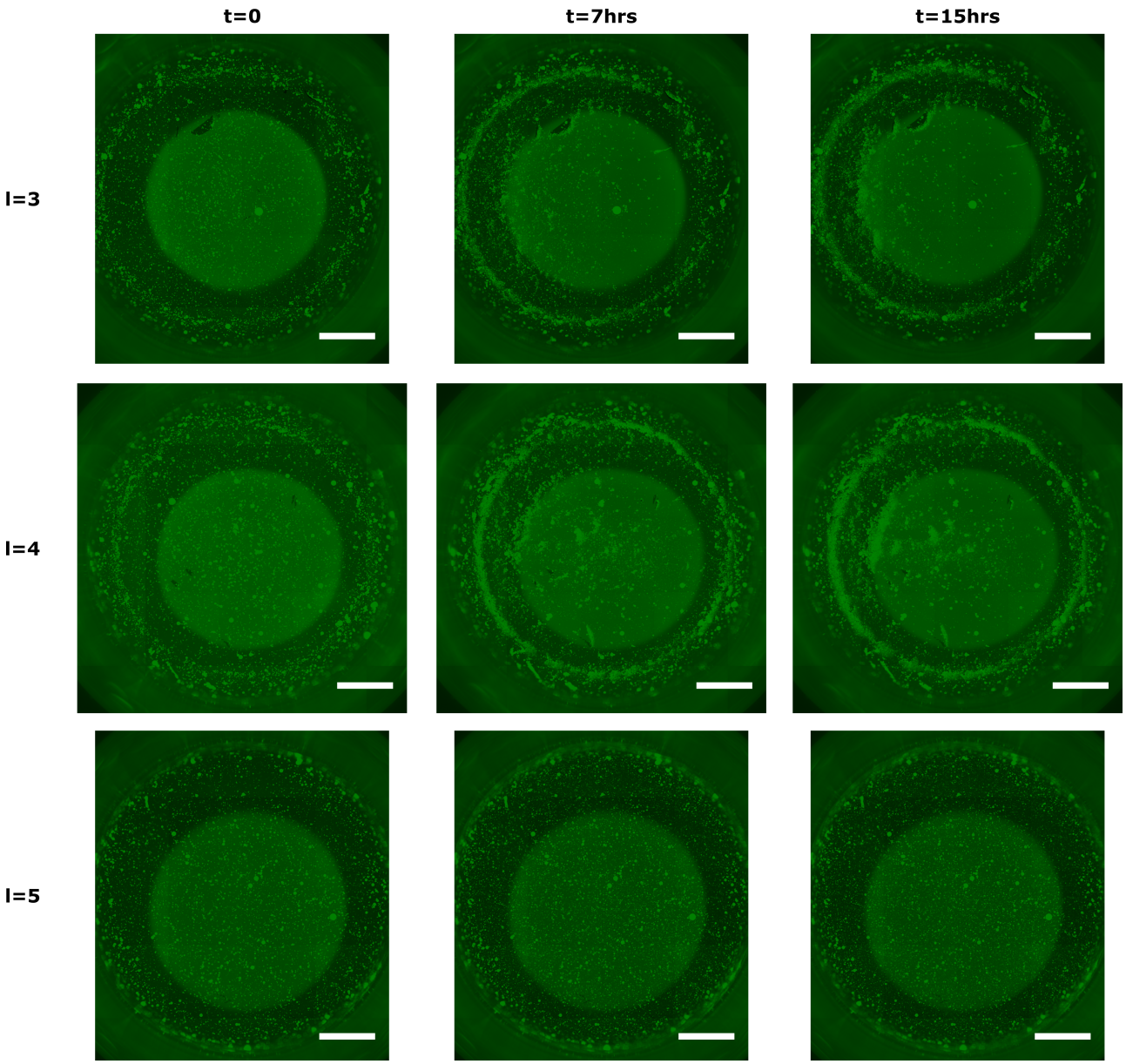


Figure 3.13: **For weakly binding systems, the adhesion strength is insufficient for the vesicles to remain attached to the substrate.** Epifluorescence microscopy images recorded of receptor-functionalised vesicles applied to ligand-coated substrates, for sticky end length systems $l = 3$, 5 and 5 nt, and at times $t = 0$, 7 and 15 hours from the start of the time lapse recording. Each image comprises of multiple fields of view stitched together, such that the entire well is displayed in the stitched image; scale bars correspond to a length of 1 mm. Fluorescence has been excited in the calcein within the vesicles, and in the Alexa Fluor 488 modification of the ligand constructs.

the binding strength was insufficient to keep the GUVs adhered to the substrate. Instead, the GUVs were observed to drift unidirectionally across the well at speeds significantly higher than would be expected from diffusive motion, as can be seen in Figure 3.13. This motion was attributed to convection flows in the sample, or perhaps due to the substrate not being perfectly level which would cause the vesicles to roll over the surface due to gravity. In addition, constructs with longer sticky ends ($l = 8$–10 nt) were designed and experimentally tested; GUVs in these systems showed negligible drift, consistent with the data for $l = 7$ nt in Figure 3.10.

Comparison of theoretical predictions with simulations and experimental results

Theoretical predictions of the vesicle drift velocities (from Equation 3.29) for the $l = 5$, 6 and 7 nt systems were compared with experiments and simulations. In Figure 3.14, simulation results for the average vesicle displacement along the gradient over time are plotted for varying steepness of ligand-density gradient, as well as varying bridge density (relative to the ligand density), along with theoretical predictions of the vesicle drift velocity calculated using Equation 3.29. As can be seen from the plots in Figure 3.14, the theoretical predictions significantly overestimate the simulated drift velocities, although the discrepancies between simulations and theory decrease at lower bridge densities n_b. One potential reason for this discrepancy is that for large n_b (and thus larger drift forces), the system may deviate from the linear response regime under which the fluctuation-dissipation theorem applies. This observation is in agreement with previous findings that coarse-grained dynamics in non-equilibrium conditions are not necessarily described by a simple Langevin equation [299, 300].

In Figure 3.15, simulation results for the average vesicle displacement along the gradient over time are plotted again, with the bridge density fixed at the lowest bridge density ($\rho_b(x_{\mathrm{CM}})/\rho(x_{\mathrm{CM}}) = 0.21$) from Figure 3.14, and the gradient steepness λ varied over a greater range. From the plots it appears that for small values of λ, the gap between theory and simulations decreases further. Furthermore, for small values of λ, the drift velocities no longer appear to depend on vesicle size, which is in agreement with the theoretical prediction of drift velocity in Equation 3.29, if we assume $c = \pi R^2$ in the weakly-binding regime.

Regardless of discrepancies between absolute values of drift velocities between simulations and theory, it must be noted that the theoretical predictions show the same trends as the simulation results between drift velocity, gradient steepness and bridge density. The first trend observed in Figure 3.14 is that drift velocity increases with increasing bridge density. This is as expected, as for a steeper gradient, there is a greater difference in binding affinity across the width of the vesicle. There is thus a greater probability for free receptors to bind ligands on the side of the vesicle facing up the gradient, and the set of constraining bridges thus migrates up the gradient at a faster rate, corresponding to faster vesicle drift. The second trend observed in Figure 3.14 is that vesicle drift velocity increases with decreasing bridge density. This also makes sense from the perspective of vesicles being more mobile at lower bridge densities (*i.e.* higher diffusion coefficients as predicted by Equation 3.16).

The theoretical drift velocities are also significantly higher than experimental drift velocities, although the theoretical prediction in Equation 3.29 is not expected to be valid under experimentally relevant conditions as the equation only applies in the weakly-binding regime. However, the drift velocity would still be expected to follow the general scaling of Equation 3.8. As previously mentioned, Figure 3.9 indicates that under experimental condition for sticky end lengths $l = 5$, 6 and 7 nt, the system is in a saturation regime where the bridge density $\langle n_{\mathrm{b}} \rangle$ is limited by either the ligand density or the receptor density. If this is the case, the R and n_{b} dependencies in Equation 3.29 should be unchanged when comparing experiments with different sticky end length l, resulting in $v_{\mathrm{drift}} \propto k_{\mathrm{off}}$.

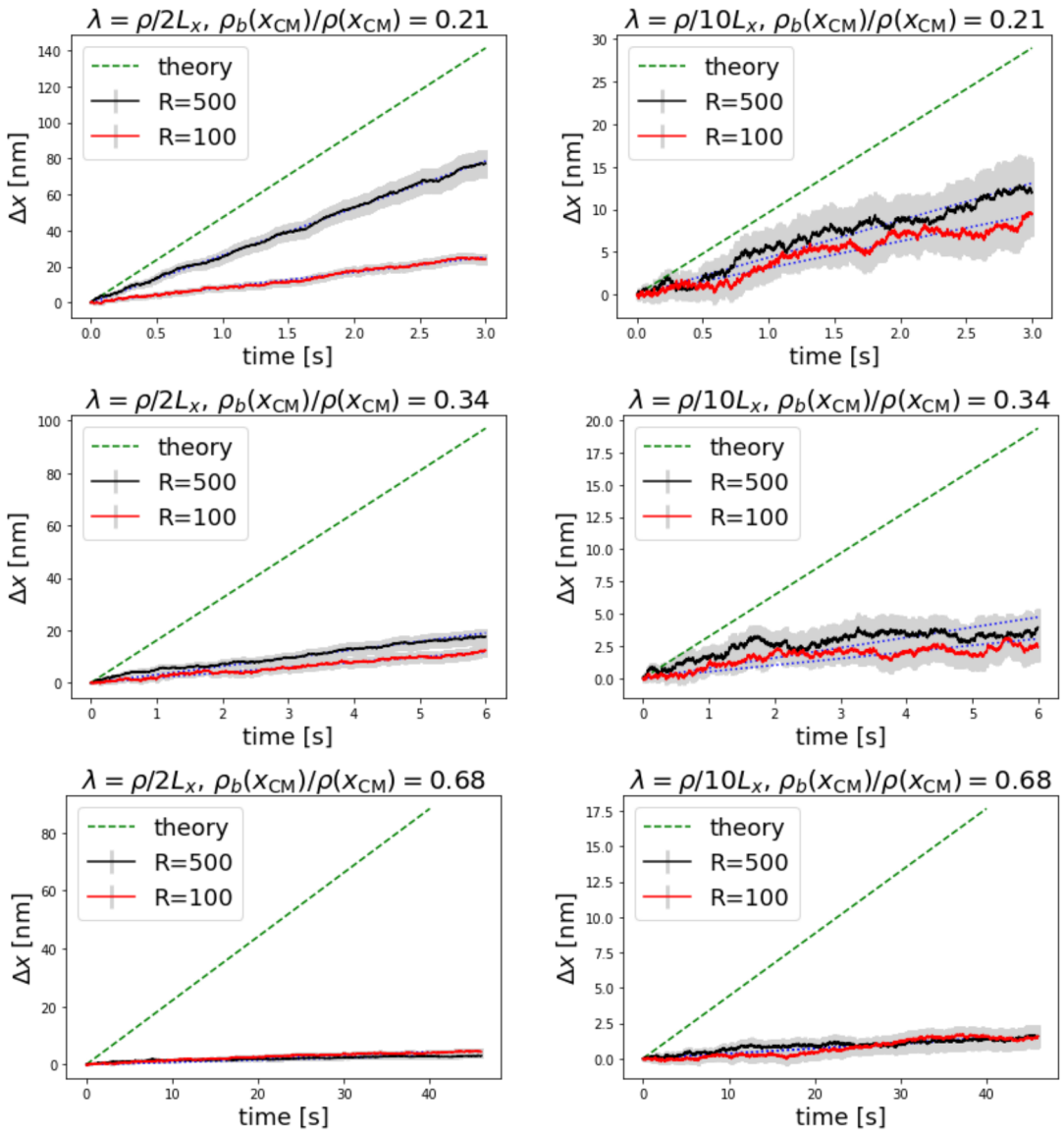


Figure 3.14: **Comparison of simulated and theoretical vesicle displacements along the gradient over time, for varying gradients and bridge densities.** The plots show the mean displacements of vesicles parallel to the gradient, for varying gradient steepness λ and receptor-ligand bridge density ρ_b, predicted by simulation and by theory (Equation 3.29). In each plot, simulation results for two vesicle sizes (radius $R = 100\,\text{nm}$ and $500\,\text{nm}$) are displayed, and straight lines have been fitted to them. x refers to the distance along the gradient, and $\rho(x_{\text{CM}})$ is the ligand density within the contact region between the vesicle and substrate. $\rho = 0.021\,\text{nm}^{-2}$ is the reference ligand density, while $L_x = 10\,\mu\text{m}$ is the reference gradient length scale. The bridge density $\rho_b(x_{\text{CM}})$ has been tuned by varying the off rates of the sticky ends. All plots in this figure were generated by Prof. Bortolo Mognetti.

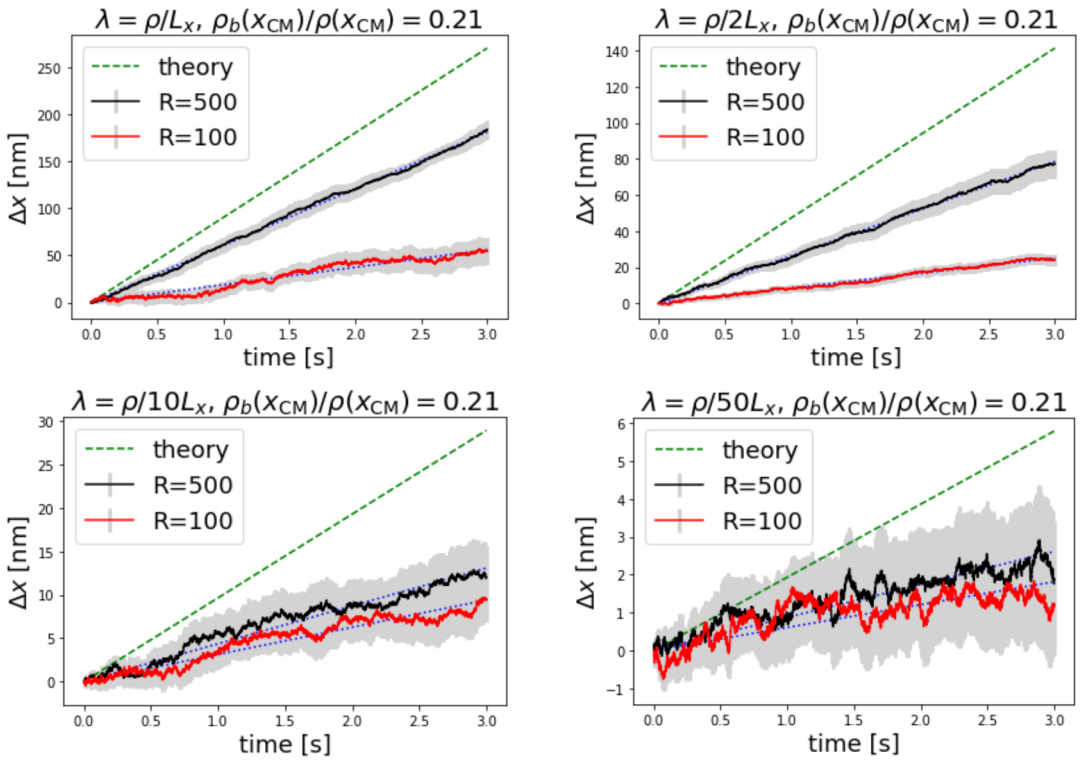


Figure 3.15: **Comparison of simulated and theoretical vesicle displacements along the gradient over time, for varying gradients.** Mean average vesicle displacements parallel to the gradient are plotted for different gradient steepness λ as predicted by simulations of vesicles with radius $R = 500\,\text{nm}$ and $100\,\text{nm}$, and by theory (Equation 3.29). In each plot, simulation results for two vesicle sizes (radius $R = 100\,\text{nm}$ and $500\,\text{nm}$) are displayed, and straight lines have been fitted to them. x refers to the distance along the gradient, and $\rho(x_{CM})$ is the ligand density within the contact region between the vesicle and substrate. $\rho = 0.021\,\text{nm}^{-2}$ is the reference ligand density, while $L_x = 10\,\mu\text{m}$ is the reference gradient length scale. The bridge density $\rho_b(x_{CM})$ has been tuned by varying the off rates of the sticky ends. All plots in this figure were generated by Prof. Bortolo Mognetti.

To verify the predicted proportionality between drift velocity and rate of receptor-ligand unbinding, the ratio between drift velocities for systems with different sticky end length were computed, and compared with the ratio of the k_{off} values. The experimental drift velocities were extracted from the linear fits in Figure 3.10 to calculate an experimental drift velocity ratio of $v_{drift}^{l=5}/v_{drift}^{l=6} = 5.84$. Likewise, for simulations the drift velocities were extracted from the linear fits in Figure 3.11 to attain a simulation drift velocity ratio of 4.90. Both of these values are in good agreement with the ratio between the receptor-ligand unbinding rates, $k_{off}^{l=5}/k_{off}^{l=6} = 6.30$, obtained using the values reported in Table 3.1. The small discrepancy may (partly) arise from using the same α for both sticky end lengths when computing k_{off} using Equation 3.1, as α could vary depending on the length and base sequence of the sticky end. While similar comparisons could not be carried out for the low-mobility system with $l = 7\,\text{nt}$ due to the stochastic component of the motion overwhelming the drift velocity, the analysis for $l = 5\,\text{nt}$ and $l = 6\,\text{nt}$ supports a scenario where the drift velocity is dictated by unbinding rates, in alignment with the model leading to Equation 3.8.

3.4.2 Effect of varying DNA density on vesicle mobility

After observing the directional drift of vesicles along the ligand-density gradient and the increase in vesicle mobility by reducing the receptor-ligand binding strength, this prompted an investigation into whether or not the drift velocity could readily be increased by other means. One obvious avenue towards increasing the drift velocity of the vesicles would be to decrease the density of receptors and ligands, which would correspond to a decrease in density of receptor-ligand bridges between the vesicles and the substrate. A range of DNA densities were tested, by diluting the concentration of receptors and ligands before functionalisation of the vesicles and substrates respectively. The dilution was achieved by mixing the DNA constructs with inert versions that lacked the sticky ends. For example, to halve the receptor density, the receptor constructs were mixed with a sample of inert receptor constructs in a 1:1 ratio, before incubation with the GUVs. The motility experiments were then repeated by applying the receptor-functionalised GUVs to the ligand-density gradients and recording time lapses of the vesicles.

From these experiments, it was observed that the vesicle motion typically fit into one of three regimes: (1) the vesicles remain adhered to the substrate through the entirety of the time lapse, with minimal motion; (2) the vesicles exhibit Lévy-type motion, with bursts of speed punctuated by periods of minimal motion where the vesicle appears to be adhered to the substrate; and (3) the vesicles do not appear to adhere to the substrate and instead flow rapidly across the well. It was observed that the range of receptor and ligand densities in which the vesicles remained adhered to the substrate was relatively narrow. In the mobile $l = 5\,\mathrm{nt}$ system, the receptor and ligand densities could only be reduced by an order of magnitude before the adhesion was too weak to prevent the vesicles from being carried by convection flows. Therefore, it appeared that in the experimental setup used for vesicle motility experiments in this chapter, it would not be possible to achieve significantly higher drift velocities by simply reducing the densities of DNA constructs.

3.4.3 Effect of vesicle size on directional motion

Another factor that was observed to affect the vesicle drift velocity along the gradient was the size of the GUVs. As mentioned before, the GUVs samples used for the vesicle motility experiments in this chapter were polydisperse, with diameters ranging from 1–50 μm (see Figure 3.3). As the diameters of GUVs were measured during the automated tracking process outlined in Section 2.6, this allowed the relationship between vesicle size and motion to be studied.

When binning the experimental trajectories by vesicle diameter, it was observed that larger vesicles travel along the gradient with greater drift velocities on average, as shown in Figure 3.16. This trend is most visible in the $l = 5\,\mathrm{nt}$ system where vesicles are the most mobile, but is also present for the less mobile $l = 6\,\mathrm{nt}$ system. Simulated trajectories for vesicles of varying diameters confirm the experimental trends for $l = 5$ and $6\,\mathrm{nt}$, which can also be seen in Figure 3.16. In both experiments and simulations, the mean drift velocity is typically

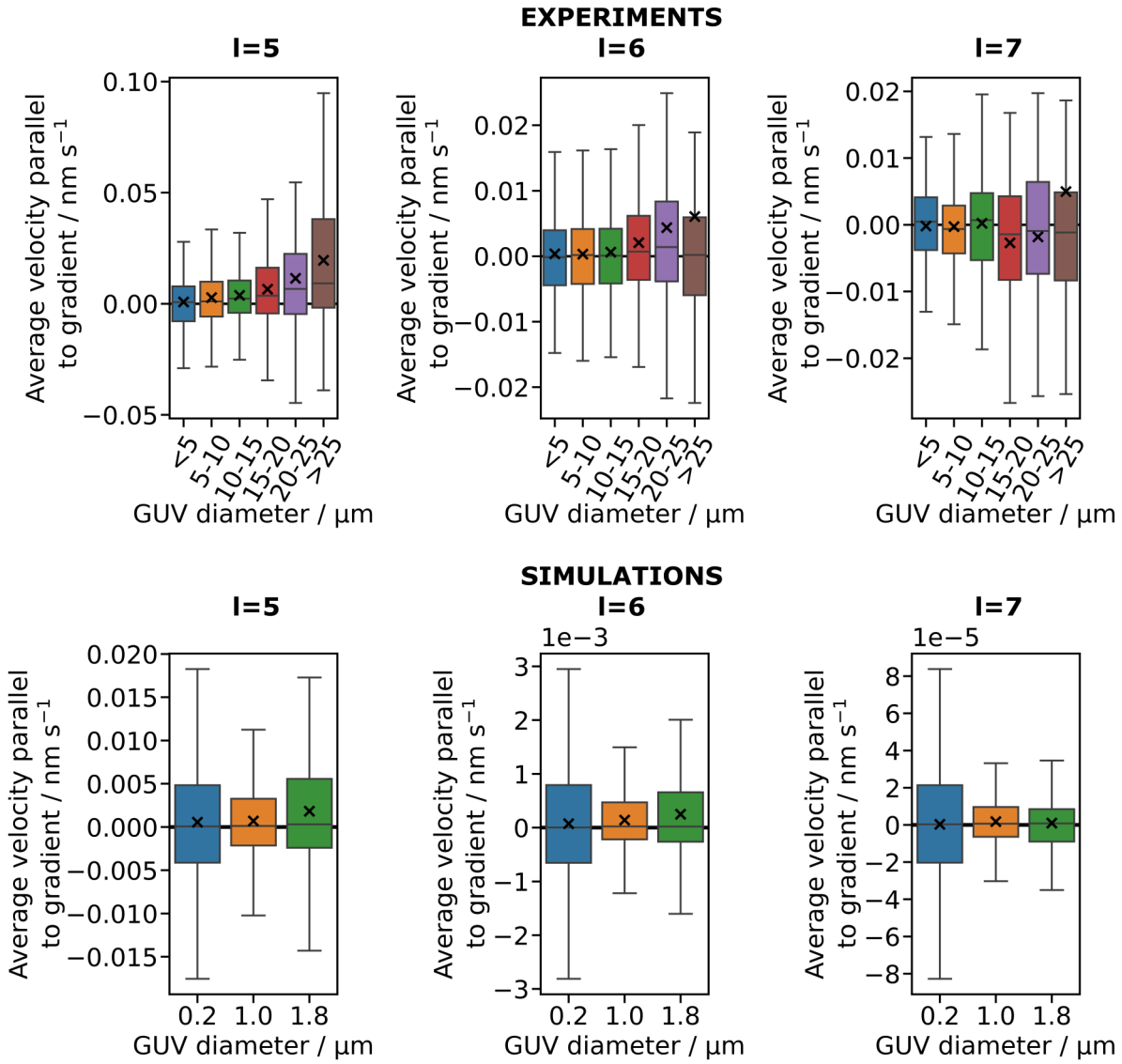


Figure 3.16: **Drift velocity increases with increasing vesicle diameter.** The box plots illustrate the relationship between GUV size and the average drift velocity along the gradient, for sticky end lengths $l = 5$, 6 and 6 nt, where the average velocity has been calculated as total displacement parallel to the gradient divided by the trajectory duration. Positive values indicate motion of the vesicles towards regions of higher ligand surface density. For each box plot, the mean is marked with a cross. Note that outliers have been excluded for better visualisation, and the experimental data have been filtered to the "mobile" vesicle population; full data are shown in Figures C.7 and C.8 in the Appendix, respectively.

greater than the median, due to the vesicle velocity distribution having a positive skew. There is not a clear relationship between vesicle size and drift velocity for the least mobile system, $l = 7$ nt, in neither experiments nor simulations. This is likely due to the drifting motion being overwhelmed by the stochastic component of the motion, in this low-mobility system. As a comparison, the distribution of vesicle velocities perpendicular to the gradient are plotted in Figure 3.17. From this plot, it can be seen that regardless of vesicle size, the vesicles do not exhibit a significant drift perpendicular to the gradient; this finding is consistent with the data in Figures 3.10 and 3.11.

To test the statistical significance of the relationship between vesicle size and drift velocity,

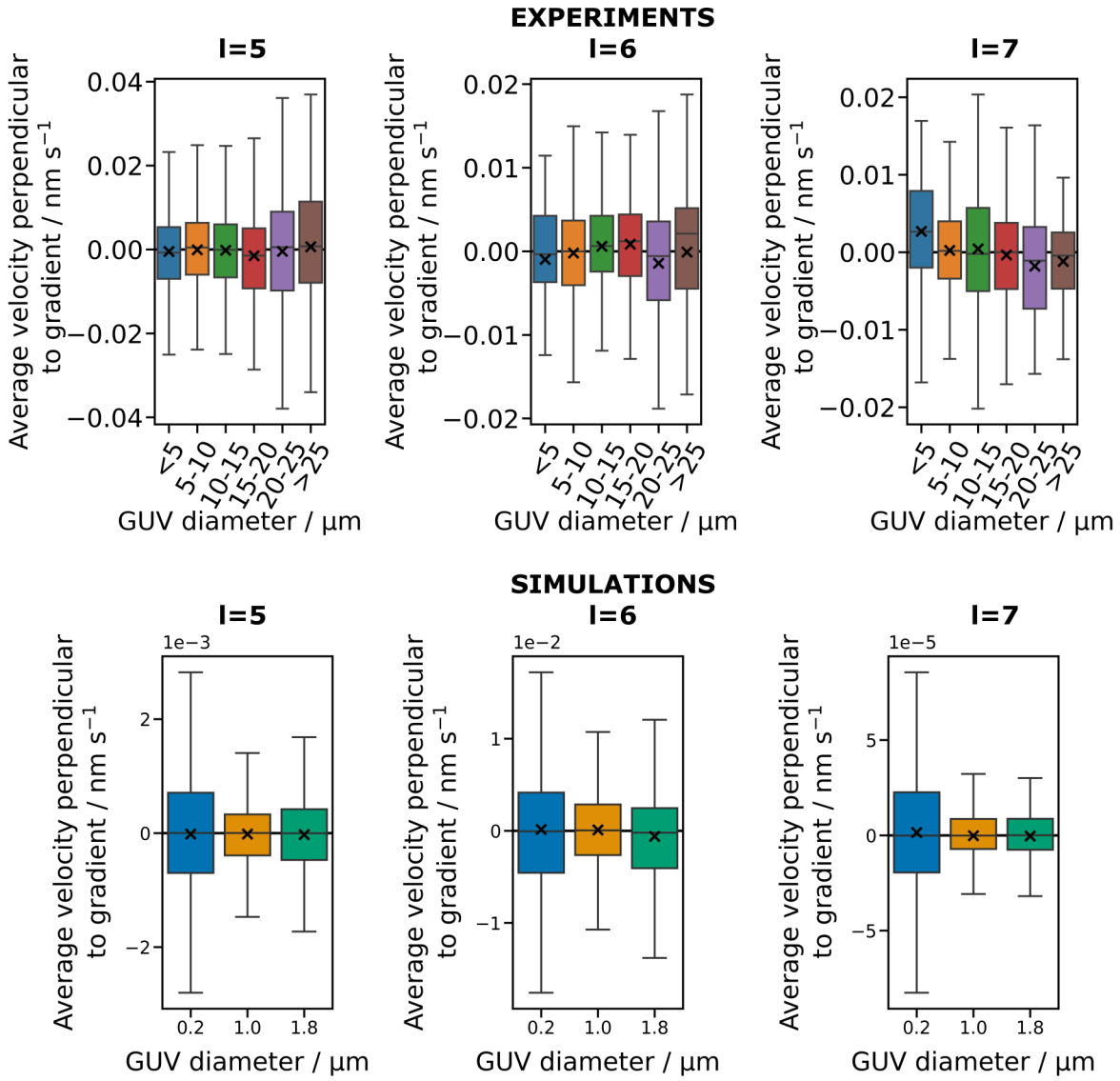


Figure 3.17: **Vesicles do not exhibit a trend between average velocity perpendicular to the gradient and vesicle diameter.** The box plots illustrate the relationship between GUV size and the average vesicle velocity perpendicular to the gradient, for sticky end lengths $l = 5$, 6 and 7 nt, where the average velocity has been calculated as total displacement perpendicular to the gradient divided by trajectory duration. For each box plot, the mean is marked with a cross. Note that outliers have been excluded for better visualisation, and the experimental data have been filtered to the "mobile" vesicle population; full data are shown in Figures C.9 and C.10 in the Appendix, respectively.

the one-sided Welch's t-test was employed. This tests the null hypothesis that the mean of a population is significantly greater than the mean of another population; however, unlike the Student's t-test, it does not assume that the populations have equal variance. The t-test was used to compare the mean displacements of vesicles binned by vesicle diameter; in this case, the null hypothesis is that the mean displacement of the bin corresponding to larger vesicles is less than or equal to the mean displacement of the other bin. Referring to the experimental data for the $l = 5$ system plotted in Figure 3.16, if the t-test is performed on the smallest ($< 5\,\mu$m) and largest ($> 25\,\mu$m) diameter bins, this yields a p-value of 7.37×10^{-6}. Alternatively, if the vesicle data from the $l = 5$ experiments are split into two groups, one with vesicle diameter

$< 15\,\mu$m, and the other with vesicle diameter $> 15\,\mu$m, Welch's t-test on these two groups gives a p-value of 1.19×10^{-6}. Likewise, splitting the $l = 6$ experimental data into two groups (the first with vesicle diameters $< 15\,\mu$m, the second with diameters $> 15\,\mu$m) and performing Welch's t-test yields a p-value of 2.30×10^{-3}. For $l = 7$, this same test returns a p-value of 0.981.

The same statistical test was also conducted on the *simulation* data plotted in Figure 3.16. In this case, the velocities of vesicles with $0.2\,\mu$m diameter were compared with those of $1.8\,\mu$m-diameter vesicles. The one-sided Welch's t-test yields p-values of 1.17×10^{-2}, 9.32×10^{-3} and 0.359 for $l = 5$, 6 and 7, respectively.

Altogether, for both experimental and simulated trajectories, the results of the t-test indicate that the null hypothesis for $l = 5$ and $l = 6$ can be rejected. This supports the earlier claim that larger vesicles drift along the ligand density gradient at a greater rate compared with smaller vesicles. Note that this does not hold for $l = 7$, although this is likely due to the drift velocity being so low that it is indistinguishable from the stochastic component of the motion (as well as tracking errors for experimental trajectories), as discussed before.

A potential explanation for the relationship between vesicle size and drift velocity along the gradient in the mobile systems ($l = 5$ and 6 nt) is that larger vesicles cover a greater extent of the gradient, corresponding to a greater change in binding affinity across the width of the contact region. For example, for a vesicle located in the centre of the gradient plotted in Figure 3.5b, the ligand density varies by $\approx 5\%$ across a $5\,\mu$m-diameter contact region, and by $\approx 20\%$ across a $20\,\mu$m-diameter contact region. The rate of bridge formation on the side of the contact region facing up the gradient would thus be higher for the larger vesicle. This means that the set of constraining bridges migrates up the gradient at a higher rate, resulting in a greater drift velocity for the larger vesicle. This effect has also been discussed in Ref. [288], where the motility of influenza virus particles along surface density gradients of adhesive molecules was studied. In this case, no directional bias was observed in the virus motion, which the authors believed was due to the small size of the virus particles relative to the steepness of the gradient.

It must be noted that the finding of larger vesicles exhibiting greater drift velocities was not initially intuitive, as larger vesicles would be expected to be less mobile due to the larger number of receptor-ligand bridges [268]. However, this effect appears to be cancelled by the ability of larger vesicles to sense a greater extent of the gradient. These two competing factors perfectly compensate each other in the theoretical prediction reported in Equation 3.21 in the weak-binding regime, where v_{drift}^{FD} is not dependent on R. Evidence of a size-dependent drift velocity in both experiments and simulations further highlights the limitations of the theoretical approach leading to Equation 3.21 in the strong-binding regime relevant to our system.

Given the findings on the impact of vesicle size relative to the gradient steepness on the drift velocity, it could be argued that varying vesicle size for a given gradient is comparable with varying gradient steepness for a given vesicle size. Therefore, the results from this section would indicate that increasing the gradient steepness would result in increased drift velocity. Although the experimental method of generating ligand-density gradients did not allow for

tuning of the gradient profile, the effect of varying the gradient steepness on drift velocity was explored in simulations, as shown in Figure 3.15. As expected, simulation results show that as the gradient steepness increases, the drift velocity of vesicles along the gradient increases.

3.5 Chapter summary and outlook

In summary, the motion of receptor-decorated vesicles adhering to a ligand-decorated surface was studied, through a combination of experiments, simulations and theory. In particular, directional bias of vesicle motion in the presence of ligand-density gradients was investigated. In experimental systems, the receptors and ligands were constructed from DNA oligonucleotides with complementary single-stranded sticky ends, whose binding kinetics could be tuned by varying the sticky end sequences. Coarse-grained simulations relied on a reaction-diffusion approach first reported in Ref. [268], which describes the binding and unbinding dynamics of receptors and ligands through a Gillespie algorithm.

In both experiments and simulations, the vesicles were observed to move over the substrate with a directional bias towards regions of higher ligand density. The magnitude of the directional drift velocity was observed to decrease with increasing receptor-ligand affinity, which could be easily controlled by changing the length of the sticky ends through which the constructs interact.

Theoretical arguments presented in this chapter demonstrate that in the regime relevant to the experimental system, directional motion is limited by the time scales of the receptor-ligand reactions. In both experiments and simulations, the ratio between the drifting velocity of systems with different sticky end lengths was found to closely match the ratio between the unbinding rates, in agreement with the predicted scaling relation. An analytic prediction of the vesicle drift velocity was also derived by using the predicted expression for the diffusion constant from Ref. [268] and applying the fluctuation-dissipation theorem. This prediction was found to significantly overestimate the simulated drift velocities, although the prediction of the diffusion constant in Ref. [268] was derived in the weak-binding regime, and thus would not be expected to apply to the experimental system in this chapter.

Another factor that was noted to affect the vesicle drift velocity was the size of the vesicle. A positive correlation was observed between vesicle size and drift velocity in both experiments and simulations; this trend was more noticeable in the more mobile systems $l = 5$ and 6 nt. A potential explanation for this trend is that larger vesicles are able to probe a greater extent of the ligand-density gradient, corresponding to a greater difference in receptor-ligand binding probabilities across the width of the contact region between the vesicle and the substrate.

All in all, the findings in this chapter offer quantitative insights on the mechanisms underpinning directional motion in multivalent systems, which is relevant to a potential passive mechanism underlying haptotaxis of cells along ligand-density gradients. Examples of haptotactic phenomena in biology include immune cell adhesion [301, 302], viral invasion [71, 72, 73], and tissue dynamics [71, 74, 301]. Although the limited drifting velocity of vesicles along the

ligand density gradients perhaps is not relevant to haptotaxis in biological contexts (which may instead be driven by active processes), comparisons could be made with the re-orientation of cells along gradients in binding affinity. An example of this includes the re-orientation of malaria due to the release of adhesin from the apical region of the parasite, which produces a transient gradient in binding energy [303]. In future studies, it would be interesting to explore additional parameter spaces such as temperature, buffer conditions and gradient steepness, as well as working in more weakly-binding regimes (*i.e.* by reducing sticky end length or decreasing DNA density); this may require alteration of the experimental setup to reduce convection effects. Ideas for future investigations are discussed in further detail in Chapter 5.

Although the speed and range of motion of the GUVs in the experimental system are limited, the findings from this chapter provide knowledge to aid future designs of synthetic cells capable of moving along surface-bound molecular gradients. Future designs of haptotactic synthetic cells with improved speed and range of motion (perhaps with the aid of active haptotaxis mechanisms) could be valuable for a vast range of applications, such as: smart drug delivery systems that can target and release drugs at specific locations in the body [304, 305, 306, 307, 308]; vesicle-based biosensors or biomedical imaging systems that signal the presence of specific molecules or conditions [309, 310, 311]; or tissue engineering applications where gradients of molecules or growth factors are used to direct cell migration and tissue formation [312, 313, 314].

Chapter 4

A burnt-bridges adaptation of the vesicle motility system

In Chapter 3, vesicle mobility while remaining attached to a substrate *via* multivalent adhesion was studied. However, the speed of the vesicle motion was limited due to restrictions of the experimental design on the strength of the multivalent adhesion and the unbinding rate of receptor-ligand bridges. Theoretically, if the strength of the multivalent adhesion were reduced (either by reducing the DNA densities, or by changing the strand designs to decrease the binding strength of receptor-ligand bridges), the vesicle drift velocity would be increased. The issue with the passive motility system is that the strength of adhesion is coupled with the off rate of GUV-substrate bridges; a fast off rate is required to ensure fast motion, but a fast off rate corresponds to weak adhesion, which means that the vesicles do not stay attached and are instead carried by convection flows in the samples.

From this finding, it became clear that the system design would need to be adapted to deter the vesicle from getting fixed in a single location on the substrate, while maintaining sufficient strength of multivalent adhesion. To achieve this, the adhesion strength would need to be decoupled from the off rate using an active mechanism. One potential solution to this problem would be a burnt-bridges approach, *i.e.* a mechanism that prevents the GUV from repeatedly re-binding to the same binding sites on the substrate due to "burning" of the GUV-substrate bridges; prior to being "burned", the bonds are essentially irreversible, thus enabling strong adhesion. Burnt-bridges mechanisms have been employed in previous work on vesicle motility, generally with the use of enzymes; for example, in Ref. [246], nicking enzymes are used to digest RNA binding sites on a substrate and encourage both directed and un-directed motion of vesicles.

In Ref. [241], a system was presented in which a bipedal DNA walker was designed to move uni-directionally along a one-dimensional DNA track, using a burnt-bridges approach. This design did not require the use of enzymes or other non-DNA material to implement the approach, but instead made use of the common DNA nanotechnology mechanism TMSD to actively displace the 'feet' of the walker from the track and prevent it from re-binding to old binding sites. By incorporating this mechanism into my vesicle motility system, the vesicle

essentially becomes a multi-footed version of the bipedal DNA walker from Ref. [241].

In this chapter, I present an adaptation of the vesicle motility system with a burnt-bridges approach. The DNA mechanism is verified in bulk before being incorporated to the vesicle system. The reaction-diffusion dynamics of the system are modelled and fitted to experimental data to gain a deeper insight of the kinetics and obtain values for key experimental parameters. Findings on vesicle motion in the burnt-bridges system are then presented, demonstrating that vesicle mobility increases with increased rate of the the bridge-burning reactions, and with decreased density of DNA on the substrate. Finally, I consider if the increased mobility of the burnt-bridges system enables increased haptotactic drift velocity along DNA surface density gradients. All work in this chapter was conducted by me, unless specified otherwise.

4.1 Overview of the burnt-bridges vesicle motility system

The burnt bridges vesicle motility system is set up in a similar way to the vesicle motility system presented in Chapter 3. GUVs are again used as the biomimetic platform to study artificial cell motility; the GUVs are functionalised with DNA constructs, which bind with complementary DNA constructs attached to a substrate. The GUV constructs (G) and substrate constructs (S) feature the same anchor moieties and dsDNA spacers as the receptor and ligand constructs in Chapter 3, respectively. However, the reactive moieties of G and S have been updated so that they no longer consist of short sticky ends; the updated sequences enable the burnt-bridges DNA mechanism, also schematised in Figure 4.1. Furthermore, a third DNA component is now included in the bulk solution, referred to as the fuel strand (F); F provides the fuel that is expended by the burnt-bridges mechanism.

As stated in the introduction to this chapter, the burnt-bridges DNA mechanism (and strand designs) are based on those for the bipedal DNA walker in Ref. [241]. The DNA mechanism involves TMSD, a process that is commonly used in DNA nanotechnology in which an invader DNA strand displaces another strand from a DNA duplex (described in more detail in Section 1.3.3).

Initially, the substrate construct (S) exists in its unbound state (stage 1 in Figure 4.1). A free GUV construct (G) binds to the complementary toehold on S, and proceeds *via* branch migration to open the hairpin structure in S. This results in the substrate-GUV (SG) bridge structure shown in stage 2 of Figure 4.1, where S and G are irreversibly bound together by 27 bp; this complementary region is much longer than the complementary sticky ends in Chapter 3 (5–7 bp) of which the binding was reversible. Due to opening of the hairpin structure in S, a toehold on S becomes exposed to a complementary overhang on the fuel strand (F). F thus binds to the toehold on S, displacing G and simultaneously opening the hairpin structure in F. This results with the final substrate-fuel (SF) structure shown in stage 3 of Figure 4.1. After formation of SF, G can no longer bind to the substrate construct, as this would require the energetically unfavourable displacement of F from SF. This corresponds to the 'bridge-burning' behaviour of the system, as the GUV cannot rebind multiple times to the same binding

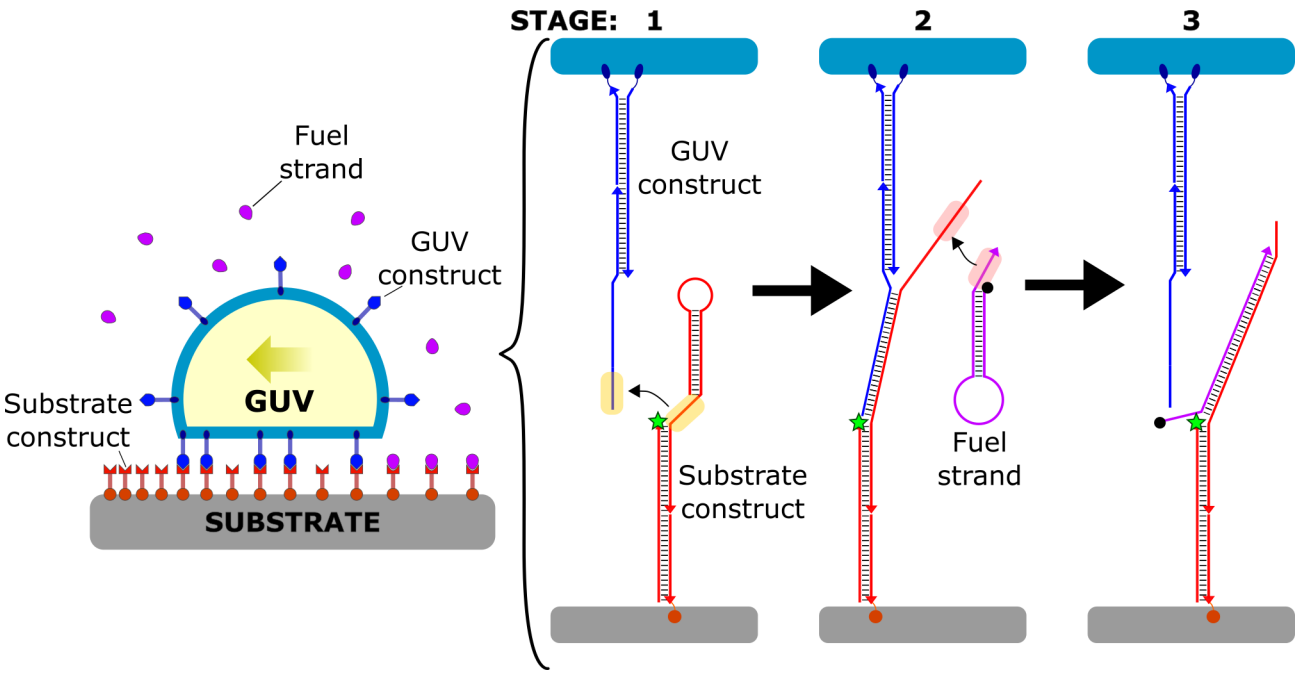


Figure 4.1: **Schematic of the burnt-bridges system.** The GUV and substrate are functionalised with complementary DNA constructs (G and S respectively), while the fuel strands (F) are in bulk solution. The burnt-bridges DNA mechanism can be broken down into two steps, each involving toehold-mediated strand displacement: binding of the G to S opens the hairpin structure in the latter (stage 1 to 2), and binding of F to a toehold on S displaces G (stage 2 to 3). The toeholds and complementary regions of invading strands are highlighted in stage 1 and stage 2. The fluorophore (Alexa Fluor 488, marked as a green star) and quencher (Iowa Black FQ, marked as a black circle), attached to S and F respectively, enable monitoring of the burnt-bridge process *via* fluorescence imaging.

site on the substrate.

As mentioned in the introduction of this chapter, the bridge-burning process enables decoupling of the binding affinity and the off rate. The binding of the 27 nt complementary sequences of S and G is irreversible, allowing for strong adhesion of the vesicles to the substrate. However, the off rate is now given by the strand displacement rate (where G is displaced from SG upon binding of F), rather than the spontaneous unbinding rate of SG in the absence of F. The bridge-burning adaptation of the vesicle motility system should thus offer more scope for experimental systems with lower bridge densities than in the passive system, as the stronger SG bonds in the bridge-burning system are more resistant to shear forces from convection flows.

4.2 Modelling the kinetics of the burnt-bridges system

4.2.1 Modelling the kinetics in bulk solution

This section focuses on the kinetics of the burnt-bridges mechanism in bulk solution (*i.e.* when the DNA constructs are not attached to the vesicle or substrate, and are simply dissolved in solution). The chemical equations for the burnt-bridges DNA mechanism in bulk solution are

simply

$$\begin{aligned} S + G &\xrightarrow{k_1} SG \\ SG + F &\xrightarrow{k_2} SF + G \end{aligned} \tag{4.1}$$

where k_1 and k_2 are effective second-order toehold-mediated strand displacement rates. As the toeholds in both cases are seven nucleotides long, fast equilibration toward the final products should be achieved, so transitional binding states are neglected and the reactions in Equation 4.1 are modelled as irreversible, second-order reactions. The concentrations of S and F can then be described with the following differential equations

$$\begin{cases} \frac{\partial[S]}{\partial t} = -k_1[S][G] \\ \frac{\partial[SF]}{\partial t} = k_2[SG][F], \end{cases} \tag{4.2}$$

where $[X]$ denotes the concentration of species X. Meanwhile, conservation of mass gives

$$\begin{cases} [S] + [SG] + [SF] = [S_0] \\ [F] + [SF] = [F_0] \\ [G] + [SG] = [G_0], \end{cases} \tag{4.3}$$

where $[S_0]$, $F_0]$ and $[G_0]$ are the initial concentrations of S, F and G respectively (prior to any reactions occurring). Equations 4.2 and 4.3 can be combined to eliminate variables and arrive at the following set of coupled differential equations in terms of $[S]$ and $[SF]$ alone:

$$\begin{cases} \frac{\partial[S]}{\partial t} = -k_1[S]([G_0] - [S_0] + [S] + [SF]) \\ \frac{\partial[SF]}{\partial t} = k_2([S_0] - [S] - [SF])([F_0] - [SF]). \end{cases} \tag{4.4}$$

The differential equations in Equation 4.4 were solved numerically using the *integrate.odeint* sub-package of the Python *scipy* library, to model the concentrations of $[S]$ and $[SF]$ over time. The bulk fluorescence intensity I_{bulk} was then calculated as

$$\begin{aligned} I_{\text{bulk}} &= \frac{[S] + \theta[SF]}{[S_0]} \\ &= \frac{[S_0] - [SF] + \theta[SF]}{[S_0]} \\ &= \frac{[S_0] + (1-\theta)[SF]}{[S_0]} \end{aligned} \tag{4.5}$$

where θ is the quenching factor that describes the reduction in fluorescence intensity when F binds to S to form SF, *i.e.* the ratio of the fluorescence of $[SF]$ to $[S]$ ($0 \leq \theta \leq 1$). The factor of $[S_0]$ in the denominator of Equation 4.5 normalises the intensity such that the maximum intensity (*i.e.* the intensity prior to any reactions occurring) is set to 1. I_{bulk} is then fitted to the experimental fluorescence intensity using the *minimize* module of the Python library *scipy.optimize*, scoring the closeness of the fit by calculating the sum of the squared

residuals. Rate constants k_1 and k_2 were fitted, with their values constrained to lie between 0–1 $\mathrm{nM^{-1}\,s^{-1}}$. The quench ratio θ was fitted and constrained to lie between 0–1. The initial concentrations of the constructs ($[S]_0$, $[G]_0$ and $[F]_0$) were also fitted, to account for pipetting errors in experiments; constraints were placed on the fits to allow an uncertainty of 10% in the initial concentrations. Furthermore, the time delay Δt between the start of the reactions (*i.e.* the addition of G to the samples) and the start of the fluorescence measurements was fitted; this was constrained to lie between 0–10 minutes. Note that Δt was not fitted by inputting this variable as a fitting parameter to the *minimize* module, as was done for the other parameters; instead, the entire fitting process was repeated such that a fit of all the other parameters was conducted for a range of discrete values of Δt (ranging from 0–10 minutes, at intervals of 20 seconds). The value of Δt corresponding to the best fit (scored by the sum of squared residuals) was chosen as the optimal fitted value.

4.2.2 Modelling the bridge-burning patterns formed within vesicle adhesion patches

As discussed in Section 4.1, in the burnt-bridges version of the vesicle motility system, vesicles adhere to the substrate *via* the binding of GUV constructs (G) and substrate constructs (S). Fuel constructs in bulk solution diffuse under the vesicle adhesion patch and displace G from the SG complexes, thus breaking the bridging points between the vesicle and substrate and preventing the GUV constructs from repeatedly re-binding to the same substrate constructs. Under certain experimental conditions, it is possible to observe the bridge-burning process propagate inwards from the perimeter of the adhesion patch as the fuel strands diffuse under the vesicle; results from this are presented later in Section 4.5. Here, I design a reaction-diffusion model that describes (and is then fitted to) experimental bridge-burning patterns; this approach was inspired by the reaction-diffusion model designed in Ref. [315] to describe the patterning of 3D DNA condensates.

In this model, the vesicle was assumed to be located on a region of the substrate with uniform density of the substrate construct (S); the substrate was thus modelled as a two-dimensional system with S evenly distributed across a flat surface. Diffusion of F strands through the contact region (filled with a DNA brush consisting of S and G constructs) was modelled with Fick's laws, and additional terms were used to describe the DNA binding kinetics. The contact region was assumed to be circular, and rotational symmetry allowed for reduction of the two-dimensional diffusion equation to a one-dimensional equation in radial coordinates. Furthermore, the surface densities of S, G and SG bridges were converted to concentrations by assuming that the constructs are uniformly distributed within a layer of thickness $L = 10\,\mathrm{nm}$ (corresponding to the approximate length of the spacer moiety of the DNA constructs) between the vesicle and the substrate.

As in the model in Section 4.3, both strand displacement reactions of the bridge-burning DNA mechanism (described in Equation 4.1) were modelled as irreversible second-order reactions, and transitional binding states are neglected. The reaction-diffusion dynamics can then

be described by the following set of coupled differential equations

$$\begin{cases} \frac{\partial[S]}{\partial t} = -k_1[S][G] \\ \frac{\partial[G]}{\partial t} = -k_1[S][G] + k_2[SG][F] + D_G \cdot \frac{1}{r}\frac{\partial}{\partial r}\left(r\frac{\partial[G]}{\partial r}\right) \\ \frac{\partial[SG]}{\partial t} = k_1[S][G] - k_2[SG][F] \\ \frac{\partial[F]}{\partial t} = -k_2[SG][F] + D_F \cdot \frac{1}{r}\frac{\partial}{\partial r}\left(r\frac{\partial[F]}{\partial r}\right) \\ \frac{\partial[SF]}{\partial t} = k_2[SG][F] \end{cases} \tag{4.6}$$

where D_G and D_F are the diffusion constants of G and F respectively, r is the radial coordinate, t is time and [...] indicates concentrations. Note that there are no diffusion terms in the equation for S, SG or SF due to immobility of binding sites on the substrate.

To simplify the model, it is assumed that G diffuses sufficiently quickly such that the distribution of unbound G constructs over the vesicle membrane is approximately uniform. The assumption holds if the binding of G to S is slow compared to the time scale to relax density fluctuations in G, an assumption also made when modelling the basic gradient motion system in Chapter 3. However, even if this assumption does not apply, it would not have a significant impact on the model results as the majority of S constructs are already bound to G constructs at the start of the experiment. Therefore, the pattern formation process is likely to be limited by the bridge-burning step (*i.e.* displacement of G from SG by F) and by the diffusion of F, rather than the re-binding of G to the remaining unbound S. Nevertheless, including the finite diffusion rate of G over the vesicle membrane could be a useful addition to future implementations of this model.

As each GUV construct must either be in its unbound G state, or bound in an SG bridge, the (uniform) concentration of G can be calculated by integrating the concentration of SG over the contact region and subtracting this from the total number of GUV constructs over the entire vesicle membrane, as follows:

$$\begin{aligned} [G(t)] &= \frac{3\pi R^2[G_0] - \iint_A [SG(r,t)]dA}{3\pi R^2} \\ &= [G_0] - \frac{1}{3\pi R^2}\iint_A [SG(r,t)]dA \\ &= [G_0] - \frac{1}{3\pi R^2}\int_0^R [SG(r,t)]\cdot 2\pi r dr \\ &= [G_0] - \frac{2}{3R^2}\int_0^R [SG(r,t)] r dr \end{aligned} \tag{4.7}$$

where $[G_0]$ indicates the concentration of G constructs on the vesicle membrane prior to adhesion to the substrate; R and A correspond to the radius and area of the contact region respectively. Expressions of the form $[X(r,t)]$ denote the concentration of species X at radial distance r and time t. Note that the vesicle is modelled as a hemisphere with total surface area $3\pi R^2$.

The vesicle is initially adhered to the substrate with uniform (*i.e.* r-independent) bridge density $\rho_{B,0}$, which is estimated in the same way as in Chapter 3. Note that under relevant

experimental conditions, we expect the bridge density to be saturated at all times, reaching its maximal value set by the concentration of free S and G. It is assumed that there are initially no F strands within the contact region, which means that SF is also initially zero throughout the contact region. The initial conditions are denoted as

$$\begin{cases} [F(r,0)] = 0, & \forall r \\ [SF(r,0)] = 0, & \forall r \\ [SG(r,0)] = \frac{\rho_{B,0}}{L}, & \forall r \\ [S(r,0)] = [S_0] - \frac{\rho_{B,0}}{L}, & \forall r \\ [G(r,0)] = [G_0] - \frac{\rho_{B,0}}{3L}, & \forall r \end{cases}$$

where $[S_0]$ is the concentration of S constructs prior to adhesion of the vesicle to the substrate, and the expression for G follows from Equation 4.7. Note that the bridge densities $\rho_{B,0}$ have been converted to concentrations by dividing by $L = 10\,\text{nm}$, as mentioned previously.

The outer edge ($r = R$) of the contact region was modelled as an interface in a two-compartment system (comprising of the interior and exterior of the contact region) that is permeable to F, and where binding is neglected. At the centre of the contact region ($r = 0$) the boundary is considered an impermeable surface. The boundary conditions are thus denoted as

$$\begin{cases} [S(r \geq R, t)] = [S_0] \\ [G(r \geq R, t)] = [G_0] - \frac{2}{3R^2} \int_0^R [SG(r,t)] r dr \\ [SG(r \geq R, t)] = 0 \\ [SF(r \geq R, t)] = 0 \\ \frac{\partial [F(r=0,t)]}{\partial r} = 0 \\ \frac{\partial [F(r=R),t]}{\partial t} = k_{in}([F_0] - \frac{1}{\lambda}[F(r=R,t)]) \end{cases} \tag{4.8}$$

where $[F_0]$ is the bulk concentration of F, k_{in} is a rate describing exchange of F between the contact region and the bulk, and λ is a partition coefficient for F in the contact region. $[F_0]$ was assumed constant in the limit of excess F. For the numerical implementation of the model, the partition coefficient was set to $\lambda = 1$; this decision was made due to the finding in Ref. [315], where the partition coefficient was observed to have no significant effect on the fitting outcomes.

Numerical implementation of model

The reaction-diffusion model was solved numerically, by discretising the radial axis into equidistant points $r_n = n\delta r$ for $n = 0, 1, 2, ..., N$ (where δr is the spacing and $N = R/\delta r$) and applying a finite differences methods described by Crank [316]. DNA concentrations in discretised radial coordinates are denoted as $[X]_n$, which is the concentration of species X at position n. The second order spatial derivative in the fourth line of Equation 4.6 can then be approximated with centred finite difference approximations, such that the differential equation for F can be reduced to

$$\frac{\delta[F]_n}{\delta t} = \begin{cases} \frac{4D_F}{(\delta r)^2}([F]_1 - [F]_0) - k_2[SG]_n[F]_n & n = 0 \\ \frac{D_F}{2n(\delta r)^2}\left((2n+1)[F]_{n+1} - 4n[F]_n + (2n-1)[F]_{n-1}\right) - k_2[SG]_n[F]_n & 0 < n < N \\ k_{in,F}([F_0] - \frac{1}{\lambda}[F]_n) & n = N. \end{cases} \tag{4.9}$$

The remaining DNA species were modelled in discretised radial coordinates as

$$\frac{\delta[S]_n]}{\delta t} = \begin{cases} -k_1[S]_n[G]_n & 0 \leq n < N \\ 0 & n = N \end{cases} \tag{4.10}$$

$$\frac{\delta[SF]_n}{\delta t} = \begin{cases} k_2[SG]_n[F]_n & 0 \leq n < N \\ 0 & n = N \end{cases} \tag{4.11}$$

$$\frac{\delta[SG]_n}{\delta t} = \begin{cases} k_1[S]_n[G]_n - k_2[SG]_n[F]_n & 0 \leq n < N \\ 0 & n = N \end{cases} \tag{4.12}$$

$$[G]_n = \begin{cases} [G_0] - \frac{2}{3R^2}\sum_{m=0}^{N}\left([SG]_m \cdot m\delta r \cdot \delta r\right) & 0 \leq n < N \\ 0 & n = N \end{cases} \tag{4.13}$$

where the expression for G follows from Equation 4.7 and applies for all n.

Modelling the intensity map

Equations 4.9 to 4.13 were solved numerically using the *odeint* function of the Python *scipy.integrate* sub-package [317]. The solution provides the concentration variation over time of the DNA species S, F, G, SG and SF. The radial coordinates were then converted back from integer values n to units of radial distance $r = n\delta r$, and the concentrations were converted to fluorescence intensity as follows:

$$I_{\text{model}}(r,t) = \frac{[S(r,t)] + [SG(r,t)] + \theta[SF(r,t)]}{[S_0]} \tag{4.14}$$

where $I_{\text{model}}(r,t)$ is the modelled fluorescence intensity at radius r and time t, and θ is the quenching factor describing the reduction in fluorescence intensity when F binds to S (as in

Section 4.3). The factor of $[S_0]$ in the denominator scales the intensity such that the maximum intensity (*i.e.* fluorescence intensity of the substrate prior to binding of F) is normalised to 1, for direct comparison with the normalised experimental data.

Gaussian smoothing was applied to the intensity profile to account for the finite imaging resolution of the experimental data. The radial intensity map $I_{\text{model}}(r,t)$ was first interpolated onto two-dimensional Cartesian coordinates (*i.e.* $I_{\text{model}}(x,y,t)$) and then convolved with a two-dimensional Gaussian point spread function (PSF). The width of the Gaussian PSF was either set to the lower bound determined by experimental diffraction blurring, or was determined by fitting the model to the boundary of the bridge-burning pattern in the experimental data. In the case of experimental diffraction blurring, light that passes through a circular aperture produces a diffraction pattern known as an Airy disk. The full width at half maximum (FWHM) of the Airy disk is calculated as [318]

$$\text{FWHM} = 0.51\frac{\lambda}{\text{NA}}. \tag{4.15}$$

The fluorophore used in experiments (Alexa Fluor 488) has an emission maximum of $\lambda = 517\,\text{nm}$, which corresponds to a FWHM of 586 nm. If we approximate the PSF with a Gaussian kernel, the width of the Gaussian point-spread function is then given by

$$\sigma = \frac{\text{FWHM}}{2\sqrt{2\ln 2}}. \tag{4.16}$$

which evaluates to $\sigma = 0.249\,\mu\text{m}$ for the experimental setup.

It is likely that the value of σ calculated from the theoretical diffraction limit is an underestimate. For example, diffraction blurring of experimental images could be greater than the theoretical value calculated from the width of the Airy disk. Furthermore, non-diffraction factors (*e.g.* imprecise identification of the centre of the contact region in experimental image data, and analysing contact regions that are not perfectly circular) could also contribute to blurring or distortion of the experimental radial intensity maps. Therefore, σ was alternatively left as a fitting parameter. Once σ is determined (either by the diffraction-limited value, or by fitting to experimental data), the intensity map $I_{\text{model}}(x,y,t)$ is convolved with the Gaussian PSF, and then converted back to radial coordinates ($I_{\text{model}}(r,t)$).

Extracting pattern intensity maps from experimental image data

Time lapse data of bridge-burning patterns were initially loaded in the image analysis software Fiji [319]. Patterns were selected for analysis to have sufficiently large radius for the propagation of the bridge-burning front to be clearly visible, and to have an approximately circular outer perimeter. The patterns were selected and cropped manually (*e.g.* see Figure 4.2a), to aid identification of pattern regions during later automated steps in the image analysis.

Intensity profiles were measured for each frame of the cropped time lapse data using custom software written in Python. First, the centre of the bridge-burning pattern was located in each frame of the time lapse. The image was first smoothed with a Gaussian filter to reduce noise, and binarised such that the burned regions were distinguishable (see Figure 4.2b). The Python

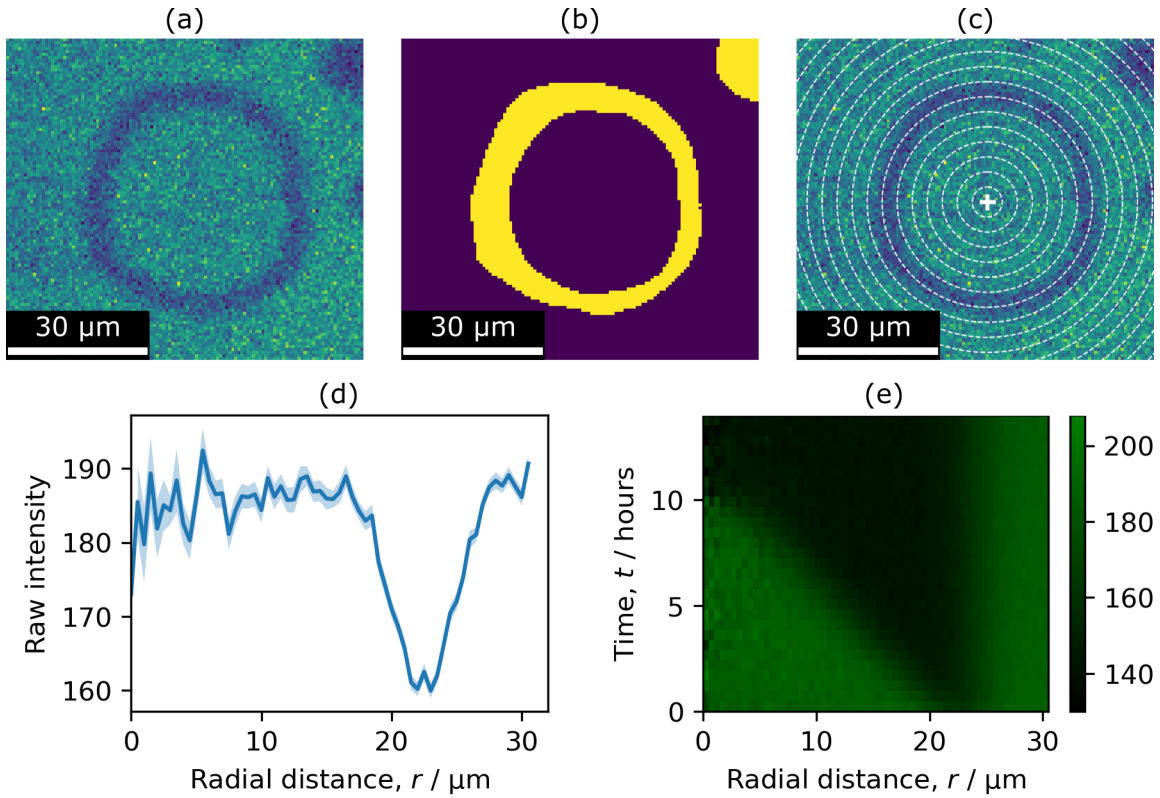


Figure 4.2: **Extracting the intensity profile of a bridge-burning pattern.** A snapshot from a time lapse of a bridge-burning pattern at time $t = 0$ is shown in (a), while (b) shows the same snapshot after Gaussian smoothing and binarisation. The measured centre of the pattern is marked with a cross in (c), along with equally-spaced concentric circles representing the radial-binning process; note that the width of radial bins is larger than the actual width of $0.5\,\mu$m, for ease of visualisation. (d) shows the azimuthally-averaged intensity as a function of radial distance r at time $t = 0$ (*i.e.* $I(r, t = 0)$), with the standard error of the mean shaded. The intensity map $I(r, t)$ is shown in (e), with a colour bar indicating the intensity values.

library *OpenCV* [260] was then used to locate the centre of the burned contact region. This was done by first locating contours in the binarised image using OpenCV's *findContours* function, of which the largest was identified as the approximate edge of the contact region. A rough estimate of the radius of the contact region was obtained by fitting a circle to the contour, using the Python library *Circle-Fit*. The centre of the burned region was then fine-tuned by applying a template-matching method using OpenCV's *matchTemplate* function. For images where an annular region had previously been detected (*i.e.* the *findContours* function detected two concentric circles), an annular template was applied; otherwise, a circular template was applied. A distance transform was applied to the image and template prior to the template-matching process to account for error in the radius estimate, similar to the use of the distance transform to locate vesicles in polydisperse samples (outlined in Sections 2.6 and 3.2.5).

After locating the centre of the contact region, each pixel in the image was binned based on distance r from the centre of the contact region, and the average pixel intensity for each radial-distance bin was calculated; see Figure 4.2c for a representation of the binning process, and Figure 4.2d for a radial intensity profile for a given time point. This corresponds to taking an azimuthal average of the intensity. The azimuthally-averaged radial intensity profile was

measured for each time-point t of the time lapse, to attain a 2D intensity map $J(r,t)$ (*e.g.* see Figure 4.2e).

Finally, the intensity map $J(r,t)$ was background-subtracted and normalised. The intensity of the region of the image outside the contact region was averaged over, providing the maximal signal J_{max}. The background signal J_0 was estimated by averaging the pixel intensity in a manually selected rectangular region that did not contain any substrate DNA. The intensity map was then background-subtracted and normalised to obtain the experimental intensity map

$$I_{\text{exp}}(r,t) = \frac{J(r,t) - J_0}{J_{max} - J_0}. \tag{4.17}$$

Note that this corresponds to an approximate normalised intensity of 1 in unburned regions of the substrate.

Fitting model results to experimental data

This section details the steps taken to fit parameters of the reaction-diffusion model (in Section 4.5) to experimental data of bridge-burning pattern formation. The modelled intensity map $I_{\text{model}}(r,t)$ was fitted to the experimental intensity map $I_{\text{exp}}(r,t)$, where $I(r,t)$ is the fluorescence intensity at radial distance r from the centre of the vesicle contact region and time t from the start of the experiment.

The fitting process was conducted in several stages, by grouping correlated parameters and fitting each group separately, to improve the time efficiency of the process. The parameter groups influence different aspects of the intensity profile, such that the fit results of one group have an insignificant correlation with the fit results of another group. θ was fitted directly to the fluorescence intensity of the burned region of the substrate. R and σ were fitted to the diameter and blurring of the boundary of the burned pattern, respectively. Δt, k_{in} and D_F were fitted together as they determine the position of the propagating bridge-burning front in the intensity map. Finally, k_1 and k_2 were fitted together as they correspond to the blurring of the propagating bridge-burning front.

Parameters were typically optimised by varying the parameter value inputs to the model, and calculating the residual map *i.e.* the difference between the model and experimental intensity for each point in $I(r,t)$ (see Figure 4.3). The similarity of the model to the experimental data was then scored by calculating the mean squared value of the residual map,

$$Score = \frac{1}{N}\sum_{r,t}(I_{\text{model}}(r,t) - I_{\text{exp}}(r,t))^2, \tag{4.18}$$

where the summation is carried out over all radial distance bins r and all time points t, and N is the total number of residuals summed over. The parameter values that minimised the score function were taken to be the optimal values.

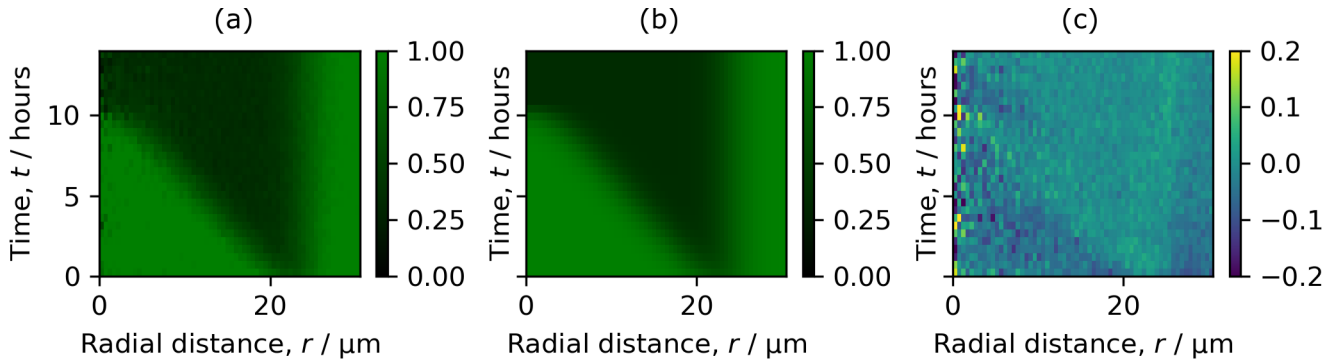


Figure 4.3: **Comparison of an experimental bridge-burning pattern with a fitted model, and the corresponding residual map.** The normalised intensity map $I_{\text{exp}}(r,t)$ extracted from the experimental pattern data in Figures 4.9 and 4.2 is displayed in (a), while the fitted model intensity map $I_{\text{model}}(r,t)$ is shown in (b). The residual map $I_{\text{model}}(r,t) - I_{\text{exp}}(r,t)$ is shown in (c).

Fitting θ

The quenching factor θ was the first parameter to be fitted, as it can be directly extracted from the normalised fluorescence intensity in 'burned' regions of the substrate (see Figure 4.4). To measure θ, the burned region of the normalised experimental intensity map $I(r,t)$ was smoothed (by time-averaging over the last five frames of the time lapse, then applying a rolling mean with a window size of 10 pixels). θ was then determined as the minimum value of the smoothed, normalised intensity data.

Fitting R and σ

The radius R of the vesicle contact region was fitted to the boundary of the bridge-burning pattern (see Figure 4.4). An initial estimate for R was determined as a radial distance approximately midway along the boundary between the minimum fluorescence 'burned' region of the substrate, and the maximum fluorescence 'unburned' region of the substrate. The estimate of R was then refined by modelling the boundary region of the radial intensity profile with the step function $I_{\text{step}}(r) = \theta$ for $r < R$, $I_{\text{step}}(r) = 1$ for $r \geq R$. R was varied, and $I_{\text{step}}(r)$ was compared with the boundary region of the experimental data (averaged over the second half of the time lapse duration to ensure sufficient bridge-burning within the boundary). The fit of R was scored by calculating the sum of squared residuals (see Equation 4.18), to find the optimal value of R.

The width σ of the Gaussian PSF applied to the modelled intensity data was also optionally fitted to the boundary region of the radial intensity profile, instead of setting σ to the lower bound determined by the theoretical diffraction limit (see Section 4.2.2). The reasoning for fitting σ to the boundary is that the blurring of the boundary in experimental data depends solely on the finite resolution of the image data (at least theoretically). On the contrary, blurring of other features of the experimental intensity map $I(r,t)$ such as the propagating bridge-burning front may also be limited DNA reaction rates k_1 and k_2. It must however be

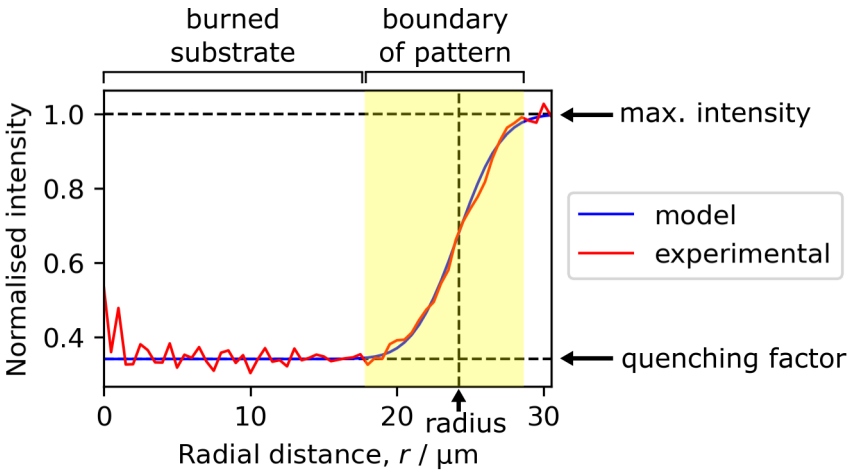


Figure 4.4: **Fitting the quenching factor and experimental image resolution to the normalised intensity profile of an experimental bridge-burning pattern.** The plot displays the radial intensity profile of a bridge-burning pattern at time $t = 14$ hours, extracted from the pattern shown in Figure 4.9 and 4.2. Both the experimental data and fitted model are shown. The boundary region of the bridge-burning pattern is highlighted in yellow. The intensity has been normalised as described in Equation 4.17 such that the intensity outside the burned region is approximately 1. The quenching factor θ can be extracted from the normalised intensity within the burned region of the substrate. In this case, the width σ of the Gaussian point spread function applied to the model has been fitted to the boundary region of the experimental intensity profile, as described in Section 4.2.2.

noted that the value of σ fitted to the boundary of the pattern may be an overestimate of the image blurring in other regions of the pattern, as the blurriness of the boundary would be particularly affected by non-circularity of the contact region perimeter.

To fit both R and σ, the same step function $I_{\text{step}}(r)$ was interpolated onto two-dimensional Cartesian coordinates (*i.e.* $I_{\text{step}}(x, y)$), convolved with a Gaussian PSF, and compared with the experimental boundary region by calculating the sum of squared residuals. A grid-search was performed over ranges of R and σ to find the combination of these parameters that minimised the sum of squared residuals.

Fitting Δt, k_{in} and D_F

Δt, k_{in} and D_F were fitted together as they influence the position and shape of the propagating bridge-burning front in the intensity map $I(r, t)$. Δt corresponds to translation of the intensity map along the t-axis, while k_{in} and D_F determine the rate at which the bridge-burning front propagates towards the centre of the contact region over time.

To incorporate the time delay Δt to the model, the modelled intensity map was shifted in time (*i.e.* $I_{\text{model}}(r, t) \mapsto I_{\text{model}}(r, t + \Delta t)$. Δt, k_{in} and D_F were then optimised by varying all three variables and scoring the fit of the model to experimental data with Equation 4.18 to find the combination of Δt, k_{in} and D_F that minimised the score. The optimal values of k_{in} and D_F were further fine-tuned using the *minimize* function from the Python sub-package *scipy.optimize* [317]. Note that *scipy.optimize* was not used for the initial coarse-grained opti-

misation as the function is prone to locating local minima, due to noise in experimental data.

Fitting k_1 and k_2

Finally, the DNA strand displacement rate constants k_1 and k_2 were fitted together as their primary effect on the system is to influence the blurriness of the propagating bridge-burning front; as the values of the rate constants decrease, the propagating front becomes more blurred. Unlike other fitting parameters, these parameters generally did not exhibit clear minima in their scoring functions. Under the relevant experimental conditions, k_1 does not have an observable effect on the model solution. This makes sense as k_1 is the rate at which G binds to unbound S, but the majority of S is already bound to G at the start of the experiment. This means that the bridge-burning process is predominantly limited by the rate at which F displaces G from S, and the rate at which F enters and diffuses through the contact region. As k_1 does not have an observable effect on the model results under experimentally relevant conditions, k_1 is set to the fixed value of $10^5\,\mathrm{M}^{-1}\,\mathrm{s}^{-1}$, based on strand displacement rate constants reported in literature [193, 320].

k_2 was observed to affect the model results, although the fitted value of k_2 is sensitive to σ, the width of the Gaussian PSF applied to the model results. This is because both σ and k_2 contribute to the blurriness of the propagating bridge-burning front. Therefore, if σ is underestimated (*e.g.* by setting σ to the lower bound defined by the diffraction limit), it is likely that k_2 will be underestimated to account for the reduced contribution to the blur from σ. By the same reasoning, if σ is over-estimated (*e.g.* by inaccurate fitting of σ to the boundary of the pattern), it is likely that k_2 will be over-estimated, or that there will no longer be an upper bound in the scoring function for k_2 as the blurriness of the propagation front is predominated by the contribution from σ.

4.3 Verifying and fitting the bridge-burning DNA mechanism in bulk solution

Although the reactive moieties of the DNA constructs responsible for the burnt-bridges mechanism had already been designed and tested in Ref. [241], it was important to check that the mechanism would still work as expected once the DNA constructs and experimental system had been modified to be incorporated into the existing vesicle mobility set-up.

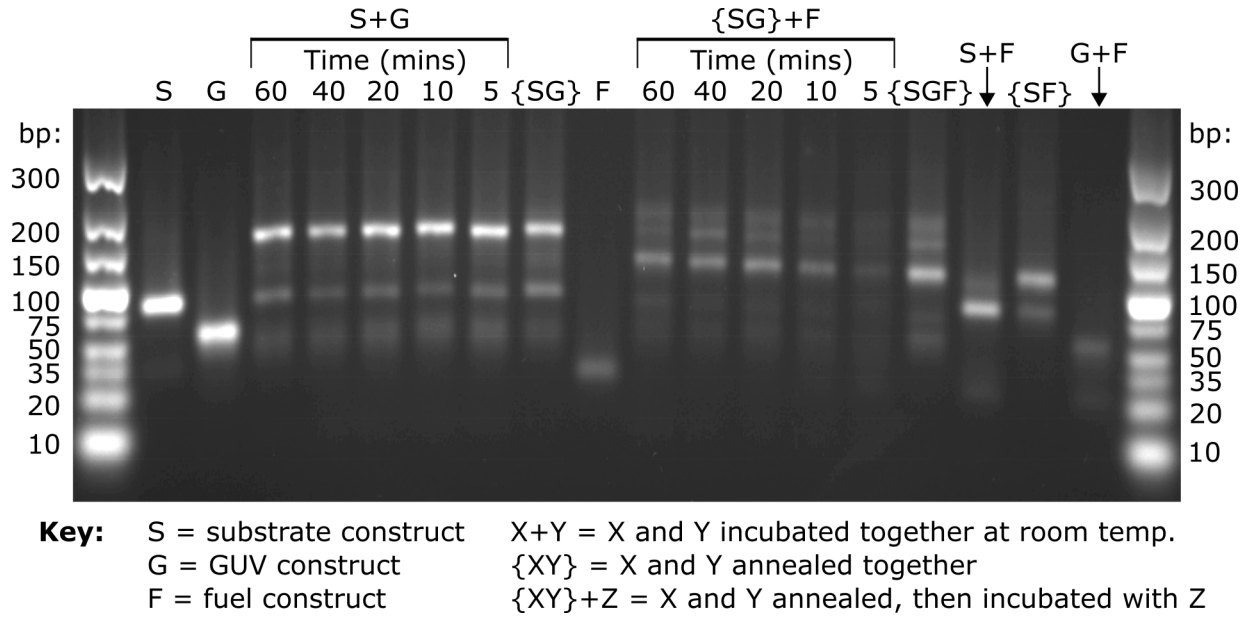


Figure 4.5: **Agarose gel electrophoresis confirms the successful formation of DNA constructs for the burnt-bridges system.** Gel results are shown for the substrate (S), GUV (G) and fuel (F) constructs of the burnt-bridges system; reference ladder bands are displayed in the outer two lanes. The results include samples in which multiple species of constructs have been mixed in a 1:1 ratio, and either left to incubate at room temperature (with incubation period ranging between 5–60 minutes, as labelled) or annealed *via* the process outlined in Section 2.1.2, before running the gel. Note that the concentrations of the gel samples were chosen to maintain the same total concentration of S, G and F per sample; as F is a smaller construct than S and G, the bands corresponding to F appear less bright.

4.3.1 Agarose gel electrophoresis to verify constructs and binding kinetics

As an initial check, agarose gel electrophoresis was run to verify the formation of the DNA constructs; the gel results are displayed in Figure 4.5. For this gel, S, G and F constructs were prepared by mixing the appropriate amounts of their constituent strands in buffer (4 mM $MgCl_2$, 15 mM KCl, 1×TE) and annealing *via* the process outlined in Section 2.1.2; the gel results for S, G and F show bright bands corresponding to DNA structures of the expected sizes, indicating successful formation of the desired constructs.

The kinetics of the burnt-bridges mechanism (detailed in Section 4.1) were also checked *via* the gel electrophoresis by including samples consisting of various mixtures of S, G and F, in the same buffer conditions (4 mM $MgCl_2$, 15 mM KCl, 1×TE). First, the binding kinetics of S and G (stage 1 to 2 in Figure 4.1) were verified, by mixing S and G in a 1:1 ratio (such that their final concentrations were both equal to 250 μM) and incubating at room temperature, for incubation periods ranging between 5–60 minutes. These samples (labelled as $S + G$ in Figure 4.5) were run on the gel, along with a further sample ($\{SG\}$) with the same composition that was instead annealed *via* the method outlined in Section 2.1.2. The gel results indicate the formation of a larger DNA structure which corresponds to the successful binding of S and G. The brightness of the bands for the non-annealed $S + G$ samples appear similar for incubation periods of 5–

60 minutes (and similar to the brightness of bands for the annealed sample), indicating that the majority of S and G bind within five minutes of incubation at room temperature under these conditions. Furthermore, it is apparent that a small quantity of S and G remain unbound. This could be due to an excess of either S or G; alternatively, truncation defects in a small proportion of constructs could inhibit binding of G to the toehold on S.

Second, the kinetics of binding of F to SG and subsequent displacement of G (stage 2 to 3 in Figure 4.1) were verified in the same gel. This was achieved by mixing an annealed sample of S and G ($\{SG\}$) with F (such that the final concentrations of S, G and F were all equal to 250 μM) and incubating at room temperature, for incubation periods ranging between 5–60 minutes. These samples (labelled as $\{SG\} + F$ in Figure 4.5) were run on the gel, along with a further sample ($\{SGF\}$) with the same composition that was instead annealed. All of these samples exhibit a new band corresponding to a DNA construct that is slightly smaller than SG, but larger than the individual constructs (S, G and F); this indicates successful formation of SF, which indeed is smaller than SG. The brightness of the band corresponding to SF appears to increase with incubation period, especially for periods ranging from 5–20 minutes; this suggests that it takes > 20 minutes for the majority of binding and displacement reactions to occur under these conditions. Furthermore, it indicates that the process $SG + F \rightarrow SF + G$ is slower than the process $S + G \rightarrow SG$, indicating a slower branch migration rate (perhaps as the former involves two branch migration processes while the latter only involves one). Furthermore, differences in the sequence or binding affinity of the toehold may matter, as the system is at the boundary of where strand displacement rate becomes independent of toehold length ($\approx$ 6–7 nt) [193]. There are other faint bands visible for these samples, corresponding to S, G and SG, as well as an additional band corresponding to an even larger DNA construct which most likely consists of S, G and F bound together (before G is displaced). The band corresponding to G is expected as this is displaced by F from SG. However, the other bands indicate that the mechanism has not fully completed, even in the annealed sample; this could be due to small inaccuracies in concentrations of strands or constructs within the samples, or defects in constructs which prevents the mechanisms from completing.

Some additional samples were run on the gel to check for unwanted binding. A sample of $S + F$ was prepared by mixing S and F in the same buffer conditions such that their final concentrations were equal to 250 μM, and incubating for over one hour at room temperature; this was compared with a sample that had instead been annealed. For the annealed sample, the gel indicates formation of SF, with a slight excess of S remaining. On the contrary, for the non-annealed sample, the majority of the constructs remain unbound; this is expected, as the mechanism requires G to catalyse the binding of F to S. However, there appears to be a faint band corresponding to SF for the non-annealed sample, which suggests that a small proportion of S and F are able to bind; this could be due to defects leading to improper formation (or absence) of the hairpin structure in S, or due to spontaneous unbinding of the hairpin structure in a small proportion of S constructs.

Finally, a sample consisting of G and F mixed together in the same buffer conditions (with

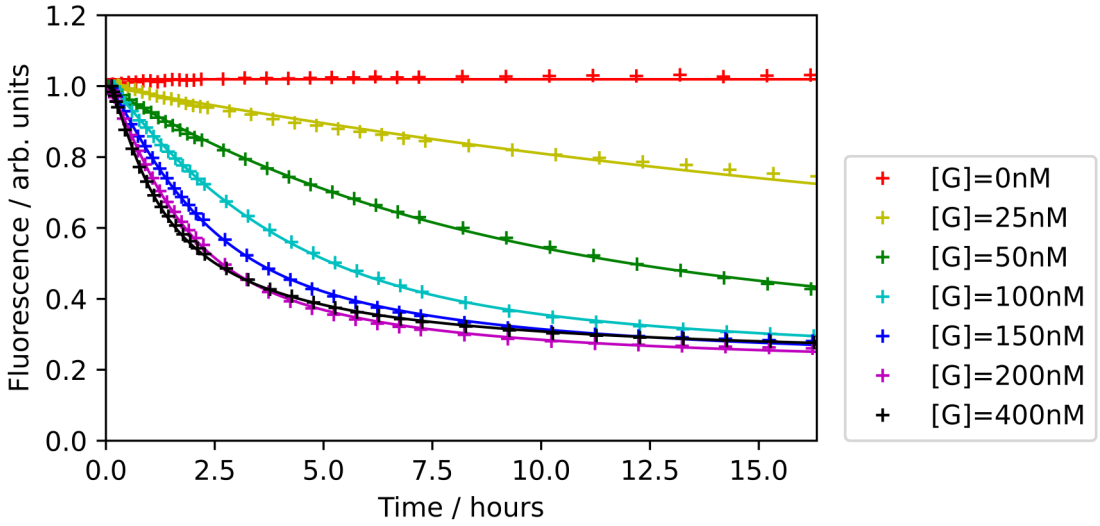
final concentrations of 250 μM) and incubated for over one hour at room temperature was also run on the gel. As expected, this sample only exhibits bands corresponding to G and F, as these constructs do not have complementary regions that would enable binding.

4.3.2 Fluorescence experiments to fit the kinetics in bulk

The burnt-bridges process and catalytic behaviour of the GUV construct were further verified by conducting fluorescence measurements on a plate reader. To conduct these experiments, S and F were modified with a fluorophore (Alexa Fluor 488) and quencher (Iowa Black FQ), respectively, as depicted in Figure 4.1. The fluorescence of samples with $[S] = 200\,\text{nM}$, $[F] = 200\,\text{nM}$, and $[G]$ varied between 0–400 nM (where $[X]$ denotes the concentration of construct X) were measured over time on a plate reader. The buffer conditions were kept the same, with 4 mM $MgCl_2$, 15 mM KCl and 1×TE. For each sample, S and F were mixed first to ensure minimal reactions; G was then added immediately before starting the fluorescence measurements. For each condition, five repeats were conducted and averaged over; the fluorescence measurements were background-subtracted, using the average fluorescence recorded from three wells filled with buffer solution. The fluorescence measurements were normalised by the average fluorescence recorded from three wells filled with buffer solution and $[S] = 200\,\text{nM}$, to account for any variation in fluorescence that isn't related to the DNA mechanism (*e.g.* due to photobleaching). The fluorescence measurements were then re-scaled such that the initial fluorescence is equal to 1, to allow comparison between data series.

Results from this experiment are shown in Figure 4.6. For all samples with non-zero concentration of G, the fluorescence decreases over time as expected, as G catalyses the binding of F to S which brings the quencher in proximity with the fluorophore. As the concentration of G is increased, the rate at which the fluorescence drops towards the plateau also increases, which again indicates the role of G in the burnt-bridges mechanism. In particular, the data series appear to eventually plateau at similar fluorescence values, regardless of the concentration of G. This verifies the catalytic behaviour of G; once F displaces G from SG, the G construct is free to bind to another S construct. If G did not behave as a catalyst (*i.e.* it remained bound to S), one would expect that the data series would no longer all converge towards the same final fluorescence value, especially for $G < 200\,\text{nM}$.

The experimental fluorescence data were fitted by modelling the DNA mechanism, as detailed in Section 4.2.1. In Figure 4.6, the model has been fitted separately to each data series, such that a separately list of fitted parameters is generated for each concentration of G. On first inspection of the fitted curves in Figure 4.6, they appear to agree well with the experimental data, although comparison of the fitted parameters indicates that the model fitting results of the rate constants and quenching ratio for $[G] = 0$–$50\,\text{nM}$ are not consistent with the results of the data from higher concentrations of G. This is to be expected; at such low concentrations of G, the mechanism proceeds sufficiently slowly that the fluorescence has not started to plateau. These samples would have to be measured for a longer time period to collect enough data to accurately fit the model. On the other hand, for the data series that start to plateau within

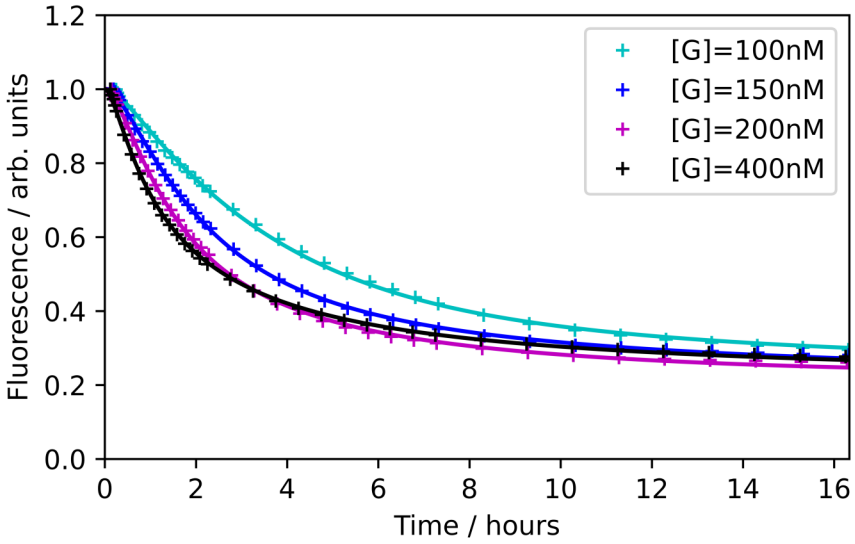


[G] / nM	$[S]_0$ / nM	$[G]_0$ / nM	$[F]_0$ / nM	k_1 / M^{-1} s^{-1}	k_2 / M^{-1} s^{-1}	θ	Δt / s
0	186.0	0.0	200.0	1.00×10^9	1.00	0.5	50
25	220.0	27.5	180.0	9.99×10^8	4.12×10^2	0.307	580
50	218.9	45.8	205.0	9.85×10^8	6.86×10^2	0.282	100
100	206.3	90.0	208.5	7.41×10^3	7.44×10^2	0.207	391
150	205.3	135.0	198.4	7.95×10^3	8.61×10^2	0.179	220
200	220.0	180.9	210.1	4.68×10^3	1.09×10^3	0.173	220
400	180.0	368.3	181.2	4.01×10^3	1.23×10^3	0.221	340

Figure 4.6: **Fluorescence experiments verify the burnt-bridges mechanism in bulk solution and the catalytic behaviour of the GUV construct.** The fluorescence of samples with a mixture of 200 nM substrate construct (S), 200 nM fuel construct (F) and GUV construct (G) with concentration varied between 0–400 nM were measured over time on a plate reader. There is a fluorophore (Alexa Fluor 488) attached to S, while F is modified with a quencher (Iowa Black FQ); therefore, as G catalyses the binding of F to S (in the mechanism outlined in Section 4.1), the fluorescence decreases. In the plot, experimental data are shown by the markers, with smooth curves fitted to the experimental data by modelling the DNA mechanism and fitting model parameters, as described in Section 4.3.2. In this case, the model parameters were fitted separately to each data series; the fitted parameters are shown in the table. $[G]$ refers to the target concentration of G added to the sample, while $[S]_0$, $[G]_0$ and $[F]_0$ are the fitted values for the initial concentrations of S, G and F, respectively. k_1 and k_2 are the fitted values for the rate constants from Equation 4.1; θ is the fitted quenching ratio from Equation 4.5; and δt is the fitted time delay between the addition of G to the sample and the start of the fluorescence measurements. Note that experimental data points in the plot have been delayed by the fitted values for δt.

the experimental time scale (*i.e.* $[G] = 100$–400 nM), the fitted values for the rate constants and quenching ratio appear to be consistent. k_1 is estimated to be $(4\text{–}7)\times10^3\,\mathrm{M^{-1}\,s^{-1}}$, k_2 is estimated to be $(0.7\text{–}1.2)\times10^3\,\mathrm{M^{-1}\,s^{-1}}$, and θ is estimated to be 0.17–0.22. Note that $k_2 < k_1$, in agreement with the gel electrophoresis results in Figure 4.5.

The actual values for k_1, k_2 and θ should be the same for all samples. Therefore, the fitting process was repeated as before, except that a global fit was performed for the aforementioned parameters. The data for $[G] = 0$–50 nM were excluded due to there being insufficient data for an accurate fit, as mentioned before. The fit results are shown in Figure 4.7, with estimated



[G] / nM	$[S]_0$ / nM	$[G]_0$ / nM	$[F]_0$ / nM	k_1 / M^{-1} s^{-1}	k_2 / M^{-1} s^{-1}	θ	Δt / s
100	194.2	90.0	194.4	4.33×10^3	9.35×10^2	0.221	520
150	184.5	151.4	197.4				560
200	189.9	219.7	220.0				400
400	199.3	440.0	210.6				300

Figure 4.7: **A global fit of the rate constants and quenching ratio, for the bridge-burning mechanism in bulk solution.** Here, the same experimental fluorescence data as in Figure 4.6 are plotted, as shown by the markers in the plot. Curves have been fitted to the experimental data *via* the fitting process outlined in Section 4.2.1, extracting estimates for the initial concentrations of the substrate, GUV and fuel constructs ($[S]_0$, $[G]_0$ and $[F]_0$, respectively); the rate constants k_1 and k_2; the quenching ratio, θ; and the time delay between addition of G to the samples and the start of the fluorescence measurements, δt. Here, the fitting process was similarly to the fitting process for the curves in Figure 4.6, except that a global fit was conducted for k_1, k_2 and θ (rather than fitting separately to each data series). Values for the fitted parameters are displayed in the table.

values for the rate constants of $k_1 = 4.33 \times 10^3\,\mathrm{M^{-1}\,s^{-1}}$ and $k_2 = 9.35 \times 10^2\,\mathrm{M^{-1}\,s^{-1}}$. The reactions described by these rate constants both involve toehold-mediated strand displacement, a process whose rate constant can range between 10^1–$10^6\,\mathrm{M^{-1}\,s^{-1}}$ [193], which agrees with the fitted rate constants. For this toehold length, rate constants on the order of $\approx 10^5$–$10^6\,\mathrm{M^{-1}\,s^{-1}}$ would have been expected based on findings in Ref. [193], but it is not unusual to find smaller values if one has more complex geometries of DNA constructs, such as the hairpin structures in this system; furthermore, the experiments in Ref. [193] were conducted at higher concentration of $MgCl_2$ (12.5 mM), which could result in an increase in strand displacement rate.

θ is estimated to be 0.221 from the global fit. To consider the magnitude of θ, it is helpful to think about the distance between the quencher (Iowa Black FQ) and fluorophore (Alexa Fluor 488). When S and F bind to form SF, the Iowa Black FQ modification on F and the Alexa Fluor 488 modification on S are separated by a 9 nt ssDNA strand. As the length per nucleotide of an ssDNA strand is 0.676 nm [321], this corresponds to a contour length of ≈ 6 nm between the fluorophore-quencher pair; the actual end-to-end distance would be significantly less than this, due to the flexibility of ssDNA. The Förster distances of fluorophore-quencher pairs (*i.e.*

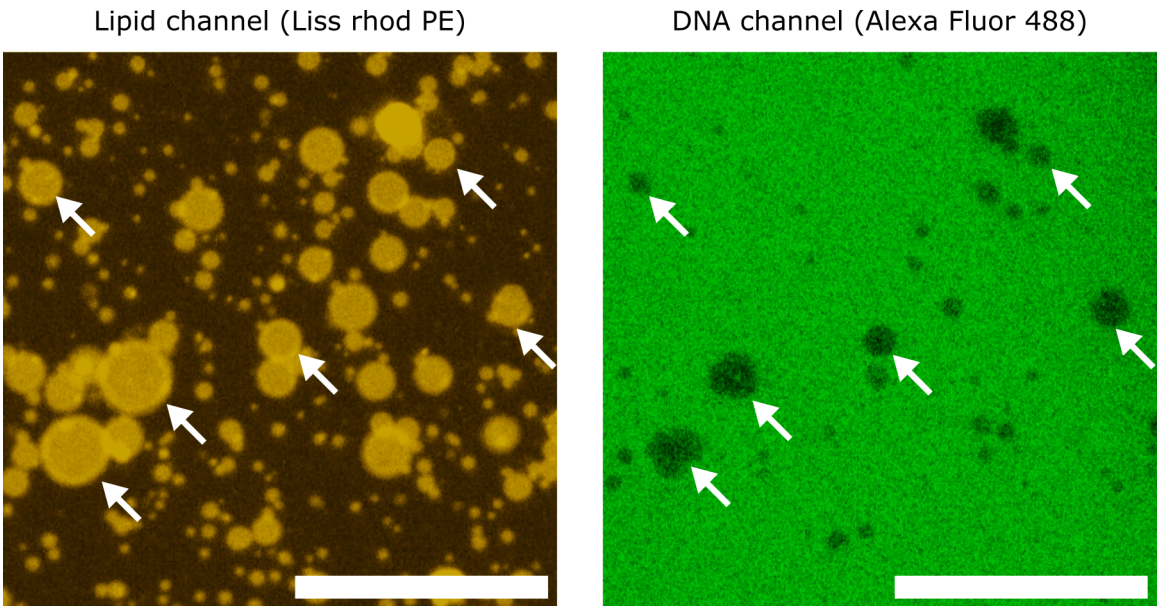


Figure 4.8: **Fluorescence quenching allows for visualisation of the bridge-burning process in the vesicle motility system.** Here, epifluorescence microscopy images of vesicles in the burnt-bridges system detailed in Section 4.4 are shown in the lipid and DNA fluorescence channels, with scale bars of 300 μm; the images were taken 12 hours after the start of the experiment. Fluorescence is excited in the Alexa Fluor 488 modification on the substrate constructs. Bridge-burning within vesicle contact regions appears in the DNA channel as local reduction of the fluorescence intensity due to the quencher modification on the fuel strand F. To aid comparison between the two channels, several of the larger vesicles and corresponding bridge-burning regions are labelled with arrows.

the distance at which the fluorescence of the fluorophore is quenched by 50%) are typically around 3–6 nm [322]. Therefore, if the separation between the fluorophore and quencher pair is comparable to or less than the Förster distance, one would expect the quenching ratio to be close to (or smaller than) 0.5.

4.4 Verifying the bridge-burning mechanism in the experimental vesicle system

Following the verification of the burnt-bridges DNA mechanism in bulk solution, the mechanism was incorporated into the vesicle motility system, by functionalising the GUVs and substrate with G and S constructs, respectively. The DNA-functionalised vesicles were applied to the substrate and allowed to settle, before the fuel strand F was added in bulk solution; further details on the experimental method can be found in Section 2.4.

To verify the bridge-burning process, the S and F constructs were modified with a fluorophore (Alexa Fluor 488) and quencher (Iowa Black FQ), respectively, as depicted in Figure 4.1. This enabled visualisation of the bridge-burning process, as the binding of F to S is accompanied by a reduction in fluorescence intensity due to increased proximity of the fluorophore-quencher pair. Figure 4.8 displays microscopy images of vesicles and the corresponding fluorescence sig-

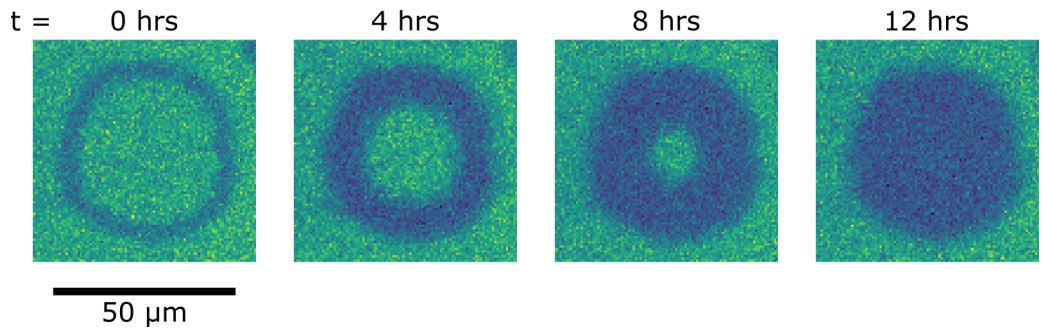


Figure 4.9: **Visible propagation of a bridge-burning front within the contact region of a vesicle on a substrate.** The epifluorescence micrographs show a bridge-burning pattern forming over time within a region on the substrate to which a vesicle is adhered. The fuel strand (modified with a quencher) diffuses under the vesicle, displacing GUV constructs from existing substrate-GUV bridges and binding in their place, leading to a drop in fluorescence intensity. The experiment was conducted under the conditions detailed in Section 4.5.

nal from the S constructs, in an experimental system with $[F] = 5\,\mu$M and 50 mM $MgCl_2$ in the bulk solution. Note that when studying the bridge-burning patterning effect on the substrate, vesicles located over the uniform, maximum DNA density region of the substrates are studied, rather than in the gradient region. The DNA fluorescence channel shows a reduction in fluorescence intensity that is localised to the vesicle contact regions; this verifies the binding of F to SG bridges. Furthermore, some of the "burned" contact regions appear to be significantly smaller than the vesicles, suggesting that the vesicles do not deform to a hemispherical shape, as assumed in the numerical model in Chapter 3.

Furthermore, under certain experimental conditions, it is possible to observe propagation of bridge burning inward from the perimeter of the vesicle contact region; an example is shown in Figure 4.9. This is due to fuel (F) strands diffusing under the vesicle and displacing GUV constructs from substrate-GUV (SG) bridges *via* TMSD. The quencher on F is brought in proximity with the fluorophore on S in the structure SF, leading to a local reduction in fluorescence intensity. This results in a dark front propagating inwards through the vesicle contact region (in the DNA fluorescence channel) as the fuel diffuses and binds to the substrate.

The effect of varying the concentration of $MgCl_2$ in the bulk solution on the rate of bridge-burning was investigated by conducting a series of experiments. In these experiments, the concentration of the fuel strand F was kept at $5\,\mu$M, while the concentration of $MgCl_2$ was varied from 5–50 mM. Epifluorescence micrographs from these experiments are displayed in Figure 4.10. Here, it can again be seen that dark rings and circles appear due to the bridge-burning mechanism occurring within the vesicle contact regions. The bridge-burning propagates inwards from the perimeter of the vesicle contact regions, as the fuel strand diffuses in and binds to the substrate constructs. From the experimental image data, it appears that as the concentration of $MgCl_2$ increases, the rate at which the dark rings close inwards also increases. This indicates that an increase in $MgCl_2$ concentration corresponds to an increase in rate of the bridge-burning DNA mechanism. This can be explained by the fact that the higher the divalent salt concentration, the higher the stability of toehold binding; the toehold binding is required

to initialise the toehold-mediated strand displacement reactions as part of the bridge-burning mechanism. However, it is important to note that an increase in divalent salt concentration would also strengthen the binding between the strands which we wish to separate with the TMSD mechanism (*i.e.* the incumbent and substrate strands), which could result in incomplete displacement of the incumbent strand from the substrate strand. The possibility of increased $MgCl_2$ concentration resulting in incomplete displacement of the incumbent strand in this experimental system is discussed further in Section 4.5.1.

4.5 Fitting the reaction-diffusion dynamics of experimental bridge-burning patterning of substrates

The patterning effect of the propagation of bridge burning through the vesicle contact region is reminiscent of previous research conducted by the group, in which controllable patterning of 3D DNA condensates was achieved [315]. In both cases, the patterning occurs as a result of reaction-diffusion dynamics, in which patterning strands diffuse into a region with multiple binding sites and displace other strands. In Ref. [315], a reaction-diffusion model was fitted to experimental data to further understand the system and obtain key parameters; here a similar model is applied, with the key difference being that the patterning occurs across a 2D surface (*i.e.* the substrate) as opposed to within a 3D condensate. A derivation of the model applicable to the burnt-bridges vesicle system is presented in Section 4.2.2.

To fit this reaction-diffusion model, data were analysed from an experimental system where vesicles were functionalised with G constructs, while the substrate was functionalised with S constructs. Note that for the model fitting, vesicles from the uniform, maximum density region of the substrate were selected. As the methods used to functionalise the vesicles and substrates are the same as the methods used in Chapter 3, the resulting DNA densities should remain the same, *i.e.* the density of G is $\rho_G \approx 0.008\,\mathrm{nm}^{-2}$, and the density of S is $\rho_S \approx 0.03\,\mathrm{nm}^{-2}$. The vesicles were then applied to the substrate, before adding F in bulk solution. Further details on the experimental method can be found in Section 2.4. In this case, the composition of the solution external to the vesicles was tuned to 1×TE, 50 mM $MgCl_2$ and 15 mM KCl, along with 5 μM of the fuel strand F. These conditions enabled visualisation of the propagation of bridge-burning fronts, as the high DNA density allowed for sufficient signal-to-noise ratio, while the high concentration of $MgCl_2$ increased reaction rates due to increased stabilisation of toehold binding. The vesicles were not observed to move significantly under these experimental conditions, likely due to the high density of bridges; as the SG bridges cannot spontaneously unbind in this system (unlike the much weaker receptor-ligand bridges in Chapter 3), motion of the vesicles requires the "burning" of large numbers of SG bridges. Another potential reason is that at such a high concentration of $MgCl_2$, G is not fully displaced from SG bridges due to increased stability of intermediate structures in the mechanism; this possibility is discussed in more detail later in this section, but is not expected to significantly affect the fit of the model.

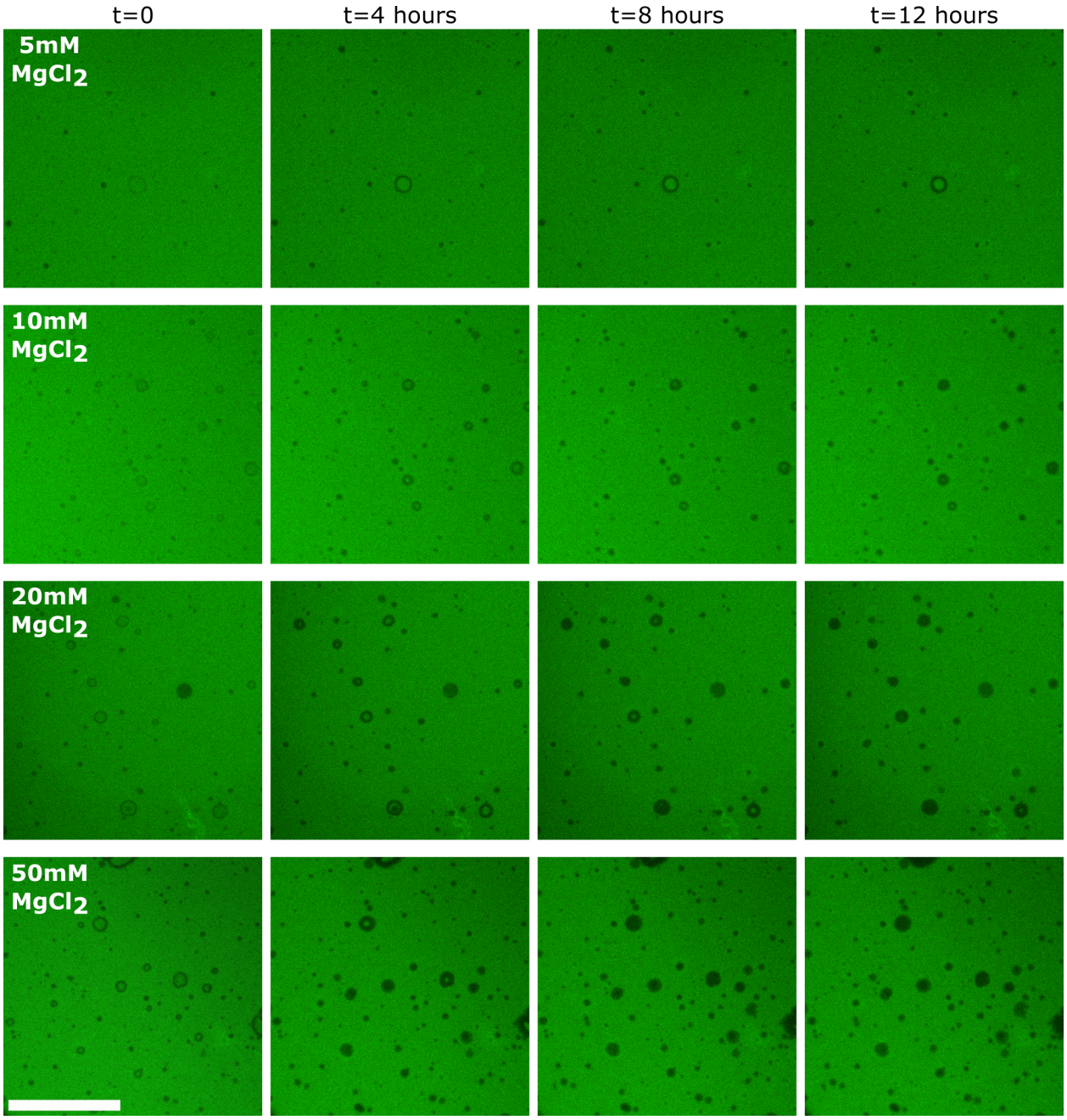


Figure 4.10: **Increasing the concentration of magnesium in bulk solution appears to increase the rate of bridge-burning.** Epifluorescence microscopy images taken at 4-hour intervals are displayed from experimental samples of the burnt-bridges vesicle motility system; the experiments were run with 5 mM, 10 mM, 20 mM and 50 mM $MgCl_2$ in bulk solution, as detailed in Section 4.4. The scale bar in the bottom-left corresponds to a distance of 200 μm. Fluorescence is excited in the Alexa Fluor 488 modification on the DNA constructs attached to the substrate. The GUV constructs are modified with a quencher, causing local fluorescence quenching within the vesicle contact regions that results in dark rings or circles.

4.5.1 Fit results from the reaction-diffusion model

Data were analysed from two separate samples under the experimental conditions discussed above, collating bridge-burning patterns from 83 GUVs. Distributions of the fitted model parameters are displayed in Figure 4.11. The typical radii of the analysed vesicle contact regions are noticeably higher than the typical radius of experimental vesicles imaged in Chapter 3. However, this is primarily due to selection bias; the bridge-burning patterns of larger vesicles were chosen for analysis as larger patterns are more visible and offer more pixels to average over when calculating radial intensity, resulting in more accurate intensity maps. Furthermore, it takes longer for the bridge-burning front to propagate to the centre of the contact region for larger vesicles, thus offering more time points over which to fit the model to experimental data.

The quenching ratio θ was fitted to values ranging between 0.28–0.50, with a mean value of 0.40. This is noticeably higher than the value obtained in Section 4.3.2 when modelling the kinetics of the burnt-bridges mechanism in bulk solution, where θ was fitted to 0.221 in the global fit (see Figure 4.7). A potential reason for this discrepancy could be inaccuracy in the background subtraction of fluorescence signals in either the experiments in bulk or the vesicle experiments. An alternative possibility is that the bridge-burning within the vesicle contact regions was incomplete, such that the fluorescence intensity in the contact region had yet to reach its final quenched value; however, if this were the case, one would expect to see the fluorescence in the "burned" regions of the substrate continue to gradually decrease over time, which was not observed. Further discrepancies in θ could also be caused by off-plane fluorescence contributions in the vesicle experiment (such as excess substrate constructs in bulk solution); crowding effects due to the denser environments in the vesicle system that cause strands to interact with each other and take different conformations; interactions of the quencher with the lipids (as quenchers are quite hydrophobic); or differences in the polymer properties of DNA due to the higher salt concentration, resulting in a different fluorophore-quencher distance.

A further plausible explanation is that at such a high concentration of $MgCl_2$, the intermediate structure SGF formed by the binding of F to SG is sufficiently stable that G remains partially bound to S; the increased proximity of the quencher on F to the fluorophore on S would result in some quenching of the fluorescence signal, but the quencher would not be as close to the fluorophore if G is still partially bound. The difference in magnesium concentration compared to the experiments in bulk solution in Section 4.3.2 could explain why G behaves as a catalyst (*i.e.* fully unbinds from SG) in the bulk experiments, but potentially remains partially bound in the experiments in this section. Incomplete displacement of G from SG would explain why the vesicles are not observed to move under these experimental conditions. If G remains bound in SG bridges rather than being displaced by F, a small excess of unbound S would remain. If we approximate the vesicles as hemispheres with total surface area $3\pi R^2$, and assume that all G constructs on the vesicle membrane bind to S constructs on the substrate, this corresponds to a density of G of $3\rho_G \approx 0.024\,\mathrm{nm}^{-2}$ (as the G constructs become concentrated within the contact region with area πR^2). Remembering that the density of S on the substrate is $\rho_S \approx 0.03\,\mathrm{nm}^{-2}$, this corresponds to an excess of $\approx 0.006\,\mathrm{nm}^{-2}$ of unbound S within the

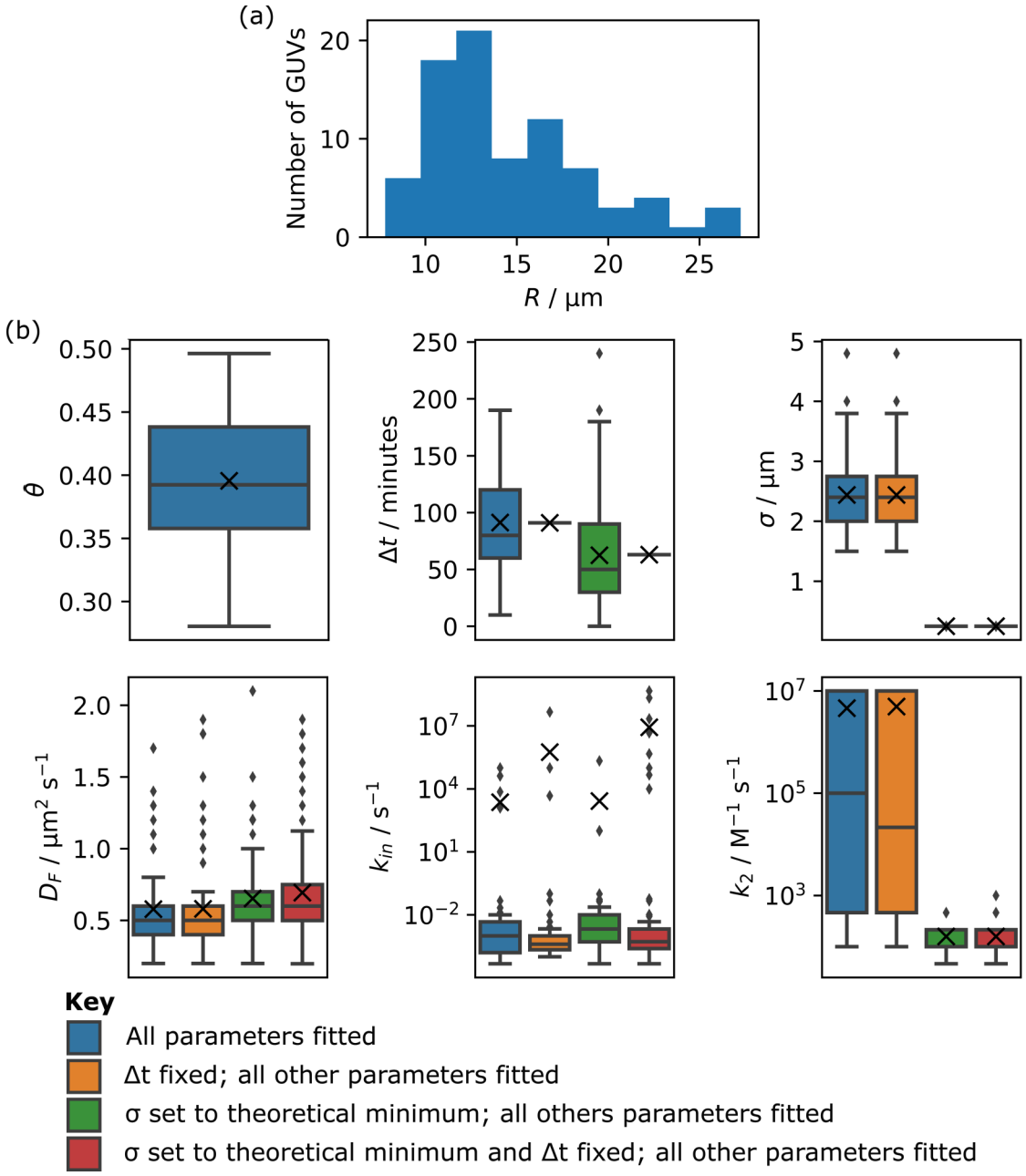


Figure 4.11: **Distributions of parameters fitted to experimental bridge-burning pattern data.** The plots in this figure show the distributions of parameters fitted to bridge-burning image data, as described in Section 4.2.2. (a) shows a histogram of the radius R of bridge-burning patterns. (b) shows box plots of the quenching ratio θ; time delay Δt between the start of reactions and start of image acquisition; width σ of the Gaussian point spread function applied to simulated patterns to model finite image resolution; diffusion coefficient D_F of the fuel strand in the contact region; rate k_{in} describing the exchange of the fuel strand between the contact region and the bulk; and rate constant k_2 (see Equation 4.1). The means of the distributions are marked by a cross. The parameters were initially all fitted (indicated in blue); Δt was then fixed at the mean value from the previous fit, before repeating the fit of all other parameters (indicated in orange). In the third version of the fitting process (indicated in green), all parameters were fitted except for σ, which was set to the theoretical minimum defined by the diffraction limit, *i.e.* $\sigma = 0.249\,\mu$m, as calculated from Equation 4.16. In the fourth version (indicated in red), σ was again set to the theoretical minimum, and ΔT was set to the mean value of ΔT from the previous fit; all other parameters were then fitted.

contact region, *i.e.* approximately 20% of the total density of substrate constructs. If no G constructs are available to bind to this excess of S, F would not be able to bind to these S constructs, so their fluorescence would remain unchanged. The total fluorescence (normalised by the maximum signal) in the "burned" region (with 20% of S "unburned") would then be $I_{exp} = 0.2 \times 1 + 0.8 \times \theta$. As the fluorescence was observed to drop to 40% of initial value (based on the fit result for θ), this implies the true quenching ratio is $\theta = (0.4 - 0.2)/0.8 = 0.25$. This is in much closer agreement with the fitted value of θ from the experiments in bulk, thus supporting the hypothesis that G does not fully unbind from SG when the concentration of $MgCl_2$ is so high. Nevertheless, even if this were the case, this would have negligible effect on the fitting of the other experimental parameters, as the model is largely insensitive to the rate constants k_1 and k_2; instead, the propagation rate of the bridge-burning front is limited by D_F and k_{in}. This behaviour would however be undesirable for the vesicle motility system, as the GUV-substrate bridges would remain permanently bound; the magnesium concentration would need to be lowered to enable complete bridge dissociation, such as to a similar concentration as in the bulk experiments in Section 4.3.2 (4 mM $MgCl_2$) where it was verified that the GUV constructs were being fully displaced from the SG complexes.

The width σ of the Gaussian PSF applied to simulated patterns to emulate finite image resolution was fitted to values on the order of microns, with a mean value of 2.4 μm. This is an order of magnitude higher than the theoretical minimum set by the diffraction limit ($\sigma = 0.249\,\mu$m, as calculated by Equation 4.16). However, it is not a surprise that the fitted value of σ is greater than this theoretical minimum, as one would expect additional blurring of the experimental radially-averaged intensity profiles due to inaccuracies in locating the centre of the contact region, and non-circularity of the contact region. Furthermore, the image resolution (0.64 μm per pixel) and relatively low signal-to-noise ratio at these DNA densities also limit the resolution of the extracted intensity maps.

The diffusion coefficient D_F of fuel strands in the contact region was fitted to values on the order of $10^{-1}\,\mu m^2 s^{-1}$, with a median of $0.5\,\mu m^2 s^{-1}$. These values are comparable to the diffusion coefficient of DNA constructs in Ref. [315], where the diffusion coefficients were measured to be on the order of 10^{-1}–$10^{0}\,\mu m^2 s^{-1}$. It makes sense that D_F is on the smaller end of this scale, as the fuel strand is larger than the constructs in Ref. [315], thus resulting in slower diffusion. Further discrepancies in the diffusion rates between these systems would arise from differences in the environment through which the strands are diffusing. In the experimental system presented in this chapter, the fuel strands are diffusing through a dense DNA brush within the GUV adhesion patch, while in Ref. [315] the DNA strands are diffusing through a 3-dimensional DNA condensate. Note that the distribution of D_F noticeably has a heavy positive tail, corresponding to a few cases where the bridge-burning front propagated at a significantly higher rate than usual; this behaviour was also observed by eye, such that the outliers cannot be explained by fitting errors. The increase in propagation of the bridge-burning front could potentially correspond to cases in which the density of substrate constructs is lower (which could be caused by non-uniformity in the coverage) or the density of GUV constructs is higher

(due to random attachment of G constructs to vesicle membranes during the functionalisation process).

The fit results for the rate k_{in} of fuel strand exchange between the contact region and the bulk span a wide range of magnitudes, although the majority were fitted to be on the order of $10^{-3}\,\mathrm{s}^{-1}$. This is again comparable to the material exchange rates in Ref. [315] which were found to be on the order of 10^{-4}–$10^{-3}\,\mathrm{s}^{-1}$. Although the experimental setup is different between the vesicle system presented here and the DNA condensate system in Ref. [315], it is plausible that as the diffusion coefficients are comparable across these systems, the material exchange rates could also be comparable. Furthermore, the heat map in Figure 4.12a shows that the fitting outcome for k_{in} is correlated with the fitting outcome for D_F. This is expected, as both affect the rate at which the bridge-burning front propagates inwards through the vesicle contact region.

The fit results for the rate constant k_2 (which defines the rate at which F displaces G from SG) also span a wide range of magnitudes, from 10^2–$10^7\,\mathrm{M}^{-1}\,\mathrm{s}^{-1}$. This is as expected, as the accuracy of the fitted value of k_2 is limited by the image resolution; the fit result for k_2 is also sensitive to the fit result for σ, as both contribute to the blurriness of the propagating bridge-burning front. Lower values of k_2 correspond to increased blurring, which places a lower limit on the fit results for k_2 (below which the simulated patterns would become even more blurred than the experimental patterns); this limit is evident in Figure 4.12d. This means that the order of magnitude of k_2 must be at least $10^2\,\mathrm{M}^{-1}\,\mathrm{s}^{-1}$ under these experimental conditions. This lower limit is comparable with the estimate of k_2 obtained by fitting the kinetics in bulk solution in Section 4.3, where k_2 was estimated as $9.35\times10^2\,\mathrm{M}^{-1}\,\mathrm{s}^{-1}$. However, it must be noted that the magnesium concentration was much lower in the bulk experiments, which would correspond to a decrease in the toehold displacement rate and thus k_2 [323, 324, 325]. Further discrepancies between the value obtained for k_2 in this section compared with the value obtained from the bulk fluorescence experiments could arise from the effect of anchoring the constructs, which constrains their configurations relative to when dissolved in bulk solution. This would be expected to decrease the reaction rates, an effect which was discussed when introducing the correction factor α in Chapter 3. Finally, the heat map in Figure 4.12(b) shows that there is negligible correlation between the fitting outcomes of k_2 and D_F, as expected; these affect different aspects of the radial intensity map, as discussed in Section 4.2.2.

Model fit results when setting Δt to the mean fitted time delay

When including the time delay Δt (between the start of the reactions and the start of image acquisition) as a parameter to fit to each individual pattern, the fitted values of Δt span 10–190 minutes, with a mean of 91 minutes. As can be seen in Figure 4.12c, the fit result for the time delay is sensitive to the fitting outcome for D_F, as both affect the position of the propagating bridge-burning front in the radial intensity map.

As the experimental samples (from which the pattern data were extracted) were set up and recorded at the same time, the time delay should be approximately equal for all vesicles.

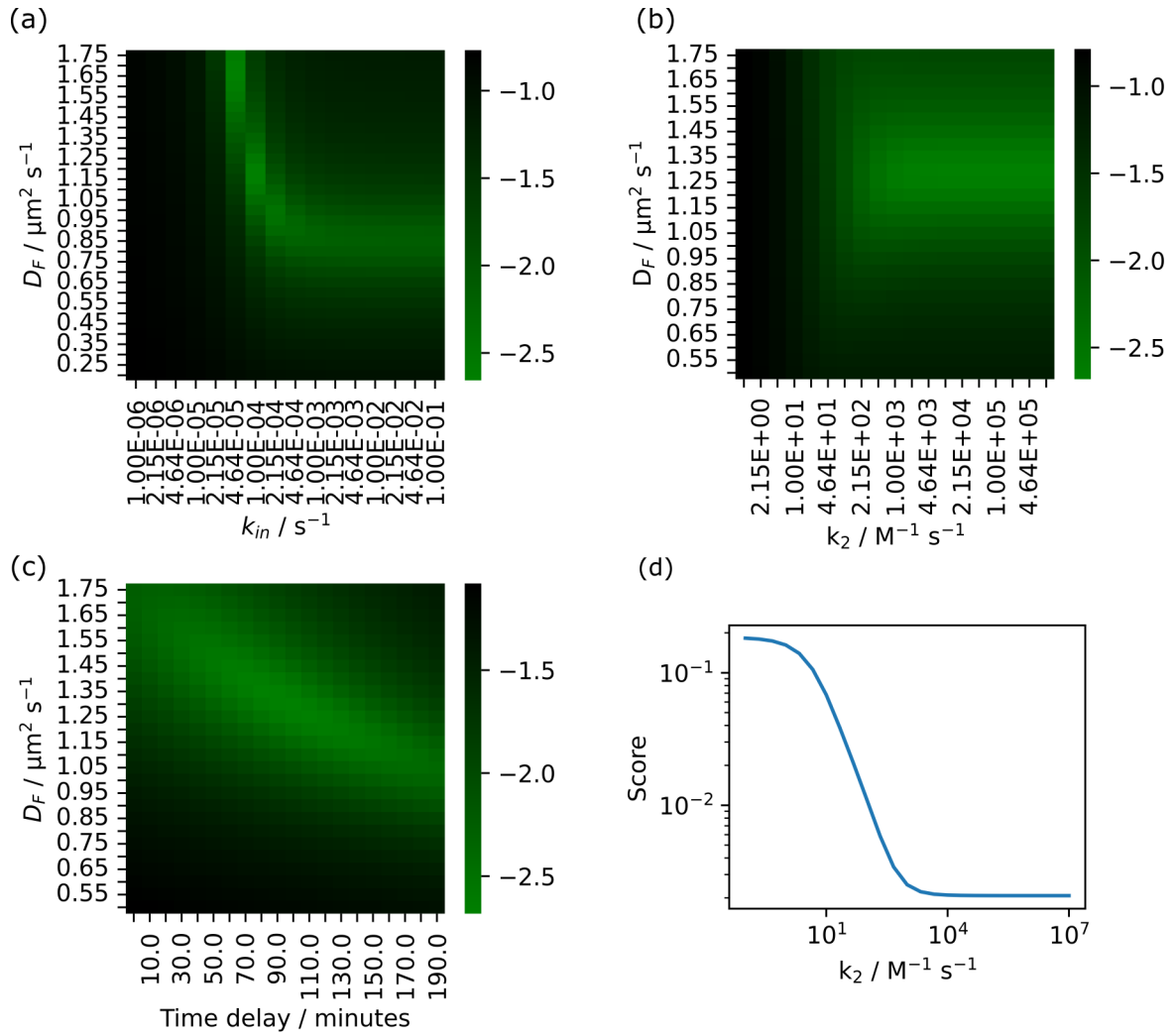


Figure 4.12: **Plots of the mean squared residuals reveal the precision and correlations of the reaction-diffusion model.** The plots illustrate the score of the reaction diffusion model fit, calculated as the mean squared residual (see Equation 4.18), when varying fitting parameters. The residuals plotted here correspond to the burnt-bridges pattern fitted in Figure 4.3. In (a), (b) and (c), the heat maps show how the score changes as pairs of fitting parameters are varied; the colour bar indicates the base-10 logarithm of the score. In (d), the line plot shows how the score changes as k_2 is varied. All other fixed parameters are set to their fitted values.

Therefore, the entire fitting process was repeated as before, but with the time delay fixed at 91 minutes. The fit results remained largely unchanged (see Figure 4.11), except for k_{in}; this is expected, as both Δt and k_{in} are fitted to the position of the propagating front in the intensity maps. The median fitted value for k_{in} is now on the order of $10^{-4}\,\mathrm{s}^{-1}$, which is still consistent with the material exchange rates observed in Ref. [315].

Model fit results when setting σ to the theoretical minimum

The fitting process was also repeated with σ set to the theoretical minimum defined by the diffraction limit (*i.e.* $\sigma = 0.249\,\mu$m, as calculated by Equation 4.16), while fitting all other variables; results from this fit are also displayed in Figure 4.11. The most noticeable impact is on k_2, for which the majority of fitted values are now on the order of $10^2\,\mathrm{M}^{-1}\,\mathrm{s}^{-1}$. Although this is consistent with the value for k_2 fitted to the experiments in bulk, it is likely that k_2 is underestimated when σ is set to its theoretical minimum, as k_2 is then decreased to account for the blurriness of the image. The distribution of fit results for Δt has also shifted to lower values, which is most likely to adjust the position of the propagating front in the intensity map to reduce the gap between the front and the perimeter of the region; the mean value of Δt is 63 minutes. Meanwhile, the distributions of D_F and k_{in} have shifted to higher values; an underestimate of Δt corresponds to an overestimate of D_F and k_{in}, as all three parameters are fitted to the position of the propagating front in the intensity map.

As a final version of the fitting process, σ was kept at its theoretical minimum, while Δt was set to 63 minutes (the mean from the previous fitting process). The results are shown in Figure 4.11 and are similar to the results when only fixing σ, except for a decrease in the typical magnitude of k_{in}.

4.6 Vesicle motility experiments

In this section, I present experimental results from vesicle motility experiments with the burnt-bridges mechanism, as depicted in Figure 4.1. Vesicles were functionalised with the GUV constructs (G) and applied to substrates functionalised with the substrate constructs (S); the fuel constructs (F) were then applied in bulk solution. Further details on the experimental method can be found in Chapter 2. As the methods used to functionalise the vesicles and substrates are the same as the methods used in Chapter 3, the resulting DNA densities should remain the same, *i.e.* the density of G is $\rho_G \approx 0.008\,\mathrm{nm}^{-2}$, and the density of S in the maximum density region of the substrate is $\rho_S \approx 0.03\,\mathrm{nm}^{-2}$. Vesicles are tracked within the DNA density gradient region on the substrate, to maintain consistency with the vesicle motility experiments presented in Chapter 3; as the same method of surface density gradient generation was employed, the gradient profile remains similar to the example profile depicted in Figure 3.5b. Across all vesicle motility experiments, the bulk solution contains 30 mM NaCl, 15 mM KCl and 1×TE, while the concentration of F and $MgCl_2$ in bulk solution varies between experiments. The bulk solution also contains glucose, with concentration chosen to maintain iso-osmolarity with the interior solution of the vesicles.

The vesicles were produced *via* electroformation, as was done for vesicle experiments in Chapter 3; this results in samples with polydisperse size distributions. Frequency density histograms of the vesicles analysed in Sections 4.6.1 and 4.6.2 are displayed in Figure 4.13. As can be seen, the vesicle size distributions are similar to the distributions observed for vesicles in Chapter 3 (see Figure 3.3b). The distributions vary slightly little between the different

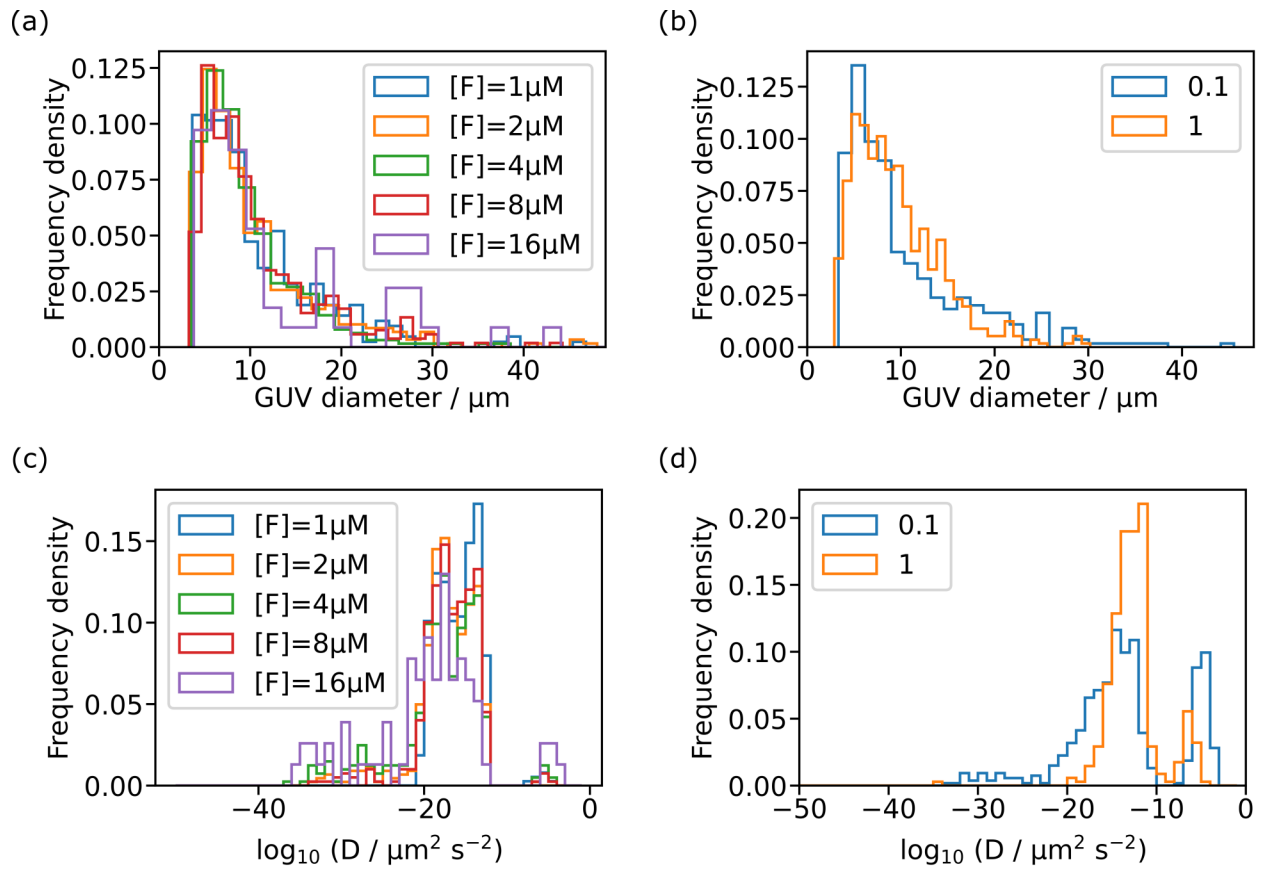


Figure 4.13: **Distributions of GUV diameter and estimated diffusion coefficient for vesicles studied in the burnt-bridges motility experiments.** The frequency density histograms display the distributions of GUV diameter and estimated diffusion coefficient of vesicles analysed in Section 4.6. Note that the diffusion coefficients have been estimated *via* MSD analysis, as outlined in Section 2.6.4. In (a) and (c), data are shown for vesicles in experiments discussed in Section 4.6.1, where the fuel concentration $[F]$ was varied up to 16 μM. In (b) and (d), data are shown for vesicles in experiments discussed in Section 4.6.2, where the relative density of reactive S constructs on the substrate is set to either 0.1 or 1.

experimental conditions, but this can be explained due to typical sample-to-sample variation. Again, the majority of analysed vesicles have diameters of approximately 10 μm, although the measured diameters are observed to reach over 40 μm.

MSD analysis was applied to the vesicle trajectory data to obtain estimates of the diffusion coefficient of each vesicle, as was done in Chapter 3; the method for conducting the MSD analysis is outlined in Section 2.6.4. Distributions of the estimated diffusion coefficients for vesicles analysed in Sections 4.6.1 and 4.6.2 are shown in Figure 4.13. Note that the distributions of estimated diffusion coefficients look different to the distributions observed for the passive system (see Figure 3.6). For the passive system, the vast majority of vesicles were estimated to have diffusion coefficients greater than $10^{-8}\,\mu\text{m}^2\,\text{s}^{-1}$, while a small minority of vesicles were estimated to have diffusion coefficients below this value; this small proportion of vesicles was deemed to be an immobile population of vesicles, after inspecting the MSD plots, vesicle trajectories and image data. On the other hand, the distributions in Figure 4.13 indicate that the majority of diffusion coefficient estimates range between 10^{-20}–$10^{-10}\,\mu\text{m}^2\,\text{s}^{-1}$, with a small minority resting

below this range. It must first be noted that the method of estimating the diffusion coefficients (*i.e.* applying a linear fit to the MSD plot) may be less applicable to vesicle trajectories in the active system presented here, as one would expect a greater drift component (either due to preferential drift along the gradient of S, or due to convection flows) which would give a quadratic dependence of the MSD on the time delay. The linear fit here is thus only applied to gauge which vesicles may be immobile in the experimental samples. Inspection of the MSD plots, vesicle trajectories and image data show that the small proportion of vesicles corresponding to estimated diffusion coefficients of $\approx 10^{-20}\,\mu\mathrm{m}^2\,\mathrm{s}^{-1}$ or lower appear to be immobile; this value is thus used as the cut-off value for filtering out the immobile vesicle population in subsequent data analysis. This cut-off value is significantly lower than the value used to filter the immobile vesicle population in Chapter 3; however, this could be due to the difference in number of data points in the plot of MSD against time delay, as vesicles were recorded over longer durations for the work in this chapter. As there are more data points to fit the diffusion coefficient to, this could affect the error tolerance or precision of the fitting algorithm, resulting in the diffusion coefficients of immobile vesicles being fitted to smaller values.

For the rest of this chapter, I discuss my findings regarding the mobility of vesicles in the burnt-bridges adaptation of the vesicle motility system. I first focus on the general mobility of vesicles (rather than the drift velocity along the gradient), and presenting the effect of varying the fuel strand concentration and the density of substrate constructs on the vesicle mobility, in Sections 4.6.1 and 4.6.2, respectively. Finally, I discuss if the improved mobility of vesicles in the burnt-bridges system can be translated to a boosted haptotactic drift velocity along surface density gradients of DNA constructs.

4.6.1 Effect of varying fuel concentration on vesicle mobility

To investigate the effect of varying the concentration of the fuel strand F on the vesicle mobility, experiments with fuel concentration varied from 0–16 μM were conducted, with a bulk $MgCl_2$ concentration of 4 mM. The concentration of $MgCl_2$ was chosen to match the concentration employed for experiments in Ref. [241], as well as the experiments in bulk solution in Section 4.3.2, where it was verified that the GUV construct G is fully displaced from substrate-GUV (SG) bridges during the bridge-burning process. For each fuel concentration, two repeats of the experiment were carried out. The vesicles were imaged over 19 hours (at 30 minute intervals) and tracked *via* the methods outlined in Chapter 2.

Distributions of the absolute vesicle displacement for each fuel concentration are displayed in Figure 4.14. When no fuel strand is present (*i.e.* a fuel concentration of 0 μM), the vesicles appear to be immobile in time lapse recordings; indeed, the data in Figure 4.14 show that the majority of vesicles are observed to travel less than a micron, which is in the remit of experimental noise and tracking error. For fuel concentrations of 1–8 μM, although the mean and median absolute displacements remain limited (less than a micron), the distributions noticeably have heavy positive tails with displacements surpassing a micron. Furthermore, as the

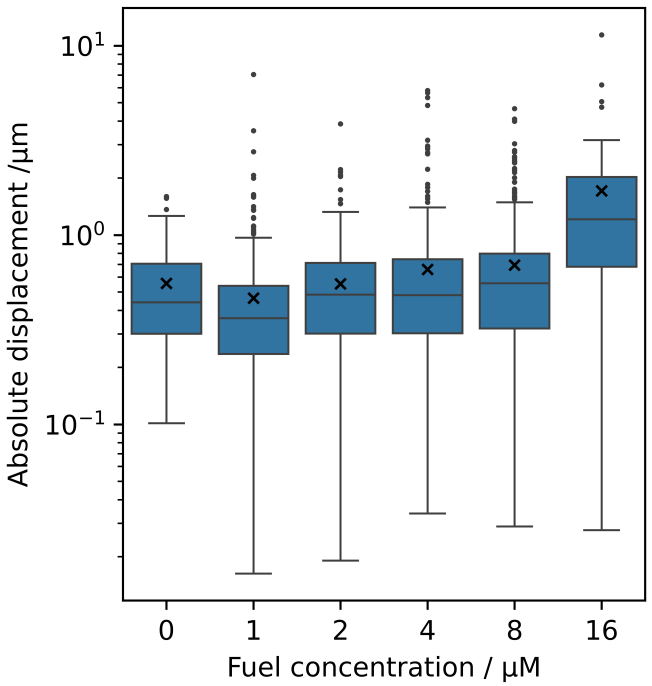


Figure 4.14: **Increased fuel concentration in the burnt-bridges system results in increased vesicle mobility.** Distributions of absolute vesicle displacement (over 19 hours) are plotted, for experiments with varied concentration of the fuel strand F. The mean absolute displacement is marked with a cross, and outliers are shown. Note that the data have been filtered to the mobile vesicle population as discussed in Section 4.6; box plots with all data (including the immobile population) are shown in Figure C.11.

fuel concentration increases, the number of vesicles that travel distances greater than a micron increases, indicating an increase in vesicle mobility; this is reflected in the gradual increase in mean absolute displacement. For the highest fuel concentration (16 μM), the majority of vesicles are observed to travel distances on the order of microns, a noticeable increase in mobility compared with the lower fuel concentration systems.

These findings verify that the mobility of vesicles in the active adaptation of the motility system depend on the bridge-burning mechanism; an increase in fuel concentration would lead to an increased rate of displacement of the GUV construct G from substrate-GUV (SG) bridges, and thus an increased rate of bridge-burning. Therefore, the rate of vesicle motion no longer depends on the rate of spontaneous unbinding of SG bridges, but instead depends on the strand displacement rates of the bridge-burning mechanism. One would expect this increase in bridge-burning rate and vesicle mobility to plateau above a certain fuel concentration, corresponding to saturation of toeholds on SG bridges such that the bridge-burning rate is no longer limited by the fuel concentration.

It must be noted that the total displacements observed in these experiments (again referring to Figure 4.14) are on the order of 10^{-1}–10^{0} μm, comparable with the displacements observed in the experimental system presented in Chapter 3. Although these displacements may sound limited, one must remember that the experimental DNA densities correspond to a bridge spacing on the order of 10 nm (as discussed in Section 3.4.1). Displacements of these magnitudes thus require the "burning" of a large number of bridges to allow the vesicle to move micron-scale

distances. Later sections in this chapter will discuss other experimental parameters that can be tuned to further increase vesicle mobility.

4.6.2 Effect of varying substrate DNA density on vesicle mobility

Similar to in Chapter 3, the effect of varying the surface density of substrate constructs was explored. To reduce the density, the reactive substrate constructs were mixed with inert versions of the constructs that lacked the reactive moiety, before being applied to the substrate. As an example, to reduce the density of substrate construct by a factor of 10, the substrate constructs were mixed with the inert constructs in a 1:9 ratio; the combined density of DNA constructs in the maximum density region of the substrate thus remains at $\rho_S \approx 0.03\,\mathrm{nm}^{-2}$, while the density of reactive substrate constructs (to which the GUV constructs can bind) is reduced to $\rho_S/10 \approx 0.003\,\mathrm{nm}^{-2}$.

Vesicle motility experiments were conducted with the density of reactive substrate constructs varied over several orders of magnitude: ρ_S, $\rho_S/10$, $\rho_S/100$, $\rho_S/1000$ and $\rho_S/10,000$. For these experiments, the concentration of $MgCl_2$ in bulk solution was set to 10 mM, while the concentration of fuel strand was set to 5 μM; each experiment was repeated twice. Data corresponding to reactive substrate construct densities of $\rho_S/10$ and ρ_S (each recorded over two repeats of the experiment) are shown in Figure 4.15, for vesicles recorded over 19 hours. The plots show that vesicles travel significantly longer distances when the density is reduced by a factor of 10, with absolute displacements on the order of microns. This indicates that as the density of reactive substrate constructs is decreased, the vesicle mobility increases. A decrease in density of substrate constructs corresponds to less bridges to "burn", such that the binding affinity of the substrate drops more quickly over time as fuel strands bind to the substrate constructs. Furthermore, considering the theoretical model presented in Chapter 3, an increase in spacing between substrate constructs corresponds to a greater shift of the vesicle position between successive updates of the set of constraining bridges.

It is promising that the burnt-bridges system appears to achieve significantly greater vesicle mobilities than the passive system presented in Chapter 3, where there was a sharper cut-off between immobility at higher S densities and lack of adhesion at low S densities. Here, we observe that simply decreasing the density of S by a factor of 10 appears to increase vesicle velocities by an order of magnitude, and the vesicles appear to remain attached to the substrate during their motion. It is likely that the stronger binding between S and G constructs (due to the longer complementary DNA sequences) is more robust to breakage due to shear forces from convection flows, which helps to keep the vesicles adhered at lower bridge densities.

However, when considering the trajectories of vesicles in systems where the density of substrate construct S has been reduced by a factor of 10 (see Figure 4.15), there is a noticeable bias in the average vesicle displacement in the direction of decreasing x. This is most likely due to the effects of small convection flows in the sample (similar to the convection flow-driven motion of vesicles in the sticky end length l = 3–4 nt systems in Chapter 3), which typically causes a uni-directional drift of vesicles across the well. One would however hope that this

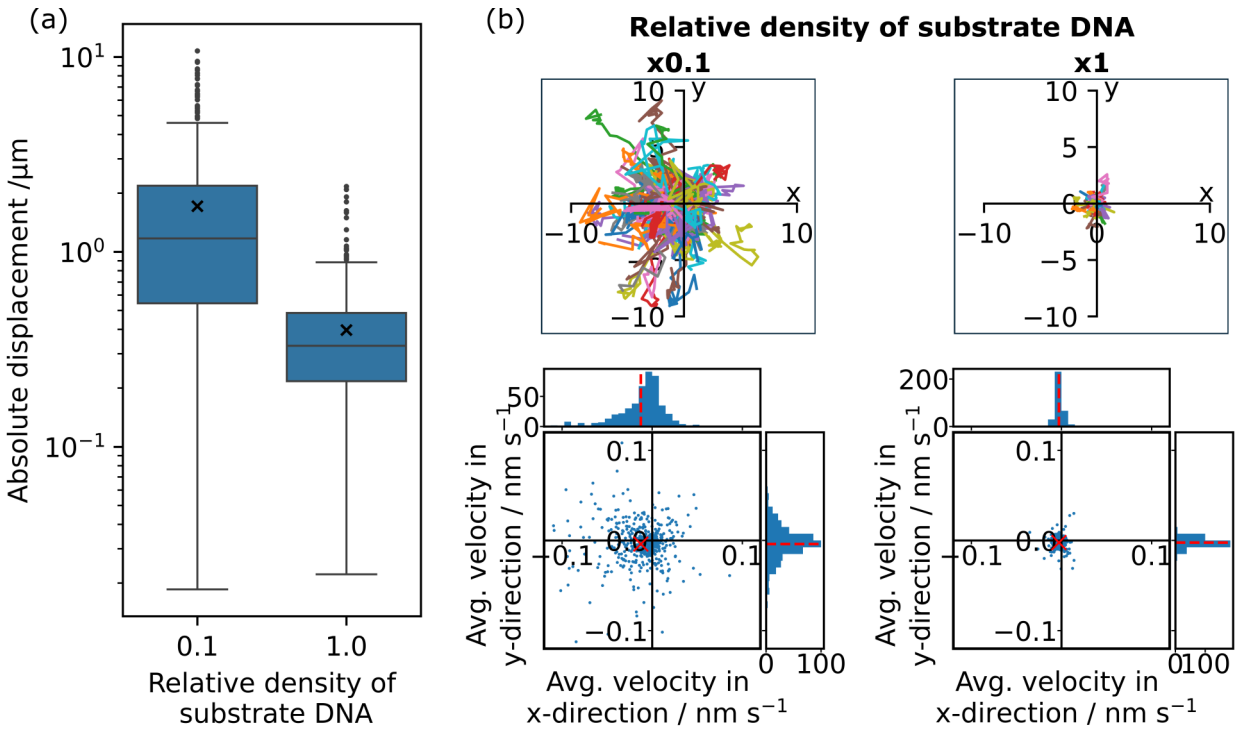


Figure 4.15: **Increased density of substrate DNA results in decreased vesicle mobility.** In (a), the distributions of absolute vesicle displacement over 19 hours are plotted, for experiments with varied surface density of substrate construct S; these experiments are discussed in Section 4.6.2. The mean absolute displacement is marked with a cross, and outliers are shown. In (b), the trajectories and distributions of average vesicle velocity corresponding to the data in (a) are plotted, where the data have been filtered to the mobile vesicle population. Here, the trajectories and distributions are plotted in the x- and y-directions; the trajectories are plotted in distance units of microns. The histograms show the number of vesicles in each velocity bin. The average velocity has been calculated by dividing the total displacement by the total duration of the trajectory. Note that the data have been filtered to the mobile vesicle population, as described in Section 4.6; plots with all data (including the immobile population) are shown in Figure C.12.

unidirectional drift would be averaged out when considering motion relative to the gradient direction (which changes direction around the perimeter of the circular region of the substrate coated with S); we see if this is the case in Section 4.6.3.

When the density of reactive substrate constructs is reduced by a factor of 100 or more, the adhesive force is no longer sufficient to keep all of the vesicles attached to the substrate under these experimental conditions. Instead, vesicles are observed to travel over the width of the well, most likely carried by small convection flows in the sample. Smaller vesicles appear to be more readily detached from the substrate by convection flows. For example, when the density of reactive substrate constructs is reduced by a factor of 100, convection-driven motion is only observed in vesicles with diameters on the order of a few microns. When the density is reduced by a factor of 1000, convection-driven motion is also seen in vesicles with diameters up to approximately 10 μm. When the density is reduced by a factor of 10,000, only the largest vesicles (with diameters greater than 20 μm) appear to remain attached to the substrate throughout the time lapse recordings. The observation that larger vesicles are more resistant

to being detached from the substrate by shear flow can be explained by the fact that larger vesicles are attached to the substrate by a larger number of SG bridges, as the number of bridges n_b scales as R^2, where R is the radius of the vesicle. The overall multivalent adhesion strength is thus stronger, which enables the vesicle to withstand shear forces from convection flows. This makes sense if the shear force on the vesicle from the convection flow scales with the vesicle radius at a slower rate than R^2. Considering the hydrodynamic force of a shear flow on a spherical particle, one can assume the system is described by a low Reynolds number if the convection flow rate is sufficiently slow. The shear force is then given by Stokes' law [326]: $F_d = 6\pi\mu R\nu$, where F_d is the Stokes' drag force, μ is the dynamic viscosity of the fluid, R is the radius of the particle, and ν is the velocity of the flow relative to the particle. The drag force thus increases with vesicle radius at a slower rate than the multivalent adhesion strength, which enables larger vesicles to remain attached to the substrate at lower bridge densities while smaller vesicles are carried away by flows.

Finally, an alternative approach to increasing the vesicle mobility would be to increase the density of G constructs on the vesicle membranes. As observed in Section 4.3.2, as the concentration of G increases towards the concentration of S, the rate of bridge-burning increases. However, once G is in excess of S, there is no significant impact on the bridge-burning rate of further increasing the concentration of G. Considering the vesicle motility systems investigated in this section, the density of G constructs is already comparable to the density of S on the substrate, such that binding sites on the substrate are near saturation. Therefore, one would not expect a significant improvement in vesicle mobility upon increase in density of G, as the bridge-burning rate is already at the boundary where it is no longer limited by the density of G.

4.6.3 Vesicle motion relative to the gradient direction

So far, the effect of fuel concentration and density of S constructs on the general mobility of vesicles has been explored, regardless of the direction of travel. In this section, we consider the direction of the motion relative to the gradient, to see if the vesicles still exhibit the bias in motion towards regions on the substrate with higher DNA density that was observed in the passive system in Chapter 3. Vesicle mobility was observed to be at its maximum (while allowing vesicles to remain adhered) in the system presented in Section 4.6.2, in which the surface density of S constructs was reduced by a factor of 10. From here on, we consider this most mobile vesicle system in the context of motion relative to the gradient.

In Figure 4.16, the trajectories and distributions of average velocities of vesicles relative to the gradient direction are plotted. Unlike observations made in the less mobile, passive motility system presented in Chapter 3, there is a lack of preferential drift along the gradient towards higher DNA densities on the substrate. A likely reason for this is due to the balance between the signal (*i.e.* the directional drift of vesicles along the DNA surface density gradient) and the noise (*i.e.* stochastic motion and effects of flow). It was noted in Section 4.6.2 that the effects of convection flows on the vesicle motion become more prevalent in the more mobile system; it

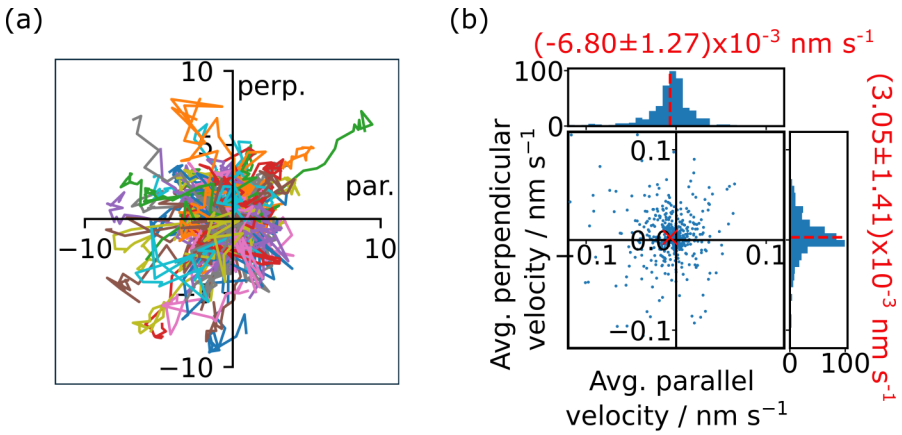


Figure 4.16: **Convection effects appear to overcome directional drift along the gradient in the more mobile burnt-bridges vesicle motility system.** In (a), the trajectories of vesicles from experiments where the density of S constructs was reduced by a factor of 10 are plotted, with distance units of microns in the directions parallel and perpendicular to the gradient; the vesicles were tracked over 19.5 hours. The experimental conditions are detailed in Section 4.6.2. In (b), the distributions of average vesicle velocities parallel and perpendicular to the gradient are plotted; the histograms show the number of GUVs per velocity bin. The average velocity has been calculated as total displacement over the trajectory, divided by the trajectory duration. The mean of the distributions are marked and annotated in red. Note that the data have been filtered to the mobile vesicle population, and the axes in (b) have been cropped to exclude outliers and aid visualisation of the mean of the distributions; full data are shown in Figure C.13.

is likely that these effects overwhelm the effects of drift due to the gradient in binding affinity, which is why a directional drift along the gradient is not observed. However, in the passive (and less mobile) system presented in Chapter 3, the lack of an active mechanism to induce vesicle motion allows the vesicles to resist the effects of convection flows and gradually diffuse over the substrate.

Further evidence that the effect of convection flows is more significant is that the motion perpendicular to the gradient no longer averages to zero, as can be seen in Figure 4.16b. For systems that are less affected by convection flows (such as the passive experimental system with higher bridge densities, considered in Chapter 3), averaging the vesicle velocities relative to the gradient over vesicles located around the circular gradient region is sufficient to remove the effects of unidirectional flow across the well. However, it appears that the effect of the flow on the vesicles in this system is large enough that it is no longer cancelled out.

Overall, although the active, burnt-bridges adaptation of the vesicle motility system presented in this chapter does improve the mobility of adherent vesicles, this unfortunately does not translate to an increased rate of haptotactic drift, due to the impact of unavoidable flows in the samples. Nevertheless, the results from these experiments show great potential for future adaptations of this system in which flows are further minimised; for example, by conducting the experiments in sealed microfluidic chambers.

4.7 Chapter summary and outlook

In summary, the passive vesicle motility system from Chapter 3 was updated to incorporate a burnt-bridges mechanism. This update was implemented with the aim of improving vesicle mobility, as a limitation noted in Chapter 3 was that the vesicles appeared to be fixed in place when the adhesion strength was sufficient to keep the vesicles attached to the substrate. As in Chapter 3, the system consists of GUVs functionalised with DNA constructs (referred to as G) adhered to a substrate coated with complementary DNA constructs (referred to as S) through the binding of numerous SG bridges. Here, a third DNA component (the fuel strand, F) is added in the bulk solution. This fuel strand binds to SG bridges, displacing G *via* toehold-mediated strand displacement, and preventing G from rebinding to the "burned" S construct.

This burnt-bridges mechanism was adapted from designs for the bipedal DNA walker presented in Ref. [241], for application to the multivalent vesicle motility system. To check the adapted constructs, experiments were initially conducted in bulk solution, verifying that G behaves as a catalyst for the binding of S and F, and that F displaces G from SG bridges, as expected. The kinetics of the DNA reactions in bulk solution were fitted to the experimental data, to obtain estimates of key experimental parameters. The rate constant k_1 for the binding of S and G was fitted to $4.33 \times 10^3\,\mathrm{M^{-1}\,s^{-1}}$, while the rate constant k_2 for the binding of F to SG (and simultaneous displacement of G) was fitted to $9.35 \times 10^3\,\mathrm{M^{-1}\,s^{-1}}$. Both of these reactions involve toehold-mediated strand displacement, a process whose rate constant can range between 10^1–$10^6\,\mathrm{M^{-1}\,s^{-1}}$ [193], which agrees with the fit results. Finally, the quenching ratio θ for the quenching of the fluorophore attached to S upon binding of the quencher-modified F strand was fitted to 0.221.

After verifying the mechanism in bulk solution, I then progressed to implementing the burnt-bridges adaptation of the vesicle motility system. A substrate patterning effect was observed in systems with high DNA density and high magnesium concentration, in which the bridge-burning can be seen to propagate inwards from the perimeter of the vesicle contact region as the fuel strands diffuse under the vesicle and bind to S. A reaction-diffusion model was designed and fitted to the experimental bridge-burning patterns, similar to the model employed in Ref. [315] in which a 3D reaction-diffusion system was implemented. In particular, the diffusion coefficient D_F of the fuel strand in the contact region was fitted with a median value of $0.5\,\mu\mathrm{m^2 s^{-1}}$, while the fuel strand exchange rate k_{in} between the contact region and the bulk was fitted to be on the order of 10^{-4}–$10^{-3}\,\mathrm{s^{-1}}$; these values are comparable with results from Ref. [315]. Furthermore, although the fit result for k_2 could only offer a lower bound of $10^2\,\mathrm{M^{-1}\,s^{-1}}$ on the actual value due to the limited image resolution, this is still consistent with the fit result from the experiments in bulk. Finally, the quenching ratio θ was fitted to a mean value of 0.40, which is significantly higher than the value obtained from the fitting of experiments in bulk. This, along with the immobility of vesicles under these experimental conditions, suggests that at such high magnesium concentrations, the SGF complex (consisting

of S, G and F bound together) is sufficiently stable such that G is not fully displaced from the SG bridge. This is an important insight for the following vesicle motility experiments, as the mobility of vesicles depends on the full displacement of G from SG bridges; I thus focused on systems with lower magnesium concentrations for the subsequent vesicle motility experiments.

When studying the motion of vesicles in the burnt-bridges system, it was observed that when increasing the concentration of fuel in bulk solution, this resulted in greater vesicle mobility. This is as expected; an increase in fuel supply would result in an increased rate of bridge-burning, which allows GUV-substrate bridges to unbind such that the vesicle can move. Furthermore, it was observed that increasing the surface density of DNA constructs on the substrate resulted in increased vesicle mobility. This effect was also observed in the passive system in Chapter 3, although in the burnt-bridges system, the stronger binding between GUV constructs and substrate constructs enables the vesicles to remain adhered at lower bridge densities and resist detachment due to shear forces from small convection flows in the sample. Finally, motion relative to the gradient direction is investigated; here, there no longer appears to be a directional drift of vesicles along the gradient. However, it is likely that due to the increased mobility of the system, the effects of convection flows play a bigger role, and overwhelm any subtle directional drift that may be present. In future implementations of vesicle motility systems, it would thus be important to address the effects of convection flows in the sample, perhaps by conducting the experiments in a microfluidic system with smaller sample volumes.

Overall, the results from the burnt-bridges system give an insight into the vast potential of an active motility system to improve on the limited mobility of passive systems, as well as allowing further control over the extent of vesicle mobility. Although the burnt-bridges mechanism perhaps strays further from the biological context of motility and haptotaxis of adherent cells (compared with the passive system), the experimental findings could again provide helpful insights for the design of future biomimetic systems for application in synthetic biology, biosensing, therapeutics, and more. Ideas for future investigations and adaptations of active biomimetic motility systems are discussed in Section 5.2.

Chapter 5

Conclusions and future research directions

In this chapter, I summarise the contents and key findings of this thesis, before discussing some potential avenues for future research on the topic of artificial cell motility in multivalent adhesion systems.

5.1 Summary

In this thesis, I present two systems in which vesicles are adhered to substrates *via* DNA-mediated multivalent binding interactions; dissociation of the DNA bridges between the vesicle and the substrate enables the vesicle to gradually move over the substrate. I investigate this motion and the key parameters that effect the mobility of the vesicles, in particular over substrates featuring a surface density gradient of DNA.

In **Chapter 3**, a *passive* vesicle motility system is presented, in which the adhesion is mediated by the binding of simple DNA sticky ends. These sticky ends are sufficiently short such that the binding is weak and reversible, and the GUV-substrate bridges repeatedly bind and unbind, enabling the vesicle to diffuse over the substrate. Experimental results are compared with coarse-grained simulations, both demonstrating that the vesicles diffuse with a directional bias towards regions of the substrate with higher DNA density. This drift velocity is also observed to increase with decreasing DNA binding strength, and with increased GUV size. A theoretical framework for the system is also presented, with an analytic prediction for the drift velocity; although this prediction does not appear to apply to systems with as high bridge density as in experiments, the experimental and simulation data still appear to be consistent with the theoretically predicted scaling relation between the drift velocity and the unbinding rate of complementary sticky ends.

In **Chapter 4**, an *active* vesicle motility system is presented, with the aim of improving on the limited vesicle mobility of the passive system. Here, "active" refers to the incorporation of a burnt-bridges DNA mechanism, where the vesicles catalyse bridge-burning within their contact regions on the substrate such that the vesicle cannot re-attach to the same binding sites. This

mechanism is first verified in bulk solution, and the DNA reaction kinetics are modelled to obtain estimates of the reaction rate constants. The focus then moves to the implementation of the burnt-bridges mechanism in the vesicle motility system. Here, it is possible to visualise the "burning" of vesicle contact regions, as well as the propagation of the bridge-burning front. A reaction-diffusion model is fitted to the experimental data, obtaining further estimates of key experimental parameters that agree with the results from the experiments in bulk and are also consistent with findings in literature. Finally, the effect of varying the fuel concentration and density of DNA on the substrate on the vesicle mobility is explored; it was observed that vesicle mobility increases with increasing fuel concentration and with decreasing substrate DNA density, as expected. The latter was observed to increase vesicle displacements by an order of magnitude, compared with the passive system presented in Chapter 3. This more mobile system was then investigated in terms of motion relative to the gradient; in this case, directional drift along the gradient was no longer observed, although it is likely that adverse effects from convection flows become more prevalent in higher mobility systems.

Overall, the findings from this thesis provide insights into the biophysics of multivalent adhesion and mobility of adherent cells. Results from the passive system uncovered a directional drift of vesicles towards regions of higher DNA density on the substrate, which constitutes a simple form of haptotaxis. Although the observed drift velocities in the passive system are negligible compared with the haptotaxis rates of living cells, the passive mechanism could perhaps be related to the re-orientation of living cells in the presence of gradients of binding sites. Furthermore, the findings from the burnt-bridges adaptation of the vesicle motility system give a taster of the vast potential of active vesicle motility systems; ideas for further investigations and adaptations of active motility systems are discussed in Section 5.2. Altogether, this research provides key design rules that could help with the future development of motile biomimetic systems, with the potential for application in synthetic biology, biosensing, therapeutics and much more.

5.2 Directions for future research

5.2.1 Further exploration of the vesicle motility systems

Adapting the experimental set-up to improve on current limitations

A key limitation of the vesicle motility systems presented in this thesis is the presence of convection flows in samples. These mean that only systems with high multivalent adhesion strength can be experimentally implemented, such that the vesicles are not carried away by spurious flows and prevented from remaining attached to the substrate. Unfortunately, in the current experimental set-up, it is impossible to completely eliminate convection flows, even with measures to reduce flows such as covering the well plates in adhesive foil to reduce evaporation of the samples. It would be highly beneficial to adapt the set-up in a way that further reduces

(or completely removes) unwanted flows. Flows could be minimised by conducting the experiments in sealed microfluidic devices with smaller sample volumes. This would allow for much more precise measurements of vesicle drift velocity and diffusion coefficients *via* mean squared displacement analysis. In addition, the ability to implement systems with lower multivalent adhesion strength should help to achieve increased vesicle mobility.

It would also be useful to set up the surface density gradient of DNA molecules in a way that allows for tuning of the gradient profile. This would enable investigation of the effect of gradient steepness on the vesicle drift velocity, to verify the trends observed in simulations in Chapter 3. Alternative methods to generate tuneable density gradients are discussed in Section 3.2.3; these include microfluidic methods in which gradients are generated either *via* diffusion, or by gradually flowing the adhesive molecules over the substrate. Furthermore, a technique such as optical tweezers could be used to place vesicles at precise positions along the gradients. This would improve comparison of trajectories of different vesicles compared to the current system, in which experimental vesicles are located at random points along the gradient profile.

Further experimental parameters to explore

It would be interesting to experiment with the system from Chapter 3 in the weakly binding regime, such as with shorter sticky ends or lower DNA densities. Experiments with lower DNA densities could enable quantitative comparisons with theory and simulations, which was not possible in the high-density systems experimented with in this PhD (as the theory presented in Section 3.3.3 did not appear to be applicable to systems with high bridge density, and simulation length scales had to be reduced to keep simulations affordable). In the weakly binding regime, predictions from theory (and extrapolation from trends in experimental and simulation results between binding strength and drift velocity) would indicate that the vesicles would diffuse at a greater rate, resulting in a greater drift velocity along the gradient. In addition, as mentioned before, it would be useful to vary the gradient profiles in experiments for comparison with the results from theory and simulations; an increase in gradient profile would also be expected to increase the vesicle drift velocity.

The effect of further experimental parameters on the vesicle motion could be investigated, such as the temperature and buffer conditions. Regarding the experimental system from Chapter 3, an increase in temperature would be expected to increase the unbinding rate of receptor-ligand bridges, thus increasing vesicle mobility in accordance with the observed trend between unbinding rate and vesicle drift velocity in Chapter 3. Regarding the buffer conditions, parameters such as the salt concentration, pH and viscosity could be explored. A decrease in salt concentration would correspond to decreased screening of the electrostatic repulsion between charged DNA molecules and thus decreased stability of receptor-ligand bridges; this could again help to increase vesicle mobility due to increased unbinding rate of bridges. Changing the pH could also affect the stability of receptor-ligand bridges, again impacting the mobility of vesicles. Increasing the viscosity of the external medium would increase the drag on the vesicle,

and thus also be expected to decrease the drift velocity.

It would also be interesting to explore further parameters relating to the vesicles themselves. For example, varying the lipid composition of the vesicle membranes could affect the flexibility of the membranes. Remembering that the vesicles deform when adhered to a substrate to form a flat adhesion patch, it would make sense that increased flexibility of the membrane would correspond to increased deformation (and a larger adhesion patch). Furthermore, vesicles could be made to be more deformable by introducing osmotic mismatches between the interior and exterior solutions of the vesicles. An increase in size of the adhesion patch could have a similar effect to increasing the size of vesicles (as discussed in Chapter 3), thus helping to increase vesicle drift velocity.

Finally, the burnt-bridges system presented in Chapter 4 could be extended by including a functionality to halt the burnt-bridges process and subsequently arrest vesicle motion. For example, an additional "stop" strand could be added in bulk solution that is fully complementary to the fuel strand; this could bind to excess fuel strands, such that there are no fuel strands left to displace the GUV strands from the substrate.

5.2.2 An enzymatic approach to the burnt-bridges system

An alternative approach to the burnt-bridges system presented in Chapter 4 would be to replace the toehold strand displacement mechanisms with enzymatic activity. For example, after a GUV-substrate bridge forms (due to the binding of complementary constructs anchored to the respective surfaces), enzymes in bulk solution recognise the bridge sequence, and subsequently nick or cleave it. The truncated substrate constructs would no longer be able to bind to GUV constructs, corresponding to "burning" of the region of the substrate that the GUV had initially adhered to.

This could be achieved with the use of *nicking enzymes*. These are enzymes that cut one strand of a dsDNA construct at a specific location corresponding to a nucleotide sequence, referred to as the restriction site [327, 328]. Furthermore, nicking enzymes are endonucleases, which are enzymes that hydrolyse the phosphodiester bond within a polynucleotide chain. The benefit of only nicking one strand of the GUV-substrate bridge (rather than cleaving both strands) would be that strand modification could be restricted to just the substrate constructs, leaving the GUV constructs to be able to re-bind to unmodified substrate constructs.

An example of a nicking enzyme that could potentially be used is Nt.CviPII. This enzyme recognises CCD sequences (denoted in the 5'-3' direction) in dsDNA, where D can be any nucleobase of A, G or T; the enzyme then cuts the phosphodiester bond at the 5' end of this sequence, *i.e.* before the 5' cytosine [329]. A schematic of a potential vesicle motility system using Nt.CviPII to achieve a burnt-bridges effect is shown in Figure 5.1. Here, the substrate and GUV constructs feature complementary sticky ends that can bind together. The substrate sticky end features two repeats of the CCD sequence, corresponding to two enzyme nicking sites; therefore, after the sticky ends bind, the Nt.CviPII enzymes should theoretically nick the substrate sticky end at two locations. This removes the sticky end from the substrate

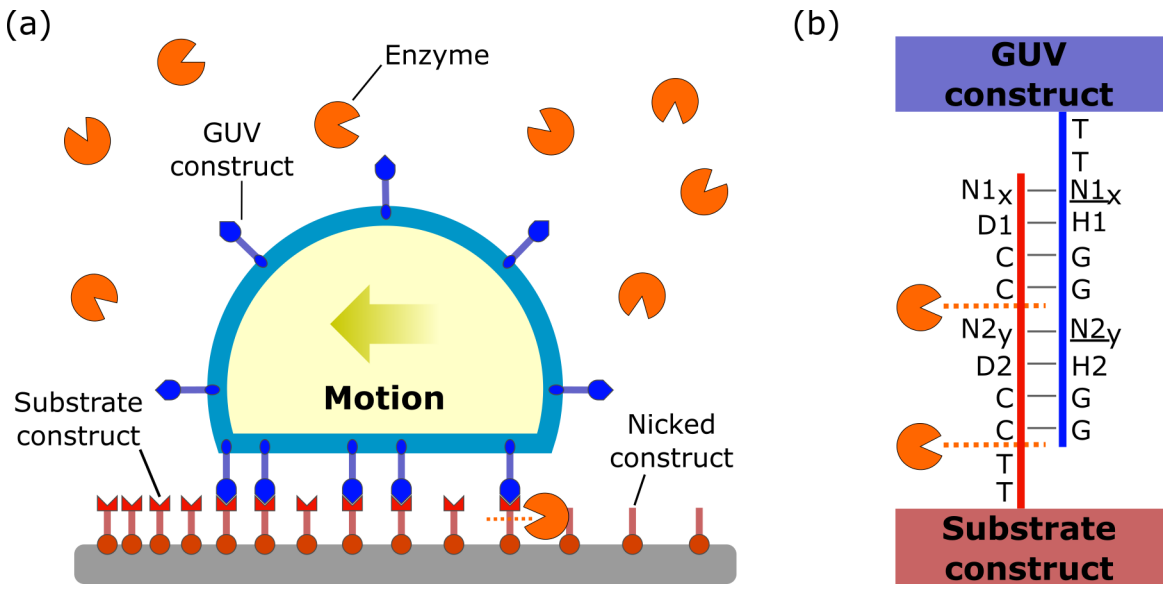


Figure 5.1: **Schematic of a vesicle motility system where enzymes are used to implement a burnt-bridges mechanism.** (a) shows a schematic of the experimental system, where the GUV and substrate are functionalised with DNA constructs featuring complementary sticky ends that can bind together. Nt.CviPII enzymes in bulk solution recognise CCD 5'-3' nucleobase sequences in the bound substrate constructs, nicking the constructs such that the sticky ends of the substrate constructs are truncated. (b) shows an example of potential sequences for the sticky ends, featuring CCD sequences in the substrate construct sticky end (where D can be any nucleobase of A, G or T) and HGG sequences in the GUV construct sticky end (where H can be any nucleobase of A, C or T). The sticky ends also feature optional sequences of variable length (*i.e.* complementary sequences $\mathrm{N1}_x$ and $\underline{\mathrm{N1}}_x$ that are x nucleotides long, and complementary sequences $\mathrm{N2}_y$ and $\underline{\mathrm{N2}}_y$ that are y nucleotides long); these can consist of any nucleotide sequence as long as they don't contain the sequence CCD, which would result in unwanted enzyme activity. The enzyme nicking sites are illustrated.

construct such that it cannot re-bind to the GUV constructs. Two fragments of the substrate sticky end are left bound to the GUV construct, until they either spontaneously dissociate (if sufficiently short) or are displaced by an unmodified substrate sticky end *via* toehold-mediated strand displacement. The optional sequences $\mathrm{N1}_x$, $\underline{\mathrm{N1}}_x$, $\mathrm{N2}_y$ and $\underline{\mathrm{N2}}_y$ have variable length and nucleobase sequence, and can be changed to tune the binding strength of the complementary sticky ends.

It must be noted that an attempt was made during this PhD at designing and implementing the experimental system in Figure 5.1. Preliminary experiments in bulk solution (comparing samples of substrate and GUV constructs mixed together, with and without the nicking enzyme Nt.CviPII) unfortunately did not exhibit any enzyme activity, despite attempts made to conduct experiments under conditions as close to the optimal conditions of the enzyme as possible. Specifically, the experiment was run at room temperature in 20 μl samples with buffer conditions of 10 mM Tris-HCl, 50 mM NaCl, 10 mM $MgCl_2$, 0.1 mg ml^{-1} bovine serum albumin (BSA) and 2.93% glycerol; DNA concentrations of 1 μM substrate construct and 1 μM GUV construct (corresponding to a total DNA mass of approximately 0.468 μg); and 0.468 units of Nt.CviPII (New England Biolabs, UK) where applicable. By definition, one unit of Nt.CviPII

corresponds to the amount of enzyme that will completely digest 1 μg of substrate DNA in a 50 μl sample in 60 minutes [330]. A lack of enzyme activity could be due to many reasons, such as sub-optimal buffer conditions and temperature; contaminants in the samples (such as traces of EDTA, although the DNA samples were prepared in Tris buffer rather than TE); over-exposure of the enzymes to temperatures above -20°C resulting in denaturation. Due to time constraints, the attempt at implementing this system was discontinued. However, for those who may want to consider working on this system, a helpful guide for optimising restriction endonuclease reactions can be found at Ref. [330].

An alternative to using nicking enzymes would be to use ribonuclease H (abbreviated as RNase H). Rather than recognising specific sequences in dsDNA, RNase H instead catalyses the cleavage of RNA in an DNA/RNA duplex. RNase H has been used to engineer motility in vesicle systems; for example, in Ref. [246], vesicles were functionalised with DNA strands that bound to complementary strands attached to a substrate. RNase H enzymes in bulk solution then cleave the RNA in DNA/RNA duplexes, such that the DNA unbinds; this enables the vesicles to diffuse over the substrate rather than being fixed in one place. This system could be re-purposed to include surface density gradients in the RNA coverage on the substrate. Furthermore, the non-sequence-specific nature of RNase H means that the burnt-bridges mechanism should theoretically not be so sensitive to errors (such as truncation errors) in the construct sequences.

Overall, it would be interesting to implement an enzyme-driven burnt-bridges approach to the vesicle motility system, as this could potentially boost vesicle motility and achieve higher drift velocities along surface density gradients of DNA or RNA compared with systems that rely on spontaneous dissociation of DNA duplexes or strand displacement reactions.

5.2.3 Extending the theoretical framework and numerical model

It would be helpful to gain a better understanding of the discrepancy between the theoretical predictions and the results of experiments and simulations in Chapter 3. The current belief is that for high bridge density (and thus larger drift forces), the system may deviate from the linear response regime under which the fluctuation-dissipation theorem applies. It would be interesting to extend or adapt the theory in light of this revelation, such that it is possible to make quantitative comparisons with simulations and experiments.

Furthermore, it would be useful to run simulations of systems on the same length scales as experiments; simulated vesicles were an order of magnitude smaller than experimental vesicles in Chapter 3, which limited quantitative comparisons between experimental and simulated drift velocities. Simulations on the same length scales as experiments were found to be unfeasible in terms of computation time, but perhaps there could be ways to further optimise simulations or run the simulations on high performance computing clusters with increased processor speeds.

Alternatively, simulations could be developed to take finer-grained details into account, such as the lateral diffusion of individual DNA constructs over the vesicle membrane, to verify the assumption that the DNA constructs diffuse at a sufficiently rate that they uniformly sample all available binding sites within the time it takes for them to re-bind. The impact of the

flexibility and curvature of the vesicle membrane on the resulting motion could also be modelled, to compare with experiments in which the membrane flexibility and vesicle deformability are varied (as mentioned in the previous section).

Finally, the numerical model and theory presented in Chapter 3 could be extended to describe the burnt-bridges adaptation of the vesicle motility system presented in Chapter 4. The simulation results and theory could then be compared with experimental findings, and also help to direct the design of future implementations of the burnt-bridges system to optimise vesicle mobility and drift velocity.

References

[1] Hannah Sleath, Bortolo Mognetti, Yuval Elani, and Lorenzo Di Michele. Chemotactic crawling of multivalent vesicles along ligand-density gradients. *arXiv preprint arXiv:2310.09990*, 2023.

[2] Robert Hooke. *Micrographia: or some physiological descriptions of minute bodies made by magnifying glasses with observations and inquiries thereupon.* Jo. Martyn and Ja. Allestry, London, 1665.

[3] Bruce Alberts. *Molecular biology of the cell.* Garland science, 2017.

[4] Stephen P Bell and Anindya Dutta. DNA replication in eukaryotic cells. *Annual review of biochemistry*, 71(1):333–374, 2002.

[5] Jerry J Zimmerman, Amélie von Saint André-von Arnim, and Jerry McLaughlin. Cellular respiration. In *Pediatric critical care*, pages 1058–1072. Elsevier, 2011.

[6] JEAN Lucas-Lenard and FRITZ Lipmann. Protein biosynthesis. *Annual review of biochemistry*, 40(1):409–448, 1971.

[7] Kivie Moldave. Eukaryotic protein synthesis. *Annual review of biochemistry*, 54(1):1109–1149, 1985.

[8] Ralph A Bradshaw and Edward A Dennis. *Handbook of cell signaling.* Academic press, 2009.

[9] Barry M Gumbiner. Cell adhesion: the molecular basis of tissue architecture and morphogenesis. *Cell*, 84(3):345–357, 1996.

[10] Song Li, Jun-Lin Guan, and Shu Chien. Biochemistry and biomechanics of cell motility. *Annu. Rev. Biomed. Eng.*, 7:105–150, 2005.

[11] Meyer B Jackson. *Molecular and cellular biophysics.* Cambridge University Press, 2006.

[12] Rick Horwitz. Cellular biophysics. *Biophysical journal*, 110(5):993–996, 2016.

[13] Mark S Bretscher. The molecules of the cell membrane. *Scientific American*, 253(4): 100–109, 1985.

[14] Sandra Tan, Hwee Tong Tan, and Maxey CM Chung. Membrane proteins and membrane proteomics. *Proteomics*, 8(19):3924–3932, 2008.

[15] Carl-Henrik Heldin, Benson Lu, Ron Evans, and J Silvio Gutkind. Signals and receptors. *Cold Spring Harbor Perspectives in Biology*, 8(4):a005900, 2016.

[16] Martin J Humphries. Integrin activation: the link between ligand binding and signal transduction. *Current opinion in cell biology*, 8(5):632–640, 1996.

[17] Amelia Ahmad Khalili and Mohd Ridzuan Ahmad. A review of cell adhesion studies for biomedical and biological applications. *International journal of molecular sciences*, 16 (8):18149–18184, 2015.

[18] Lance Kam and Steven G Boxer. Cell adhesion to protein-micropatterned-supported lipid bilayer membranes. *Journal of Biomedical Materials Research: An Official Journal of The Society for Biomaterials, The Japanese Society for Biomaterials, and The Australian Society for Biomaterials and the Korean Society for Biomaterials*, 55(4):487–495, 2001.

[19] Jennifer M Halbleib and W James Nelson. Cadherins in development: cell adhesion, sorting, and tissue morphogenesis. *Genes & development*, 20(23):3199–3214, 2006.

[20] Anna Huttenlocher, Rebecca R Sandborg, and Alan F Horwitz. Adhesion in cell migration. *Current opinion in cell biology*, 7(5):697–706, 1995.

[21] Jason Mercer, Mario Schelhaas, and Ari Helenius. Virus entry by endocytosis. *Annual review of biochemistry*, 79:803–833, 2010.

[22] James C Sacchettini, Linda G Baum, and C Fred Brewer. Multivalent protein-carbohydrate interactions: a new paradigm for supermolecular assembly and signal transduction. *Biochemistry*, 40(10):3009–3015, 2001.

[23] Huafeng Xu and David E Shaw. A simple model of multivalent adhesion and its application to influenza infection. *Biophysical journal*, 110(1):218–233, 2016.

[24] Brian E Collins and James C Paulson. Cell surface biology mediated by low affinity multivalent protein-glycan interactions. *Current opinion in chemical biology*, 8(6):617–625, 2004.

[25] Mathai Mammen, Seok-Ki Choi, and George M Whitesides. Polyvalent interactions in biological systems: implications for design and use of multivalent ligands and inhibitors. *Angewandte Chemie International Edition*, 37(20):2754–2794, 1998.

[26] Anne Marie Krachler, Hyeilin Ham, and Kim Orth. Outer membrane adhesion factor multivalent adhesion molecule 7 initiates host cell binding during infection by gram-negative pathogens. *Proceedings of the National Academy of Sciences*, 108(28):11614–11619, 2011.

[27] George I Bell. A theoretical model for adhesion between cells mediated by multivalent ligands. *Cell Biochemistry and Biophysics*, 1:133–147, 1979.

[28] John J Skehel and Don C Wiley. Receptor binding and membrane fusion in virus entry: the influenza hemagglutinin. *Annual review of biochemistry*, 69(1):531–569, 2000.

[29] Nicholas K Sauter, Mark D Bednarski, Beth A Wurzburg, John E Hanson, George M Whitesides, John J Skehel, and Don C Wiley. Hemagglutinins from two influenza virus variants bind to sialic acid derivatives with millimolar dissociation constants: a 500-MHz proton nuclear magnetic resonance study. *Biochemistry*, 28(21):8388–8396, 1989.

[30] Michele A Wozniak, Katarzyna Modzelewska, Lina Kwong, and Patricia J Keely. Focal adhesion regulation of cell behavior. *Biochimica et Biophysica Acta (BBA)-Molecular Cell Research*, 1692(2-3):103–119, 2004.

[31] Patrick Varilly, Stefano Angioletti-Uberti, Bortolo M Mognetti, and Daan Frenkel. A general theory of DNA-mediated and other valence-limited colloidal interactions. *The Journal of chemical physics*, 137(9):094108, 2012.

[32] Meng Liu, Azzurra Apriceno, Miguel Sipin, Edoardo Scarpa, Laura Rodriguez-Arco, Alessandro Poma, Gabriele Marchello, Giuseppe Battaglia, and Stefano Angioletti-Uberti. Combinatorial entropy behaviour leads to range selective binding in ligand-receptor interactions. *Nature communications*, 11(1):4836, 2020.

[33] Christine Linne, Daniele Visco, Stefano Angioletti-Uberti, Liedewij Laan, and Daniela J Kraft. Direct visualization of superselective colloid-surface binding mediated by multivalent interactions. *Proceedings of the National Academy of Sciences*, 118(36):e2106036118, 2021.

[34] Bortolo Matteo Mognetti, Pietro Cicuta, and Lorenzo Di Michele. Programmable interactions with biomimetic DNA linkers at fluid membranes and interfaces. *Reports on progress in physics*, 82(11):116601, 2019.

[35] Stefano Angioletti-Uberti. Theory, simulations and the design of functionalized nanoparticles for biomedical applications: a soft matter perspective. *npj Computational Materials*, 3(1):48, 2017.

[36] Tine Curk, Jure Dobnikar, and Daan Frenkel. Design principles for super selectivity using multivalent interactions. *Multivalency: Concepts, Research & Applications*, pages 75–101, 2018.

[37] Roberta Lanfranco, Pritam Kumar Jana, Lucia Tunesi, Pietro Cicuta, Bortolo Matteo Mognetti, Lorenzo Di Michele, and Gilles Bruylants. Kinetics of nanoparticle-membrane adhesion mediated by multivalent interactions. *Langmuir*, 35(6):2002–2012, 2019.

[38] Omar A Amjad, Bortolo M Mognetti, Pietro Cicuta, and Lorenzo Di Michele. Membrane adhesion through bridging by multimeric ligands. *Langmuir*, 33(5):1139–1146, 2017.

[39] VB Shenoy and LB Freund. Growth and shape stability of a biological membrane adhesion complex in the diffusion-mediated regime. *Proceedings of the National Academy of Sciences*, 102(9):3213–3218, 2005.

[40] Lucia Parolini, Bortolo M Mognetti, Jurij Kotar, Erika Eiser, Pietro Cicuta, and Lorenzo Di Michele. Volume and porosity thermal regulation in lipid mesophases by coupling mobile ligands to soft membranes. *Nature communications*, 6(1):5948, 2015.

[41] Paul A Beales and T Kyle Vanderlick. Specific binding of different vesicle populations by the hybridization of membrane-anchored DNA. *The Journal of Physical Chemistry A*, 111(49):12372–12380, 2007.

[42] Paul A Beales, Jin Nam, and T Kyle Vanderlick. Specific adhesion between DNA-functionalized "Janus" vesicles: size-limited clusters. *Soft Matter*, 7(5):1747–1755, 2011.

[43] Paul A Beales and T Kyle Vanderlick. Application of nucleic acid-lipid conjugates for the programmable organisation of liposomal modules. *Advances in colloid and interface science*, 207:290–305, 2014.

[44] W Benjamin Rogers, William M Shih, and Vinothan N Manoharan. Using DNA to program the self-assembly of colloidal nanoparticles and microparticles. *Nature Reviews Materials*, 1(3):1–14, 2016.

[45] Dmytro Nykypanchuk, Mathew M Maye, Daniel Van Der Lelie, and Oleg Gang. DNA-guided crystallization of colloidal nanoparticles. *Nature*, 451(7178):549–552, 2008.

[46] Kristina M Flavier and Steven G Boxer. Vesicle fusion mediated by solanesol-anchored DNA. *Biophysical Journal*, 113(6):1260–1268, 2017.

[47] Yee-Hung M Chan, Bettina van Lengerich, and Steven G Boxer. Effects of linker sequences on vesicle fusion mediated by lipid-anchored DNA oligonucleotides. *Proceedings of the National Academy of Sciences*, 106(4):979–984, 2009.

[48] Lorenzo Di Michele, Pritam Kumar Jana, and Bortolo Matteo Mognetti. Steric interactions between mobile ligands facilitate complete wrapping in passive endocytosis. *Physical Review E*, 98(3):032406, 2018.

[49] Peter Friedl and Darren Gilmour. Collective cell migration in morphogenesis, regeneration and cancer. *Nature reviews Molecular cell biology*, 10(7):445–457, 2009.

[50] Andy Aman and Tatjana Piotrowski. Cell migration during morphogenesis. *Developmental biology*, 341(1):20–33, 2010.

[51] Vincent Falanga. Wound healing and its impairment in the diabetic foot. *The Lancet*, 366(9498):1736–1743, 2005.

[52] Anne J Ridley, Martin A Schwartz, Keith Burridge, Richard A Firtel, Mark H Ginsberg, Gary Borisy, J Thomas Parsons, and Alan Rick Horwitz. Cell migration: integrating signals from front to back. *Science*, 302(5651):1704–1709, 2003.

[53] Peter Friedl and Katarina Wolf. Tumour-cell invasion and migration: diversity and escape mechanisms. *Nature reviews cancer*, 3(5):362–374, 2003.

[54] Matthew F Krummel, Frederic Bartumeus, and Audrey Gérard. T cell migration, search strategies and mechanisms. *Nature Reviews Immunology*, 16(3):193–201, 2016.

[55] Ronald N Germain, Ellen A Robey, and Michael D Cahalan. A decade of imaging cellular motility and interaction dynamics in the immune system. *Science*, 336(6089):1676–1681, 2012.

[56] Joseph B Keller and SI Rubinow. Swimming of flagellated microorganisms. *Biophysical Journal*, 16(2):151–170, 1976.

[57] Alexey J Merz, Magdalene So, and Michael P Sheetz. Pilus retraction powers bacterial twitching motility. *Nature*, 407(6800):98–102, 2000.

[58] Jørgen Henrichsen. Twitching motility. *Annual review of microbiology*, 37(1):81–93, 1983.

[59] Peter JM Van Haastert. Amoeboid cells use protrusions for walking, gliding and swimming. *PloS one*, 6(11):e27532, 2011.

[60] HG Othmer. Eukaryotic cell dynamics from crawlers to swimmers. *Wiley Interdisciplinary Reviews: Computational Molecular Science*, 9(1):e1376, 2019.

[61] EG Govorunova and OA Sineshchekov. Chemotaxis in the green flagellate alga Chlamydomonas. *Biochemistry (Moscow)*, 70:717–725, 2005.

[62] Wayne Bell and Ralph Mitchell. Chemotactic and growth responses of marine bacteria to algal extracellular products. *The Biological Bulletin*, 143(2):265–277, 1972.

[63] Michael Eisenbach and Laura C Giojalas. Sperm guidance in mammals—an unpaved road to the egg. *Nature reviews Molecular cell biology*, 7(4):276–285, 2006.

[64] Anat Bahat and Michael Eisenbach. Sperm thermotaxis. *Molecular and cellular endocrinology*, 252(1-2):115–119, 2006.

[65] KENNETH V Thimann and GM Curry. Phototropism and phototaxis. *Comparative biochemistry*, 1:243–309, 1960.

[66] Jaime A Espina, Cristian L Marchant, and Elias H Barriga. Durotaxis: the mechanical control of directed cell migration. *The FEBS journal*, 289(10):2736–2754, 2022.

[67] Jindan Wu, Zhengwei Mao, Huaping Tan, Lulu Han, Tanchen Ren, and Changyou Gao. Gradient biomaterials and their influences on cell migration. *Interface focus*, 2(3):337–355, 2012.

[68] Richard B Frankel and Richard P Blakemore. Magnetite and magnetotaxis in microorganisms. *Bioelectromagnetics: Journal of the Bioelectromagnetics Society, The Society for Physical Regulation in Biology and Medicine, The European Bioelectromagnetics Association*, 10(3):223–237, 1989.

[69] Maria E Mycielska and Mustafa BA Djamgoz. Cellular mechanisms of direct-current electric field effects: galvanotaxis and metastatic disease. *Journal of cell science*, 117(9): 1631–1639, 2004.

[70] D P Häder. Polarotaxis, gravitaxis and vertical phototaxis in the green flagellate, Euglena gracilis. *Archives of microbiology*, 147:179–183, 1987.

[71] Erik de Vries, Wenjuan Du, Hongbo Guo, and Cornelis AM de Haan. Influenza A virus hemagglutinin-neuraminidase-receptor balance: preserving virus motility. *Trends in microbiology*, 28(1):57–67, 2020.

[72] Michael D Vahey and Daniel A Fletcher. Influenza A virus surface proteins are organized to help penetrate host mucus. *Elife*, 8:e43764, 2019.

[73] Martin Delguste, Caroline Zeippen, Bénédicte Machiels, Jan Mast, Laurent Gillet, and David Alsteens. Multivalent binding of herpesvirus to living cells is tightly regulated during infection. *Science advances*, 4(8):eaat1273, 2018.

[74] Michael L Basara, James B McCarthy, David W Barnes, and Leo T Furcht. Stimulation of haptotaxis and migration of tumor cells by serum spreading factor. *Cancer research*, 45(6):2487–2494, 1985.

[75] Marc M Thibault, Caroline D Hoemann, and Michael D Buschmann. Fibronectin, vitronectin, and collagen I induce chemotaxis and haptotaxis of human and rabbit mesenchymal stem cells in a standardized transmembrane assay. *Stem cells and development*, 16(3):489–502, 2007.

[76] Xuan Luo, Valentine Seveau de Noray, Laurene Aoun, Martine Biarnes-Pelicot, Pierre-Olivier Strale, Vincent Studer, Marie-Pierre Valignat, and Olivier Theodoly. Lymphocytes perform reverse adhesive haptotaxis mediated by LFA-1 integrins. *Journal of Cell Science*, 133(16):jcs242883, 2020.

[77] Timothy P O'Connor, Janet S Duerr, and David Bentley. Pioneer growth cone steering decisions mediated by single filopodial contacts in situ. *Journal of Neuroscience*, 10(12): 3935–3946, 1990.

[78] Samantha J King, Sreeja B Asokan, Elizabeth M Haynes, Seth P Zimmerman, Jeremy D Rotty, James G Alb Jr, Alicia Tagliatela, Devon R Blake, Irina P Lebedeva, Daniel Marston, et al. Lamellipodia are crucial for haptotactic sensing and response. *Journal of cell science*, 129(12):2329–2342, 2016.

[79] Cecilia MM Motta, Kevin J Endres, Chrys Wesdemiotis, Rebecca K Willits, and Matthew L Becker. Enhancing schwann cell migration using concentration gradients of laminin-derived peptides. *Biomaterials*, 218:119335, 2019.

[80] O Moreno-Arotzena, C Borau, N Movilla, M Vicente-Manzanares, and JM García-Aznar. Fibroblast migration in 3D is controlled by haptotaxis in a non-muscle myosin II-dependent manner. *Annals of Biomedical Engineering*, 43:3025–3039, 2015.

[81] Stephen B Carter. Principles of cell motility: the direction of cell movement and cancer invasion. 1965.

[82] Jie Liu, Zhongzhen Liu, Keng Chen, Wei Chen, Xiyuan Fang, Meng Li, Xuening Zhou, Ning Ding, Huan Lei, Chen Guo, et al. Kindlin-2 promotes rear focal adhesion disassembly and directional persistence during cell migration. *Journal of cell science*, 134(1):jcs244616, 2021.

[83] Gregor Kirfel, Alexander Rigort, Bodo Borm, and Volker Herzog. Cell migration: mechanisms of rear detachment and the formation of migration tracks. *European journal of cell biology*, 83(11-12):717–724, 2004.

[84] Joshua A Broussard, Donna J Webb, and Irina Kaverina. Asymmetric focal adhesion disassembly in motile cells. *Current opinion in cell biology*, 20(1):85–90, 2008.

[85] Ali Salehi-Reyhani, Oscar Ces, and Yuval Elani. Artificial cell mimics as simplified models for the study of cell biology. *Experimental Biology and Medicine*, 242(13):1309–1317, 2017.

[86] Samuel K Sia, Brian M Gillette, and Genevieve J Yang. Synthetic tissue biology: tissue engineering meets synthetic biology. *Birth Defects Research Part C: Embryo Today: Reviews*, 81(4):354–361, 2007.

[87] Andreas Meyer, Rene Pellaux, and Sven Panke. Bioengineering novel in vitro metabolic pathways using synthetic biology. *Current opinion in microbiology*, 10(3):246–253, 2007.

[88] Simon Ausländer, David Ausländer, and Martin Fussenegger. Synthetic biology–the synthesis of biology. *Angewandte Chemie International Edition*, 56(23):6396–6419, 2017.

[89] Daniel G Gibson, John I Glass, Carole Lartigue, Vladimir N Noskov, Ray-Yuan Chuang, Mikkel A Algire, Gwynedd A Benders, Michael G Montague, Li Ma, Monzia M Moodie, et al. Creation of a bacterial cell controlled by a chemically synthesized genome. *science*, 329(5987):52–56, 2010.

[90] SO Kärenlampi and AJ von Wright. Genetically modified microorganisms. 2016.

[91] Mark T Dertzbaugh. Genetically engineered vaccines: an overview. *Plasmid*, 39(2): 100–113, 1998.

[92] Mònica Campàs, Beatriz Prieto-Simón, and Jean-Louis Marty. A review of the use of genetically engineered enzymes in electrochemical biosensors. In *Seminars in cell & developmental biology*, volume 20, pages 3–9. Elsevier, 2009.

[93] Kien T Nguyen, Xiaowei He, Dylan C Alexander, Chen Li, Jian-Qiao Gu, Carmela Mascio, Andrew Van Praagh, Larry Mortin, Min Chu, Jared A Silverman, et al. Genetically engineered lipopeptide antibiotics related to A54145 and daptomycin with improved properties. *Antimicrobial agents and chemotherapy*, 54(4):1404–1413, 2010.

[94] Gordon P Moore. Genetically engineered antibodies. *Clinical chemistry*, 35(9):1849–1853, 1989.

[95] Petra Schwille. Bottom-up synthetic biology: engineering in a tinkerer's world. *Science*, 333(6047):1252–1254, 2011.

[96] Yuval Elani. Construction of membrane-bound artificial cells using microfluidics: a new frontier in bottom-up synthetic biology. *Biochemical Society Transactions*, 44(3):723–730, 2016.

[97] Arthur A Spector and Mark A Yorek. Membrane lipid composition and cellular function. *Journal of lipid research*, 26(9):1015–1035, 1985.

[98] Eduardo Perozo, Anna Kloda, D Marien Cortes, and Boris Martinac. Physical principles underlying the transduction of bilayer deformation forces during mechanosensitive channel gating. *Nature structural biology*, 9(9):696–703, 2002.

[99] Nicoletta Kahya, Dag Scherfeld, Kirsten Bacia, and Petra Schwille. Lipid domain formation and dynamics in giant unilamellar vesicles explored by fluorescence correlation spectroscopy. *Journal of Structural Biology*, 147(1):77–89, 2004.

[100] Michael Schaich, Jehangir Cama, Kareem Al Nahas, Diana Sobota, Hannah Sleath, Kevin Jahnke, Siddharth Deshpande, Cees Dekker, and Ulrich F Keyser. An integrated microfluidic platform for quantifying drug permeation across biomimetic vesicle membranes. *Molecular pharmaceutics*, 16(6):2494–2501, 2019.

[101] Jessica MA Blair, Mark A Webber, Alison J Baylay, David O Ogbolu, and Laura JV Piddock. Molecular mechanisms of antibiotic resistance. *Nature reviews microbiology*, 13 (1):42–51, 2015.

[102] Lynn L Silver. A Gestalt approach to Gram-negative entry. *Bioorganic & medicinal chemistry*, 24(24):6379–6389, 2016.

[103] Jean-Marie Pagès, Chloë E James, and Mathias Winterhalter. The porin and the permeating antibiotic: a selective diffusion barrier in Gram-negative bacteria. *Nature Reviews Microbiology*, 6(12):893–903, 2008.

[104] David A Six, Thomas Krucker, and Jennifer A Leeds. Advances and challenges in bacterial compound accumulation assays for drug discovery. *Current opinion in chemical biology*, 44:9–15, 2018.

[105] Susanne F Fenz and Kheya Sengupta. Giant vesicles as cell models. *Integrative Biology*, 4(9):982–995, 2012.

[106] Douglas A Lauffenburger and Alan F Horwitz. Cell migration: a physically integrated molecular process. *cell*, 84(3):359–369, 1996.

[107] TJ Mitchison and LP Cramer. Actin-based cell motility and cell locomotion. *Cell*, 84(3): 371–379, 1996.

[108] Hidetake Miyata and Hirokazu Hotani. Morphological changes in liposomes caused by polymerization of encapsulated actin and spontaneous formation of actin bundles. *Proceedings of the National Academy of Sciences*, 89(23):11547–11551, 1992.

[109] Makoto Honda, Kingo Takiguchi, Satoshi Ishikawa, and Hirokazu Hotani. Morphogenesis of liposomes encapsulating actin depends on the type of actin-crosslinking. *Journal of molecular biology*, 287(2):293–300, 1999.

[110] Arpita Upadhyaya, Jeffrey R Chabot, Albina Andreeva, Azadeh Samadani, and Alexander van Oudenaarden. Probing polymerization forces by using actin-propelled lipid vesicles. *Proceedings of the National Academy of Sciences*, 100(8):4521–4526, 2003.

[111] Cheemeng Tan, Saumya Saurabh, Marcel P Bruchez, Russell Schwartz, and Philip LeDuc. Molecular crowding shapes gene expression in synthetic cellular nanosystems. *Nature nanotechnology*, 8(8):602–608, 2013.

[112] Germán Rivas, Frank Ferrone, and Judith Herzfeld. Life in a crowded world: workshop on the biological implications of macromolecular crowding, 2004.

[113] Keitaro Ishikawa, Kanetomo Sato, Yasufumi Shima, Itaru Urabe, and Tetsuya Yomo. Expression of a cascading genetic network within liposomes. *FEBS letters*, 576(3):387–390, 2004.

[114] Jonghyeon Shin and Vincent Noireaux. An E. coli cell-free expression toolbox: application to synthetic gene circuits and artificial cells. *ACS synthetic biology*, 1(1):29–41, 2012.

[115] Can Xu, Shuo Hu, and Xiaoyuan Chen. Artificial cells: from basic science to applications. *Materials Today*, 19(9):516–532, 2016.

[116] Wakana Sato, Tomasz Zajkowski, Felix Moser, and Katarzyna P Adamala. Synthetic cells in biomedical applications. *Wiley Interdisciplinary Reviews: Nanomedicine and Nanobiotechnology*, 14(2):e1761, 2022.

[117] Theresa M Allen and Pieter R Cullis. Liposomal drug delivery systems: from concept to clinical applications. *Advanced drug delivery reviews*, 65(1):36–48, 2013.

[118] Aldo Jesorka and Owe Orwar. Liposomes: technologies and analytical applications. *Annu. Rev. Anal. Chem.*, 1:801–832, 2008.

[119] HAH Rongen, A Bult, and WP Van Bennekom. Liposomes and immunoassays. *Journal of immunological methods*, 204(2):105–133, 1997.

[120] Marta Bally, Kelly Bailey, Kaori Sugihara, Dorothee Grieshaber, Janos Vörös, and Brigitte Städler. Liposome and lipid bilayer arrays towards biosensing applications. *Small*, 6(22):2481–2497, 2010.

[121] Kira A Podolsky and Neal K Devaraj. Synthesis of lipid membranes for artificial cells. *Nature Reviews Chemistry*, 5(10):676–694, 2021.

[122] Neha P Kamat, Joshua S Katz, and Daniel A Hammer. Engineering polymersome protocells. *The journal of physical chemistry letters*, 2(13):1612–1623, 2011.

[123] Xiaoliang Wang, Xiaoman Liu, and Xin Huang. Bioinspired protein-based assembling: toward advanced life-like behaviors. *Advanced Materials*, 32(25):2001436, 2020.

[124] Masahiro Takinoue and Shoji Takeuchi. Droplet microfluidics for the study of artificial cells. *Analytical and bioanalytical chemistry*, 400:1705–1716, 2011.

[125] Jiahao Pan, Jianping Chen, Xuejiao Wang, Ying Wang, and Jun-Bing Fan. Pickering emulsion: from controllable fabrication to biomedical application. *Interdisciplinary Medicine*, 1(3):e20230014, 2023.

[126] Michael Ian Gurr, John L Harwood, Keith N Frayn, et al. *Lipid biochemistry*, volume 409. Springer, 2002.

[127] Eoin Fahy, Dawn Cotter, Manish Sud, and Shankar Subramaniam. Lipid classification, structures and tools. *Biochimica et Biophysica Acta (BBA)-Molecular and Cell Biology of Lipids*, 1811(11):637–647, 2011.

[128] Donald J Hanahan. *A guide to phospholipid chemistry*. Oxford University Press, 1997.

[129] Samuel Safran. *Statistical thermodynamics of surfaces, interfaces, and membranes*. CRC Press, 2018.

[130] Marc CA Stuart and Egbert J Boekema. Two distinct mechanisms of vesicle-to-micelle and micelle-to-vesicle transition are mediated by the packing parameter of phospholipid-detergent systems. *Biochimica et Biophysica Acta (BBA)-Biomembranes*, 1768(11):2681–2689, 2007.

[131] John F Nagle and Stephanie Tristram-Nagle. Lipid bilayer structure. *Current opinion in structural biology*, 10(4):474–480, 2000.

[132] Stephanie Tristram-Nagle and John F Nagle. Lipid bilayers: thermodynamics, structure, fluctuations, and interactions. *Chemistry and physics of lipids*, 127(1):3–14, 2004.

[133] John R Silvius et al. Thermotropic phase transitions of pure lipids in model membranes and their modifications by membrane proteins. *Lipid-protein interactions*, 2:239–281, 1982.

[134] Frederick A Heberle and Gerald W Feigenson. Phase separation in lipid membranes. *Cold Spring Harbor perspectives in biology*, 3(4):a004630, 2011.

[135] F Ross Hallett, Jackie Marsh, Bernie G Nickel, and Janet M Wood. Mechanical properties of vesicles, II. a model for osmotic swelling and lysis. *Biophysical journal*, 64(2):435–442, 1993.

[136] Abolfazl Akbarzadeh, Rogaie Rezaei-Sadabady, Soodabeh Davaran, Sang Woo Joo, Nosratollah Zarghami, Younes Hanifehpour, Mohammad Samiei, Mohammad Kouhi, and Kazem Nejati-Koshki. Liposome: classification, preparation, and applications. *Nanoscale research letters*, 8:1–9, 2013.

[137] Vladimir P Torchilin and Volkmar Weissig. *Liposomes: a practical approach*. Number 264. Oxford University Press, 2003.

[138] Ahmed Gouda, Omar S Sakr, Maha Nasr, and Omaima Sammour. Ethanol injection technique for liposomes formulation: an insight into development, influencing factors, challenges and applications. *Journal of Drug Delivery Science and Technology*, 61:102174, 2021.

[139] Qingyue Zhong and Hongwei Zhang. Preparation ofsmall unilamellar vesicle liposomes using detergent dialysis method. In *Liposomes: Methods and Protocols*, pages 49–56. Springer, 2023.

[140] Luka Šturm and Nataša Poklar Ulrih. Basic methods for preparation of liposomes and studying their interactions with different compounds, with the emphasis on polyphenols. *International journal of molecular sciences*, 22(12):6547, 2021.

[141] Miglena I Angelova and Dimiter S Dimitrov. Liposome electroformation. *Faraday discussions of the Chemical Society*, 81:303–311, 1986.

[142] Evelin Aurelia Kubatta and Heinz Rehage. Characterization of giant vesicles formed by phase transfer processes. *Colloid and Polymer Science*, 287:1117–1122, 2009.

[143] Bo Yu, Robert J Lee, and L James Lee. Microfluidic methods for production of liposomes. *Methods in enzymology*, 465:129–141, 2009.

[144] Yung-Chieh Tan, Kanaka Hettiarachchi, Maria Siu, Yen-Ru Pan, and Abraham Phillip Lee. Controlled microfluidic encapsulation of cells, proteins, and microbeads in lipid vesicles. *Journal of the American Chemical Society*, 128(17):5656–5658, 2006.

[145] Siddharth Deshpande, Yaron Caspi, Anna EC Meijering, and Cees Dekker. Octanol-assisted liposome assembly on chip. *Nature communications*, 7(1):10447, 2016.

[146] Jeanne C Stachowiak, David L Richmond, Thomas H Li, Allen P Liu, Sapun H Parekh, and Daniel A Fletcher. Unilamellar vesicle formation and encapsulation by microfluidic jetting. *Proceedings of the national academy of sciences*, 105(12):4697–4702, 2008.

[147] Andreas Jahn, Wyatt N Vreeland, Don L DeVoe, Laurie E Locascio, and Michael Gaitan. Microfluidic directed formation of liposomes of controlled size. *Langmuir*, 23(11):6289–6293, 2007.

[148] Chee Guan Koh, Xulang Zhang, Shujun Liu, Sharon Golan, Bo Yu, Xiaojuan Yang, Jingjiao Guan, Yan Jin, Yeshayahu Talmon, Natarajan Muthusamy, et al. Delivery of antisense oligodeoxyribonucleotide lipopolyplex nanoparticles assembled by microfluidic hydrodynamic focusing. *Journal of Controlled Release*, 141(1):62–69, 2010.

[149] Robert A Weinberg. The molecules of life. *Scientific American*, 253(4):48–57, 1985.

[150] Francis H Crick. On protein synthesis. In *Symp Soc Exp Biol*, volume 12, page 8, 1958.

[151] Marvin H Caruthers. Chemical synthesis of DNA and DNA analogs. *Accounts of chemical research*, 24(9):278–284, 1991.

[152] Mikael Madsen and Kurt V Gothelf. Chemistries for DNA nanotechnology. *Chemical reviews*, 119(10):6384–6458, 2019.

[153] Paul WK Rothemund. Folding DNA to create nanoscale shapes and patterns. *Nature*, 440(7082):297–302, 2006.

[154] Kevin Jahnke, Vanessa Huth, Ulrike Mersdorf, Na Liu, and Kerstin Göpfrich. Bottom-up assembly of synthetic cells with a DNA cytoskeleton. *ACS nano*, 16(5):7233–7241, 2022.

[155] Roger Rubio-Sánchez, Bortolo Matteo Mognetti, Pietro Cicuta, and Lorenzo Di Michele. DNA-origami line-actants control domain organization and fission in synthetic membranes. *Journal of the American Chemical Society*, 2023.

[156] Layla Malouf, Diana A Tanase, Giacomo Fabrini, Ryan A Brady, Miguel Paez-Perez, Adrian Leathers, Michael J Booth, and Lorenzo Di Michele. Sculpting DNA-based synthetic cells through phase separation and phase-targeted activity. *Chem*, 9(11):3347–3364, 2023.

[157] Nadrian C Seeman. An overview of structural DNA nanotechnology. *Molecular biotechnology*, 37:246–257, 2007.

[158] Marcello DeLuca, Ze Shi, Carlos E Castro, and Gaurav Arya. Dynamic DNA nanotechnology: toward functional nanoscale devices. *Nanoscale Horizons*, 5(2):182–201, 2020.

[159] Nadrian C Seeman. Nucleic acid junctions and lattices. *Journal of theoretical biology*, 99 (2):237–247, 1982.

[160] Dage Liu, Mingsheng Wang, Zhaoxiang Deng, Richard Walulu, and Chengde Mao. Tensegrity: construction of rigid DNA triangles with flexible four-arm DNA junctions. *Journal of the American Chemical Society*, 126(8):2324–2325, 2004.

[161] Paul J Paukstelis, Jacek Nowakowski, Jens J Birktoft, and Nadrian C Seeman. Crystal structure of a continuous three-dimensional DNA lattice. *Chemistry & biology*, 11(8): 1119–1126, 2004.

[162] Paul WK Rothemund, Axel Ekani-Nkodo, Nick Papadakis, Ashish Kumar, Deborah Kuchnir Fygenson, and Erik Winfree. Design and characterization of programmable DNA nanotubes. *Journal of the American Chemical Society*, 126(50):16344–16352, 2004.

[163] C Chad Harrell, Punit Kohli, Zuzanna Siwy, and Charles R Martin. DNA-nanotube artificial ion channels. *Journal of the American Chemical Society*, 126(48):15646–15647, 2004.

[164] Shifeng Hou, Jiahai Wang, and Charles R Martin. Template-synthesized DNA nanotubes. *Journal of the American Chemical Society*, 127(24):8586–8587, 2005.

[165] Yu He, Tao Ye, Min Su, Chuan Zhang, Alexander E Ribbe, Wen Jiang, and Chengde Mao. Hierarchical self-assembly of DNA into symmetric supramolecular polyhedra. *Nature*, 452 (7184):198–201, 2008.

[166] Ryosuke Iinuma, Yonggang Ke, Ralf Jungmann, Thomas Schlichthaerle, Johannes B Woehrstein, and Peng Yin. Polyhedra self-assembled from DNA tripods and characterized with 3D DNA-PAINT. *science*, 344(6179):65–69, 2014.

[167] Ralf Dahm. Friedrich Miescher and the discovery of DNA. *Developmental biology*, 278 (2):274–288, 2005.

[168] F Miescher. Letter i; to Wilhelm His; Tübingen, February 26th, 1869. *Die histochemischen und physiologischen arbeiten von Friedrich Miescher-aus dem wissenschaftlichen Briefwechsel von F. Miescher*, 1:33–38, 1869.

[169] L Pray. Discovery of DNA structure and function: Watson and Crick. 2008.

[170] Rosalind E Franklin and Raymond G Gosling. Molecular configuration in sodium thymonucleate. *Nature*, 171(4356):740–741, 1953.

[171] James D Watson and Francis HC Crick. Molecular structure of nucleic acids: a structure for deoxyribose nucleic acid. *Nature*, 171(4356):737–738, 1953.

[172] Rosalind E Franklin and Raymond George Gosling. The structure of sodium thymonucleate fibres, I. the influence of water content. *Acta Crystallographica*, 6(8-9):673–677, 1953.

[173] Y Mitsui, R Langridge, BARBARA E SHORTLE, CHARLES R CANTOR, ROBERT C GRANT, MASAHIKO KODAMA, and ROBERT D WELLS. Physical and enzymatic studies on poly d(I-C). Poly d(I-C), an unusual double-helical DNA. *Nature*, 228(5277): 1166–1169, 1970.

[174] Peter Yakovchuk, Ekaterina Protozanova, and Maxim D Frank-Kamenetskii. Base-stacking and base-pairing contributions into thermal stability of the DNA double helix. *Nucleic acids research*, 34(2):564–574, 2006.

[175] John SantaLucia Jr. A unified view of polymer, dumbbell, and oligonucleotide DNA nearest-neighbor thermodynamics. *Proceedings of the National Academy of Sciences*, 95 (4):1460–1465, 1998.

[176] John SantaLucia Jr and Donald Hicks. The thermodynamics of DNA structural motifs. *Annu. Rev. Biophys. Biomol. Struct.*, 33:415–440, 2004.

[177] Bortolo Matteo Mognetti, ME Leunissen, and Daan Frenkel. Controlling the temperature sensitivity of DNA-mediated colloidal interactions through competing linkages. *Soft Matter*, 8(7):2213–2221, 2012.

[178] Roger M Wartell and Albert S Benight. Thermal denaturation of DNA molecules: a comparison of theory with experiment. *Physics Reports*, 126(2):67–107, 1985.

[179] Jacobus Henricus Van't Hoff and Jacobus Henricus Hoff. *Etudes de dynamique chimique*. F. Muller & Company, 1884.

[180] Jong-Shik Shin and Niles A Pierce. A synthetic DNA walker for molecular transport. *Journal of the American Chemical Society*, 126(35):10834–10835, 2004.

[181] Peng Yin, Hao Yan, Xiaoju G Daniell, Andrew J Turberfield, and John H Reif. A unidirectional DNA walker that moves autonomously along a track. *Angewandte Chemie*, 116(37):5014–5019, 2004.

[182] Jianbang Wang, Zhenzhen Li, and Itamar Willner. Dynamic reconfigurable DNA nanostructures, networks and materials. *Angewandte Chemie International Edition*, 62(18): e202215332, 2023.

[183] Joshua A Johnson, Abhilasha Dehankar, Jessica O Winter, and Carlos E Castro. Reciprocal control of hierarchical DNA origami-nanoparticle assemblies. *Nano Letters*, 19(12): 8469–8475, 2019.

[184] Sisi Fan, Dongfang Wang, Jin Cheng, Yan Liu, Tao Luo, Daxiang Cui, Yonggang Ke, and Jie Song. Information coding in a reconfigurable DNA origami domino array. *Angewandte Chemie*, 132(31):13091–13097, 2020.

[185] Jue Yin, Junke Wang, Renjie Niu, Shaokang Ren, Dexu Wang, and Jie Chao. DNA nanotechnology-based biocomputing. *Chemical Research in Chinese Universities*, 36: 219–226, 2020.

[186] Heini Ijäs, Iiris Hakaste, Boxuan Shen, Mauri A Kostiainen, and Veikko Linko. Reconfigurable DNA origami nanocapsule for pH-controlled encapsulation and display of cargo. *ACS nano*, 13(5):5959–5967, 2019.

[187] Alexander E Marras, Ze Shi, Michael G Lindell III, Randy A Patton, Chao-Min Huang, Lifeng Zhou, Hai-Jun Su, Gaurav Arya, and Carlos E Castro. Cation-activated avidity for rapid reconfiguration of DNA nanodevices. *ACS nano*, 12(9):9484–9494, 2018.

[188] Richie E Kohman and Xue Han. Light sensitization of DNA nanostructures via incorporation of photo-cleavable spacers. *Chemical Communications*, 51(26):5747–5750, 2015.

[189] Patrick M Arnott and Stefan Howorka. A temperature-gated nanovalve self-assembled from DNA to control molecular transport across membranes. *ACS nano*, 13(3):3334–3340, 2019.

[190] Jonathan List, Michael Weber, and Friedrich C Simmel. Hydrophobic actuation of a DNA origami bilayer structure. *Angewandte Chemie International Edition*, 53(16):4236–4239, 2014.

[191] Felix Kroener, Andreas Heerwig, Wolfgang Kaiser, Michael Mertig, and Ulrich Rant. Electrical actuation of a DNA origami nanolever on an electrode. *Journal of the American Chemical Society*, 139(46):16510–16513, 2017.

[192] Stephanie Lauback, Kara R Mattioli, Alexander E Marras, Maxim Armstrong, Thomas P Rudibaugh, Ratnasingham Sooryakumar, and Carlos E Castro. Real-time magnetic actuation of DNA nanodevices via modular integration with stiff micro-levers. *Nature communications*, 9(1):1446, 2018.

[193] David Yu Zhang and Erik Winfree. Control of DNA strand displacement kinetics using toehold exchange. *Journal of the American Chemical Society*, 131(47):17303–17314, 2009.

[194] Feng Li, Yanan Tang, Sarah M Traynor, Xing-Fang Li, and X Chris Le. Kinetics of proximity-induced intramolecular DNA strand displacement. *Analytical chemistry*, 88 (16):8152–8157, 2016.

[195] Bernard Yurke, Andrew J Turberfield, Allen P Mills Jr, Friedrich C Simmel, and Jennifer L Neumann. A DNA-fuelled molecular machine made of DNA. *Nature*, 406(6796): 605–608, 2000.

[196] Niranjan Srinivas, Thomas E Ouldridge, Petr Šulc, Joseph M Schaeffer, Bernard Yurke, Ard A Louis, Jonathan PK Doye, and Erik Winfree. On the biophysics and kinetics of toehold-mediated DNA strand displacement. *Nucleic acids research*, 41(22):10641–10658, 2013.

[197] Levon M Khachigian. Deoxyribozymes as catalytic nanotherapeutic agents. *Cancer research*, 79(5):879–888, 2019.

[198] Marcel Hollenstein. Nucleic acid enzymes based on functionalized nucleosides. *Current Opinion in Chemical Biology*, 52:93–101, 2019.

[199] Claudia Höbartner. How DNA catalyses RNA ligation. *Nature Catalysis*, 2(6):483–484, 2019.

[200] Bernard Cuenoud and Jack W Szostak. A DNA metalloenzyme with DNA ligase activity. *Nature*, 375(6532):611–614, 1995.

[201] Yanhong Sun, Rulong Ma, Shijin Wang, Guiying Li, Yongjie Sheng, Hongyue Rui, Jin Zhang, Jiacui Xu, and Dazhi Jiang. New cofactors and inhibitors for a DNA-cleaving DNAzyme: superoxide anion and hydrogen peroxide mediated an oxidative cleavage process. *Scientific Reports*, 7(1):378, 2017.

[202] Wenhu Zhou, Runjhun Saran, and Juewen Liu. Metal sensing by DNA. *Chemical reviews*, 117(12):8272–8325, 2017.

[203] Chenxiang Lin, Evaldas Katilius, Yan Liu, Junping Zhang, and Hao Yan. Self-assembled signaling aptamer DNA arrays for protein detection. *Angewandte Chemie*, 118(32):5422–5427, 2006.

[204] Yee-Wai Cheung, Jane Kwok, Alan WL Law, Rory M Watt, Masayo Kotaka, and Julian A Tanner. Structural basis for discriminatory recognition of Plasmodium lactate dehydrogenase by a DNA aptamer. *Proceedings of the National Academy of Sciences*, 110 (40):15967–15972, 2013.

[205] Kumari Asha, Prashant Kumar, Melvin Sanicas, Clement A Meseko, Madhu Khanna, and Binod Kumar. Advancements in nucleic acid based therapeutics against respiratory viral infections. *Journal of Clinical Medicine*, 8(1):6, 2018.

[206] Harmanjit Kaur, Munish Shorie, Manju Sharma, Ashok K Ganguli, and Priyanka Sabherwal. Bridged Rebar Graphene functionalized aptasensor for pathogenic E. coli O78: K80: H11 detection. *Biosensors and Bioelectronics*, 98:486–493, 2017.

[207] Dongsheng Liu and Shankar Balasubramanian. A proton-fuelled DNA nanomachine. *Angewandte Chemie International Edition*, 42(46):5734–5736, 2003.

[208] Maung Nyan Win and Christina D Smolke. Higher-order cellular information processing with synthetic RNA devices. *Science*, 322(5900):456–460, 2008.

[209] Jongmin Kim, Kristin S White, and Erik Winfree. Construction of an in vitro bistable circuit from synthetic transcriptional switches. *Molecular systems biology*, 2(1):68, 2006.

[210] Zeyu Xiao and Omid C Farokhzad. Aptamer-functionalized nanoparticles for medical applications: challenges and opportunities. *ACS nano*, 6(5):3670–3676, 2012.

[211] Hang Xing, Kevin Hwang, Ji Li, Seyed-Fakhreddin Torabi, and Yi Lu. DNA aptamer technology for personalized medicine. *Current opinion in chemical engineering*, 4:79–87, 2014.

[212] Bernard Tinland, Alain Pluen, Jean Sturm, and Gilbert Weill. Persistence length of single-stranded DNA. *Macromolecules*, 30(19):5763–5765, 1997.

[213] Chad A Mirkin, Robert L Letsinger, Robert C Mucic, and James J Storhoff. A DNA-based method for rationally assembling nanoparticles into macroscopic materials. *Nature*, 382:607—-609, 1996.

[214] A Paul Alivisatos, Kai P Johnsson, Xiaogang Peng, Troy E Wilson, Colin J Loweth, Marcel P Bruchez Jr, and Peter G Schultz. Organization of 'nanocrystal molecules' using DNA. *Nature*, 382(6592):609–611, 1996.

[215] Sung Yong Park, Abigail K R Lytton-Jean, Byeongdu Lee, Steven Weigand, George C Schatz, and Chad A Mirkin. DNA-programmable nanoparticle crystallization. *Nature*, 451:553–556, 2008.

[216] Evelyn Auyeung, Ting ING Li, Andrew J Senesi, Abrin L Schmucker, Bridget C Pals, Monica Olvera de La Cruz, and Chad A Mirkin. DNA-mediated nanoparticle crystallization into Wulff polyhedra. *Nature*, 505(7481):73–77, 2014.

[217] Lorenzo Di Michele, Francesco Varrato, Jurij Kotar, Simon H Nathan, Giuseppe Foffi, and Erika Eiser. Multistep kinetic self-assembly of DNA-coated colloids. *Nature communications*, 4(1):2007, 2013.

[218] Lorenzo Di Michele, D Fiocco, F Varrato, Srikanth Sastry, Erika Eiser, and Giuseppe Foffi. Aggregation dynamics, structure, and mechanical properties of bigels. *Soft matter*, 10(20):3633–3648, 2014.

[219] Paul L Biancaniello, John C Crocker, Daniel A Hammer, and Valeria T Milam. DNA-mediated phase behavior of microsphere suspensions. *Langmuir*, 23(5):2688–2693, 2007.

[220] Anand Lopez and Juewen Liu. DNA oligonucleotide-functionalized liposomes: bioconjugate chemistry, biointerfaces, and applications. *Langmuir*, 34(49):15000–15013, 2018.

[221] Indriati Pfeiffer and Fredrik Höök. Bivalent cholesterol-based coupling of oligonucletides to lipid membrane assemblies. *Journal of the American Chemical Society*, 126(33):10224–10225, 2004.

[222] Yee-Hung M Chan, Peter Lenz, and Steven G Boxer. Kinetics of DNA-mediated docking reactions between vesicles tethered to supported lipid bilayers. *Proceedings of the National Academy of Sciences*, 104(48):18913–18918, 2007.

[223] Jason J Benkoski and Fredrik Höök. Lateral mobility of tethered vesicle-DNA assemblies. *The Journal of Physical Chemistry B*, 109(19):9773–9779, 2005.

[224] Minsub Chung, Randall D Lowe, Yee-Hung M Chan, Prasad V Ganesan, and Steven G Boxer. DNA-tethered membranes formed by giant vesicle rupture. *Journal of structural biology*, 168(1):190–199, 2009.

[225] Minsub Chung and Steven G Boxer. Stability of DNA-tethered lipid membranes with mobile tethers. *Langmuir*, 27(9):5492–5497, 2011.

[226] Minsub Chung, Bon Jun Koo, and Steven G Boxer. Formation and analysis of topographical domains between lipid membranes tethered by DNA hybrids of different lengths. *Faraday discussions*, 161:333–345, 2013.

[227] Kenneth G Johnson, Shannon K Bromley, Michael L Dustin, and Matthew L Thomas. A supramolecular basis for CD45 tyrosine phosphatase regulation in sustained T cell activation. *Proceedings of the National Academy of Sciences*, 97(18):10138–10143, 2000.

[228] SY Qi, Jay T Groves, and Arup K Chakraborty. Synaptic pattern formation during cellular recognition. *Proceedings of the National Academy of Sciences*, 98(12):6548–6553, 2001.

[229] Stephan Jan Bachmann, Jurij Kotar, Lucia Parolini, Anđela Šarić, Pietro Cicuta, Lorenzo Di Michele, and Bortolo Matteo Mognetti. Melting transition in lipid vesicles functionalised by mobile DNA linkers. *Soft Matter*, 12(37):7804–7817, 2016.

[230] Lucia Parolini, Jurij Kotar, Lorenzo Di Michele, and Bortolo M Mognetti. Controlling self-assembly kinetics of DNA-functionalized liposomes using toehold exchange mechanism. *ACS nano*, 10(2):2392–2398, 2016.

[231] Stefano Fusco, Hen-Wei Huang, Kathrin E Peyer, Christian Peters, Moritz Häberli, Andre Ulbers, Anastasia Spyrogianni, Eva Pellicer, Jordi Sort, Sotiris E Pratsinis, et al. Shape-switching microrobots for medical applications: the influence of shape in drug delivery and locomotion. *ACS applied materials & interfaces*, 7(12):6803–6811, 2015.

[232] Anupama J Thubagere, Wei Li, Robert F Johnson, Zibo Chen, Shayan Doroudi, Yae Lim Lee, Gregory Izatt, Sarah Wittman, Niranjan Srinivas, Damien Woods, et al. A cargo-sorting DNA robot. *Science*, 357(6356):eaan6558, 2017.

[233] Daniel Kagan, Rawiwan Laocharoensuk, Maria Zimmerman, Corbin Clawson, Shankar Balasubramanian, Dae Kang, Daniel Bishop, Sirilak Sattayasamitsathit, Liangfang Zhang, and Joseph Wang. Rapid delivery of drug carriers propelled and navigated by catalytic nanoshuttles. *Small*, 6(23):2741–2747, 2010.

[234] Joseph Wang. Self-propelled affinity biosensors: moving the receptor around the sample. *Biosensors and Bioelectronics*, 76:234–242, 2016.

[235] Jie Wu, Shankar Balasubramanian, Daniel Kagan, Kalayil Manian Manesh, Susana Campuzano, and Joseph Wang. Motion-based DNA detection using catalytic nanomotors. *Nature Communications*, 1(1):36, 2010.

[236] Chengzhi Hu, Salvador Pané, and Bradley J Nelson. Soft micro-and nanorobotics. *Annual Review of Control, Robotics, and Autonomous Systems*, 1:53–75, 2018.

[237] Sami Nummelin, Boxuan Shen, Petteri Piskunen, Qing Liu, Mauri A Kostiainen, and Veikko Linko. Robotic DNA nanostructures. *ACS Synthetic Biology*, 9(8):1923–1940, 2020.

[238] Nobutaka Hirokawa. Kinesin and dynein superfamily proteins and the mechanism of organelle transport. *Science*, 279(5350):519–526, 1998.

[239] Yu He and David R Liu. Autonomous multistep organic synthesis in a single isothermal solution mediated by a DNA walker. *Nature nanotechnology*, 5(11):778–782, 2010.

[240] William B Sherman and Nadrian C Seeman. A precisely controlled DNA biped walking device. *Nano letters*, 4(7):1203–1207, 2004.

[241] Peng Yin, Harry MT Choi, Colby R Calvert, and Niles A Pierce. Programming biomolecular self-assembly pathways. *Nature*, 451(7176):318–322, 2008.

[242] Dongbao Yao, Sanchita Bhadra, Erhu Xiong, Haojun Liang, Andrew D Ellington, and Cheulhee Jung. Dynamic programming of a DNA walker controlled by protons. *ACS nano*, 14(4):4007–4013, 2020.

[243] Mingxu You, Yan Chen, Xiaobing Zhang, Haipeng Liu, Ruowen Wang, Kelong Wang, Kathryn R Williams, and Weihong Tan. An autonomous and controllable light-driven DNA walking device. *Angewandte Chemie International Edition*, 51(10):2457–2460, 2012.

[244] John H Reif. The design of autonomous DNA nano-mechanical devices: walking and rolling DNA. *Natural Computing*, 2:439–461, 2003.

[245] Alisina Bazrafshan, Travis A Meyer, Hanquan Su, Joshua M Brockman, Aaron T Blanchard, Selma Piranej, Yuxin Duan, Yonggang Ke, and Khalid Salaita. Tunable DNA origami motors translocate ballistically over μm distances at nm/s speeds. *Angewandte Chemie*, 132(24):9601–9608, 2020.

[246] Jing Pan, Yancheng Du, Hengming Qiu, Luke R Upton, Feiran Li, and Jong Hyun Choi. Mimicking chemotactic cell migration with DNA programmable synthetic vesicles. *Nano letters*, 19(12):9138–9144, 2019.

[247] Tosan Omabegho, Ruojie Sha, and Nadrian C Seeman. A bipedal DNA Brownian motor with coordinated legs. *science*, 324(5923):67–71, 2009.

[248] Jonathan Bath, Simon J Green, Katherine E Allen, and Andrew J Turberfield. Mechanism for a directional, processive, and reversible DNA motor. *Small*, 5(13):1513–1516, 2009.

[249] Kyle Lund, Anthony J Manzo, Nadine Dabby, Nicole Michelotti, Alexander Johnson-Buck, Jeanette Nangreave, Steven Taylor, Renjun Pei, Milan N Stojanovic, Nils G Walter, et al. Molecular robots guided by prescriptive landscapes. *Nature*, 465(7295):206–210, 2010.

[250] Hongzhou Gu, Jie Chao, Shou-Jun Xiao, and Nadrian C Seeman. A proximity-based programmable DNA nanoscale assembly line. *Nature*, 465(7295):202–205, 2010.

[251] Kevin Yehl, Andrew Mugler, Skanda Vivek, Yang Liu, Yun Zhang, Mengzhen Fan, Eric R Weeks, and Khalid Salaita. High-speed DNA-based rolling motors powered by RNase H. *Nature nanotechnology*, 11(2):184–190, 2016.

[252] Aaron T Blanchard, Alisina S Bazrafshan, Jacob Yi, Julia T Eisman, Kevin M Yehl, Teng Bian, Andrew Mugler, and Khalid Salaita. Highly polyvalent DNA motors generate 100+ pN of force via autochemophoresis. *Nano letters*, 19(10):6977–6986, 2019.

[253] Alisina Bazrafshan, Maria-Eleni Kyriazi, Brandon Alexander Holt, Wenxiao Deng, Selma Piranej, Hanquan Su, Yuesong Hu, Afaf H El-Sagheer, Tom Brown, Gabriel A Kwong, et al. DNA gold nanoparticle motors demonstrate processive motion with bursts of speed up to 50 nm per second. *ACS nano*, 15(5):8427–8438, 2021.

[254] Tae-Gon Cha, Jing Pan, Haorong Chen, Janette Salgado, Xiang Li, Chengde Mao, and Jong Hyun Choi. A synthetic DNA motor that transports nanoparticles along carbon nanotubes. *Nature nanotechnology*, 9(1):39–43, 2014.

[255] Pengfei Zhan, Kevin Jahnke, Na Liu, and Kerstin Göpfrich. Functional DNA-based cytoskeletons for synthetic cells. *Nature Chemistry*, 14(8):958–963, 2022.

[256] Tian Jin, Xuehua Xu, Jun Fang, Nilgun Isik, Jianshe Yan, Joseph A Brzostowski, and Dale Hereld. How human leukocytes track down and destroy pathogens: lessons learned from the model organism Dictyostelium discoideum. *Immunologic Research*, 43:118–127, 2009.

[257] Yancheng Du, Jing Pan, Hengming Qiu, Chengde Mao, and Jong Hyun Choi. Mechanistic understanding of surface migration dynamics with DNA walkers. *The Journal of Physical Chemistry B*, 125(2):507–517, 2021.

[258] Joseph N Zadeh, Conrad D Steenberg, Justin S Bois, Brian R Wolfe, Marshall B Pierce, Asif R Khan, Robert M Dirks, and Niles A Pierce. NUPACK: analysis and design of nucleic acid systems. *Journal of computational chemistry*, 32(1):170–173, 2011.

[259] Kang Li. The image stabilizer plugin for ImageJ. http://www.cs.cmu.edu/~kangli/code/Image_Stabilizer.html, February 2008.

[260] G. Bradski. The OpenCV Library. *Dr. Dobb's Journal of Software Tools*, 2000.

[261] Yohsuke T Fukai and Kyogo Kawaguchi. LapTrack: linear assignment particle tracking with tunable metrics. *Bioinformatics*, page btac799, December 2022. ISSN 1367-4803. doi: 10.1093/bioinformatics/btac799.

[262] Yohsuke T. Fukai. laptrack. https://doi.org/10.5281/zenodo.5519537, 2021.

[263] Albert Einstein. Über die von der molekularkinetischen Theorie der Wärme geforderte Bewegung von in ruhenden Flüssigkeiten suspendierten Teilchen. *Annalen der physik*, 4, 1905.

[264] Marian Von Smoluchowski. Zur kinetischen theorie der brownschen molekularbewegung und der suspensionen. *Annalen der physik*, 326(14):756–780, 1906.

[265] András Perl, Alberto Gomez-Casado, Damien Thompson, Henk H Dam, Pascal Jonkheijm, David N Reinhoudt, and Jurriaan Huskens. Gradient-driven motion of multivalent ligand molecules along a surface functionalized with multiple receptors. *Nature chemistry*, 3(4):317–322, 2011.

[266] Theresa Chang, Dorota I Rozkiewicz, Bart Jan Ravoo, EW Meijer, and David N Reinhoudt. Directional movement of dendritic macromolecules on gradient surfaces. *Nano letters*, 7(4):978–980, 2007.

[267] SF Shimobayashi, B Matteo Mognetti, Lucia Parolini, D Orsi, Pietro Cicuta, and Lorenzo Di Michele. Direct measurement of DNA-mediated adhesion between lipid bilayers. *Physical Chemistry Chemical Physics*, 17(24):15615–15628, 2015.

[268] Janna Lowensohn, Laurie Stevens, Daniel Goldstein, and Bortolo Matteo Mognetti. Sliding across a surface: particles with fixed and mobile ligands. *The Journal of Chemical Physics*, 156(16):164902, 2022.

[269] Anping Liu and Xiaoyang Qi. Molecular dynamics simulations of DOPC lipid bilayers: The effect of Lennard-Jones parameters of hydrocarbon chains. *Computational molecular bioscience*, 2(3):78, 2012.

[270] Xingyu Jiang, Qiaobing Xu, Stephan KW Dertinger, Abraham D Stroock, Tzung-may Fu, and George M Whitesides. A general method for patterning gradients of biomolecules on surfaces using microfluidic networks. *Analytical chemistry*, 77(8):2338–2347, 2005.

[271] Noo Li Jeon, Stephan KW Dertinger, Daniel T Chiu, Insung S Choi, Abraham D Stroock, and George M Whitesides. Generation of solution and surface gradients using microfluidic systems. *Langmuir*, 16(22):8311–8316, 2000.

[272] Noo Li Jeon, Harihara Baskaran, Stephan KW Dertinger, George M Whitesides, Livingston Van De Water, and Mehmet Toner. Neutrophil chemotaxis in linear and complex gradients of interleukin-8 formed in a microfabricated device. *Nature biotechnology*, 20 (8):826–830, 2002.

[273] Wajeeh Saadi, Shur-Jen Wang, Francis Lin, and Noo Li Jeon. A parallel-gradient microfluidic chamber for quantitative analysis of breast cancer cell chemotaxis. *Biomedical microdevices*, 8:109–118, 2006.

[274] Amir Shamloo, Ning Ma, Mu-ming Poo, Lydia L Sohn, and Sarah C Heilshorn. Endothelial cell polarization and chemotaxis in a microfluidic device. *Lab on a chip*, 8(8): 1292–1299, 2008.

[275] Bobak Mosadegh, Carlos Huang, Jeong Won Park, Hwa Sung Shin, Bong Geun Chung, Sun-Kyu Hwang, Kun-Hong Lee, Hyung Joon Kim, James Brody, and Noo Li Jeon. Generation of stable complex gradients across two-dimensional surfaces and three-dimensional gels. *Langmuir*, 23(22):10910–10912, 2007.

[276] Natalja Strelnikova, Florian Herren, Cora-Ann Schoenenberger, and Thomas Pfohl. Formation of actin networks in microfluidic concentration gradients. *Frontiers in Materials*, 3:20, 2016.

[277] Nithya Murugesan, Siddhartha Singha, Tapobrata Panda, and Sarit K Das. A diffusion based long-range and steady chemical gradient generator on a microfluidic device for studying bacterial chemotaxis. *Journal of Micromechanics and Microengineering*, 26(3): 035011, 2016.

[278] Shing-Yi Cheng, Steven Heilman, Max Wasserman, Shivaun Archer, Michael L Shuler, and Mingming Wu. A hydrogel-based microfluidic device for the studies of directed cell migration. *Lab on a Chip*, 7(6):763–769, 2007.

[279] Irmeli Barkefors, Sara Thorslund, Fredrik Nikolajeff, and Johan Kreuger. A fluidic device to study directional angiogenesis in complex tissue and organ culture models. *Lab on a Chip*, 9(4):529–535, 2009.

[280] Vinay V Abhyankar, Mary A Lokuta, Anna Huttenlocher, and David J Beebe. Characterization of a membrane-based gradient generator for use in cell-signaling studies. *Lab on a Chip*, 6(3):389–393, 2006.

[281] Bo Liedberg and Pentti Tengvall. Molecular gradients of ω-substituted alkanethiols on gold: preparation and characterization. *Langmuir*, 11(10):3821–3827, 1995.

[282] Pamela Zengel, Anna Nguyen-Hoang, Christoph Schildhammer, Roman Zantl, Valentin Kahl, and Elias Horn. μ-slide chemotaxis: a new chamber for long-term chemotaxis studies. *BMC cell biology*, 12:1–14, 2011.

[283] Sara Morgenthaler, Seunghwan Lee, Stefan Zürcher, and Nicholas D Spencer. A simple, reproducible approach to the preparation of surface-chemical gradients. *Langmuir*, 19 (25):10459–10462, 2003.

[284] Sung-Hwan Choi and Bi-min Zhang Newby. Micrometer-scaled gradient surfaces generated using contact printing of octadecyltrichlorosilane. *Langmuir*, 19(18):7427–7435, 2003.

[285] Isabelle Caelen, André Bernard, David Juncker, Bruno Michel, Harry Heinzelmann, and Emmanuel Delamarche. Formation of gradients of proteins on surfaces with microfluidic networks. *Langmuir*, 16(24):9125–9130, 2000.

[286] Dmitry Ershov, Minh-Son Phan, Joanna W Pylvänäinen, Stéphane U Rigaud, Laure Le Blanc, Arthur Charles-Orszag, James RW Conway, Romain F Laine, Nathan H Roy, Daria Bonazzi, et al. TrackMate 7: integrating state-of-the-art segmentation algorithms into tracking pipelines. *Nature Methods*, 19(7):829–832, 2022.

[287] Jean-Yves Tinevez, Nick Perry, Johannes Schindelin, Genevieve M Hoopes, Gregory D Reynolds, Emmanuel Laplantine, Sebastian Y Bednarek, Spencer L Shorte, and Kevin W Eliceiri. TrackMate: an open and extensible platform for single-particle tracking. *Methods*, 115:80–90, 2017.

[288] PH Erik Hamming, Nico J Overeem, Kevin Diestelhorst, Tren Fiers, Malte Tieke, Gaël M Vos, Geert-Jan PH Boons, Erhard van der Vries, Stephan Block, and Jurriaan Huskens. Receptor density-dependent motility of influenza virus particles on surface gradients. *ACS applied materials & interfaces*, 2023.

[289] B Alberts, A Johnson, J Lewis, D Morgan, M Raff, K Roberts, and P Walter. Molecular biology of the cell, 6th edition. 2014.

[290] Nicholas R Markham and Michael Zuker. DINAMelt web server for nucleic acid melting prediction. *Nucleic acids research*, 33(suppl_2):W577–W581, 2005.

[291] Nicholas R Markham and Michael Zuker. UNAFold: software for nucleic acid folding and hybridization. *Bioinformatics: structure, function and applications*, pages 3–31, 2008.

[292] Roumen A Dimitrov and Michael Zuker. Prediction of hybridization and melting for double-stranded nucleic acids. *Biophysical Journal*, 87(1):215–226, 2004.

[293] Stef AJ van der Meulen and Mirjam E Leunissen. Solid colloids with surface-mobile DNA linkers. *Journal of the American Chemical Society*, 135(40):15129–15134, 2013.

[294] Pritam Kumar Jana and Bortolo Matteo Mognetti. Translational and rotational dynamics of colloidal particles interacting through reacting linkers. *Physical Review E*, 100(6): 060601, 2019.

[295] Daniel T Gillespie. Exact stochastic simulation of coupled chemical reactions. *The journal of physical chemistry*, 81(25):2340–2361, 1977.

[296] Bortolo Mognetti. Model diffusion. https://github.com/bmognetti/Gradient-of-Ligands-/blob/main/ModelDiffusion_LE.ipynb, 2023.

[297] Francisco J Martinez-Veracoechea, Bortolo M Mognetti, Stefano Angioletti-Uberti, Patrick Varilly, Daan Frenkel, and Jure Dobnikar. Designing stimulus-sensitive colloidal walkers. *Soft matter*, 10(19):3463–3470, 2014.

[298] Andy WC Lau and Tom C Lubensky. State-dependent diffusion: Thermodynamic consistency and its path integral formulation. *Physical Review E*, 76(1):011123, 2007.

[299] Christoph Widder, Fabian Koch, and Tanja Schilling. Generalized Langevin dynamics simulation with non-stationary memory kernels: How to make noise. *The Journal of Chemical Physics*, 157(19), 2022.

[300] Roland R. Netz. Derivation of the non-equilibrium generalized Langevin equation from a generic time-dependent Hamiltonian, 2023.

[301] Klaus Ley, Carlo Laudanna, Myron I Cybulsky, and Sussan Nourshargh. Getting to the site of inflammation: the leukocyte adhesion cascade updated. *Nature Reviews Immunology*, 7(9):678–689, 2007.

[302] William A Muller. Leukocyte-endothelial cell interactions in the inflammatory response. *Laboratory investigation*, 82(5):521–534, 2002.

[303] Sabyasachi Dasgupta, Thorsten Auth, Nir S Gov, Timothy J Satchwell, Eric Hanssen, Elizabeth S Zuccala, David T Riglar, Ashley M Toye, Timo Betz, Jake Baum, et al. Membrane-wrapping contributions to malaria parasite invasion of the human erythrocyte. *Biophysical journal*, 107(1):43–54, 2014.

[304] Michael A Fischbach, Jeffrey A Bluestone, and Wendell A Lim. Cell-based therapeutics: the next pillar of medicine. *Science translational medicine*, 5(179):179ps7–179ps7, 2013.

[305] Adrian Joseph, Claudia Contini, Denis Cecchin, Sophie Nyberg, Lorena Ruiz-Perez, Jens Gaitzsch, Gavin Fullstone, Xiaohe Tian, Juzaili Azizi, Jane Preston, et al. Chemotactic synthetic vesicles: Design and applications in blood-brain barrier crossing. *Science Advances*, 3(8):e1700362, 2017.

[306] Michael H Kershaw, Gang Wang, Jennifer A Westwood, Russell K Pachynski, H Lee Tiffany, Francesco M Marincola, Ena Wang, Howard A Young, Philip M Murphy, and Patrick Hwu. Redirecting migration of T cells to chemokine secreted from tumors by genetic modification with CXCR2. *Human gene therapy*, 13(16):1971–1980, 2002.

[307] Edmund K Moon, Carmine Carpenito, Jing Sun, Liang-Chuan S Wang, Veena Kapoor, Jarrod Predina, Daniel J Powell Jr, James L Riley, Carl H June, and Steven M Albelda. Expression of a functional CCR2 receptor enhances tumor localization and tumor eradication by retargeted human T cells expressing a mesothelin-specific chimeric antibody receptor. *Clinical cancer research*, 17(14):4719–4730, 2011.

[308] Jeffrey M Karp and Grace Sock Leng Teo. Mesenchymal stem cell homing: the devil is in the details. *Cell stem cell*, 4(3):206–216, 2009.

[309] Jacopo Sforzi, Lorenzo Palagi, and Silvio Aime. Liposome-based bioassays. *Biology*, 9 (8):202, 2020.

[310] Qingtao Liu and Ben J Boyd. Liposomes in biosensors. *Analyst*, 138(2):391–409, 2013.

[311] Federico Mazur, Marta Bally, Brigitte Städler, and Rona Chandrawati. Liposomes and lipid bilayers in biosensors. *Advances in colloid and interface science*, 249:88–99, 2017.

[312] Nelson Monteiro, Albino Martins, Rui L Reis, and Nuno M Neves. Liposomes in tissue engineering and regenerative medicine. *Journal of the Royal Society Interface*, 11(101): 20140459, 2014.

[313] Mojtaba Shafiei, Mohamed Nainar Mohamed Ansari, Saiful Izwan Abd Razak, and Muhammad Umar Aslam Khan. A comprehensive review on the applications of exosomes and liposomes in regenerative medicine and tissue engineering. *Polymers*, 13(15): 2529, 2021.

[314] Naboneeta Sarkar and Susmita Bose. Liposome-encapsulated curcumin-loaded 3D printed scaffold for bone tissue engineering. *ACS applied materials & interfaces*, 11(19):17184–17192, 2019.

[315] Adrian Leathers, Michal Walczak, Ryan A Brady, Assala Al Samad, Jurij Kotar, Michael J Booth, Pietro Cicuta, and Lorenzo Di Michele. Reaction-diffusion patterning of DNA-based artificial cells. *Journal of the American Chemical Society*, 144(38):17468–17476, 2022.

[316] John Crank. *The mathematics of diffusion*. Oxford university press, 1979.

[317] Pauli Virtanen, Ralf Gommers, Travis E. Oliphant, Matt Haberland, Tyler Reddy, David Cournapeau, Evgeni Burovski, Pearu Peterson, Warren Weckesser, Jonathan Bright, Stéfan J. van der Walt, Matthew Brett, Joshua Wilson, K. Jarrod Millman, Nikolay Mayorov, Andrew R. J. Nelson, Eric Jones, Robert Kern, Eric Larson, C J Carey, İlhan Polat, Yu Feng, Eric W. Moore, Jake VanderPlas, Denis Laxalde, Josef Perktold, Robert Cimrman, Ian Henriksen, E. A. Quintero, Charles R. Harris, Anne M. Archibald, Antônio H. Ribeiro, Fabian Pedregosa, Paul van Mulbregt, and SciPy 1.0 Contributors. SciPy 1.0: fundamental algorithms for scientific computing in Python. *Nature Methods*, 17:261–272, 2020. doi: 10.1038/s41592-019-0686-2.

[318] Microscope resolution: Concepts, factors and calculation. URL https://www.leica-microsystems.com/science-lab/life-science/microscope-resolution-concepts-factors-and-calculation/.

[319] Johannes Schindelin, Ignacio Arganda-Carreras, Erwin Frise, Verena Kaynig, Mark Longair, Tobias Pietzsch, Stephan Preibisch, Curtis Rueden, Stephan Saalfeld, Benjamin Schmid, et al. Fiji: an open-source platform for biological-image analysis. *Nature methods*, 9(7):676–682, 2012.

[320] Sifang Chen and Georg Seelig. Programmable patterns in a DNA-based reaction-diffusion system. *Soft Matter*, 16(14):3555–3563, 2020.

[321] Qingjia Chi, Guixue Wang, and Jiahuan Jiang. The persistence length and length per base of single-stranded DNA obtained from fluorescence correlation spectroscopy measurements using mean field theory. *Physica A: Statistical Mechanics and its Applications*, 392(5):1072–1079, 2013.

[322] Melissa Massey, W Russ Algar, and Ulrich J Krull. Fluorescence resonance energy transfer (FRET) for DNA biosensors: FRET pairs and Förster distances for various dye-DNA conjugates. *Analytica chimica acta*, 568(1-2):181–189, 2006.

[323] Drew Lysne, Tim Hachigian, Chris Thachuk, Jeunghoon Lee, and Elton Graugnard. Leveraging steric moieties for kinetic control of DNA strand displacement reactions. *Journal of the American Chemical Society*, 145(30):16691–16703, 2023.

[324] Jun Wang, Hayashi Raito, Naohiko Shimada, and Atsushi Maruyama. A cationic copolymer enhances tesponsiveness and robustness of DNA circuits. *Small*, 19(42):2304091, 2023.

[325] Jinbo Zhu, Filip Bošković, Bao-Nguyen T Nguyen, Jonathan R Nitschke, and Ulrich F Keyser. Kinetics of toehold-mediated DNA strand displacement depend on FeII4L4 tetrahedron concentration. *Nano Letters*, 21(3):1368–1374, 2021.

[326] George Gabriel Stokes. On the effect of internal friction of fluids on the motion of pendulums. *Trans. Camb. phi1. S0c*, 9(8):106, 1850.

[327] Tadahiko Ando, Jun Takagi, Taeko Kosawa, and Yonosuke Ikeda. Isolation and characterization of enzymes with nicking action from phage T4-infected Escherichia coli. *The Journal of Biochemistry*, 66(1):1–10, 1969.

[328] Richard D Morgan, Celine Calvet, Matthew Demeter, Rafael Agra, and Huimin Kong. Characterization of the specific DNA nicking activity of restriction endonuclease N. BstNBI, 2000.

[329] Penghua Zhang, Priscilla Hiu-Mei Too, James C Samuelson, Siu-Hong Chan, Tamas Vincze, Stephanie Doucette, Stefan Bäckström, Konstantinos D Potamousis, Timothy M Schramm, Dan Forrest, et al. Engineering BspQI nicking enzymes and application of N. BspQI in DNA labeling and production of single-strand DNA. *Protein expression and purification*, 69(2):226–234, 2010.

[330] Optimizing restriction endonuclease reactions. URL https://www.neb.com/en-gb/protocols/2012/12/07/optimizing-restriction-endonuclease-reactions.

Appendix A

Nanostructures and their sequences

Throughout this section, construct structures and strand sequences are given in the 5'-3' direction. Domain structures in strand sequences are indicated with spaces in the strand sequences.

A.1 Nanostructures for Chapter 3

Table A.1: **Receptor and ligand constructs for Chapter 3, and the oligonucleotides they are composed of.** The constructs are self-assembled through the annealing process outlined in the Methods to a final construct concentration of 2 μM. Constructs require strands in 1:1 stoichiometric ratios.

Construct	**Strands**
Ligand	$S_1 + S_5 + S_6$
Receptor	$S_2 + S_3 + S_4$

Table A.2: **Sequences and modifications of oligonucleotide strands for Chapter 3.** Strands S_1 and S_2 have optional terminal Alexa Fluor 488 (NHS ester) modifications. Strands S_6, S_3 and S_4 have terminal modifications of biotin, cholesterol-TEG and cholesteryl-TEG respectively. Sequences for inert versions of strands B_2 and B_5 that lack the reactive moiety (*i.e.* the sticky end) are also included.

Strand	**Sticky end length / nt**	**Sequence (5' to 3')**
S_1	all	CGCGACTTCCTCGCCGCG CGCGAGTTCGAGCTACGC (—AF488)
S_2	0 (inert)	GAGAGTAGGACCGGCGCG
	3	CGC TT GAGAGTAGGACCGGCGCG
	4	CCGC TT GAGAGTAGGACCGGCGCG
	5	GCCGC TT GAGAGTAGGACCGGCGCG
	6	GCACGC TT GAGAGTAGGACCGGCGCG
	7	CGGTGCG TT GAGAGTAGGACCGGCGCG (—AF488)
	8	GCGTCCAC TT GAGAGTAGGACCGGCGCG
	9	GCTGCGACC TT GAGAGTAGGACCGGCGCG
	10	GGCACGGACG TT GAGAGTAGGACCGGCGCG
S_3	all	CGTTTGCAGGAACGAGAC TT — Cholesterol-TEG
S_4	all	Cholesteryl-TEG — TT GTCTCGTTCCTGCAAACG CGCGC-CGGTCCTACTCTC
S_5	0 (inert)	GCGTAGCTCGAACTCGCG
	3	GCG TT GCGTAGCTCGAACTCGCG
	4	GCGG TT GCGTAGCTCGAACTCGCG
	5	GCGGC TT GCGTAGCTCGAACTCGCG
	6	GCGTGC TT GCGTAGCTCGAACTCGCG
	7	CGCACCG TT GCGTAGCTCGAACTCGCG
	8	GTGGACGC TT GCGTAGCTCGAACTCGCG
	9	GGTCGCAGC TT GCGTAGCTCGAACTCGCG
	10	CGTCCGTGCC TT GCGTAGCTCGAACTCGCG
S_6	all	CGCGGCGAGGAAGTCGCG — Biotin

A.2 Nanostructures for Chapter 4

Table A.3: **Receptor and ligand constructs for Chapter 4, and the oligonucleotides they are composed of.** The constructs are self-assembled through the annealing process outlined in the Methods to a final construct concentration of 2 μM. Constructs require strands in 1:1 stoichiometric ratios. Note that strands S_1, S_3, S_4 and S_6 are the same strand sequences used for nanostructures in Chapter 3; strands B_2, B_5 and B_7 are new strand sequences specific to the burnt-bridges system in Chapter 4.

Construct	**Strands**
Substrate	$S_1 + B_5 + S_6$
GUV	$B_2 + S_3 + S_4$
Fuel	B_7

Table A.4: **Sequences and modifications of oligonucleotide strands for Chapter 4.** Strands S_1, S_3, S_4, S_6 and S_7 have terminal modification of Alexa Fluor 488 (NHS ester), cholesterol-TEG, cholesteryl-TEG, biotin and Iowa Black FQ respectively. Sequences for inert versions of strands B_2 and B_5 that lack the reactive moiety are also included.

Strand	**Sequence (5' to 3')**
S_1	CGCGACTTCCTCGCCGCG CGCGAGTTCGAGCTACGC (—AF488)
B_2	TTCATCA CTAACTCGCACTACTTACAG AT GAGAGTAGGACCG-GCGCG
B_2 (inert)	GAGAGTAGGACCGGCGCG
S_3	CGTTTGCAGGAACGAGAC TT — Cholesterol-TEG
S_4	Cholesteryl-TEG — TT GTCTCGTTCCTGCAAACG CGCGCCGGTCC-TACTCTC
B_5	CTAACTCGC ACTACTTAC GCTCAACTTCATCA CT GTAAGTAGTGC-GAGTTAG TGATGAA TT GCGTAGCTCGAACTCGCG
B_5 (inert)	GCGTAGCTCGAACTCGCG
S_6	CGCGGCGAGGAAGTCGCG — Biotin
B_7	IABkFQ — ACGCTCAAC TTCATCACT AACTCGCACTACTTAC AGT-GATGAAGTTGAGCGT AAGTAGT

Appendix B

Supplementary theory for Chapter 3

B.1 Proof of Equation 3.18

This section outlines the derivation of Equation 3.18 using Equation 3.4. From Equation 3.17 we calculate

$$\begin{aligned}\beta V'_{\text{multi}}(x_{\text{CM}}) &= -\frac{n'_b(x_{\text{CM}})N_R}{N_R - n_b(x_{\text{CM}})} + \frac{n_b(x_{\text{CM}})N'_L(x_{\text{CM}}) - N_L(x_{\text{CM}})n'_b(x_{\text{CM}})}{N_L(x_{\text{CM}}) - n_b(x_{\text{CM}})} + n'_b(x_{\text{CM}}) \\ &\quad + N'_L(x_{\text{CM}}) \log\left[1 - \frac{n_b(x_{\text{CM}})}{N_L(x_{\text{CM}})}\right] \\ &\equiv \Lambda + N'_L(x_{\text{CM}}) \log\left[1 - \frac{n_b(x_{\text{CM}})}{N_L(x_{\text{CM}})}\right]\end{aligned} \tag{B.1}$$

By deriving Equation 3.4 we obtain

$$\begin{aligned}n'_b(x_{\text{CM}}) &= K_{\text{eq}}\left[N'_L(x_{\text{CM}}) - n'_b(x_{\text{CM}})\right]\left[N_R - n_b(x_{\text{CM}})\right] - K_{\text{eq}}\left[N_L(x_{\text{CM}}) - n_b(x_{\text{CM}})\right] n'_b(x_{\text{CM}}) \\ &= \frac{n_b(x_{\text{CM}})\left[N'_L(x_{\text{CM}}) - n'_b(x_{\text{CM}})\right]}{N_L(x_{\text{CM}}) - n_b(x_{\text{CM}})} - \frac{n_b(x_{\text{CM}})n'_b(x_{\text{CM}})}{N_R - n_b(x_{\text{CM}})}\end{aligned} \tag{B.2}$$

where in the second line we have used Equation 3.4. From the previous equation we obtain an expression for $n'_b(x_{\text{CM}})$ as a function of $N'_L(x_{\text{CM}})$

$$n'_b(x_{\text{CM}}) = \frac{\left[N_R - n_b(x_{\text{CM}})\right] n_b(x_{\text{CM}})N'_L(x_{\text{CM}})}{N_L(x_{\text{CM}})N_R - n_b(x_{\text{CM}})^2} \tag{B.3}$$

By using the previous equation in Equation B.1 we can prove that the first three terms in the right-hand-side of the latter cancel, therefore proving Equation 3.18. Specifically

$$
\begin{aligned}
\Lambda &= -\frac{n_b'(x_{\rm CM})N_R}{N_R - n_b(x_{\rm CM})} + \frac{n_b(x_{\rm CM})N_L'(x_{\rm CM}) - N_L(x_{\rm CM})n_b'(x_{\rm CM})}{N_L(x_{\rm CM}) - n_b(x_{\rm CM})} + n_b'(x_{\rm CM}) \\
&= -\frac{n_b(x_{\rm CM})N_R N_L'(x_{\rm CM})}{N_L(x_{\rm CM})N_R - n_b(x_{\rm CM})^2} + \frac{n_b(x_{\rm CM})N_L'(x_{\rm CM})}{N_L(x_{\rm CM}) - n_b(x_{\rm CM})} \\
&\quad -\frac{N_L(x_{\rm CM})}{N_L(x_{\rm CM}) - n_b(x_{\rm CM})}\frac{[N_R - n_b(x_{\rm CM})]\, n_b(x_{\rm CM})N_L'(x_{\rm CM})}{N_L(x_{\rm CM})N_R - n_b(x_{\rm CM})^2} \\
&\quad +\frac{[N_R - n_b(x_{\rm CM})]\, n_b(x_{\rm CM})N_L'(x_{\rm CM})}{N_L(x_{\rm CM})N_R - n_b(x_{\rm CM})^2} \\
&= \frac{n_b(x_{\rm CM})N_L'(x_{\rm CM})}{N_L(x_{\rm CM}) - n_b(x_{\rm CM})} - \frac{N_L(x_{\rm CM})}{N_L(x_{\rm CM}) - n_b(x_{\rm CM})}\frac{[N_R - n_b(x_{\rm CM})]\, n_b(x_{\rm CM})N_L'(x_{\rm CM})}{N_L(x_{\rm CM})N_R - n_b(x_{\rm CM})^2} \\
&\quad -\frac{n_b(x_{\rm CM})^2 N_L'(x_{\rm CM})}{N_L(x_{\rm CM})N_R - n_b(x_{\rm CM})^2} \\
&= \frac{n_b(x_{\rm CM})N_L'(x_{\rm CM})}{N_L(x_{\rm CM}) - n_b(x_{\rm CM})} \\
&\quad -\frac{n_b(x_{\rm CM})N_L'(x_{\rm CM})}{N_L(x_{\rm CM})N_R - n_b(x_{\rm CM})^2}\left[\frac{N_L(x_{\rm CM})\,[N_R - n_b(x_{\rm CM})]}{N_L(x_{\rm CM}) - n_b(x_{\rm CM})} + n_b(x_{\rm CM})\right] \\
&= \frac{n_b(x_{\rm CM})N_L'(x_{\rm CM})}{N_L(x_{\rm CM}) - n_b(x_{\rm CM})} - \frac{n_b(x_{\rm CM})N_L'(x_{\rm CM})}{N_L(x_{\rm CM})N_R - n_b(x_{\rm CM})^2}\frac{N_L(x_{\rm CM})N_R - n_b(x_{\rm CM})^2}{N_L(x_{\rm CM}) - n_b(x_{\rm CM})} \\
&= 0
\end{aligned}
$$

Appendix C

Supplementary figures

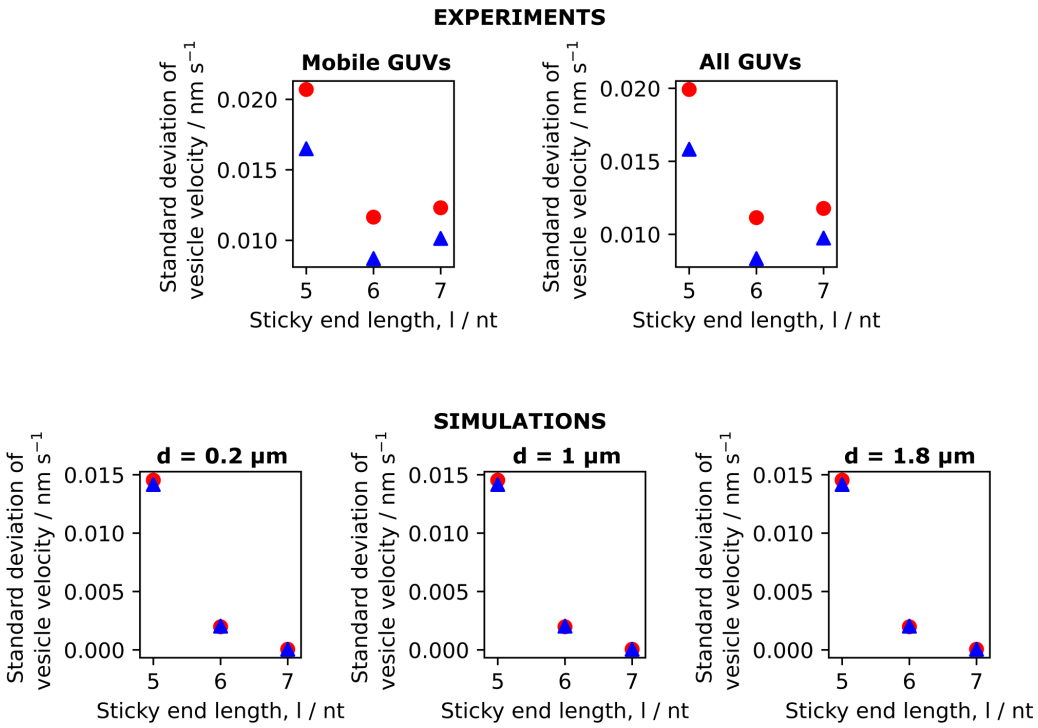


Figure C.1: **Full data showing that vesicles functionalised with longer sticky ends diffuse more slowly.** Standard deviation of average vesicle velocity versus sticky end length, as per the vesicle motility experiments in Chapter 3); the velocity is decomposed into components parallel and perpendicular to the gradient direction. The plots show the same comparison as in Figure 3.12, although in this case both the mobile population and entire vesicle sample are shown for experimental vesicle data, and simulation results for all simulated vesicle diameters are shown.

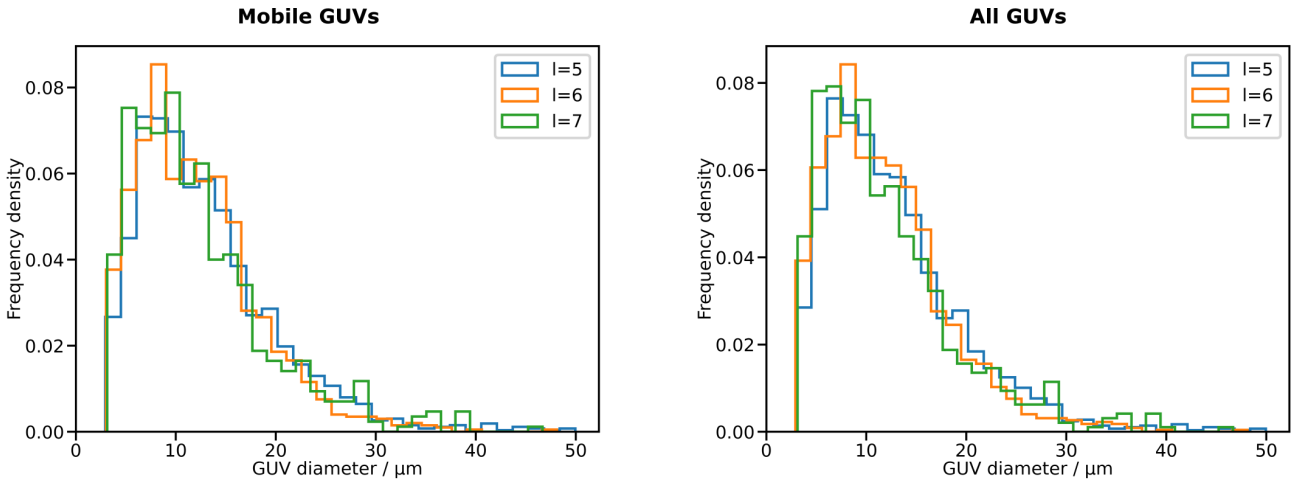


Figure C.2: **Size distributions of vesicles recorded in vesicle motility experiments in Chapter 3, shown for the mobile vesicle population and for all vesicles combined.** This figure is the equivalent of Figure 3.3b, but with an additional plot showing data for all vesicles (*i.e.* the mobile and immobile populations combined). Data are shown for sticky end lengths $l = 5$, 6 and 7 nt in both plots. Vesicle diameters were measured as part of the automated tracking process outlined in Section 3.2.5.

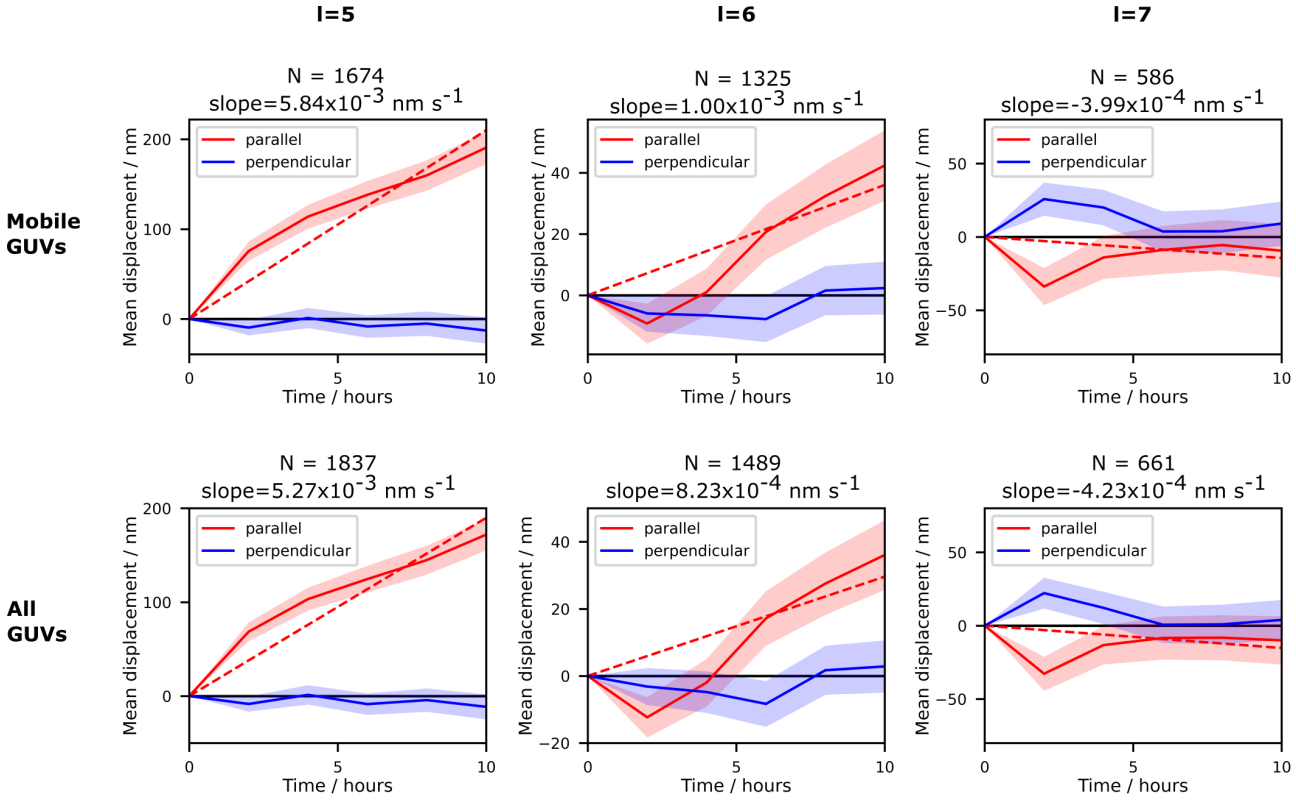


Figure C.3: **Full experimental data showing that vesicle drift velocity increases with decreasing sticky end length.** These plots are the equivalent of the line plots in Figure 3.10 in which only data for the mobile vesicle population are shown; here, additional plots are included to show data for all vesicles (*i.e.* the mobile and immobile populations combined).

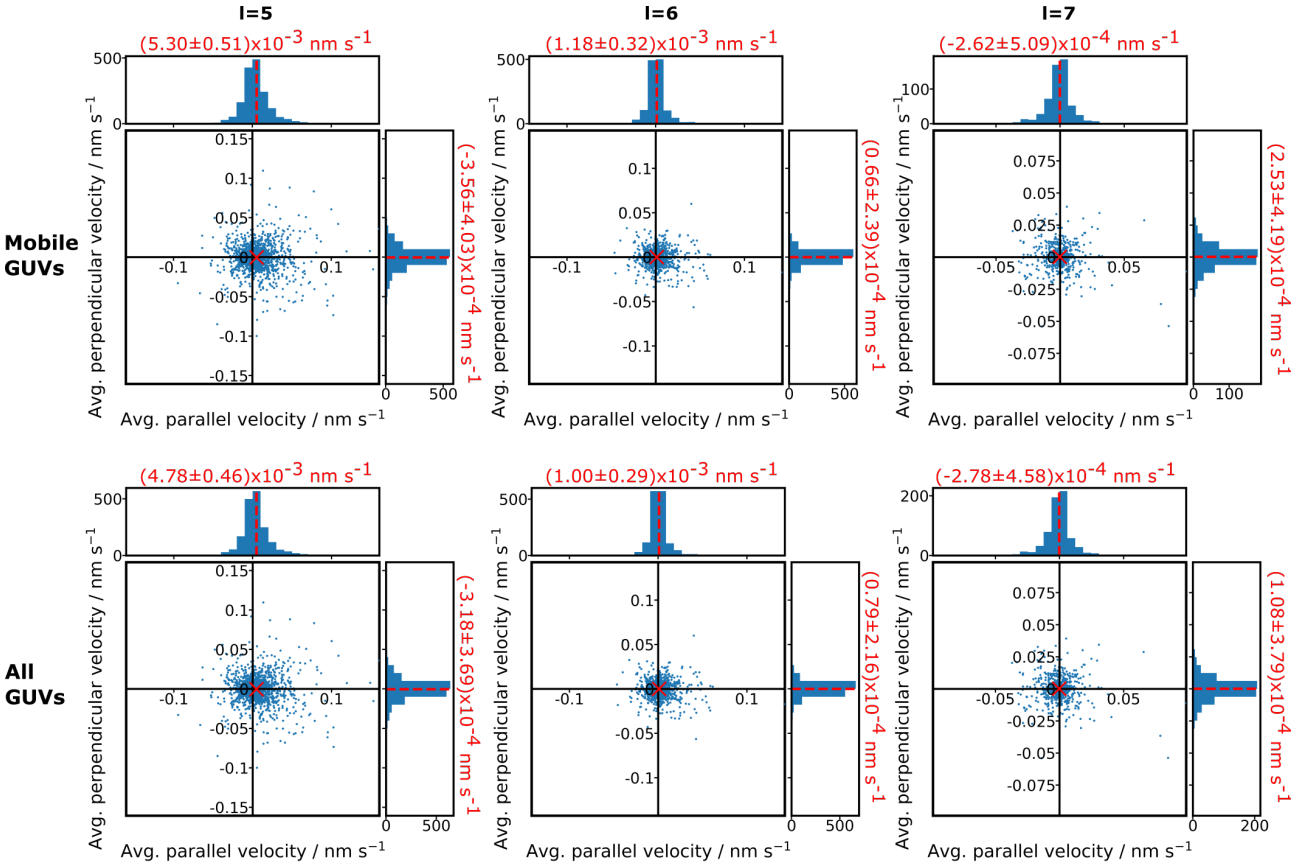


Figure C.4: **Full experimental distributions of vesicle velocities relative to the gradient direction.** These plots are the equivalent of the scatter plots in Figure 3.10 in which only data for the mobile (or mobile) vesicle population are shown; here, additional plots are included to show data for all vesicles (*i.e.* the mobile and immobile populations combined). The axes of the lots have been left uncropped here to show the full distributions of vesicle velocities.

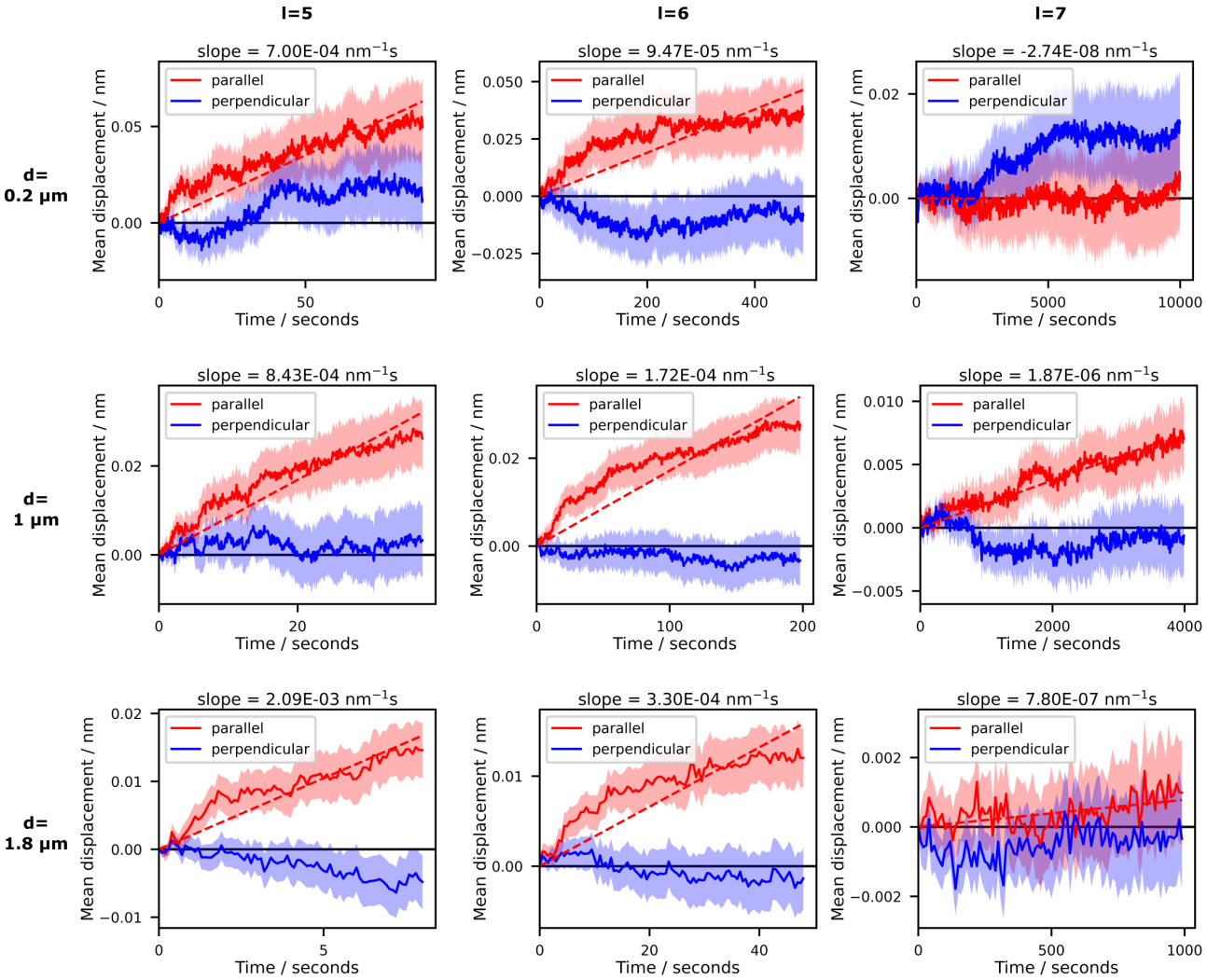


Figure C.5: **Full trajectory data from simulations, for varying vesicle diameter and sticky end length.** These plots are the equivalent of the line plots in Figure 3.11 in which data were shown for 1 μm-diameter vesicles, and the trajectory durations were cropped to a common length for ease of comparison; here, the full simulated durations are shown instead for vesicles of diameter $d = 0.2$, 1 and 1.8 μm.

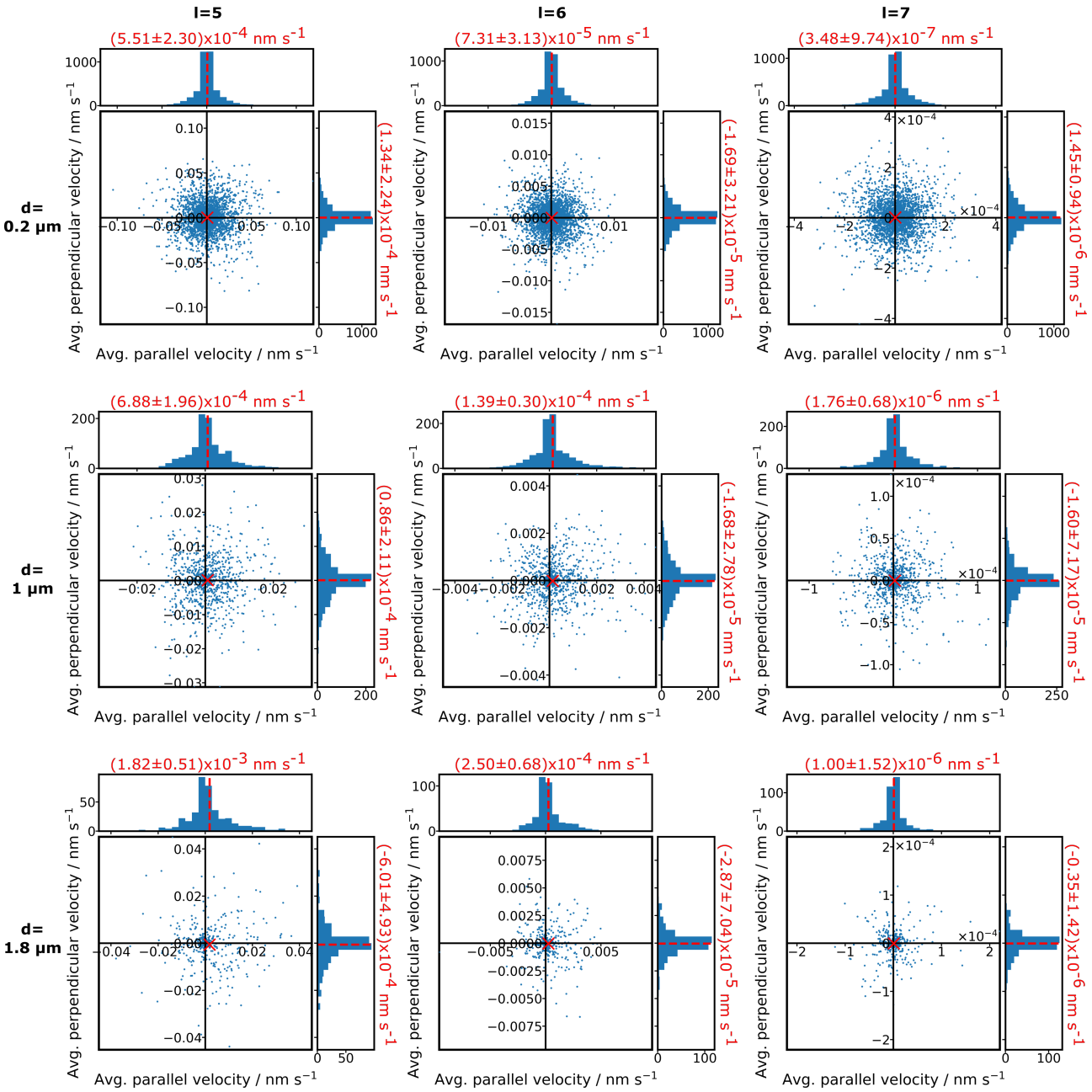


Figure C.6: **Full distributions of simulated vesicle velocities relative to the gradient, for varying vesicle diameter and sticky end length.** These plots are the equivalent of the scatter plots in Figure 3.11 in which data were shown for 1 μm-diameter vesicles, and the axes were cropped to enable ease of visualisation. Here, data are shown for vesicles of diameter $d = 0.2$, 1 and 1.8 μm, and the axes have been left uncropped to show the full velocity distributions.

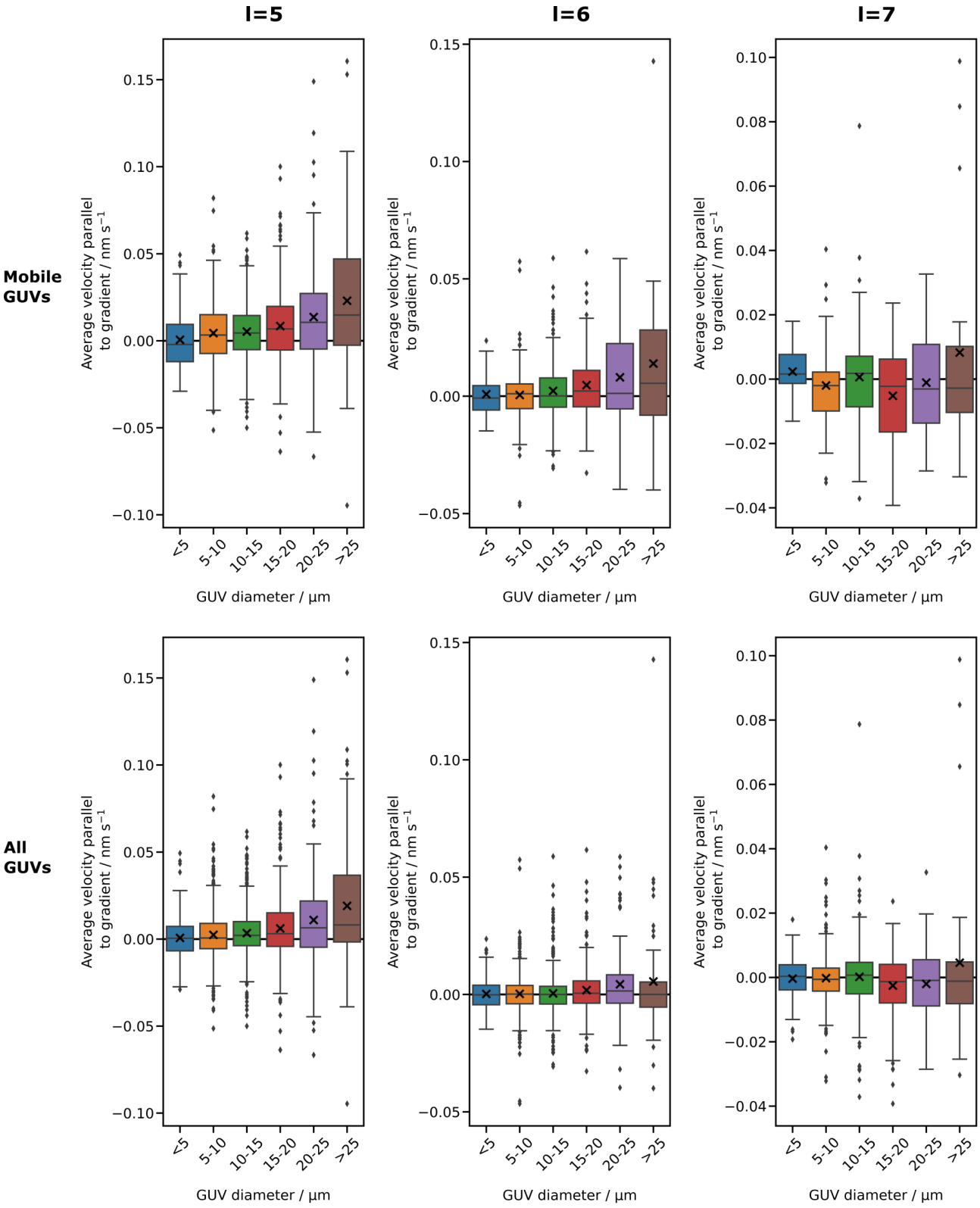


Figure C.7: **Full distributions of average vesicle velocity parallel to the gradient binned by vesicle size, from experimental data.** Data are shown for sticky end lengths $l = 5$, 6 and 7 nt. These plots are the equivalent of the experimental data plotted in Figure 3.16, but in this case data are plotted for the filtered (mobile) vesicle population and for all vesicles combined, and all outliers are shown. The average vesicle velocities have been calculated as total displacement parallel to the gradient divided by the trajectory duration, where positive values indicate motion along the gradient in the direction of increasing ligand density. The mean of the distribution for each vesicle size range is marked with a cross.

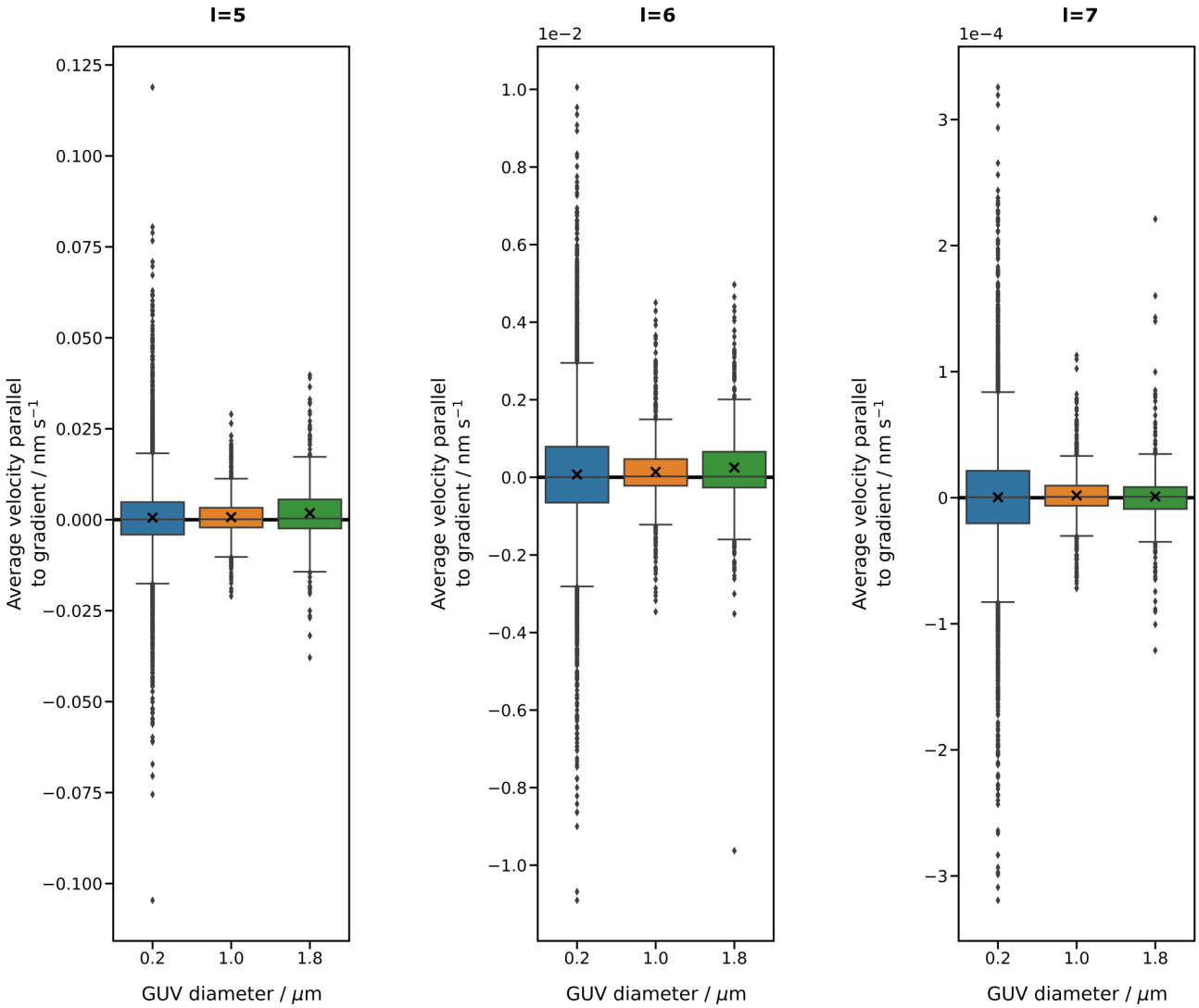


Figure C.8: **Full distributions of average vesicle velocity parallel to the gradient binned by vesicle size, from simulation results.** Data are shown for sticky end lengths $l = 5$, 6 and 7 nt. These plots are the equivalent of the simulation data plotted in Figure 3.16, but in this case all outliers are shown. The average vesicle velocities have been calculated as total displacement parallel to the gradient divided by the trajectory duration, where positive values indicate motion along the gradient in the direction of increasing ligand density. The mean of the distribution for each vesicle size range is marked with a cross.

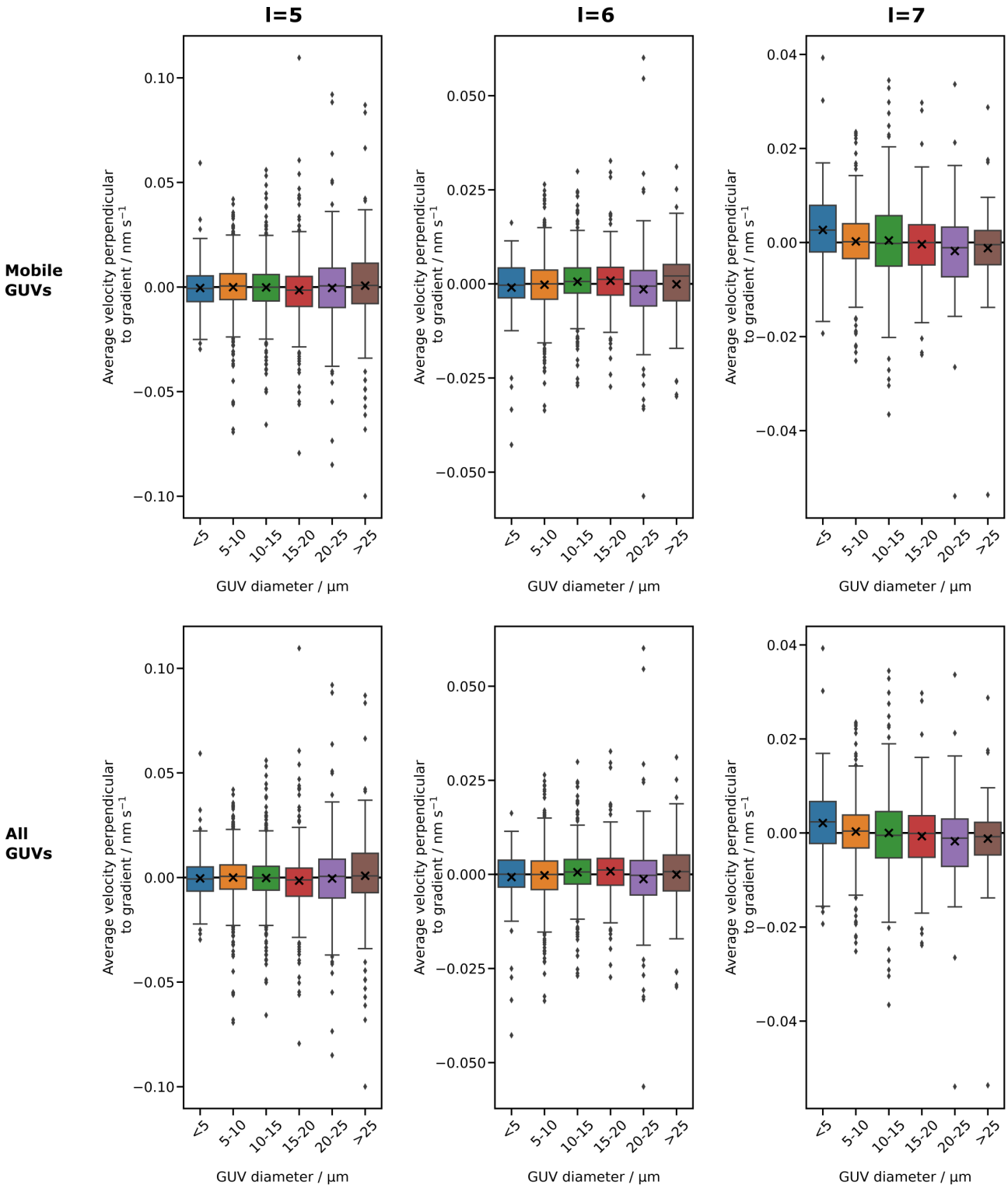


Figure C.9: **Full distributions of average vesicle velocity perpendicular to the gradient binned by vesicle size, from experimental data.** Data are shown for sticky end lengths $l = 5$, 6 and 7 nt. These plots are the equivalent of the experimental data plotted in Figure 3.17, but in this case data are plotted for the filtered (mobile) vesicle population and for all vesicles combined, and all outliers are shown. The average vesicle velocities have been calculated as total displacement perpendicular to the gradient divided by the trajectory duration. The mean of the distribution for each vesicle size range is marked with a cross.

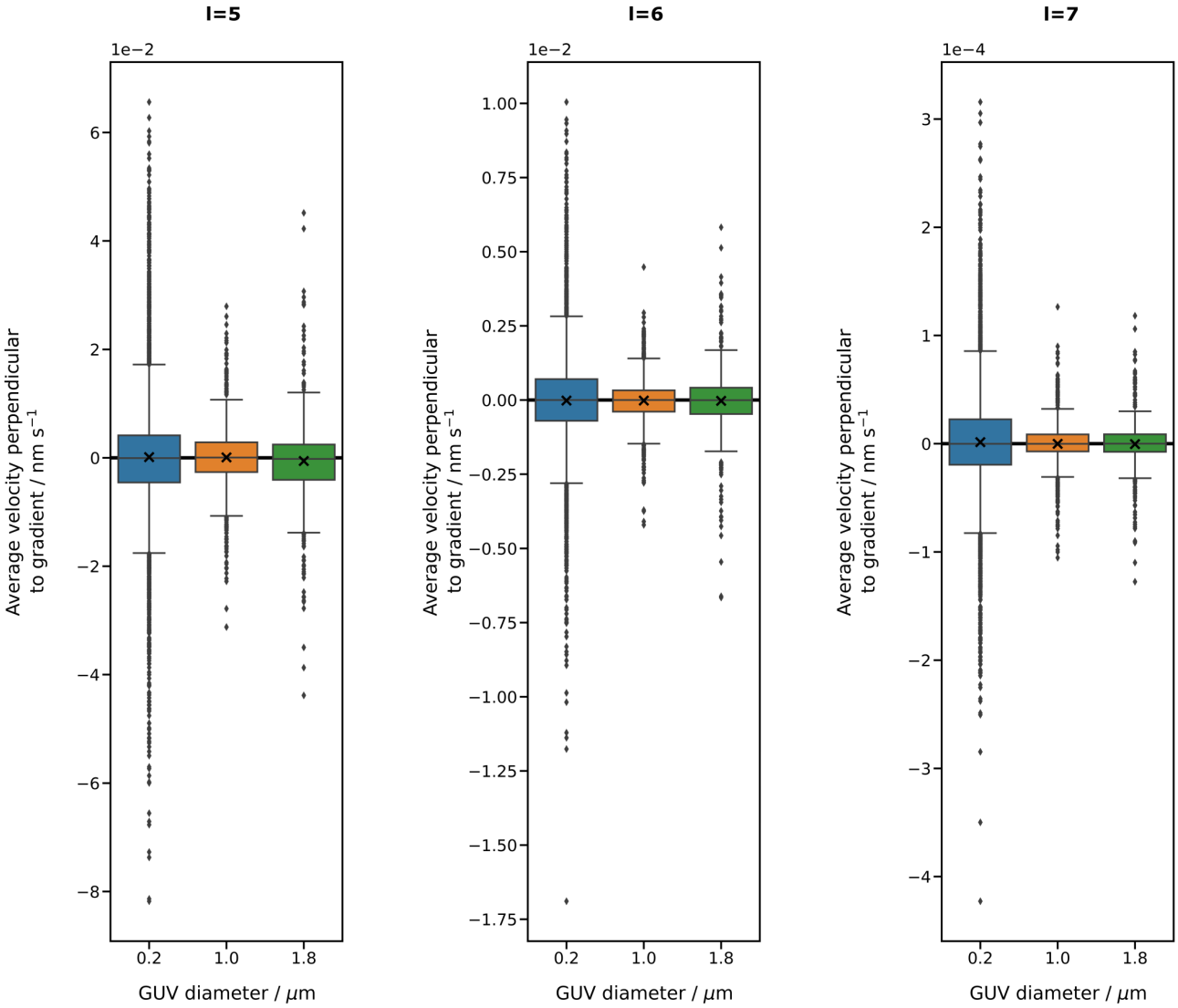


Figure C.10: **Full distributions of average vesicle velocity perpendicular to the gradient binned by vesicle size, from simulation results.** Data are shown for sticky end lengths $l = 5$, 6 and 7 nt. These plots are the equivalent of the simulation data plotted in Figure 3.17, but in this case data are plotted for the filtered (mobile) vesicle population and for all vesicles combined, and all outliers are shown. The average vesicle velocities have been calculated as total displacement perpendicular to the gradient divided by the trajectory duration. The mean of the distribution for each vesicle size range is marked with a cross.

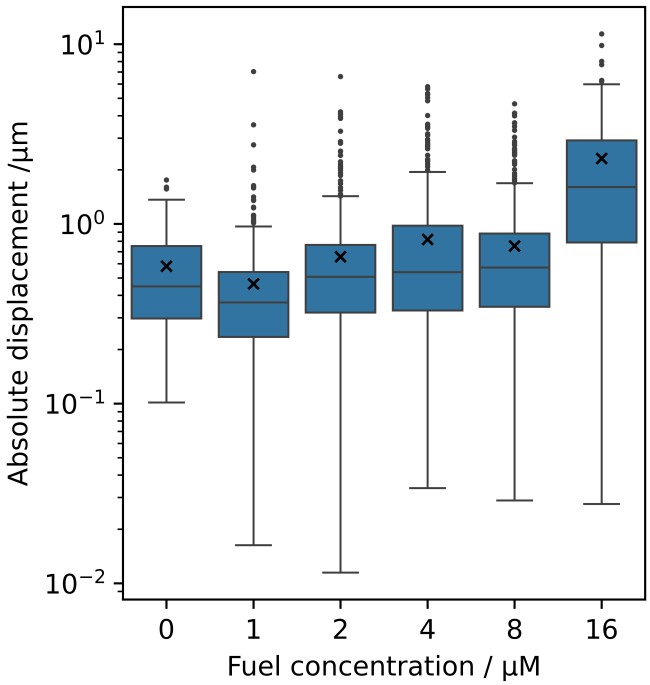


Figure C.11: **Full distributions of absolute vesicle displacement for varying fuel concentration in the burnt-bridges adaptation of the vesicle motility system.** The box plots show the distributions of absolute vesicle displacement over 19.5 hours, in burnt-bridges vesicle motility experiments described in Section 4.6.1. This plot corresponds to the same data shown in Figure 4.14, except that data for all vesicles are shown, as opposed to being filtered to the mobile vesicle population. The concentration of the fuel strand F has been varied up to 16 μM.

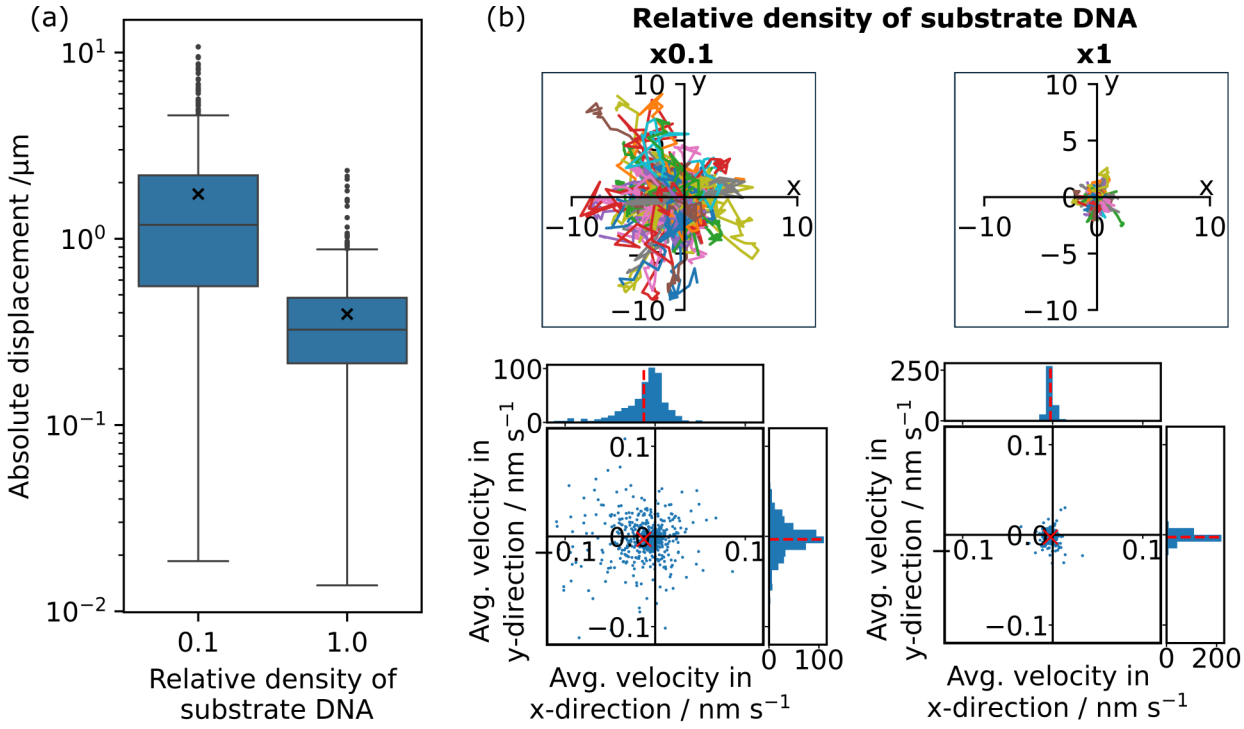


Figure C.12: **Full data from burnt-bridges vesicle motility experiments where the density of substrate DNA has been varied.** The plots show data for all vesicles in experiments discussed in Section 4.6.2. This figure corresponds to the same data shown in Figure 4.15, except that data for all vesicles are shown, as opposed to being filtered to the mobile vesicle population. The relative density of the substrate construct S has been set to either 0.1 or 1.

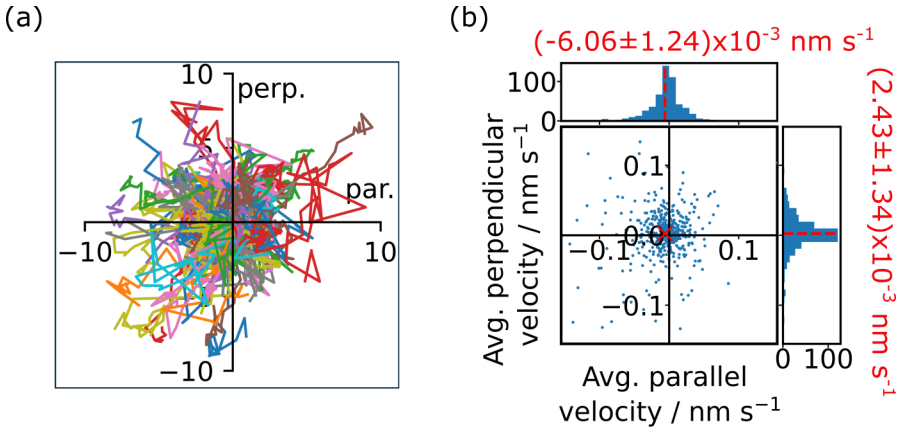


Figure C.13: **Full data from burnt-bridges vesicle motility experiments, comparing vesicle motion to the direction of the gradient.** The plots show the trajectories and average velocity distributions relative to the gradient direction, for all vesicles in experiments discussed in Section 4.6.3. This figure corresponds to the same data shown in Figure 4.16, except that data for all vesicles are shown, as opposed to being filtered to the mobile vesicle population; also, the axis limits in (b) have been set to include all data points, rather than cropping outliers. The axes in (a) are in distance units of microns. The means of the distributions in (b) are labelled and annotated in red.